

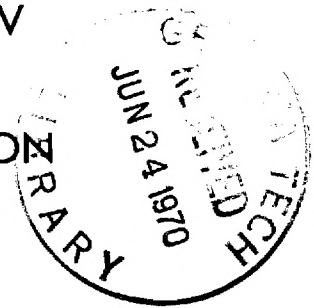
# IONIZATION AND CHARGE TRANSFER CROSS SECTIONS

FOR  $H^0$ ,  $He^0$ , and He BEAMS

IN THE ENERGY RANGE 0.15-1.00 MeV

and

DESIGN of A DIFFERENTIAL RECOIL-ION  
ANALYZER



by L. J. Puckett

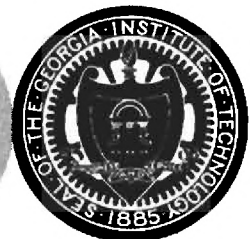
D. W. Martin

G. O. Taylor

Contract No. AT-(40-1)-2591

U. S. ATOMIC ENERGY COMMISSION  
OAK RIDGE, TENNESSEE

November 1, 1967



School of Physics  
GEORGIA INSTITUTE OF TECHNOLOGY  
Atlanta, Georgia

GEORGIA INSTITUTE OF TECHNOLOGY  
School of Physics  
Atlanta, Georgia 30332

TECHNICAL REPORT  
IONIZATION AND CHARGE TRANSFER CROSS SECTIONS  
FOR  $H^0$ ,  $He^0$ , AND  $He^{++}$  BEAMS  
IN THE ENERGY RANGE 0.15-1.00 MeV  
AND  
DESIGN OF A DIFFERENTIAL RECOIL-ION ANALYZER

By

L. J. Puckett  
D. W. Martin  
G. O. Taylor

USAEC REPORT NO.  
ORO-2591-35

Contract No. AT-(40-1)-2591  
U. S. Atomic Energy Commission  
Oak Ridge, Tennessee

November 1, 1967



## PREFACE

The text of this report is identical to that of a thesis submitted by Lawrence J. Puckett to the faculty of the Graduate Division of the Georgia Institute of Technology, in partial fulfillment of the requirements for the degree of Doctor of Philosophy. Having satisfied all other requirements, Dr. Puckett has been awarded this degree, and is now on active duty with the U.S. Army, stationed at the Ballistic Measurements Laboratory, Ballistic Research Laboratories, Aberdeen Proving Ground, Maryland.

The thesis treats in detail the results of essentially all of the measurements of ionization and charge transfer cross sections performed under Contract No. AT-(40-1)-2591 during a period of somewhat more than two years, up to about the end of 1966. Included are extensions of the earlier gross positive ion and electron production cross sections for incident  $\text{He}^{++}$  ions, and all of the similar measurements for incident neutral  $\text{H}^0$  and  $\text{He}^0$  atoms. An article summarizing these results is in preparation for submission to The Physical Review. However, the thesis contains a far more detailed treatment of the experimental apparatus and of the special difficulties encountered in these measurements than would be permissible in a journal article. In addition, the thesis treats in detail the design of a differential charge state and momentum analyzer for the slow recoil ions formed in ionizing single collisions, designed to serve as one component of a differential coincidence analyzer apparatus. Included are the results of a (non-coincidence) study of the charge states of the recoil ions formed by fast protons in helium, and of a similar preliminary study for fast protons in argon. A brief article summarizing these helium results is also in preparation for publication, but no detailed publication on the construction of the analyzer apparatus is

and title page? Imperfect volumes delay return of binding. Thanks.

A 344

BOUND BY THE NATIONAL LIBRARY BINDERY CO. OF GA.

anticipated separate from an eventual description of the entire coincidence apparatus.

Because of the large amount of experimental detail in this thesis which has not been published, it has been decided to issue the thesis in its entirety as a Technical Report. It is expected that the report will continue to be useful as a source for some of this detail even after the eventual publication of the results.

None of the companion work on optical excitation cross section measurements conducted under this same contract is included in this report.

## TABLE OF CONTENTS

	Page
PREFACE . . . . .	ii
LIST OF TABLES . . . . .	vii
LIST OF ILLUSTRATIONS . . . . .	viii
SUMMARY . . . . .	xii
Chapter	
I. INTRODUCTION . . . . .	1
PART A	
II. PHENOMENA ASSOCIATED WITH THE PASSAGE OF A FAST BEAM OF IONS OR ATOMS THROUGH A GAS . . . . .	7
III. APPARATUS AND TECHNIQUES EMPLOYED TO OBTAIN ION AND ATOM BEAMS OF SPECIFIED CHARACTER . . . . .	20
The Beam Source and Energy Determination	
The Gas Cell	
The Electrostatic Analyzer	
PART B	
IV. APPARATUS AND TECHNIQUES EMPLOYED FOR THE MEASUREMENT OF THE TOTAL "APPARENT" ION AND ELECTRON PRODUCTION CROSS SECTIONS . . . . .	32
The Collision Chamber and Associated Beam Collimator	
The Fast Beam Detector	
The Ion and Electron Collection Electrodes	
V. EXPERIMENTAL RESULTS FOR THE CROSS SECTIONS $\sigma_+$ AND $\sigma_-$ . . .	58
Summary of Experimental Procedures and Discussion of Errors	
Present Results and Comparison with Other Experimental and Theoretical Results	
Conclusions	

## TABLE OF CONTENTS (Continued)

	Page
PART C	
VI. APPARATUS AND TECHNIQUES EMPLOYED IN THE MEASUREMENTS OF THE PARTIAL IONIZATION CROSS SECTIONS . . . . .	112
Discussion of Some Fundamental Design Considerations	
General Description of Apparatus	
The Beam Collimator	
The Beam Detector	
The Collision Chamber	
The Spectrometer	
The Ion Detector	
VII. EXPERIMENTAL PROCEDURES FOR THE MEASUREMENT OF PARTIAL IONIZATION CROSS SECTIONS. . . . .	145
Evaluation Tests of Apparatus	
Procedures for Relative Cross Section Measurements	
Calculation of Absolute Cross Sections	
VIII. EXPERIMENTAL RESULTS FOR THE PARTIAL IONIZATION CROSS SECTIONS . . . . .	165
Present Results and Comparison with Other Experimental Data	
Discussion of Errors	
Conclusions	
APPENDICES. . . . .	175
I. DETERMINATION OF THE NEUTRAL BEAM INTENSITY. . . . .	176
II. DETERMINATION OF APPARENT CROSS SECTIONS FROM EXPERIMENTAL OBSERVABLES . . . . .	184
III. THE USE OF A McLEOD MANOMETER TO MEASURE GAS PRESSURES BETWEEN $10^{-2}$ AND $10^{-5}$ TORR . . . . .	187
Introduction	
Operating Principles of the McLeod Gauge	
Systematic Errors	
Preparation of the McLeod Gauge for Pressure Measurement	
Operational Procedure	
Conclusions	

## TABLE OF CONTENTS (Concluded)

	Page
IV. ALIGNMENT OF ANGULAR ROTATION MECHANISM . . . . .	213
BIBLIOGRAPHY . . . . .	216
VITA . . . . .	222
ERRATA . . . . .	223

## LIST OF TABLES

Table		Page
1.	Estimated Random Errors (%) in $\sigma_+$ and $\sigma_-$ . . . . .	61
2.	Total Estimated Errors (%) in $\sigma_+$ and $\sigma_-$ . . . . .	63
3.	Apparent Cross Sections for Production of Positive Ions $\sigma_+$ and Electrons $\sigma_-$ by an Incident Beam of $\text{He}^{++}$ . . .	64
4.	Apparent Cross Sections for Production of Positive Ions $\sigma_+$ and Electrons $\sigma_-$ by an Incident Beam of $\text{He}^0$ . . .	74
5.	Apparent Cross Sections for Production of Positive Ions $\sigma_+$ and Electrons $\sigma_-$ by an Incident Beam of $\text{H}^0$ . . . .	83
6.	Cross Sections for Production of $\text{He}^+$ and $\text{He}^{++}$ Ions in Helium Gas by Incident Protons. . . . .	166
7.	Preliminary Cross Sections for Production of $\text{Ar}^{n+}$ , $n = 1, 2, 3$ , and $4$ , in Argon Gas by Incident Protons . . . .	171
8.	Molecular Diameters. . . . .	203

## LIST OF ILLUSTRATIONS

Figure		Page
1.	Schematic View of Beam Preparation Apparatus . . . . .	21
2.	Calculated He Pressures in Gas Cell as a Function of Beam Energy for $H^0$ and $He^0$ to Attain 90 Percent Maximum Intensity. . . . .	23
3.	Calculated Pressures for which Beams of $H^0$ , $He^0$ , and $He^{++}$ Will Undergo No More than One Percent Collision of a Charge Changing Nature. . . . .	25
4.	Relationship of Gas Cell Pressure to Pressure in Electrostatic Analyzer. . . . .	27
5.	Schematic Diagram of Apparatus Employed in the Measurements of the Total Apparent Cross Sections. . . . .	33
6.	Exterior View of Electrostatic Analyzer and Collision Chamber. . . . .	34
7.	Schematic Diagram of Beam Collimator and Collision Chamber Components Employed in the Measurements of the Total Apparent Cross Sections. . . . .	36
8.	Schematic Diagram of the Fast Beam Detector. . . . .	42
9.	Slow Ion and Electron Collection Structure, and Fast Beam Detector . . . . .	48
10.	Response of the Ion and Electron Currents, Produced by $H^+ \rightarrow Ar$ , to the Collection Voltage. . . . .	52
11.	Response of the Ion and Electron Currents, Produced by $He^{++} \rightarrow Ar$ , to the Collection Voltage. . . . .	54
12.	Schematic Diagram of the Electrical Connections to the Collection Assembly. . . . .	55
13-16.	Total Apparent Cross Sections for Production of Positive Ions, $\sigma_+$ , and of Free Electrons, $\sigma_-$ , for $He^{++}$ Ions Incident on:	
13.	Helium . . . . .	65
14.	Argon. . . . .	66
15.	Molecular Hydrogen . . . . .	67
16.	Molecular Nitrogen . . . . .	68

## LIST OF ILLUSTRATIONS (Continued)

Figure		Page
17-20.	Cross Correlation Between the Total Apparent Ion and Electron Production Cross Sections, and the Total Electron Capture Cross Sections for $\text{He}^{++}$ Ions Incident On:	
17.	Helium . . . . .	69
18.	Argon. . . . .	69
19.	Molecular Hydrogen . . . . .	70
20.	Molecular Nitrogen . . . . .	70
21-24.	Total Apparent Positive Ion and Electron Production Cross Sections, and the Total Apparent Stripping Cross Sections, for $\text{He}^0$ Atoms Incident On:	
21.	Helium . . . . .	75
22.	Argon. . . . .	76
23.	Molecular Hydrogen . . . . .	77
24.	Molecular Nitrogen . . . . .	78
25-28.	Total Apparent Positive Ion and Electron Production Cross Sections, and the Stripping Cross Sections for $\text{H}^0$ Atoms Incident On:	
25.	Helium . . . . .	84
26.	Argon. . . . .	85
27.	Molecular Hydrogen . . . . .	86
28.	Molecular Nitrogen . . . . .	87
29-31.	Total Apparent Cross Sections for the Production of Positive Ions of Helium, Molecular Hydrogen, Molecular Nitrogen, and Argon by Incident:	
29.	$\text{He}^{++}$ Ions. . . . .	91
30.	$\text{He}^0$ Atoms. . . . .	92
31.	$\text{H}^0$ Atoms . . . . .	93
32-34.	Total Cross Sections for the Production of Free Electrons in Helium, Molecular Hydrogen, Molecular Nitrogen, and Argon by the Impact of:	
32.	$\text{He}^{++}$ Ions. . . . .	94
33.	$\text{He}^0$ Atoms. . . . .	95
34.	$\text{H}^0$ Atoms . . . . .	96
35-38.	Total Apparent Ionization Cross Sections $\sigma_i$ , for Hydrogen and Helium Ions and Atoms in Several Gases. Shown for Comparison is the Calculated Curve:	

$$\sigma_i = A Z^2 \frac{M}{E} \ln \left( \frac{BE}{M} \right)$$

with A and B Evaluated (for each target) from Corres-



## LIST OF ILLUSTRATIONS (Continued)

Figure		Page
	ponding Proton Data, for $Z = 1$ and $2$ . Also Shown for Comparison are the Existing Theoretical Calculations that are Pertinent to These Measurements. The Target Gases Are:	
35.	Molecular Hydrogen . . . . .	101
36.	Helium . . . . .	102
37.	Argon. . . . .	103
38.	Molecular Nitrogen . . . . .	104
39.	Overall Drawing of Apparatus Employed for the Measurements of Partial Cross Sections . . . . .	121
40.	Detailed Drawing of Collision and Analysis Regions . . . . .	124
41.	Plane View of the Field-Free Collision Region. . . . .	132
42.	Plane View of the Collision Region with Repeller Electrode Installed. . . . .	133
43.	Isometric Drawing of Repeller Electrode. . . . .	135
44.	Wiring Diagram of Electron Multiplier. . . . .	143
45.	Response of Ion Count Rate of Multiplier to Inter-dynode Voltage . . . . .	146
46.	Response of Multiplier Ion Count Rate to Ion Acceleration Voltage . . . . .	148
47.	Profile of Count Rate as Beam was Swept Across the Spectrometer Exit Slit . . . . .	150
48.	Response of Ion Count Rate of Multiplier to Repeller Voltage. . . . .	152
49.	Limiting Pressure for Thin Target Conditions . . . . .	154
50.	Partial Cross Sections for Production of $\text{He}^+$ and $\text{He}^{++}$ Ions by Incident Protons . . . . .	167
51.	Partial Cross Sections for Production of $\text{Ar}^{n+}$ ( $n = 1, 2, 3$ , and $4$ ) by Incident Protons . . . . .	172
52.	Response of the Thermocouple of the Neutral Particle Detector to the Impinging Beam . . . . .	178

## LIST OF ILLUSTRATIONS (Concluded)

Figure		Page
53.	Schematic Diagram of Electrical Connections Employed in the Calibration of the Neutral Beam Detector. . . . .	180
54.	McLeod Gauge . . . . .	190
55.	Plot of Modified McLeod Gauge Equation for This Gauge . . . . .	196
56.	Indicated McLeod Gauge Correction Factor for the Gaede Effect . . . . .	204

## SUMMARY

Absolute total apparent cross sections have been measured for the processes leading to electron and ion production in the gases He, Ar, H<sub>2</sub>, and N<sub>2</sub> by incident beams of He<sup>++</sup>, He<sup>0</sup>, and H<sup>0</sup> in the energy range 0.15 to 1.00 MeV. From these measurements absolute total apparent cross sections for ionization, electron capture, and stripping were deduced. In the same energy range, the relative cross sections were measured for production of He<sup>+</sup> and He<sup>++</sup> in helium gas by incident H<sup>+</sup>. These relative cross sections were normalized through the use of previous measurements made in this laboratory to obtain absolute cross sections. Also, preliminary results are presented on the cross sections for production of Ar<sup>+</sup> through Ar<sup>4+</sup> in argon gas by fast H<sup>+</sup>.

The primary source of the fast beams used in this investigation was a 1 MV Van de Graaff positive ion accelerator. The beams of H<sup>0</sup>, He<sup>0</sup>, and He<sup>++</sup> were obtained by allowing the H<sup>+</sup> and He<sup>+</sup> beams supplied by the accelerator to undergo charge changing collisions in a gas cell. The composite beam that emerged from the gas cell was separated into its various charge components in an electrostatic analyzer. The beam of the selected charge state was then passed into the collision region of the apparatus which followed.

For measurements of the total apparent electron and ion production cross sections, the collision chamber employed in the apparatus contained two parallel arrays of plates (arranged like a condenser) between which the beam passed. The slow ions and electrons created in the beam colli-

sions with the gas were collected on these plates by a uniform electrostatic collection field. The currents produced by the collected electrons and ions were measured on sensitive electrometers. The fast beams were trapped in a detector that served any one of three purposes. It could be used to measure (1) the net current of the beam, (2) the secondary emission current produced by the beam striking a copper foil in the detector, or (3) the net beam power, from which the "particle-current" for a neutral beam could be determined. The target gas pressure was measured by means of a cold-trapped McLeod gauge, and the possible errors associated with the use of this type of gauge are extensively discussed.

The present measurements of the total apparent electron capture cross sections for incident  $\text{He}^{++}$  are compared with the results obtained by L. I. Pivovar, et al., S. K. Allison, and V. S. Nikolaev, et al. In contrast to the present results, all of the comparison results were obtained in experiments that employed the observation of the change in the charge state of the fast beam. The agreement between the present results and those shown for comparison is generally good. It is pointed out that the disagreement among some of the comparison results is beyond the experimental errors.

The present measurements of the total apparent ionization cross sections for  $\text{He}^{\circ}$  and  $\text{H}^{\circ}$  projectiles are compared with those results of E. S. Solov'ev, et al. extending up to 0.18 MeV. Their comparison results were obtained in a similar apparatus to that which was used in the present experiment. Comparisons were also made with theoretical calculations of the ionization of  $\text{H}^{\circ}$  by incident  $\text{H}^{\circ}$  (D. R. Bates and G. Griffing) and by  $\text{He}^{\circ}$  (D. R. Bates and A. Williams). Simple procedures were used to scale

the theoretical results for the atomic target to the molecular target used in this experiment and agreement within the experimental error limits was obtained in every case.

The total stripping cross sections for the  $H^0$  projectile were compared with the results of Solov'ev and C. F. Barnett, et al. Comparisons were also made with the theoretical cross section for stripping of  $H^0$  incident on  $H^0$  (Bates and Griffing)—scaled to a molecular hydrogen target—and with the calculation of the stripping of  $H^0$  incident on He (Bates and Williams). The present results agree within the experimental error limits with Barnett's results and with theory, and in most cases with the results of Solov'ev. Reasons are presented to support the belief that the present results are more accurate than those of Solov'ev.

The results obtained with the  $He^0$  projectile for the total apparent ionization cross sections are generally in good agreement with those of Solov'ev. However, the total apparent stripping cross sections in both the present and Solov'ev's results for the  $He^0$  projectile were usually about 40 percent greater than similar quantities measured by Allison, Pivovar, et al., and Barnett, et al. Conclusions pertaining to this discrepancy are discussed.

The present results for the total apparent ionization cross sections are combined with those for  $H^+$  and  $He^+$ , which were previously measured in this laboratory, to provide a general comparison for all of the hydrogen and helium projectiles. The functional dependence of the ionization cross sections derived from the Bethe-Born approximation predicts that point charge projectiles of equal charge and velocity should have equal cross sections. In this cross section expression, the scaling pro-

cedure between various point-charge projectiles is straightforward and was used to compare the  $H^+$  and  $He^{++}$  cross sections at equivelocity. In the upper energy range of this investigation, the agreement was quite good.

The Bethe-Born cross section expression is strictly valid only for point-charge ions, and therefore it was of interest to determine the relationship between the non-point-charge atomic projectiles ( $He^{\circ}$  and  $H^{\circ}$ ) and the point-charge ions ( $H^+$  and  $He^{++}$ ). It was found that the ionization cross sections for incident  $H^{\circ}$  were uniformly lower than those of  $H^+$  by a factor of 0.64 in all four target gases. This constant offset in the  $H^{\circ}$  curve implied that the  $H^{\circ}$  projectile exhibited an effective charge equal to  $\sqrt{0.64} = 0.80$  of the proton charge. However, the same sort of uniform offset in the  $He^{\circ}$  cross section curves was not observed. In fact the separation of the two curves ranged from about zero to  $He^{\circ}$  being about a factor of 1.2 greater than  $H^+$ . It is concluded that the Born approximation calculations for the ionization collisions observed in this experiment are essentially correct for velocities greater than about  $5 \times 10^6$  m/sec, and in some cases agreement between experimental and theoretical results is obtained at even lower velocities.

A completely different apparatus was employed for the measurement of the relative cross sections for production of ions of specified charge states. In this apparatus, the collision chamber was located on top of a vertical axle. The slow ion spectrometer and beam detector were mounted on rather massive counterbalanced supports affixed to separately rotate on precision bearings about the common axle. The beam collimator, the spectrometer collimator, and the beam detector protruded through flexible

bellows into the chamber and were aimed at a common point on the rotation axis.

The detector for the proton beam was a shielded Faraday cup. The spectrometer employed a set of accelerating and focusing electrodes for the slow recoil ions and a  $60^\circ$  sector magnetic field for charge-to-mass and momentum analyses of the ions in a 5 cm radius-of-curvature geometry. Postanalysis acceleration into an electron multiplier detector was employed to provide near 100 percent ion detection efficiency.

In this apparatus, the beam was allowed to undergo collisions in two different environments. When a determination of the angular distribution of the recoil ions was attempted, a field-free collision region was employed. However, when the results showed no perceptible angular dependence, tests were undertaken which demonstrated that virtually all of the recoil ions had energies considerably less than two electron volts. Even so, it was expected that the angular spectrum of the recoil ions would be sharply peaked around  $90^\circ$ . However, considerations of the thermal motion of the target gas indicated that the expected peaks in the angular distribution, corresponding to the low energy ions that were observed, would be so broadened as to be difficult to detect. It was concluded that a heavy projectile-target combination was necessary to produce sufficient energy transfer so that the thermal motion of the target would not mask the angular distribution of the recoil ions. It was also concluded for the case of  $H^+$  incident on He that a collection field could be reliably and efficiently employed to sweep the ions into the spectrometer. The measurements with a collection field served to determine the relative cross sections for production of variously charged ions irrespective of their recoil an-

gles.

Excellent agreement was obtained between the present cross sections for production of  $\text{He}^+$  and  $\text{He}^{++}$  and those of Solov'ev up to 0.18 MeV and Wexler extending upwards from 0.80 MeV. It was observed that the cross section for production of  $\text{He}^{++}$  was less than one percent of the total ionization cross sections for all but the lowest energies employed in this investigation. In accordance with the prediction of the Born approximation, good agreement was obtained at the higher energies between the cross sections for production of  $\text{He}^+$  by protons and equivalent electrons. However, for the  $\text{He}^{++}$  production, the electron cross sections were about a factor of two larger. It thus appeared that the scaling procedure suggested by the form of the Born cross section expression was not as applicable to multiple ionization as for single (or total) ionization cross sections.

Preliminary cross section results are presented for the formation of the first four ions in argon by incident protons. Generally good agreement was obtained between the present results and those of Solov'ev and Wexler for the first two ions. However, for  $\text{Ar}^{3+}$  the present results are about a factor of ten greater than those of Solov'ev, and in rather good agreement with Wexler, whose extrapolated results are about a factor of eight greater than those of Solov'ev.

It appears that the equivalent electron cross sections for multiple ionization of argon are in substantially better agreement with the proton cross sections than they were in the helium target. Perhaps this indicates that the assumptions in the Born approximation are valid to



lower velocities for a light target such as helium.

Numerous tests were employed, and the results are discussed, to establish the validity of all of the cross section measurements presented herein.

## CHAPTER I

### INTRODUCTION

This investigation concerned the measurement of the total apparent cross sections for ion and electron production, from which apparent ionization, electron capture, and stripping cross sections were deduced. Also measured, in a separate apparatus, were the cross sections for production of slow ions of specified charge state, which, hereinafter, will be denoted as "partial ionization cross sections." The ionizing projectiles are helium and hydrogen ions and atoms in the energy range from 0.15 to 1.00 MeV. This cross section terminology is explained in detail in Chapter II; however, in order to understand the following remarks, it is sufficient to note that a measurement of a cross section for a particular event is related to the probability that the event will occur.

The ionizing and charge changing collisions associated with the passage of ions and atoms through gaseous targets are of both theoretical and applied value. Several direct practical applications are found, for example, in the field of controlled thermonuclear research. A common method of supplying a plasma with ions is through high energy injection into the containment vessel. The two problems that arise here are concerned with trapping and containment inside the vessel. In trapping a beam incident into the containment field from outside, the interest is in:

- a. dissociation cross sections for the case of molecular ion injection;

b. ionization cross sections for the case of neutral particle injection, and

c. formation of excited states for the trapping of excited neutrals by Lorentz ionization.

Consequently, a knowledge of the ionization cross sections for light high energy projectiles in various gases is of significant value.

In containment of a plasma for a sufficient time to allow it to react efficiently, when it is already trapped, the main interest is in charge changing collisions in background gas, leading to loss of ions from the plasma. In addition, these cross sections enter into consideration of a number of upper atmospheric phenomena. The density of ions and electrons in the upper atmosphere is determined to some extent by ionizing and charge changing reactions for particles from space. The capture and loss mechanisms of the Van Allen radiation belts depend on these cross sections, as well as the operation of simple laboratory gas-filled particle detectors.

A fundamental theoretical value of these measurements is that they provide checks on calculations of the magnitudes and energy dependencies for the cross sections. In principle, quantum mechanical calculations could be made for any atomic collision process if a complete set of wave functions for the partners in a collision were known. However, detailed theoretical calculations have been made only for the simplest cases, i.e., those involving electrons, protons, neutral hydrogen atoms, and singly and doubly charged helium ions as projectiles incident on targets of atomic hydrogen, helium, and lithium. Even for most of these simple cases the calculations were difficult and involved approximations whose validity

is difficult to assess except by resort to comparison with experimental results.

Most of the existing calculations for ionization processes at high energies have been made in the Born approximation. A very valuable check on this approximation is possible in the present experiment, because the projectile energies extend well into the asymptotic region where the approximation is expected to be valid.

The early experimental investigations of ionization by fast ions and atoms prior to 1951 has been thoroughly surveyed by Massey and Burhop.<sup>1</sup> The experimental work published up through the beginning of 1965 is well covered by the surveys of Allison,<sup>2</sup> Allison and Garcia-Munoz,<sup>3</sup> Fedorenko,<sup>4</sup> McDaniel,<sup>5</sup> and Nikolaev.<sup>6</sup>

It should be noted that the present investigation is divided into two rather distinct phases, and the thesis is accordingly divided into Part A, which deals with the aspects common to both phases, and into Parts B and C, which deal with the separate phases of investigation. Part A (Chapters II-III) contains a general introduction to the phenomena associated with the passage of high energy particles through a gas, and specifically the methods employed to obtain the high energy particle beams used in this experiment. Part B (Chapters IV-V) deals with the measurement techniques, the apparatus, and the results for the total apparent cross sections, while Part C (Chapters VI-VIII) pertains to the techniques, apparatus, and results for the measurements of the partial ionization cross sections.

The present results for the total apparent ionization cross sections and the partial ionization cross sections represent an extension into a

hitherto unexplored energy range for the  $H^0$ ,  $He^0$ , and  $He^{++}$  projectiles. However, Solov'ev, et al.<sup>7,8</sup> have published measurements up to 0.18 MeV on these total and partial cross sections and they are shown for comparison with the present results in Chapters V and VIII. During the period of this investigation, Wexler<sup>9</sup> performed some measurements on the partial ionization cross sections in the energy range 0.80 to 3.75 MeV. These results are also shown for comparison with the present measurements.

The results of the investigators mentioned thus far are the only measurements that compare with the directly observed quantities in this work. However, from the direct measurements of this investigation, the total apparent electron capture cross section for the ionic projectile, and the total apparent stripping cross sections for the atomic projectiles may be deduced as explained in Chapter II. The experimental results of Allison,<sup>2</sup> Pivovarov, et al.,<sup>10,11</sup> Barnett, et al.,<sup>12,13</sup> and Nikolaev, et al.<sup>14</sup> on the electron capture and stripping cross sections, together, completely span the energy range of this work and serve as comparisons for the present data.

As was previously mentioned, theoretical calculations of these cross sections are available only for the simplest cases; those that are pertinent to this investigation are the following:

1. ionization of atomic hydrogen by  $H^+$  (Bates and Griffing<sup>15</sup>);
2. ionization of atomic hydrogen by  $He^+$  (Boyd, et al.<sup>16</sup>);
3. ionization of helium by  $H^+$  (Mapleton<sup>17</sup>);
4. stripping of atomic hydrogen projectiles in collision with helium, or conversely, ionization of atomic hydrogen by incident  $He^0$  (Bates and Williams<sup>18</sup>); and

5. stripping of atomic hydrogen on atomic hydrogen, or conversely, ionization of atomic hydrogen by atomic hydrogen (Bates and Griffing<sup>19</sup>).

It should be noted, however, that the present investigation did not include an atomic hydrogen target. Consequently, all of the calculations on atomic hydrogen were approximately scaled to a molecular hydrogen target. The scaling procedure used is discussed in each case as it is presented.

PART A

## CHAPTER II

### PHENOMENA ASSOCIATED WITH THE PASSAGE OF A FAST BEAM OF IONS OR ATOMS THROUGH A GAS

The passage of a fast beam of ions or atoms through a gas leads to both elastic and inelastic collisions between the projectile and target particles. An elastic collision may be defined as one in which the kinetic energy of the system is conserved. This implies that there is no change in the total internal energy of the system. In contrast to this type of interaction is the inelastic collision in which an exchange of kinetic and internal energy occurs. This exchange of energy can assume many forms, but it is possible to divide them, according to the observed quantities, into two major groups:

(1) the excitation collision, which is characterized by a change in the atomic state of one or more electrons, or a change in the vibrational or rotational states of the system; and

(2) the charge changing collision, which occurs when the change in internal energy of either particle is sufficient to lead to the ejection of one or more free electrons, or the transfer of electrons between particles.

The latter type of collision involves the strongest of the two interactions, and it is this type of collision with which the present investigation is concerned.

For the purpose of this discussion, it should be noted that there



are three significantly distinct types of collisions that fall under the general category of charge changing collisions as defined above. These are:

- (1) the ejection of free electrons from the target,
- (2) the capture by the projectile of some of the electrons from the target, and
- (3) the ejection of free electrons from the projectile.

The cross section referring to interaction (1) will be designated as "pure ionization," or more simply, "ionization"; the cross section for (2) as "electron capture"; and the cross section for (3) as "stripping." It is possible to have combinations of these three types of events, particularly when many electrons are being rearranged as in the case of collisions between heavy particles.

To illustrate the multiplicity of events that may follow from high energy collisions, the case of fast hydrogen atoms incident on helium was chosen for discussion, because it is both simple and yet representative of the interactions that occurred in this experiment. The heavier targets such as argon, of course, make the number of possible kinds of events more numerous, simply because of the larger number of electrons that may participate in the collision. A further increase in the multiplicity of events arises when molecular targets are used, for these may lead to dissociation fragments that may themselves be multiply ionized. Therefore, to keep the discussion free of unnecessary details, a list of possible reactions for the projectile-target combination of  $\text{H}^0$  on He is presented in Equations 1-5 on the following page.

Reactants		Reaction Products	Cross Section	
$H^0 + He^0$	$\rightarrow$	$H^0 + He^+ + e$	$\sigma_{001}$	(1)
	$\rightarrow$	$H^0 + He^{++} + 2e$	$\sigma_{02}$	(2)
	$\rightarrow$	$H^+ + He^0 + e$	$\sigma_{10}$	(3)
	$\rightarrow$	$H^+ + He^+ + 2e$	$\sigma_{11}$	(4)
	$\rightarrow$	$H^+ + He^{++} + 3e$	$\sigma_{12}$	(5)

The interpretation of the symbols appearing in reaction equations is, from left to right, first the projectile and its charge state, and second the target, before the collision; following the arrow sign, the first symbol indicates the charge state of the projectile, and the remaining symbols, the character of the target molecule, after the collision. The cross section symbols that appear to the right will be explained shortly.

The projectile may or may not have experienced a change in its charge state as a result of the interaction, but in either case both theory and experiment show that it retains essentially all of its initial kinetic energy. However, the kinetic energy acquired by the target may be substantial, although it is small compared to that of the projectile, and as was previously mentioned, the target may be dissociated in addition to changing its charge state.

Reactions 1 and 2 are the only simple ionization events. Reaction 3 is the only simple stripping event. Reactions 4 and 5 represent combinations of the two preceding events. It should be noted that no electron capture event is shown for this projectile-target combination. It has

been indicated<sup>20</sup> that electron capture by  $H^0$  to form  $H^-$  is negligible in the energy range of the present investigation. In the investigation utilizing a  $He^{++}$  projectile, however, it was observed that the electron capture events accounted for a large fraction of the total number of reactions.

For the purpose of the present investigation, the concept of the collision cross section will be used as a means of expressing the probability that some particular event will occur. This concept permits the assignment to the target particle of an effective size, which is related to the probability of the occurrence of a specific event. In order to define a cross section, consider a parallel, monoenergetic beam of  $N_p$  projectiles per second to pass through a target gas of density  $m$  and thickness  $L$  which are sufficiently small such that no projectile undergoes more than one collision. The number of particles per second  $N$  undergoing collisions is proportional to the density of target particles, the number of projectiles, and the target thickness. Thus

$$N = \sigma m N_p L \quad (6)$$

where  $\sigma$  is the constant of proportionality, which has the dimensions of an area, and is defined as the cross section area per particle for the interaction considered. It is important to note that this cross section, or effective size, has no direct relation to the physical dimensions of either the target or projectile.

The cross section notation of Hasted,<sup>21</sup> shown in the right hand column of the list of Equations 1-5, is arranged to convey all the infor-

mation concerning the reaction process that is contained in the reaction equation. The symbols  ${}_{ab}^{\sigma}_{ij}$  represent the cross section for a projectile of charge a, incident on a target of charge b, to undergo a reaction that leads to a final state of the projectile of charge i, and of the target, of charge j. The summation over all experimental values represented by a subscript is denoted in a given reaction by leaving the subscript unspecified.

Measurement of the cross sections characterizing the three fundamental reactions of electron capture, stripping, and ionization may be divided into two major categories as follows:

- (a) observation of the charge states of the beam after it emerges from the collision region, and
- (b) observation of the residual slow particles formed in the collision events.

Most experiments concerned with the measurement of electron capture and stripping cross sections have been of group (a), and involved the direct observation of the fast particle that underwent a change. In contrast, for the measurement of ionization cross sections, most experiments have been of group (b) because the particle that underwent a change was the target. As will be seen later, the experiments of group (b), to which the present experiment belongs, can often be used to obtain measurements on the stripping and electron capture cross sections also. However, the experiments of group (a) cannot be used to measure the ionization cross sections.

Later in this thesis, the results on stripping and electron capture cross sections, obtained in this investigation, will be compared with

those results of other investigators, most of which were measured by the methods of group (a). In order to better understand the significance of the comparisons, a brief description of the relevant experiments and techniques used by the other investigators will be presented here.

The first experiment of group (a) with which the results of this investigation can be compared is that of Allison<sup>22, 23, 24</sup> at the University of Chicago. In 1956 and 1958 his group published results from one apparatus on both the total electron capture cross sections ( $_{20}\sigma_{1j} + _{20}\sigma_{0j}$ ) for  $\text{He}^{++}$  projectiles, and the total stripping cross sections ( $_{00}\sigma_{1j} + _{00}\sigma_{2j}$ ) for  $\text{He}^0$  projectiles in targets of helium, hydrogen, and air, over the energy range 100 to 450 keV. Results were also obtained, by modifying the apparatus, on the double capture and stripping cross sections  $_{20}\sigma_{0j}$ , and  $_{00}\sigma_{2j}$ , respectively.

The experimental procedure used by Allison's group was to prepare the  $\text{He}^0$  and  $\text{He}^{++}$  beam by passing the  $\text{He}^+$  beam produced by the accelerator through a gas cell in which it underwent charge changing collisions. In order to measure the total electron capture or stripping cross sections, the desired beam was passed into an evacuated collision chamber, which was located in a strong magnetic field. By means of this field the  $\text{He}^{++}$  could be deflected into a detector or the  $\text{He}^0$  beam could pass undeflected into the relocated detector. The total cross sections were then determined by observing the attenuation of the beam as the gas pressure in the chamber was increased.

The double electron capture cross sections and the double stripping cross sections were measured in a slightly different manner. In this case the  $\text{He}^{++}$  (or  $\text{He}^0$ ) beam was passed through a collision chamber prior to

entering the magnetic analyzer. The cross sections were determined by observing the growth of the  $\text{He}^0$  (or  $\text{He}^{++}$ ) in the analyzer as the gas pressure in the collision chamber was increased. The range of gas pressure was sufficiently low such that multiple collisions by the projectile were negligible.

The second experiment of group (a) that is of interest for comparison purposes is that of C. F. Barnett<sup>12,13</sup> (1958) at the Oak Ridge Laboratories. He and co-workers have directly measured the total stripping cross sections for  $\text{H}^0$  (between 250 and 1000 keV), and  $\text{He}^0$  (between 4 and 200 keV), which are denoted  $_{00}\sigma_{1j}$  and  $(_{00}\sigma_{1j} + _{00}\sigma_{2j})$ , respectively. Their procedure was essentially that of Allison<sup>22,24</sup> with the exception that a transverse electric field was applied inside the collision chamber, rather than a magnetic field, for the purpose of removing from the beam those projectiles that had undergone stripping reactions.

The third experiment of group (a) with which the results of the present investigation compare is that of Nikolaev, et al.<sup>25</sup> (1961) at Moscow State University. He and co-workers measured the cross section  $_{20}\sigma_{1j}$  for single electron capture by  $\text{He}^{++}$  in the targets of He, Ar, and  $\text{N}_2$  over the energy range of the present experiment. The measurement procedure was essentially that of Allison,<sup>23</sup> i.e., the beam was passed through a gas and then magnetically analyzed to determine the charge state distribution.

The most recent experiment of group (a) of direct interest is that of Pivovarov, et al.,<sup>11</sup> of the Physico-technical Institute U.S.S.R. He published results in 1961 for the single electron stripping cross section  $_{00}\sigma_{1j}$  for  $\text{He}^0$  projectiles, and the single electron capture cross section

$_{20}\sigma_{1j}$  for  $\text{He}^{++}$  projectiles over the energy range and target gases used in the present investigation.

The above data were not measured directly but were obtained in the following manner. A primary beam of singly charged helium ions produced in an electrostatic accelerator was passed through a chamber filled with the target gas. The gas pressure was sufficiently low so that multiple beam collisions were negligible, and of the events that did occur only those that led to electron capture or stripping of the projectile were directly observed. The  $\text{He}^0$  and  $\text{He}^{++}$  thus formed were separated electrostatically and measured. In this manner the cross sections  $_{10}\sigma_{0j}$  and  $_{10}\sigma_{2j}$  were determined for the  $\text{He}^+$  projectile.

One further series of measurements was necessary, however, to obtain the  $_{00}\sigma_{1j}$  and  $_{20}\sigma_{1j}$  cross sections. The collision chamber was modified, and a considerably higher target gas pressure was used to cause the beam to undergo a large number of collisions, in order that the rates of production and destruction of a given charge state of the projectile were in equilibrium. That is, the pressure was sufficiently high such that if it were increased the relative fractions of the beam in charge states  $\text{He}^0$ ,  $\text{He}^+$ , and  $\text{He}^{++}$  would remain constant; these fractions, which are generally rather complicated functions of the individual cross sections, are known as "equilibrium fractions," and are designated as  $F_{0\omega}$ ,  $F_{1\omega}$ , and  $F_{2\omega}$ , respectively. After measuring the equilibrium fractions, it was necessary for Pivovar, et al., to make several simplifying assumptions, which will be discussed later, regarding these fractions in order that they may be used to relate the directly observed values for the  $\text{He}^+$  projectile to the cross sections  $_{00}\sigma_{1j}$  and  $_{20}\sigma_{1j}$  for the  $\text{He}^0$  and  $\text{He}^{++}$

projectiles, respectively.

In 1962 Pivovar, et al.<sup>10</sup> directly measured the cross sections  $20\sigma_{1j}$  and  $20\sigma_{0j}$  for a beam of  $\text{He}^{++}$  projectiles. These direct measurements were made in the same fashion as the previously discussed direct measurements on the  $\text{He}^+$  projectile. The point, that there is substantial difference in the quoted values for  $20\sigma_{1j}$ , from the direct and indirect measurements, and the implications of this discrepancy are discussed in a later chapter.

Thus, the discussion of the general nature of the experiments that comprise group (a) is temporarily concluded.

It is now of interest to discuss the experiments of group (b), which are those that involve the observation of the residual slow collision products. It was previously stated that the present experiment belongs in this group. The only other experiment of this type that has produced results which may be directly compared to those of the present investigation is that of Solov'ev, et al.<sup>26,27</sup> of the Leningrad Physico-technical Institute. In 1961 his group published results on the total apparent ionization cross sections which will be explained shortly, and the stripping cross sections for  $\text{H}^0$  projectiles in the energy range from 10-180 keV. In 1964 results were published for the total apparent ionization cross section for  $\text{He}^0$  projectiles in the same energy range. Comparisons are made between the present results and those of Solov'ev, et al., wherever applicable.

In order to understand the manner in which cross sections are deduced in most experiments of group (b), the present experiment is used as an example.



In the present investigation the thin-target approach was used exclusively, i.e., the density of the target gas was sufficiently low such that the probability of multiple collisions by the projectile was negligible. The analysis of the slow collision products first performed consisted simply of total collection with a transverse electric field. This method served to indicate the total quantities of positive and negative charge that were left in the collision region by the passage of the projectiles. For some projectile-target combinations, a further analysis, consisting of a determination of the distribution in charge-to-mass ratios, was made of the slow positive ions.

The analysis utilizing only the collection field served to give the total apparent cross sections for the production of positive ions  $\sigma_+$  and electrons  $\sigma_-$ . The manner in which these cross sections were deduced from the measured quantities is discussed in Appendix II. The final expressions for  $\sigma_+$  and  $\sigma_-$  for this atomic projectile are

$$[\sigma_+]_{\text{He}^0} = \frac{1}{mL} \frac{I_+}{I_n} \quad (7)$$

$$[\sigma_-]_{\text{He}^0} = \frac{1}{mL} \frac{I_-}{I_n} \quad (8)$$

where

$I^+$ ,  $I^-$  = the positive ion and electron currents, respectively,

to the collection plates,

$m$  = the density of the target gas,

$L$  = the length of the collection plates, and

$I_n$  = the "current" of neutral projectiles.

It is evident that  $\sigma_+$  and  $\sigma_-$  can be represented in terms of the cross sections listed in Equations 1-5 as follows:

$$\sigma_+ = \sigma_{01} + \sigma_{11} + 2(\sigma_{02} + \sigma_{12}) \quad (9)$$

and

$$\sigma_- = \sigma_{01} + \sigma_{10} + 2(\sigma_{02} + \sigma_{11}) + 3\sigma_{12} \quad (10)$$

Thus it is seen that  $\sigma_+$  and  $\sigma_-$  are not simply the sums of the individual cross sections, but instead the measurement of  $\sigma_+$  and  $\sigma_-$  weighs each individual cross section according to the quantity of charge it yields.

It should be noted that further insight into the contributions of the individual cross sections to the measured  $\sigma_+$  and  $\sigma_-$  may be obtained by considering the difference in  $\sigma_+$  and  $\sigma_-$ . For this projectile-target combination this is

$$\sigma_- - \sigma_+ = \sigma_{10} + \sigma_{11} + \sigma_{12} \quad (11)$$

Now if one denotes the total apparent ionization cross section  $\sigma_i$  as the sum of those individual cross sections for which one slow positive ion is formed in the gas plus twice those cross sections that produce two slow positive ions, etc., then Equation 9 for the present case becomes

$$\sigma_+ = \sigma_i \quad (12)$$

Similarly, denote the total apparent stripping cross section  $\sigma_s$  as the sum of those individual cross sections for which one electron is removed from the projectile plus twice those cross sections for removal of two electrons, etc., then Equation 10 becomes for this case

$$\sigma_- = \sigma_i + \sigma_s \quad (13)$$

Therefore, Equation 11 is

$$\sigma_- - \sigma_+ = \sigma_s \quad (14)$$

Unless one wishes to make assumptions regarding the relative sizes of the individual cross sections, or use information that other investigators have obtained, this is as far as the present analysis can be pursued. However, as was mentioned previously in this chapter, one can make an analysis of the charge-to-mass ratios of the slow ions. This will produce additional information.

It should be noted that such an analysis was not performed for the  $H^0$  on He projectile-target combination, because the most immediate interest in this analysis was to check out the recently constructed spectrometer, and comparison data were available for other collision pairs. (The results obtained with this spectrometer were in excellent agreement with the existing comparison data.) However, for the purpose of continuity, the application of the charge-to-mass analysis will be discussed here for the  $H^0$  on He collision combination.

This type of analysis would distinguish between the two helium ions,

$\text{He}^+$  and  $\text{He}^{++}$ . Therefore, the relative cross sections  $\sigma(\text{He}^+)$  and  $\sigma(\text{He}^{++})$  for the formation of these two ions can be measured. These two cross sections can be represented in terms of individual cross sections as follows

$$\begin{aligned}\sigma(\text{He}^+) &= \sigma_{01} + \sigma_{11} \\ &= \sigma_{j1}\end{aligned}\tag{15}$$

and

$$\begin{aligned}\sigma(\text{He}^{++}) &= \sigma_{02} + \sigma_{12} \\ &= \sigma_{j2}\end{aligned}\tag{16}$$

These relative cross sections may then be normalized to the total apparent cross section for production of ions  $\sigma_+$ .

This is the manner in which the total apparent cross sections were obtained in this investigation for  $\sigma_+$ ,  $\sigma_-$ ,  $\sigma_i$ ,  $\sigma_s$ , and  $\sigma_c$  (where  $\sigma_c$  represents electron capture for the case of the  $\text{He}^{++}$  projectile) for the projectiles  $\text{He}^{++}$ ,  $\text{He}^0$ , and  $\text{H}^0$  on the four target gases He, Ar,  $\text{H}_2$ , and  $\text{N}_2$ . Also, for the  $\text{H}^+$  projectile on He and Ar, the partial ionization cross sections were measured.

### CHAPTER III

#### APPARATUS AND TECHNIQUES EMPLOYED TO OBTAIN ION AND ATOM BEAMS OF SPECIFIED CHARACTER

The source of the fast beams was a 0.15 to 1.0 MV Van de Graaff positive-ion accelerator, equipped with a beam analyzing and stabilizing system. Since the accelerator produced directly only the singly charged ions  $H^+$  and  $He^+$ , a gas cell in which all the projectiles could undergo charge changing collisions was located further along the beam path. As the beams of mixed charge states emerged from the gas cell they were electrostatically separated. The remainder of the apparatus could then be aligned with the desired beam component.

##### The Beam Source and Energy Determination

The radio-frequency ion source of the Van de Graaff had two gas inlets, each equipped with a thermomechanical leak. When molecular hydrogen and helium gases were used, the ion source furnished about 50 to 100 microamperes total output current.

The beam from the accelerator was passed through a  $90^\circ$  sector magnetic field (see Figure 1), which analyzed the beam into its components according to the charge-to-mass ratios. When molecular hydrogen was used in the source, it was found that the principal beam component was  $H^+$ , with  $H_2^+$  being about one-third as intense. For helium in the source, the beam was almost entirely  $He^+$ ;  $He^{++}$  was negligible.

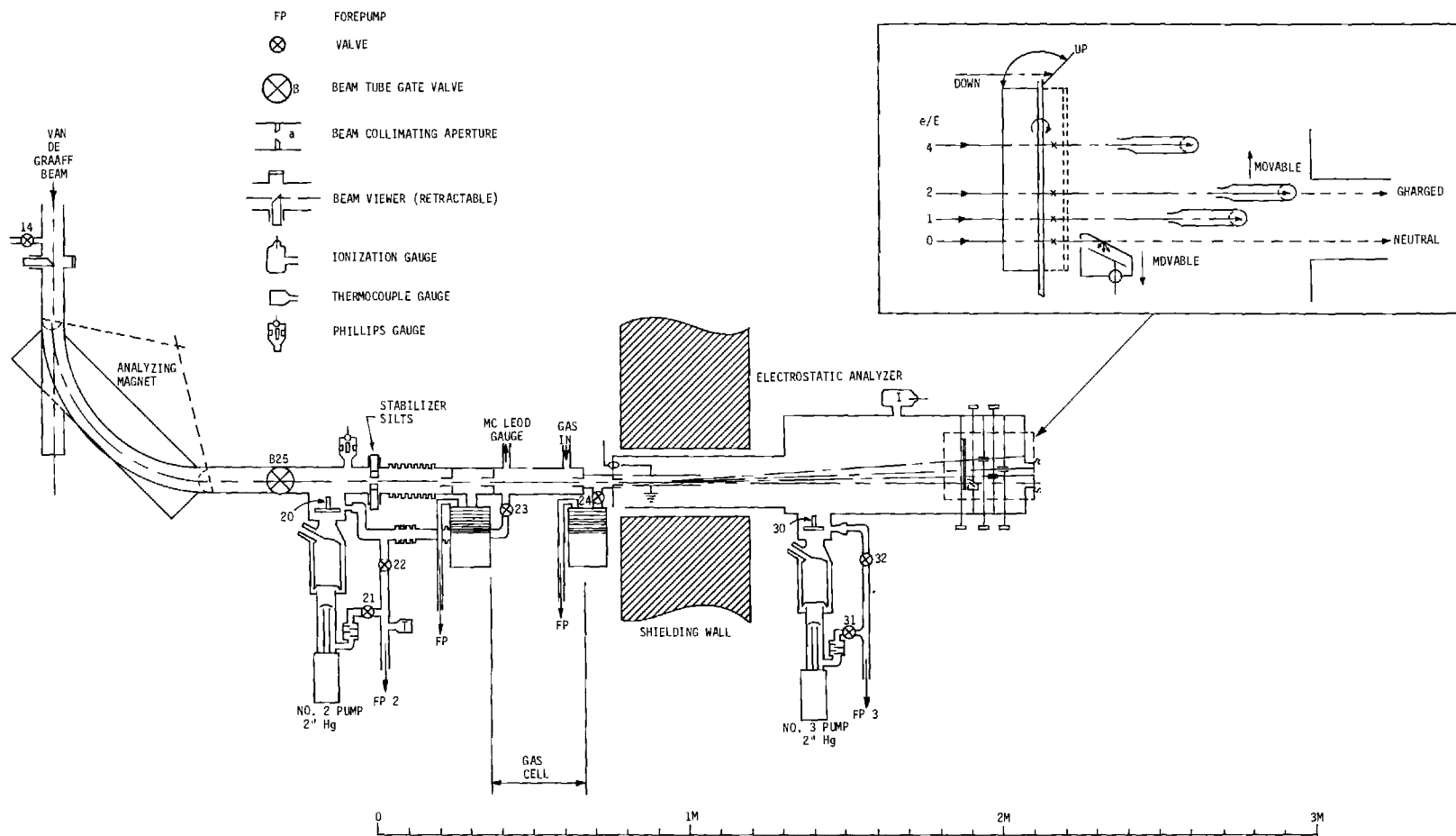


Figure 1. Schematic View of Beam Preparation Apparatus.

The energy of the beam emerging from this analyzer was stabilized by electronic regulation of the accelerator voltage to maintain equal currents to two stabilizer slit edges. This procedure amounted to imposing a constant  $90^\circ$  deflection of the beam in the regulated magnetic field. (This was the standard stabilizing system provided by the accelerator manufacturer, the High Voltage Engineering Corporation. The nominal energy spread was  $\pm 2$  keV at 1 MeV.) Thus the beam energy was determined by the magnetic field, which had been calibrated prior to the present experiment by measuring the magnetic field corresponding to the 1.019 MeV threshold of the nuclear reaction  $H^3(p, n) He^3$ , using a tritium-zirconium target. Throughout the present investigation, a Harvey Wells (Model G-501) nuclear magnetic resonance gauss meter was used for the measurement of the magnetic field.

#### The Gas Cell

The magnetically analyzed beam was next directed through a gas cell in which it was allowed to undergo charge changing collisions. Both the nature and the pressure of the gas used in this cell were dictated by the yield of the desired output beam component. The choice of the gas was based on the equilibrium fractions<sup>3</sup> of the various beam components. It was determined that, in this energy range, the gas that produced the largest fractions of  $He^0$  and  $H^0$  was helium. Similarly, for the production of  $He^{++}$ , molecular nitrogen was indicated. Figure 2 shows a plot of the required helium pressure in the gas cell in order that the components of  $He^0$  and  $H^0$  may reach 90 percent of the maximum intensities as indicated by equilibrium fractions.

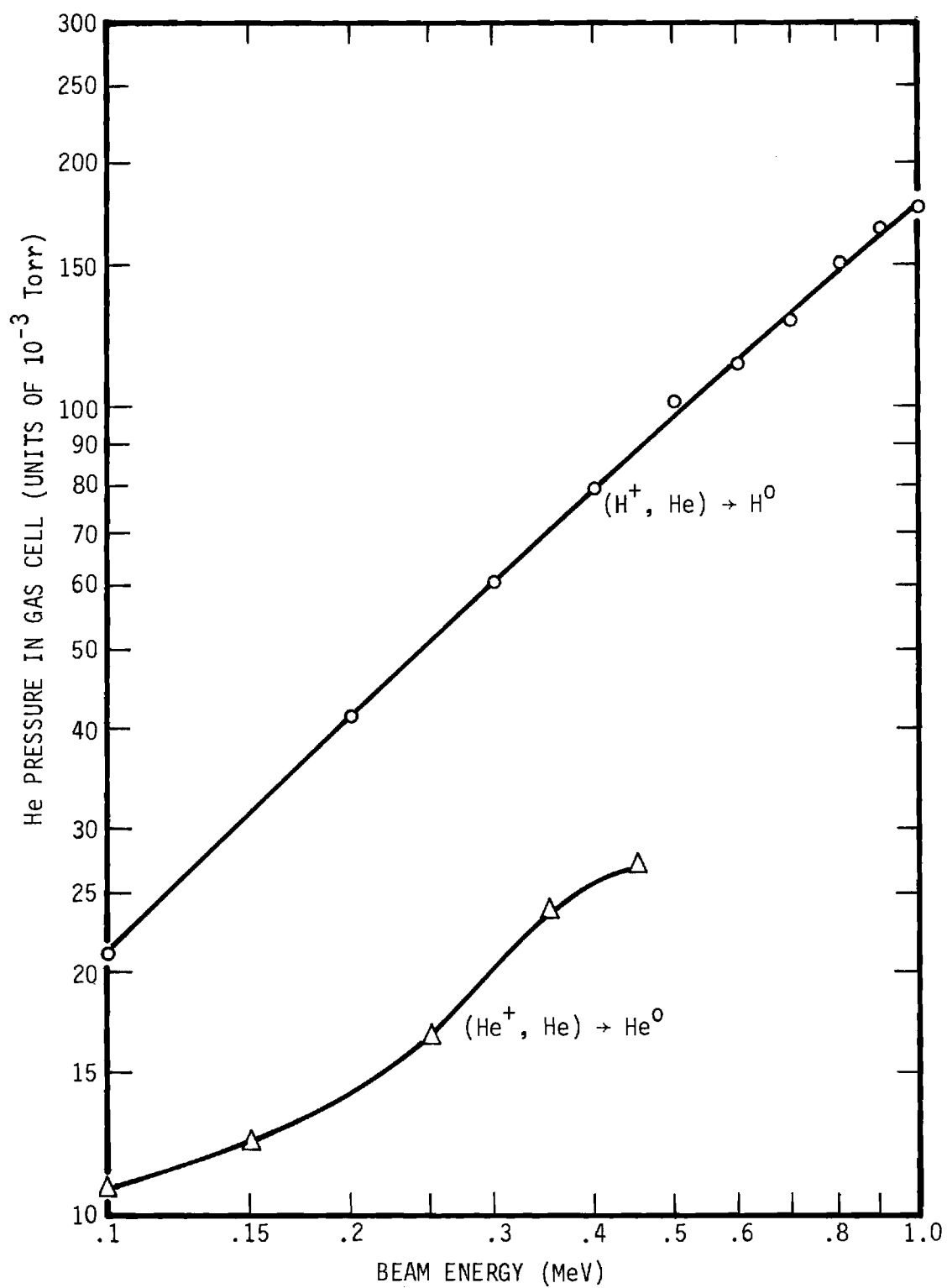


Figure 2. Calculated He Pressures in Gas Cell as a Function of Beam Energy for H<sup>0</sup> and He<sup>0</sup> to Attain 90 Percent Maximum Intensity.



The usual pressure used in this cell of length 31 cm was about 7 to  $20 \times 10^{-3}$  Torr. The gas was admitted continuously through an Edwards metering valve and was continuously pumped out through the apertures on both ends of the cell.

It was essential to confine the high pressure to the region of the gas cell as much as possible. If the gas emerging from the cell were allowed to produce a sufficient pressure rise in other parts of the system, then the beam passing through these regions would undergo additional charge changing collisions. A particularly undesirable region for this occurrence would be that following the electrostatic analyzer. High pressure in this region would cause the selected beam component to become contaminated with other charge states. If this were permitted, an error would be introduced in the experiment due to the uncertainty in beam composition. Figure 3 shows the computed maximum pressure in this region for which not more than one percent collisions of a charge changing nature would occur.

With the above considerations in mind, separately pumped chambers were installed on both ends of the gas cell for the purpose of more efficiently confining the gas to this region. The entrance aperture on the chamber preceding the gas cell and the exit aperture on the chamber following the gas cell were cylindrical channels of 1/8 inch I.D. and were 1-1/4 inches in length. These apertures were optically aligned with those of 1/16 inch I.D. and equal length mounted on either end of the gas cell. As expected, the higher impedance to the flow of gas provided by the cylindrical apertures proved very effective in producing a large pressure differential between the gas cell and adjacent chambers. With this arrangement of differentially pumped chambers and cylindrical apertures, a quite satis-

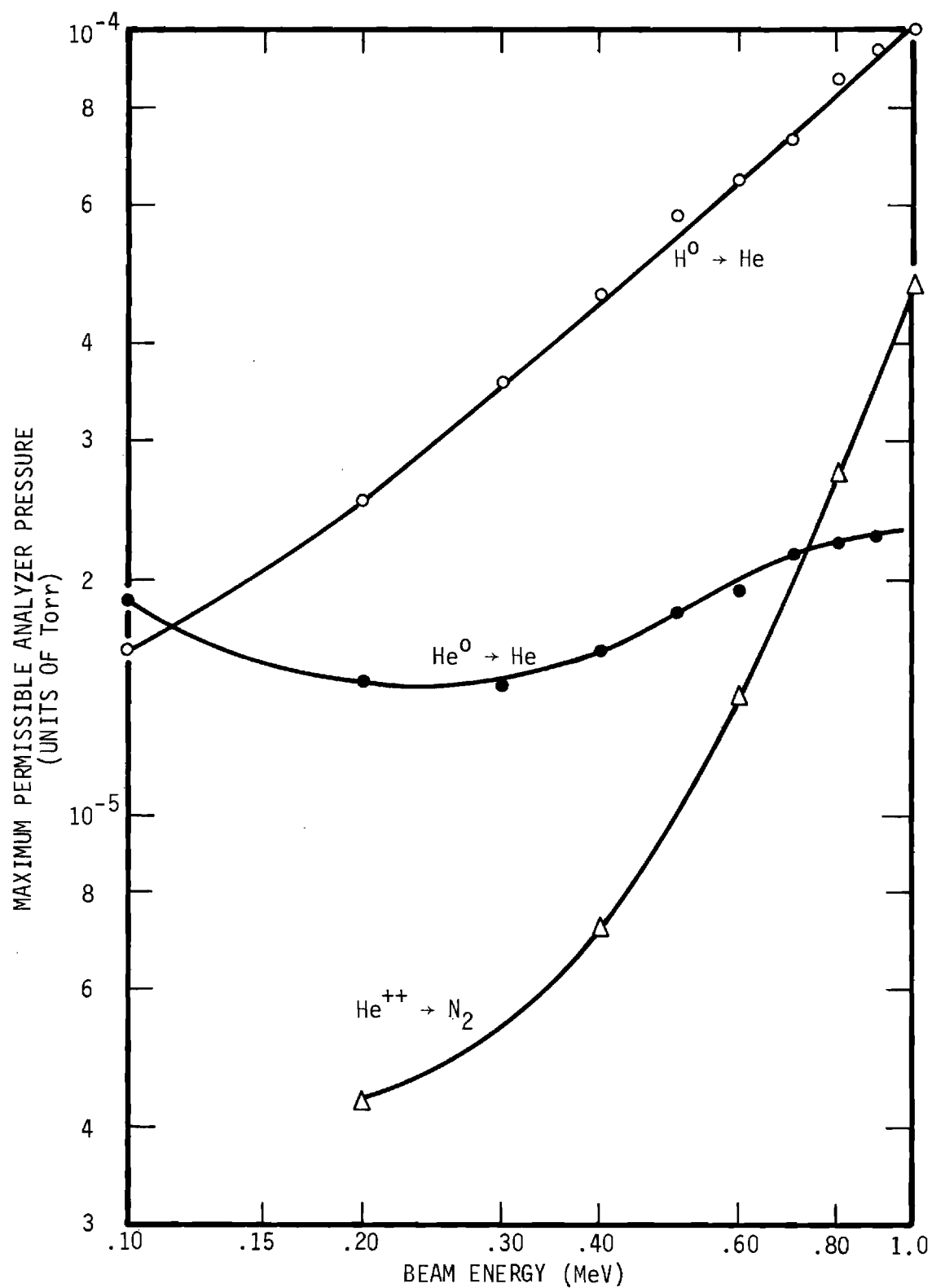


Figure 3. Calculated Pressures for Which Beams of  $H^0$ ,  $He^0$ , and  $He^{++}$  Will Undergo No More Than One Percent Collisions of a Charge Changing Nature.

factory pressure reduction between the gas cell and the remainder of the system was accomplished.

Figure 4 shows the relation of the pressure in the gas cell, as measured with a McLeod gauge, to that measured with an ion gauge, in the electrostatic analyzer following the second differential pumping chamber. The ion gauge reading was corrected for its low helium sensitivity. As is indicated in the figure, the base vacuum of the region is around  $1 \times 10^{-6}$  Torr. The pressure rise associated with  $20 \times 10^{-3}$  Torr of helium in the gas cell is only about  $1.5 \times 10^{-7}$  Torr in the analyzer. This is considerably under the upper pressure limit as indicated in Figure 3.

#### The Electrostatic Analyzer

The beam that emerges from the gas cell contains several different components. For example, if the  $\text{He}^+$  beam from the accelerator entered the gas cell, then the components that emerged from the cell would be  $\text{He}^0$ ,  $\text{He}^+$ , and  $\text{He}^{++}$ . In order to separate the desired component, this mixed beam was passed into an electrostatic analyzer. This analyzer is described in the thesis of R. A. Langley,<sup>28</sup> however, because it served a very important function in the present investigation, a description is included here also.

For clarity, in Figure 1, the electrostatic analyzer is shown rotated  $90^\circ$  about the beam axis. That is, the beam deflections produced by the analyzer are actually in a horizontal plane, rather than vertical as it appears in the figure. The analyzer deflection plates were 17 cm in length and separated by 1.2 cm. These plates were mounted on a bracket that could be rotated about the beam axis with an external control. This

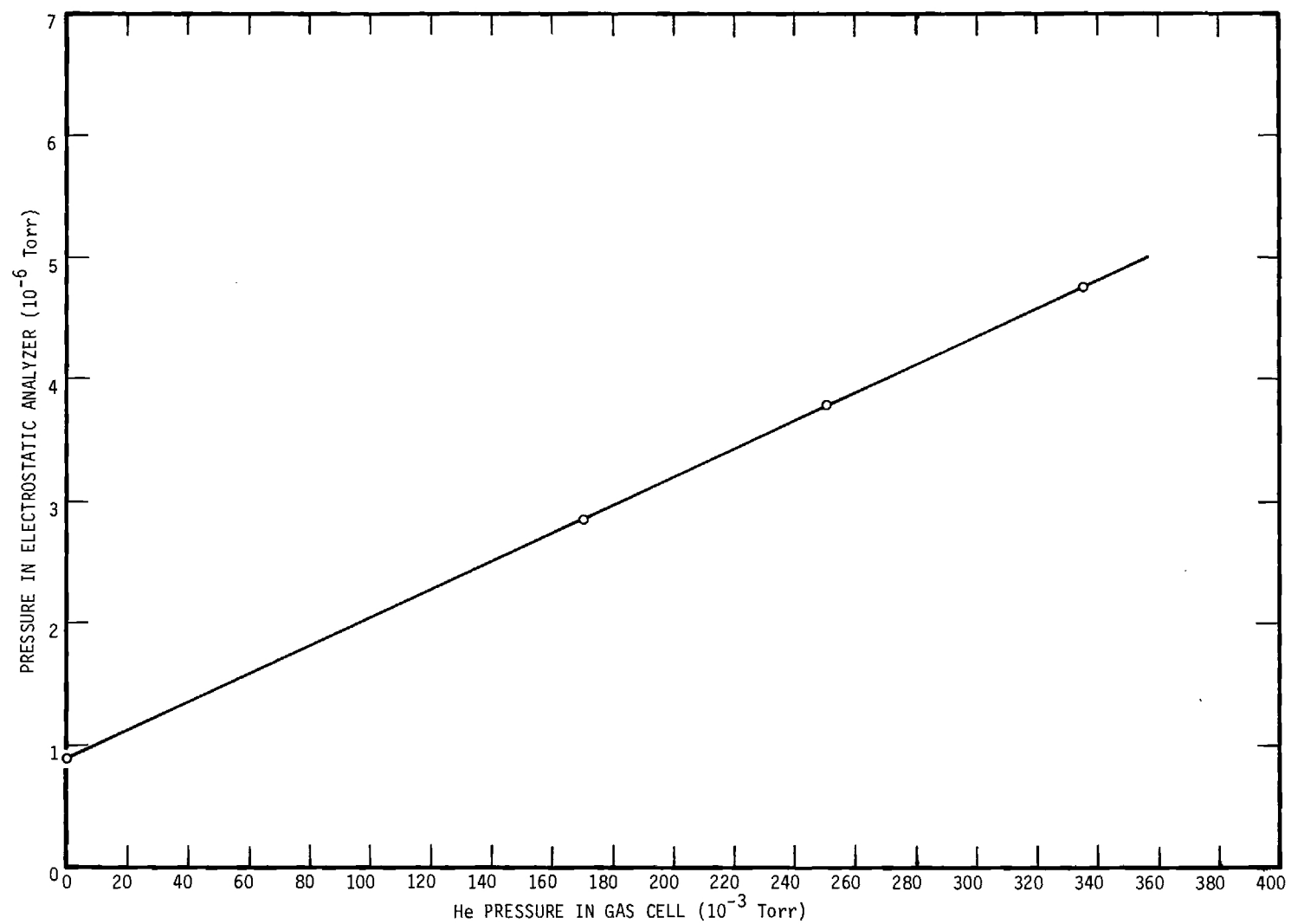


Figure 4. Relationship of Gas Cell Pressure to Pressure in Electrostatic Analyzer.

arrangement permitted the adjustment of the plane of deflection to coincide with the horizontal plane of beam detectors and the exit port located at the end of the analyzer. A high voltage power supply (Hamner Model N-413) was used to apply up to 5000 volts between the two deflection plates, one of which was grounded. A deflection voltage of about 2500 volts was used to separate the  $\text{He}^0$ ,  $\text{He}^+$ , and  $\text{He}^{++}$  components formed in the charge changing collisions of a 1 MeV  $\text{He}^+$  beam. This voltage provided about two-centimeter horizontal separation of these components at the exit port of the analyzer.

Provisions were made although not often used to measure the intensities of all the separated components that emerged from the gas cell. Near the exit end of the analyzer section are three Faraday cups and a secondary-emission neutral detector. Each detector can be independently positioned horizontally by means of a lead screw to collect one of the separated beams. A frosted glass plate which was located in this region could be rotated into position to intercept all of the separated beams. This plate provided a visual indication of the beam locations by means of the fluorescence of the glass. This arrangement of detectors is shown in the insert in Figure 1. In order to obtain the beam component desired for cross section measurements, the appropriate detector is moved aside, then that component is allowed to pass out of the analyzer through the exit port.

A major concern in this experiment is the possibility that the fast neutral beams,  $\text{H}^0$  and  $\text{He}^0$ , which are obtained through electron capture by  $\text{H}^+$  and  $\text{He}^+$  beams in the gas cell, contain an appreciable fraction of atoms in excited states. The magnitudes and even the ratios of the cross sections for most types of collisions would be different for such excited

atoms from those for ground state atoms.

As a check on the possibility of atoms excited to ordinary excited states reaching the collision chamber, the flight time from the gas cell to the collision chamber may be compared to the lifetimes of such states. Using available calculations and measurements, which relate the lifetime to the principal quantum number  $n$  of the excited state for hydrogen<sup>29</sup> and for helium,<sup>30</sup> one finds that all allowed states of hydrogen with  $n \leq 6$  and of helium with  $n \leq 7$ , are too short lived to survive the transit even at the highest beam velocities used here. A separate calculation<sup>31</sup> indicates that the probability of producing excited states with  $n > 7$  does not exceed about 0.003. Therefore, it is not expected that ordinary states of excitation, i.e., other than metastable states, can cause any difficulties in this experiment.

However,  $H^0$  and  $He^0$  both have low lying metastable states which cannot decay by allowed transitions and have sufficiently long lifetimes to reach the collision chamber. In the case of  $H^0$ , it is expected<sup>32</sup> that any atoms emerging from the gas cell in the  $2s$  metastable states would be quenched by the electric field of the electrostatic analyzer; however, these fields would have little effect on  $He^0$  metastables. In fact, no change in the cross section values, for either projectile, was observed when the analyzer field was varied from about 500 v/cm (minimum value for which charged particles were removed from the beam) to more than 4000 v/cm.

If there were indeed many non-ground state atoms in the beams, it would seem that the fraction of all beam atoms in such states should vary with the pressure and with the nature of the charge-exchange gas used in the cell. A search for such a dependence was made by observing the values

of the cross sections while the gases He, Ar, and N<sub>2</sub> were used, and the pressures were varied by a factor of more than 1000; however, no change in the cross sections was observed. Further indications of the absence of such excited states in the He<sup>0</sup> neutral beam are presented in Chapter V. It should be noted that this evidence for the lack of excited states in the He<sup>0</sup> beam is in confirmation of the work of Allison,<sup>24</sup> although Barnett, et al.<sup>12</sup> found evidence of the effects of excited states. He observed that the cross section values changed about 40 percent as the pressure in the gas cell was varied. However, the variation in gas cell pressure in the present experiment was over an even greater range than Barnett used, and it did not produce any change in the observed cross sections. Our conclusion was that the effects of excited states were unimportant in this investigation.

PART B



## CHAPTER IV

APPARATUS AND TECHNIQUES EMPLOYED FOR THE MEASUREMENT OF THE  
TOTAL APPARENT ION AND ELECTRON PRODUCTION CROSS SECTIONS

Figure 5 is a schematic diagram showing the entire apparatus. Attached to the electrostatic analyzer, which was previously discussed, is shown the portion of the apparatus that was used for the cross section measurements. As is suggested by the offset bellows shown in this figure, the entire apparatus following the electrostatic analyzer can be moved, by means of vertical and horizontal jack-screws, into alignment with the selected beam component.

When the apparatus is thus aligned, the beam passes through a three-aperture collimator, through the collision chamber, and into a beam detector. The collision chamber, which is represented in the figure as a rectangular box, although in reality it is a round enclosure, contains the target gas. As the beam underwent collisions with the gas molecules, free electrons and ions were produced. These slow collision products were collected on electrodes within the collision chamber and gave rise to the ion and electron currents used in the calculation of the cross sections (see Appendix II). Figure 6 is a photograph of the apparatus showing the electrostatic analyzer on the left and the collision chamber on the right.





Figure 6. Exterior View of Electrostatic Analyzer and Collision Chamber.

### The Collision Chamber and Associated Beam Collimator

The selected beam was passed through a three-aperture collimator, which is shown in Figure 7 before it entered the collision chamber. Prior to installation, this collimator was rigidly and carefully aligned as a unit, optically, with the aid of the telescope of a Gaertner (Model 911) cathetometer.

The beam incident on this collimator was diverging from the  $1/8$  inch diameter exit aperture of the gas cell, some two meters away. The primary geometrical collimation of the diameter and divergence of the beam was established by the first aperture ("a" in Figure 7), a knife-edged round hole of  $4/64$  inch diameter, the smallest of the three apertures. Aperture "b" was a round hole of  $5/64$  inch diameter, large enough not to further intercept the main beam defined by the preceding apertures. Its function was to intercept particles scattered from the edge of aperture "a" and from the residual gas, but its own edge was kept clear of the main beam so as not to serve as a further source of such scattered particles.

Among the scattered particles of concern here were first, of course, fast heavy beam particles which, having suffered a scattering collision, might also have suffered a change in their charge, so that they would now represent a contaminant in the beam. Possibly even more important, however, were fast "knock-on" electrons traveling with the beam with speeds of the same order of magnitude as the heavy particles. Previous experience with a less carefully designed collimator had shown that such electrons, entering the collision chamber with the beam, could be most troublesome in this experiment. More will be said on this matter later, in the discussion of saturation currents to the collecting electrodes in the col-

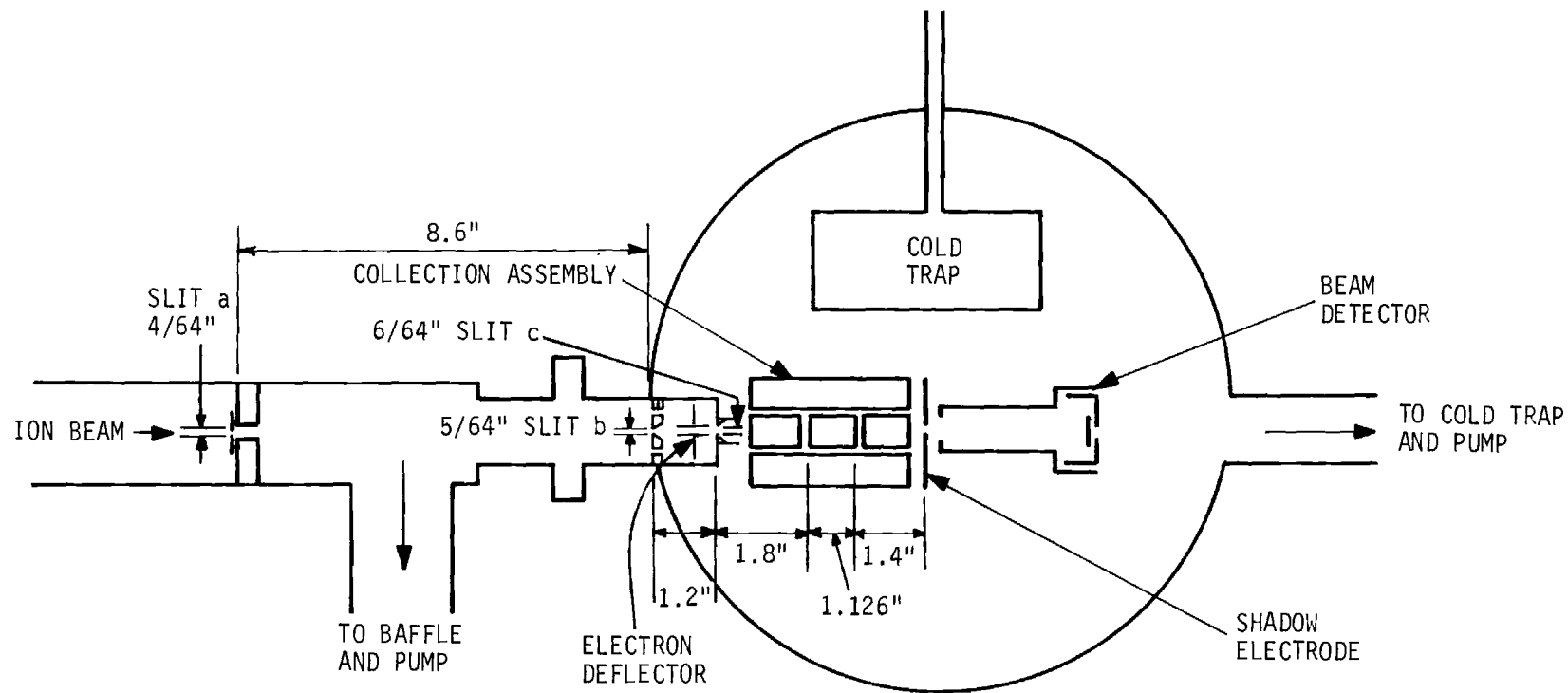


Figure 7. Schematic Diagram of Beam Collimator and Collision Chamber Components Employed in the Measurements of the Total Apparent Cross Sections.

lision chamber.

The third and last aperture ("c" in Figure 7) was the largest in diameter of the three, being a cylindrical channel of  $1/8$  inch diameter and about  $5/8$  inch long, with a knife-edged lip of  $6/64$  inch diameter at the end on which the beam is incident. Similar to aperture "b", the edges of "c" stood clear of the main beam defined by preceding apertures, so that it served the purpose of further skimming off scattered particles, without serving as a source of such particles itself. The main function of aperture "c", however, was to define the boundary between the evacuated beam tube and the target gas in the collision chamber. This boundary must be as sharply defined and as close to the measurement region as feasible in order to minimize the amount of gas the beam passes through before it reaches the measurement region. If this requirement were not satisfied to the greatest practicable degree, the charge composition of the beam incident on the measurement region could have been significantly altered by charge changing collisions in the preceding gas. To accomplish this function, aperture "c" was located in the entrance of the channel mentioned above, which projected into the collision chamber almost to the edges of the guard electrodes immediately preceding the measurement region. Pumping of the region of the beam tube between apertures "b" and "c" was accomplished through three large off-center holes in the plate that supported aperture "b", by the two-inch oil diffusion pump, with a water-cooled baffle, connected to the collimator tube between "a" and "b".

When the collision chamber was evacuated, the pressure in the collimator was about  $1 \times 10^{-6}$  Torr; however, with the target gas at a pressure of about  $5 \times 10^{-4}$  Torr, the pressure in the collimator between

apertures "a" and "b" was about  $8 \times 10^{-6}$  Torr as measured on a Veeco (Type RG-75) ionization gauge. A calculation based on the conductances of the slits and the pressures listed above indicated the pressure between slits b and c to be about  $2 \times 10^{-5}$  Torr. Since only about one percent of the projectiles underwent charge changing collisions in the chamber at  $5 \times 10^{-4}$  Torr, it was expected that a negligible number of such collisions occurred in the collimator.

One further feature was incorporated into this collimator assembly to deal with the problem of fast electrons in the beam, which has served to verify the efficacy of the careful geometrical design described above. A small pair of electrostatic deflector plates was installed in the region between apertures "b" and "c", to deflect away from aperture "c" any electrons coming through "b". Application of up to 600 volts to this deflector, calculated to be more than enough to deflect out electrons with the same velocity as the heavy beam particles, was found to have no noticeable effect on the electron current collected from the measurement region, or on the saturation curves for this current. It was concluded that the present careful design of the collimator has essentially eliminated the problem of fast electrons in the beam. Since the deflector had no effect, it was evidently not required and it was not further used except for this test.

The collision chamber was of stainless steel and the flanges were sealed with neoprene O-rings. The chamber was evacuated by a four-inch liquid nitrogen-trapped oil diffusion pump. A separate liquid nitrogen trap was suspended in the collision chamber above the ion and electron collection electrodes to assist in the removal of condensable vapors.

The collection electrodes were so oriented that the cold trap could not be seen from the beam path in order to reduce the temperature perturbation in the collision region. The base vacuum in the chamber, with the internal trap warm, was about  $2 \times 10^{-6}$  Torr as indicated on the ionization gauge. However, with the trap filled with liquid nitrogen the base vacuum increased to  $1 \times 10^{-7}$  Torr. This indicated that condensable gases made a substantial contribution to the background gas in the chamber. The significant benefit of operating with the trap cold was in the reduction of the electron and ion currents from ionization of the background gas. These currents, which will be discussed later, were reduced, by a factor greater than 20, to a negligible value compared to the ionization currents produced in the target gas.

In order to determine whether or not the cold trap significantly altered the temperature distribution of the target gas, cross section measurements were made with and without the trap being cooled. When the measurements made with the trap at room temperature were corrected for the background contributions, the two sets of cross section values were equal. Therefore, it was concluded that no systematic errors were introduced by the use of the cold trap. This conclusion was expected because the average path from the cold trap to the measurement region involved several encounters with the room temperature walls of the collision chamber. Therefore, a molecule that had lost energy to the cold surface of the trap usually had regained it before reaching the measurement region.

A cold-trapped McLeod gauge was employed for the measurement of the target gas pressure. This gauge was connected to the collision chamber with a tube that pointed directly to the collision region between the ion



and electron collection electrodes. A modified CEC (Model GM-110) McLeod gauge was used for these measurements. (Details of the gauge, operational techniques, and associated errors are discussed in detail in Appendix III.) A Veeco (Type RG-75) ionization gauge was also attached to the chamber, which provided a convenient means for preliminary measurement of the gas pressure. However, the ionization gauge could not be operated at the time that the ion and electron currents were being measured because considerable numbers of ions were repelled out of the operating ionization gauge and were attracted to the ion collection electrode.

For some of the projectiles used in this investigation, such as  $\text{He}^0$  and particularly  $\text{H}^0$ , the cross sections were small, and in order to obtain satisfactory ion and electron currents to the electrodes, it was necessary to use a rather high target gas pressure - around  $1 \times 10^{-3}$  Torr. In order to accomplish this, the gate valve B55 of Figure 5 was used as a throttling valve. This reduced the pumping speed to the chamber, and thereby the gas throughput. A large throughput could give rise to pressure gradients in the collision chamber and consequent uncertainties in the gas density in the collision region. Tests were made to insure that no detectable gradients were present.

The target gas pressure was maintained by a continuous input through a cold trap and an Edwards metering valve. The pressure was varied over the working range from about  $3 \times 10^{-5}$  to  $1 \times 10^{-3}$  Torr simply by adjusting the input rate and the constriction presented by the gate valve. The four-inch diffusion pump was operated continuously to maintain the background pressure in the chamber at a constant value, independent of the target gas pressure. In the course of this experiment, the contribution to

the measured cross sections from the background gas was always less than one percent of the total cross sections.

#### The Fast Beam Detector

The beam detector used in this investigation was designed to totally trap the beam and to provide for three observations: 1. the net current delivered by the beam; 2. secondary emission current from the beam target foil; 3. total power of the beam, through observation of the temperature rise of the target foil, by means of a thermocouple.

A diagram of this detector is shown in Figure 8 and its operating principles are contained in the following description. The charged beam was passed into the detector and impinged on the copper foil. This foil was supported by four copper wires of diameter 0.003 inch, which served as electrical connections to the brass heat sink. When the beam struck the foil, secondary electrons were ejected, which produced an apparent increase in the beam current. The sleeve on the detector, which was electrically insulated from the foil, was designed to collect all of these electrons. Therefore, in order to measure the net current delivered by the beam, which is listed as observation number one, leads from the heat sink and from the sleeve were connected together outside of the chamber, and the net current was measured by means of a Keithley (Model 415) pico-ammeter.

The second observation listed above, which was that of secondary emission current from the beam target foil, was accomplished simply by measuring only the current to the sleeve. In this measurement, the same electrometer or a Keithley (Model 410) pico-ammeter was used.

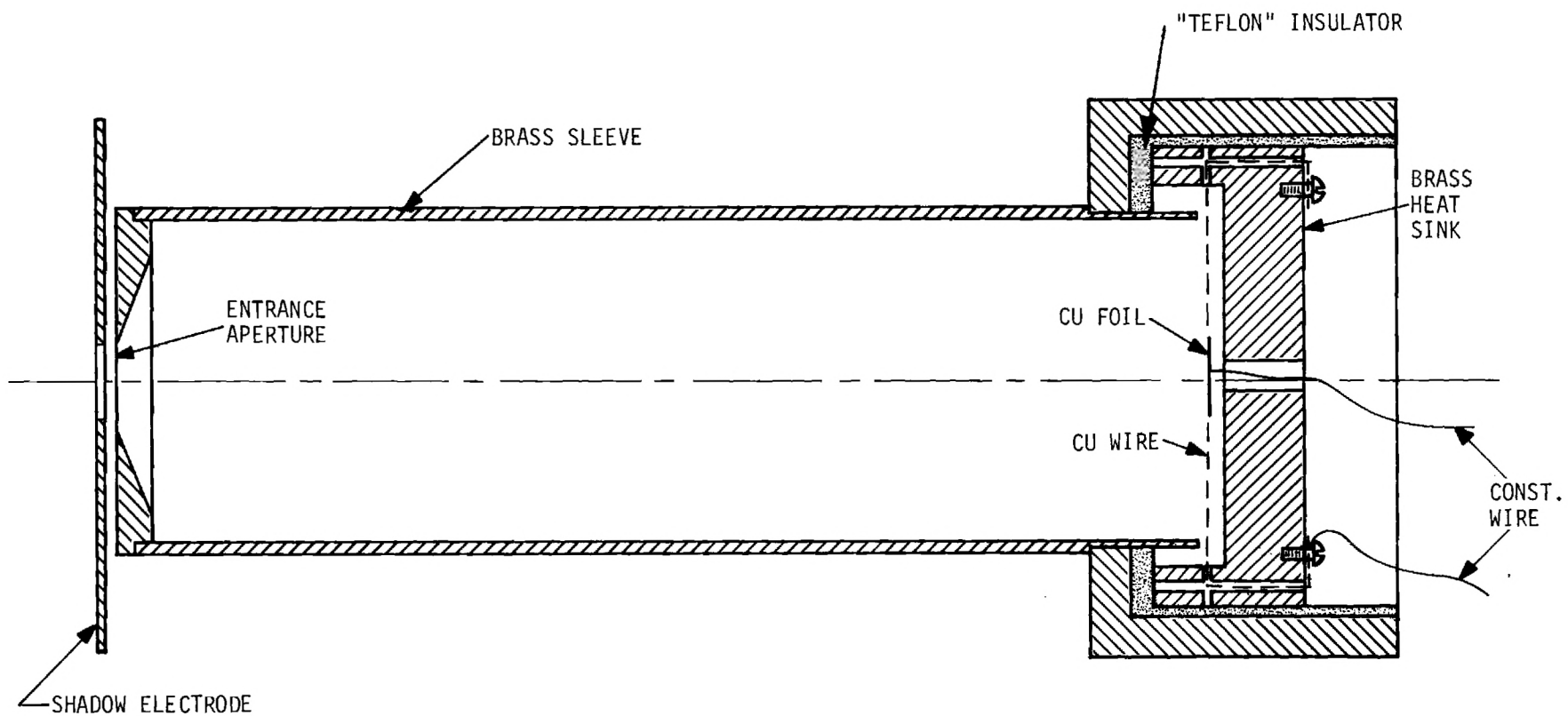


Figure 8. Schematic Diagram of the Fast Beam Detector.

Observation three, the total beam power, permitted the measurement of a beam of neutral particles. The target foil on which the beam impinged was designed and mounted such that it would be heated by the power deposited in it by the beam. The foil which was 0.28 inch in diameter and 0.002 inch thick was of small thermal capacity, and its temperature was measured by means of a copper-constantan thermocouple. One thermocouple junction was spot-welded to the back of the foil and the other was attached to the brass heat sink which served as the reference temperature. The copper wires that supported the foil were used as one leg of the thermocouple. Both ends of the constantan leg (the constantan lead from the center of the foil and the constantan lead from the heat sink) were passed out of the chamber and to a Keithley nano-voltmeter, which served to measure the emf generated in the circuit. By means of this arrangement, the temperature rise of the foil could be measured as the beam impinged on it.

The calibration procedure required is described in detail in Appendix I; however, the principles involved are briefly discussed in the following. It was verified using a beam of singly charged particles that the emf response of the thermocouple was directly proportional to the total beam power impinging on the foil, within the range of this experiment. The beam power was taken to be the product of the Van de Graaff voltage and the net beam current as measured in the detector. This calibration with the charged particle beam served to establish the proportionality constant between the beam power and the emf of the thermocouple. With this information, it was simple to deduce that the "current" of a neutral beam was just the product of this proportionality constant and the observed emf, divided by the accelerator voltage.

In a calibration of the above type, it was necessary to assure that the singly charged ion beam was not appreciably contaminated with neutral particles causing the true beam power to be greater than was calculated from the net current. After the emf generated in the thermocouple element of the detector had been measured for the charged beam, the beam was electrostatically deflected, and the emf was again read. The latter reading, which corresponded to the neutral contaminant of the beam striking the detector, amounted to only about 0.1 percent of the former reading, which in this experiment was negligible.

In performing cross section measurements with the neutral beams, it is similarly necessary to assure that the neutral beam is not appreciably contaminated with charged particles. Since most of the cross sections being measured are several times as large for charged particles as for neutrals, the possible effects of a given degree of contamination would be magnified. To test for this possibility, it was only necessary to measure the net current delivered to the detector by the nominally neutral beam. A typical test indicated that the percentage of charged projectiles present in the neutral beam was less than 0.1 percent. Thus, for the purpose of the present investigation, it was concluded that the neutral beams were not significantly contaminated with charged particles.

Considerable effort went into optimizing the design of this neutral beam detector in order to obtain both a satisfactory sensitivity, which was dictated by the low neutral beam intensity, and to produce a reasonable response time, which in turn was dictated by the rate of fluctuation of the beam intensity. The results of several tests and computations indicated that the sensitivity (equilibrium temperature rise of the foil per

unit of input beam power) was approximately equal to the inverse of the conductive power  $K$  per unit temperature of the wires supporting the foil target, i.e.,

$$\text{sens.} \left( \frac{^{\circ}\text{C}}{\text{cal/sec}} \right) \cong \frac{1}{K \left( \frac{\text{cal}}{\text{sec } ^{\circ}\text{C}} \right)} \quad (17)$$

This result indicated that thermal radiation from the foil was a negligible factor. It was also indicated that the time constant (the time required to reach  $1/\epsilon$  of the final temperature) for the thermal function of the foil was approximately given by

$$\tau(\text{sec}) \cong \frac{[Q_f + Q_w] \left( \frac{\text{cal}}{^{\circ}\text{C}} \right)}{K \left( \frac{\text{cal}}{\text{sec } ^{\circ}\text{C}} \right)} \quad (18)$$

in which  $Q_f$  and  $Q_w$  are the heat capacities of the foil and wires, respectively.

As is indicated in Equations 17 and 18, reducing  $K$  in order to increase the sensitivity also causes an increase in the time constant, which must be countered by reducing the heat capacities. In practice, the foil itself could be made small enough so that a significant portion of the total heat capacity was contributed by the supporting wires. Optimization of the detector performance thus depended on a minimal value of the ratio of the specific heat to the thermal conductivity of the supporting wire material, as well as on a large thermoelectric power coefficient of a thermo-

couple, that could be formed using these wires for one side of the circuit. It was on the basis of these considerations that copper was selected for the support wires, with constantan for the other leg of the thermocouple circuit, in preference to other pairs of metals that would have provided a thermocouple of greater sensitivity.

Calculations were made on the basis of Equations 17 and 18 to determine the optimum diameter for the copper support wires. However, in the final experimental evaluation, several sizes were tried and the final choice was made empirically. With the 0.003 inch diameter selected for the copper and constantan wires, and the 0.28 inch diameter by 0.002 inch thick copper foil, the sensitivity obtained was about 3 °C/milliwatt, or in terms of the thermocouple emf, about 0.1 millivolt/milliwatt. The time constant was about 13 seconds.

The next interesting feature of this detection scheme is the "shadow" electrode in front of the detector in Figure 8. It was designed, by making the aperture in the electrode smaller than the detector aperture, which it preceded, to serve two purposes.

The primary purpose was to suppress the escape of secondary electrons from the interior of the detector, by maintaining this electrode at a negative potential with respect to the detector. It was found that a potential of -20 volts or more was sufficient to cause the measured beam current to saturate. The convenient battery voltage of 67-1/2 volts was used throughout the present investigation.

The other purpose of the shadow electrode was to intercept any projectiles that had been scattered through large angles in the gas and thus prevent them from striking the outside surface of the detector. If

such projectiles were not intercepted, they would cause the emission of secondary electrons from the detector. These electrons (sometimes an average of three or four per particle) would create a false beam current to the detector. That is, electrons leaving the detector produce a current in the same sense as positive ions going to the detector. In this manner the effect of large angle scattered projectiles is magnified. However, with the low target gas pressures used in this experiment, less than three percent of the projectiles underwent any sort of ion producing collision, and on the basis of cross section measurements with various sized apertures, it was concluded that the number of projectiles that underwent large angle scattering was negligible.

The final aperture sizes selected were 0.6 cm for the shadow electrode, and 0.7 cm for the detector.

#### The Ion and Electron Collection Electrodes

The collection electrodes employed in this portion of the experiment were the same ones used in the apparatus described in the thesis of R. A. Langley.<sup>28</sup> A plane view of the collection electrode structure is shown in Figure 7. A photograph of the entire assembled ion and electron collection structure and the beam detector is shown in Figure 9, in which the projectile beam passes from left to right through the structure and into the beam detector. The ion and electron collection assemblies each had five plates which were separately mounted on a rigid Teflon block. All five plates of each structure were maintained at the same potential so that an equipotential surface was defined, and hence a uniform collection field was established in the collision region. Also shown in Figure 9 is



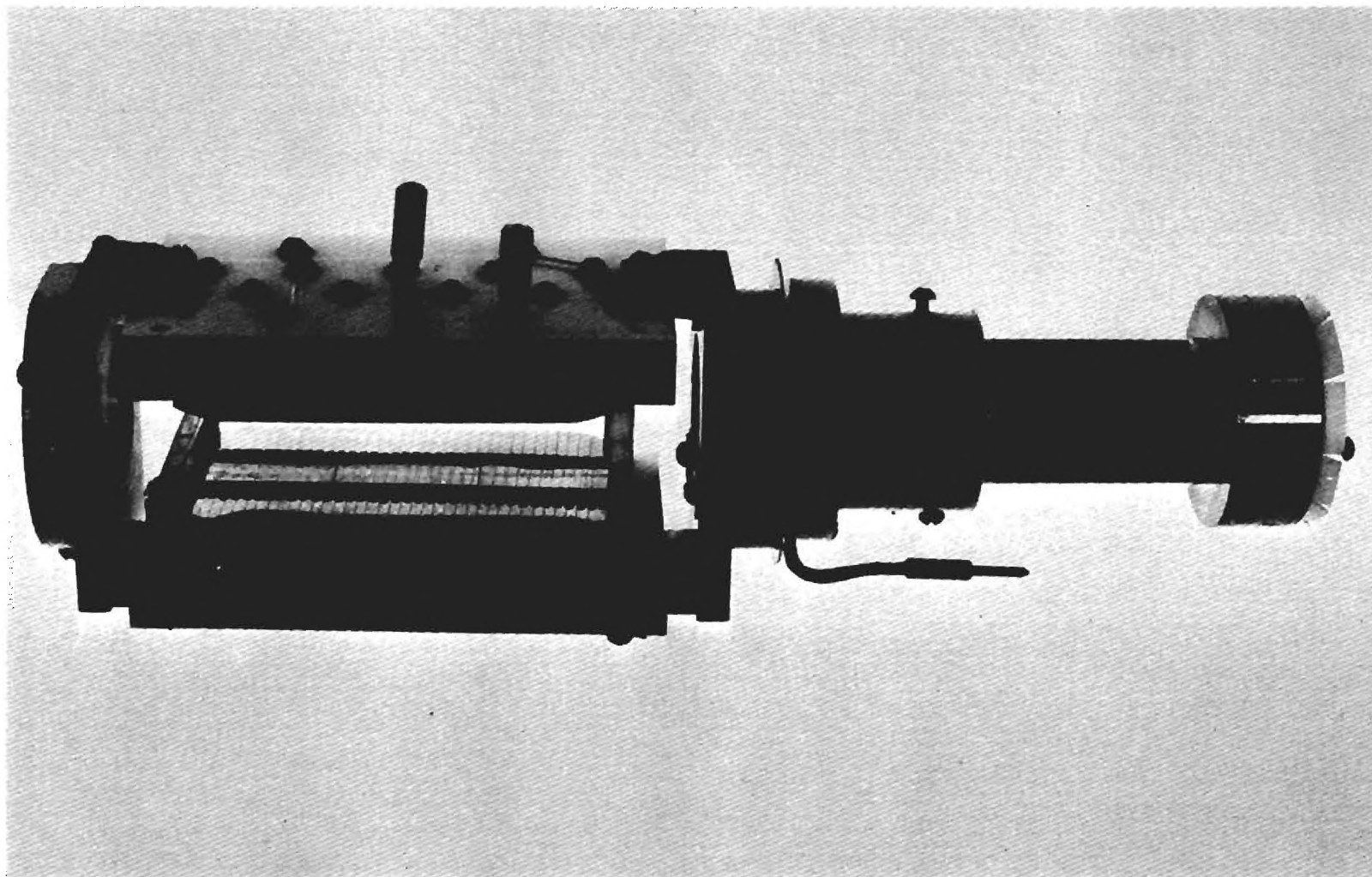


Figure 9. Slow Ion and Electron Collection Structure, and Fast Beam Detector.

a grid which was placed in front of the positive ion collector. The grid was biased negatively with respect to the ion collector to suppress the emission of secondary electrons. The suppressor grid and the electron collection assembly were each one-quarter inch from the beam path, and the ion collection assembly was mounted the same distance behind the grid. The center plate (see Figure 7) of each structure was machined to a length of  $1.106 \pm 0.001$  inches in the beam direction, and all plates were spaced 0.010 inch apart. Since only the ion current (or electron current) to this center plate was used in the cross section measurements, the other plates served only as guards, to establish a uniform field in front of the active plate. Thus, the effective length of the collision region over which the electron and ion currents were sampled was 1.116 inches (the plate length plus the plate spacing). End effects at the leading edge of this plate which were due to any average forward momentum of the slow ions should have been exactly compensated by the same effects at the other end.

A fraction of the "slow" ions produced by the fast projectiles might have substantial energies, and their initial motion might, of course, be directed toward the wrong collection assembly. In experiments utilizing heavier projectiles than were used in this investigation, Afrosimov<sup>33</sup> observed "slow" ions with several hundred electron volts energy. Therefore, a substantial collection field across the collision region was required to assure that all of the particles would reach the proper collector. This collection field was established by the potentials of the suppressor grid and the electron collection assembly. These were maintained at equal but opposite potentials so that the beam path would be in the zero poten-

tial plane. The magnitude of these voltages will hereinafter be denoted as  $V_c$ . The positive ion collection assembly was positive with respect to the suppressor grid by an amount designated as  $V_s$  in order to suppress the emission of secondary electrons from the ion collector. A convenient and satisfactory value of  $V_s$  was found in the test procedures described below to be  $V_c/3$ , and it was so maintained during the course of this experiment.

There were two necessary requirements that the voltages  $V_c$  had to meet before it could be felt that the ions and electrons were being efficiently collected. The first was that both electron and ion currents must show saturation with increasing values of  $V_c$ ; and second, the present results must verify the well established<sup>34</sup> equality of the electron and ion currents for the case of 1 MeV protons on argon. The empirically verified equality<sup>34</sup> is to be expected because, for incident protons,

$$\sigma_+ - \sigma_- = \sigma_c$$

where  $\sigma_c$  is the electron capture cross section. Barnett, et al.<sup>13</sup> have measured  $\sigma_c$  for 1 MeV protons in argon, and it is completely negligible compared to  $\sigma_+$ .

Until the beam entrance collimator had been modified and realigned as described previously, there had been considerable difficulty in obtaining proper saturation behavior in the collected current. The ion current saturated, but the electron current continued to increase as  $V_c$  was raised. The collimator had originally been constructed with equal 1/16 inch diameter apertures at "a" and "b" (Figure 7) and a third 3/32 inch diameter

aperture at "c" and had been only rather crudely aligned, optically, by means of only the unassisted eye. It has been concluded that the resulting poor alignment was the cause of the difficulty with the collected electron current. Beam particles striking the edges of the apertures could cause electrons to be ejected and to pass into the collision chamber. These electrons would, of course, have various energies and directions of motion, but some would be collected on the electron collector plate. It seemed reasonable that the current to the electron collector would continue to increase with applied voltage, up to quite large voltages, until all such electrons were being collected.

This had evidently been the trouble, because with the collimator modifications previously described, designed to minimize the number of such electrons scattered into the chamber, and with better alignment of the apertures, proper saturation currents were obtained for both electrons and ions. Sample curves are shown in Figure 10, and it appears that saturation has occurred for the  $V_c$  greater than about 250V. It should be mentioned again that once the collimator had been well aligned with the beam, no noticeable effect of the small electron deflector inside the collimator could be detected, even when potentials up to 600V were used. This observation was considered to indicate that there were no appreciable numbers of electrons present in the beam.

The second requirement on the saturation curves was that they must verify the established<sup>13, 34</sup> equality of electron and ion currents for the 1 MeV  $H^+$  on Ar. Reference to Figure 10 indicates that the saturated electron current was about two percent greater than the ion current. This difference could be attributed to the effective opacity of the grid that

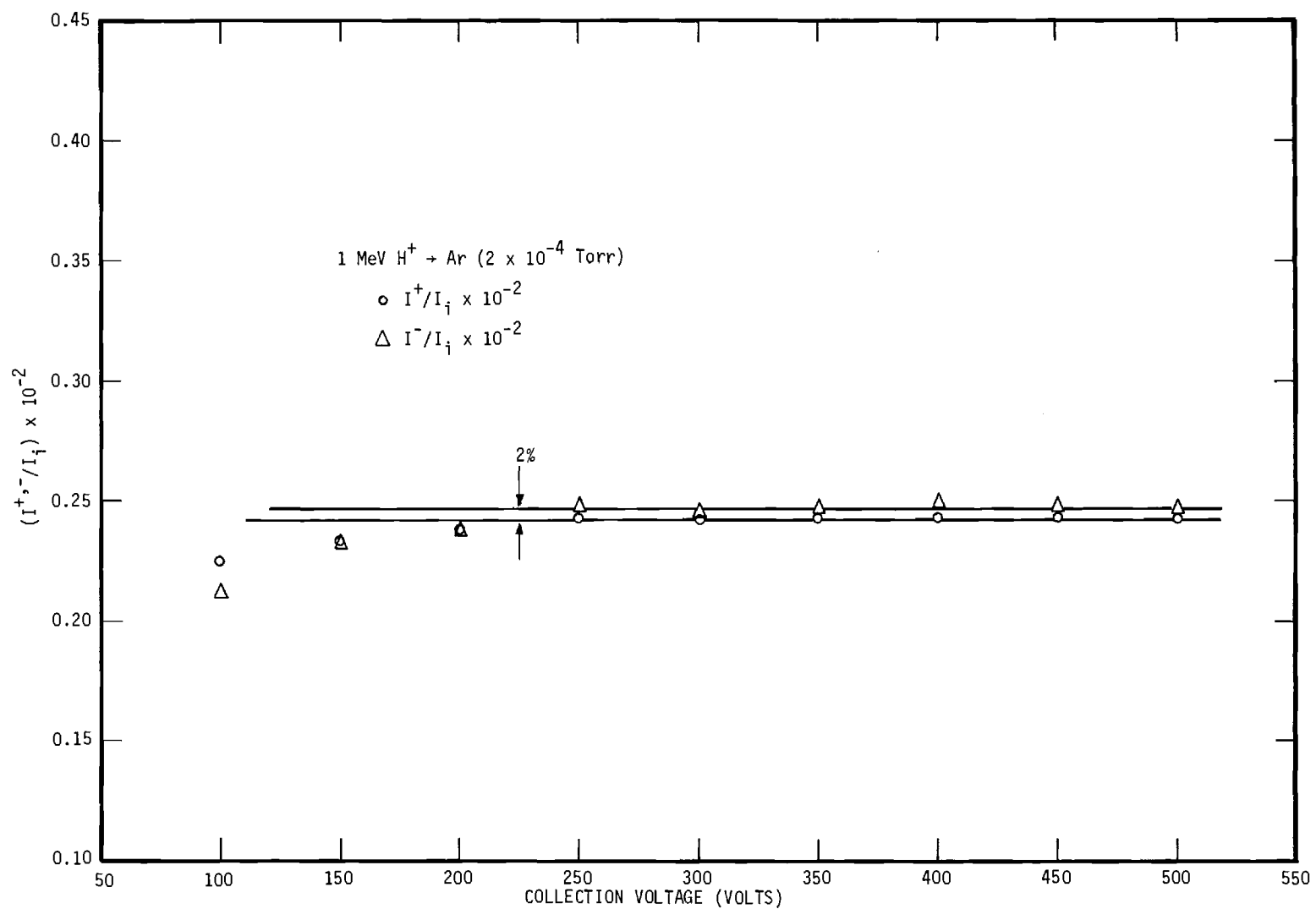


Figure 10. Response of the Ion and Electron Currents, Produced by  $H^+ \rightarrow Ar$ , to the Collection Voltage.

was mounted in front of the ion collector. It had been expected that the actual effective opacity would be at least as great as the four percent geometrical opacity, because of the focusing effects of the fields about the grid wires. This discrepancy was not resolved. Because it is known<sup>13,</sup>  
<sup>34</sup> that the electron and ion currents should be equal, it was felt that more weight should be attached to this fact than to the expected value of the grid opacity. Therefore, the empirical value of two percent effective opacity was used for the adjustment of the observed ion currents throughout this experiment.

As an overall check of the apparatus and procedures, the measurements of  $\sigma_+$  and  $\sigma_-$  by Hooper<sup>35</sup> for  $H^+$  on Ar were repeated, using collection potentials  $V_c$  of 350V. The results of single measurements at each energy point over the range from 0.2 to 1.0 MeV were within two percent of the average values obtained by Hooper. With this excellent agreement, the collimator, the detector, and the collection assembly were considered to be sufficiently tested to produce reliable results. As a double check, however, for all projectile-target combinations, it was verified that both the electron and the ion currents did saturate properly. Such a set of curves for  $He^{++}$  on argon is shown in Figure 11.

The two Keithley (Model 410) pico-ammeters used for the collected current measurements were insulated from laboratory ground and were operated with their frames at the potentials of the collectors. Figure 12 shows a schematic diagram of the electrical connections. The internal feed-back arrangement of these electrometers limited the potential difference between the input and the frame to a few millivolts for any value of the input current so that the active central plate had essentially the

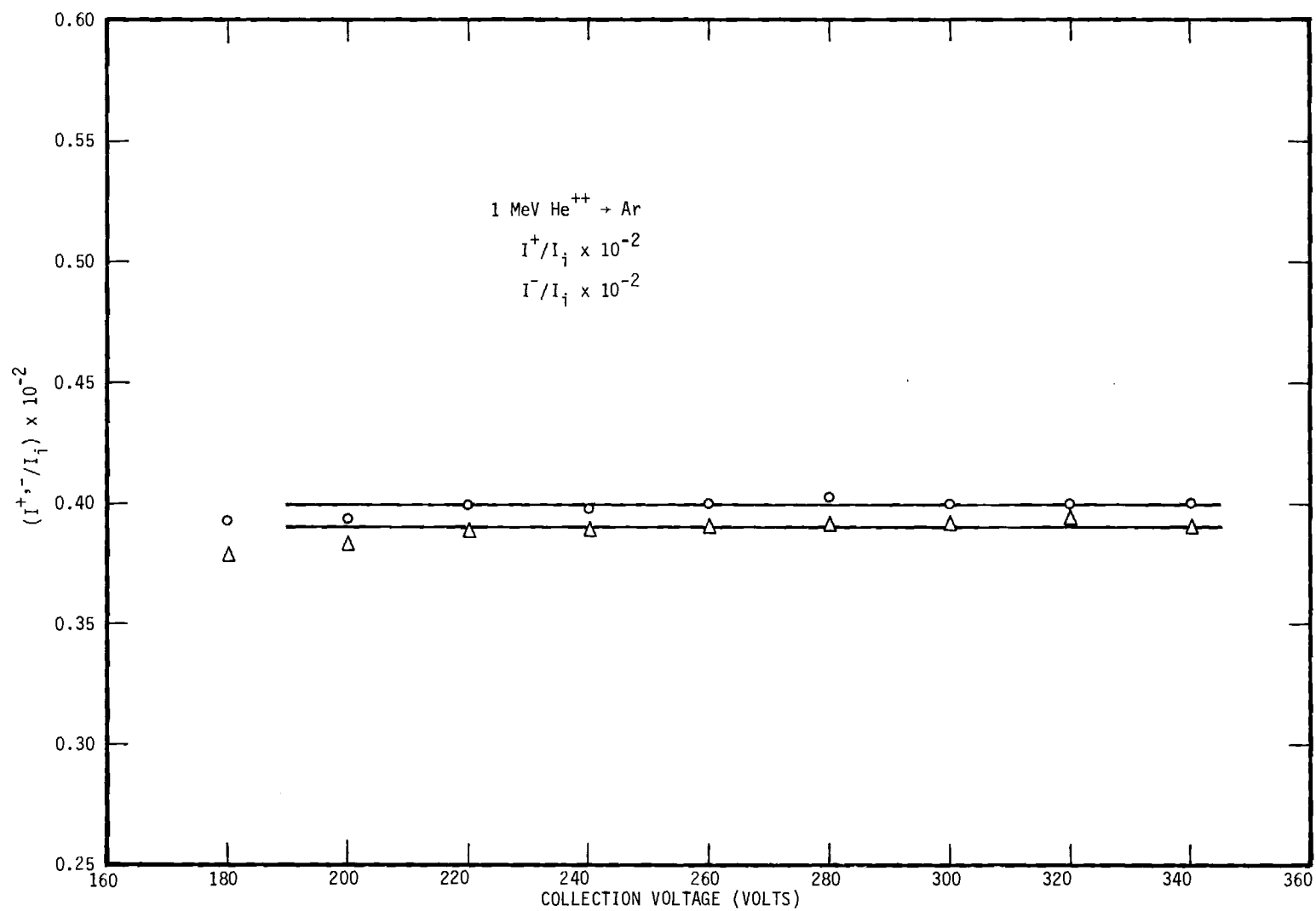


Figure 11. Response of Ion and Electron Currents, Produced by He<sup>++</sup> → Ar, to the Collection Voltage.

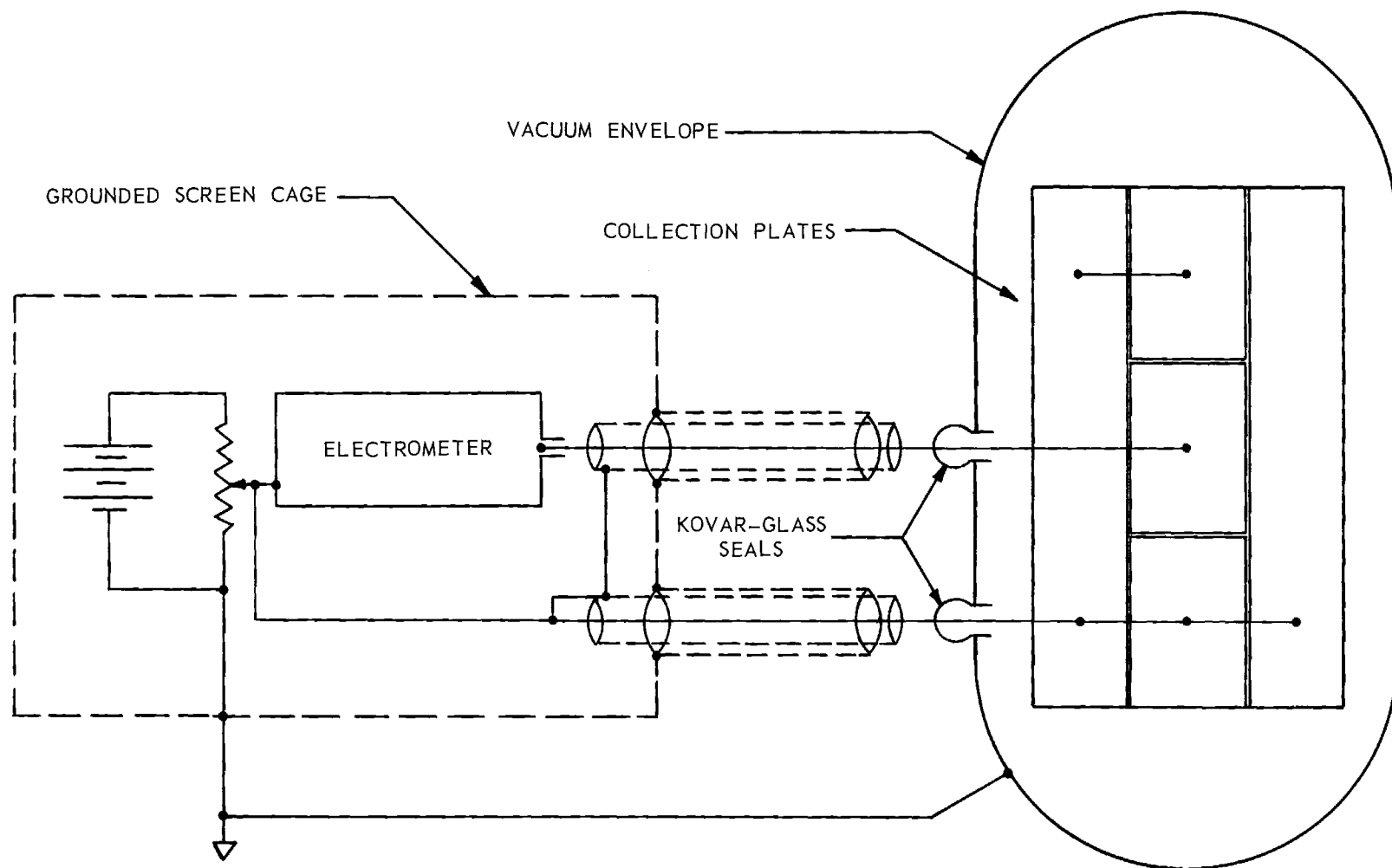


Figure 12. Schematic Diagram of the Electrical Connections to the Collection Assembly.



same potential as the guard plates. These instruments were enclosed in a well-grounded wire cage so that the pick up of ac noise in the laboratory would be minimized. AC power to the electrometers was supplied through isolation transformers which were also mounted in the shielded cage. The dc potentials were supplied to the collision chamber by shielded batteries, which also were in the cage, because any ripple or noise in this supply would be capacitively coupled into the electrometer inputs. The electrical connections from inside the collision chamber were passed through the chamber walls by means of kovar-glass seals. Each of the leads from the outside end of the seals to the electrometer cage was passed through cables with double coaxial shields. Only the outer shields were grounded. The inner shields were maintained at the same potential as their central current leads to reduce leakage. Similar guard arrangements through the chamber wall with triaxial shields would have further reduced leakage, but they were not required.

With this arrangement for the measurement of the electron and ion currents, the total background current (noise plus leakage) in the absence of the beam was about  $1 \times 10^{-13}$  amps, which was less than one percent of virtually all of the currents measured in this experiment. The background ionization currents produced when the beam was passed through only the background gas in the collision chamber were always less than one percent of the currents obtained when the target gas was admitted.

A Keithley (Model 415) pico-ammeter was used for the measurement of the net beam current, and for neutral beams a Keithley (Model 149) nano-voltmeter was used to measure the voltage output of the thermal beam power detector (refer to Appendix I for details). The pico-ammeters were

nominally calibrated by the manufacturer to  $\pm 4$  percent absolute uncertainty on the scales used in this experiment. A further calibration of their readings was made in this laboratory to  $\pm 2$  percent by means of a Gyra Electronics current source (Model CS-57).

In order to reduce the scatter of the data caused by beam fluctuations, RC damping was provided in the meter circuits of the electrometers which measured the electron and ion currents; however, the fast beam electrometer was undamped. All three instruments were located in close physical proximity to permit the investigator to read their scales in rapid succession. With this arrangement, the beam electrometer was observed until it chanced that there was a period of several seconds over which the fluctuations were at a minimum; then all three electrometers were quickly read. This procedure was repeated several times until several sets of self-consistent readings were obtained.

## CHAPTER V

EXPERIMENTAL RESULTS FOR THE CROSS SECTIONS  $\sigma_+$  AND  $\sigma_-$ Summary of Experimental Procedures and Discussion of Errors

The beams of  $H^+$  and  $He^+$  in the energy range from 0.150 to 1.00 MeV were obtained directly from a Van de Graaff accelerator. The energy of these beams was determined by  $90^\circ$  deflection in a calibrated magnetic field by means of an accurate NMR gauss meter. The nominal energy spread of the beams was  $\pm 2$  keV at 1 MeV. The  $H^0$ ,  $He^0$ , and  $He^{++}$  projectiles that were used in the present experiment were obtained from the  $H^+$  and  $He^+$  beams through charge changing collisions in a gas cell. The beam components emerging from the gas cell were electrostatically separated, and the desired component was passed into the collision chamber. As the beam traversed the collision chamber, it underwent ion and electron producing collisions with the target gas. These slow residual ions and electrons were collected on a set of collection electrodes located in the chamber. Also located in the collision chamber was the beam detector, which was designed to totally trap the beam. The slow ion and electron collectors were supplied with potentials of 300 to 400 volts to assure essentially 100 percent collection efficiency for these slow particles. An appropriately biased grid was provided to suppress secondary electron emission from the ion collection electrode.

The slow ion and electron currents were measured by means of sensitive electrometers that were absolutely calibrated to  $\pm 2$  percent, and

these electrometers were frequently interchanged to reduce systematic errors. The electronic noise, the leakage currents from the collection electrodes, and the currents produced by ionization of the background gas always totaled less than one percent of the signal for the  $\text{He}^{++}$  and  $\text{He}^0$  projectiles. For the  $\text{H}^0$  projectile, these currents were usually less than one percent, although in the upper part of the energy range (above 250 keV) the noise sometimes reached  $\pm 6$  percent. It was estimated that noise of even this magnitude was averaged, by making five or six measurements, to an effective value of only  $\pm 4$  percent. It is important to note that in a given measurement sequence several scales on each electrometer were used and, in addition, the roles of the two electrometers were interchanged. Therefore, even though the error associated with an individual scale on an electrometer is systematic, this measurement procedure made these errors essentially random, and they will be so designated in the following tables.

The charged beam  $\text{He}^{++}$  was measured by collection in a Faraday cup, using an electrometer that was calibrated to  $\pm 2$  percent in this laboratory. The neutral beams of  $\text{H}^0$  and  $\text{He}^0$  were measured by means of a thermal beam power detector, which required calibration. It is estimated that the absolute error in this calibration did not exceed  $\pm 5$  percent, and it was observed that the calibration was reproducible within about  $\pm 3$  percent from day to day. This detector could be operated in two fashions. In the first, the directly observed quantity was the emf generated in a thermocouple by the heat produced by the impinging neutral beam, and in the second, the observed quantity was the secondary emission current produced by the beam. The nano-voltmeter and the electrometer used

for these measurements were each absolutely calibrated to  $\pm 2$  percent. The noise in the nano-voltmeter and thermocouple circuit was always less than one percent of the signal for the  $\text{He}^0$  projectiles. However, in the upper part of the energy range for the  $\text{H}^0$  projectile, the noise sometimes reached  $\pm 8$  percent, but this also was estimated to be reduced, by multiple readings, to only  $\pm 5$  percent.

The largest and only known systematic error that was present in these measurements was in the determination of the target gas density. The mean temperature of the chamber which contained the gas was measured by means of thermocouples which indicated the temperature to be  $299^\circ\text{K}$  with a variation of about  $\pm 1$  degree over a period of weeks (depending on the ambient laboratory temperature). The target gas pressure was measured by means of a McLeod gauge, which is discussed in Appendix III. The possible error limits associated with the pressure determination are shown (on the last page of that appendix) to vary from one percent high to three percent low for hydrogen, and increasing with the weight of the gas up through argon, for which the pressure errors range from one percent high to 14 percent low.

The last measurement that entered the calculation of the cross sections for  $\sigma_+$  and  $\sigma_-$  was the effective lengths of the collector plates, which were believed to be determined to considerably better than one percent.

Table 1 summarizes the random errors associated with an individual cross section measurement for the three projectiles,  $\text{He}^{++}$ ,  $\text{He}^0$ , and  $\text{H}^0$ , used in this experiment. It is shown that the total error in the measurement of the individual quantities is less than the observed spread. This

Table 1. Estimated Random Errors (%) in  $\sigma_+$  and  $\sigma_-$ 

Measured Quantities	Projectiles: $\text{He}^{++}$	$\text{He}^0$	$\text{H}^0$
Slow Ion or Electron Current	$\pm 2$	$\pm 2$	$\pm 6$
$\text{He}^{++}$ Beam Current	$\pm 2$	----	----
$(\text{He}^0, \text{H}^0)$ Beam Power	---	$\pm 2$	$\pm 7$
Detector Calibration	---	$\pm 5$	$\pm 5$
Gas Pressure (Random)	$\pm 1$	$\pm 1$	$\pm 1$
Totals	$\pm 5$	$\pm 10$	$\pm 19$
Observed Spread in Individual Data Points	$\pm 8$	$\pm 12$	$\pm 30$
Standard Deviation of Observed Values	$\pm 5$	$\pm 8$	$\pm 19$

is attributed to random errors in the measurement of the ratios of the ion and electron currents to the beam current, due to beam fluctuations, and the time required to observe the three measuring instruments. The last row in Table 1 represents the standard deviation of the observed cross section values. If one assumes that the spread of the data points obeys a normal distribution, then 68 percent of all the values fall within the limits set by the standard deviation.

Table 2 summarizes the total estimated error in the cross section measurements for each projectile-target combination. These errors represent the sum of the standard deviation and the maximum estimated systematic McLeod gauge errors discussed in Appendix III.

### Present Results and Comparisons with Other Experimental and Theoretical Results

Presented in Table 3 and Figures 13-16 are the measured total apparent cross sections for the production of positive ions,  $\sigma_+$ , and electrons,  $\sigma_-$ , by fast doubly charged helium ions in targets of helium, argon, hydrogen, and nitrogen, respectively.

For the  $\text{He}^{++}$  projectile,  $\sigma_-$  is the total apparent ionization cross section  $\sigma_i$ , and the difference  $(\sigma_+ - \sigma_-)$  is the total apparent electron capture cross section  $\sigma_c$ . The values of the latter quantity from the present measurements are presented separately for the same four cases in Figures 17-20. Also shown for comparison are the  $\sigma_c$  measurements of Pivovar, et al.,<sup>10</sup> of Allison,<sup>22</sup> and Nikolaev, et al.<sup>14</sup> It should be recalled from Chapter II that the experiments of this group of investigators<sup>10,22,14</sup> all have been based upon the direct observation of the change in charge state

Table 2. Total Estimated Errors (%) in  $\sigma_+$  and  $\sigma_-$ 

Projectile \ Target:	He	Ar	H <sub>2</sub>	N <sub>2</sub>
He <sup>++</sup>	- 7 + 5	- 17 + 5	- 6 + 5	- 15 + 5
He <sup>o</sup>	- 11 + 8	- 21 + 8	- 10 + 8	- 19 + 8
H <sup>o</sup>	- 22 + 19	- 32 + 19	- 21 + 19	- 30 + 19



Table 3. Apparent Cross Sections for Production of Positive Ions  $\sigma_+$  and Electrons  $\sigma_-$   
by an Incident Beam of  $\text{He}^{++}$   
(All Cross Sections are in Units of  $10^{-16} \text{ cm}^2$  per Molecule.)

Projectile Energy (keV)	Helium		Argon		Hydrogen		Nitrogen	
	$\sigma_+$	$\sigma_-$	$\sigma_+$	$\sigma_-$	$\sigma_+$	$\sigma_-$	$\sigma_+$	$\sigma_-$
180	5.55	1.37	----	----	-----	----	25.2	13.7
200	5.50	1.55	26.3	16.3	11.7	6.20	24.5	14.3
250	4.98	1.93	24.3	16.8	10.5	6.70	23.2	14.9
300	4.61	2.21	22.6	17.2	9.35	6.85	21.4	15.0
350	4.28	2.44	21.4	17.3	8.65	6.97	20.4	15.2
400	3.93	2.47	20.4	17.3	7.92	6.85	19.4	15.2
500	3.48	2.51	18.7	16.7	6.90	6.34	17.9	14.9
600	3.12	2.50	17.5	16.2	6.20	5.90	16.3	14.3
700	2.84	2.43	16.5	15.6	5.61	5.37	15.2	13.7
800	2.61	2.30	15.5	14.9	5.01	4.91	14.3	13.2
900	2.40	2.19	14.8	14.3	4.67	4.59	13.5	12.7
1000	2.24	2.06	14.2	13.7	4.23	4.17	12.9	12.2

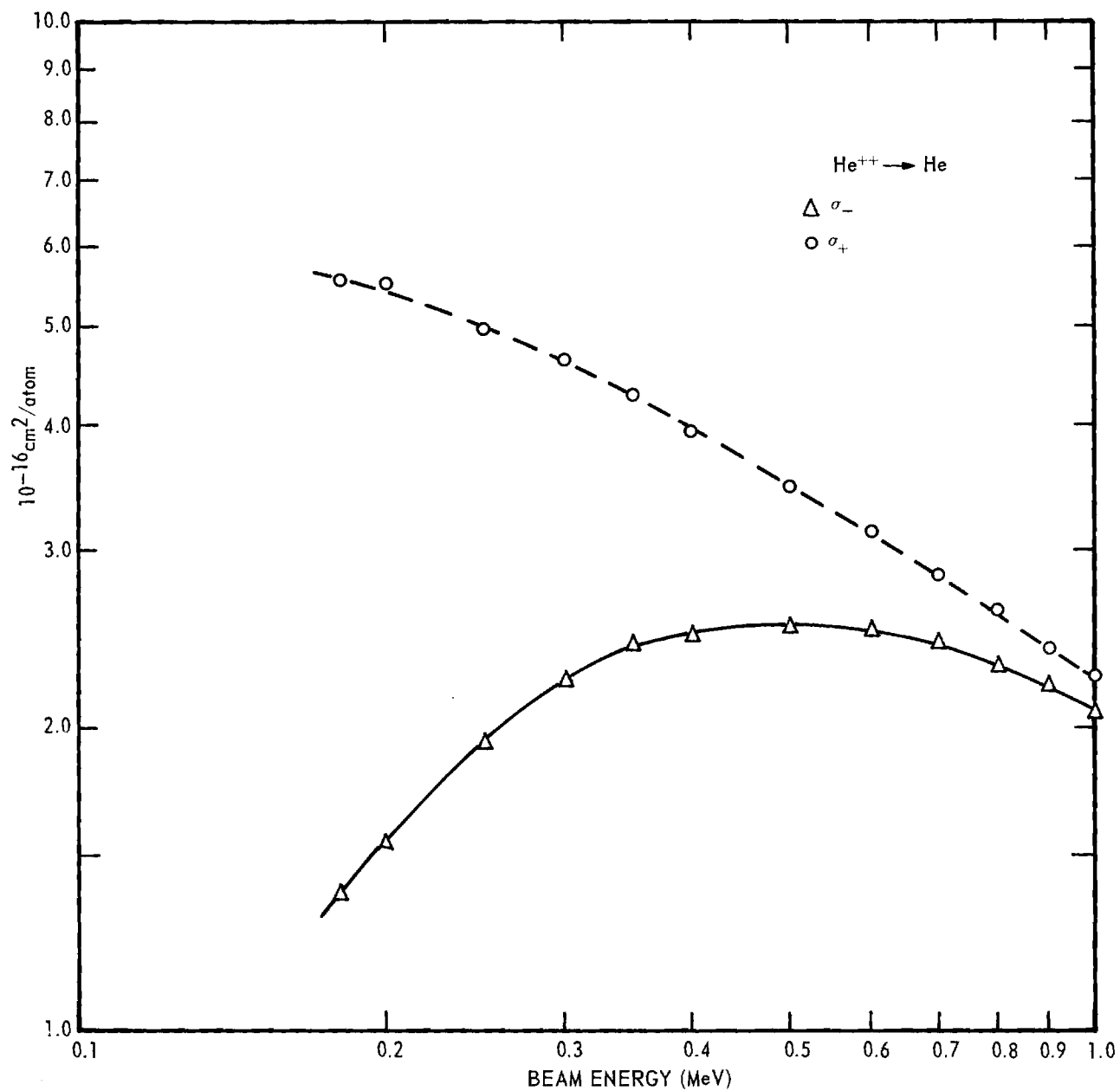


Figure 13. Total Apparent Cross Sections for Production of Positive Ions,  $\sigma_+$ , and of Free Electrons,  $\sigma_-$ , for  $\text{He}^{++}$  Ions Incident on Helium.

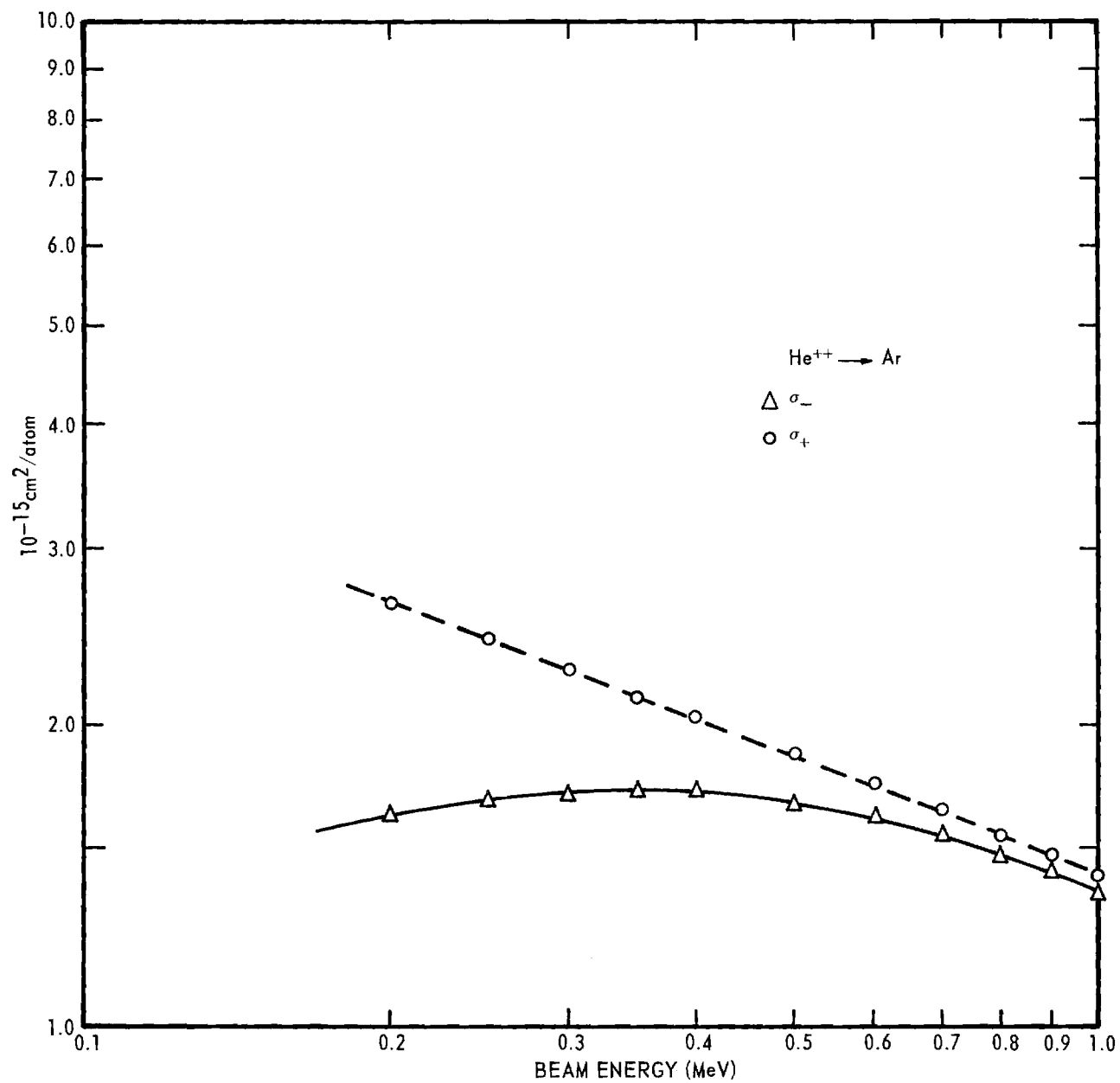


Figure 14. Total Apparent Cross Sections for Production of Positive Ions,  $\sigma_+$ , and of Free Electrons,  $\sigma_-$ , for  $\text{He}^{++}$  Ions Incident on Argon.

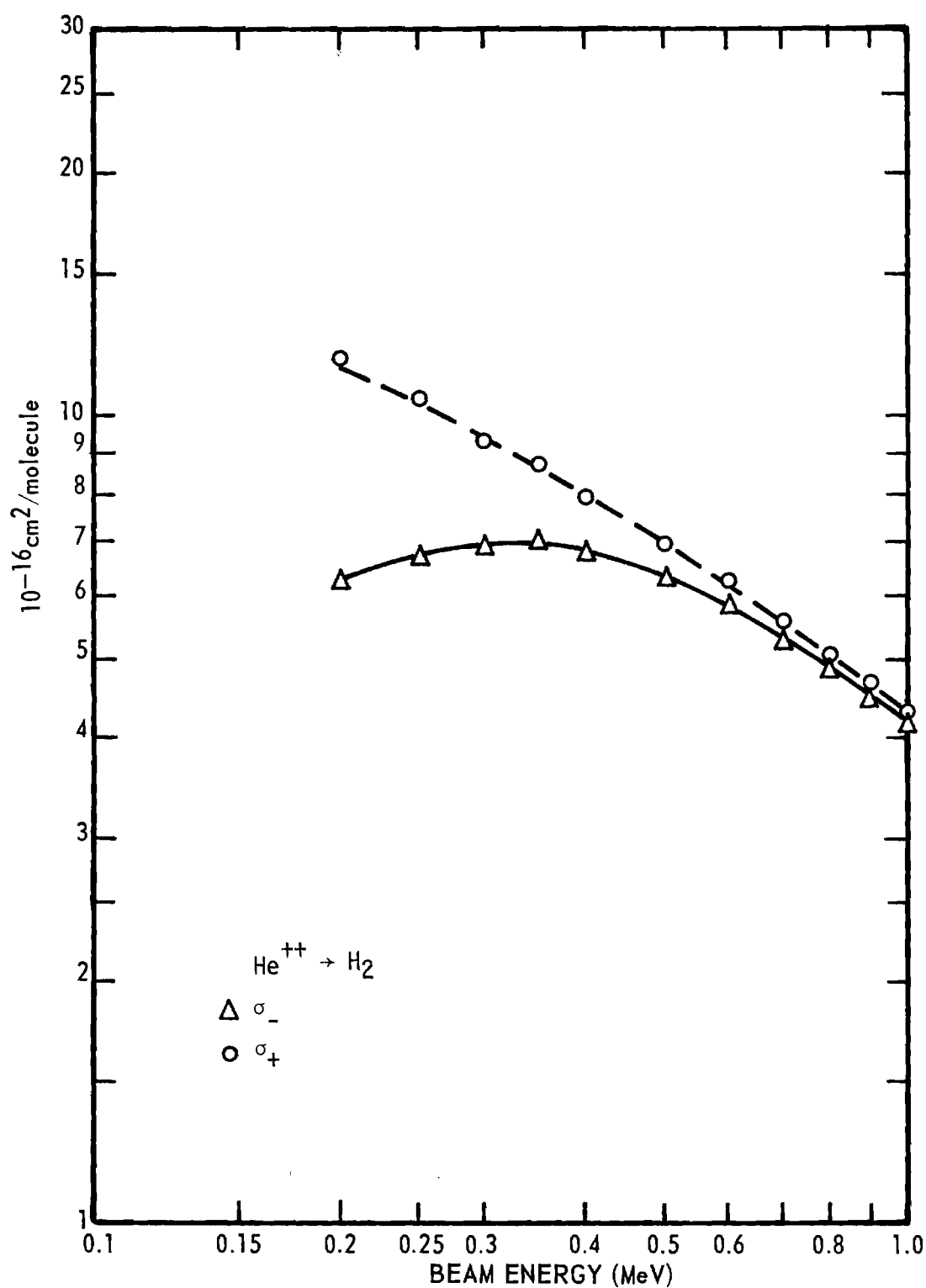


Figure 15. Total Apparent Cross Sections for Production of Positive Ions,  $\sigma_+$ , and of Free Electrons,  $\sigma_-$ , for  $\text{He}^{++}$  Ions Incident on Molecular Hydrogen.

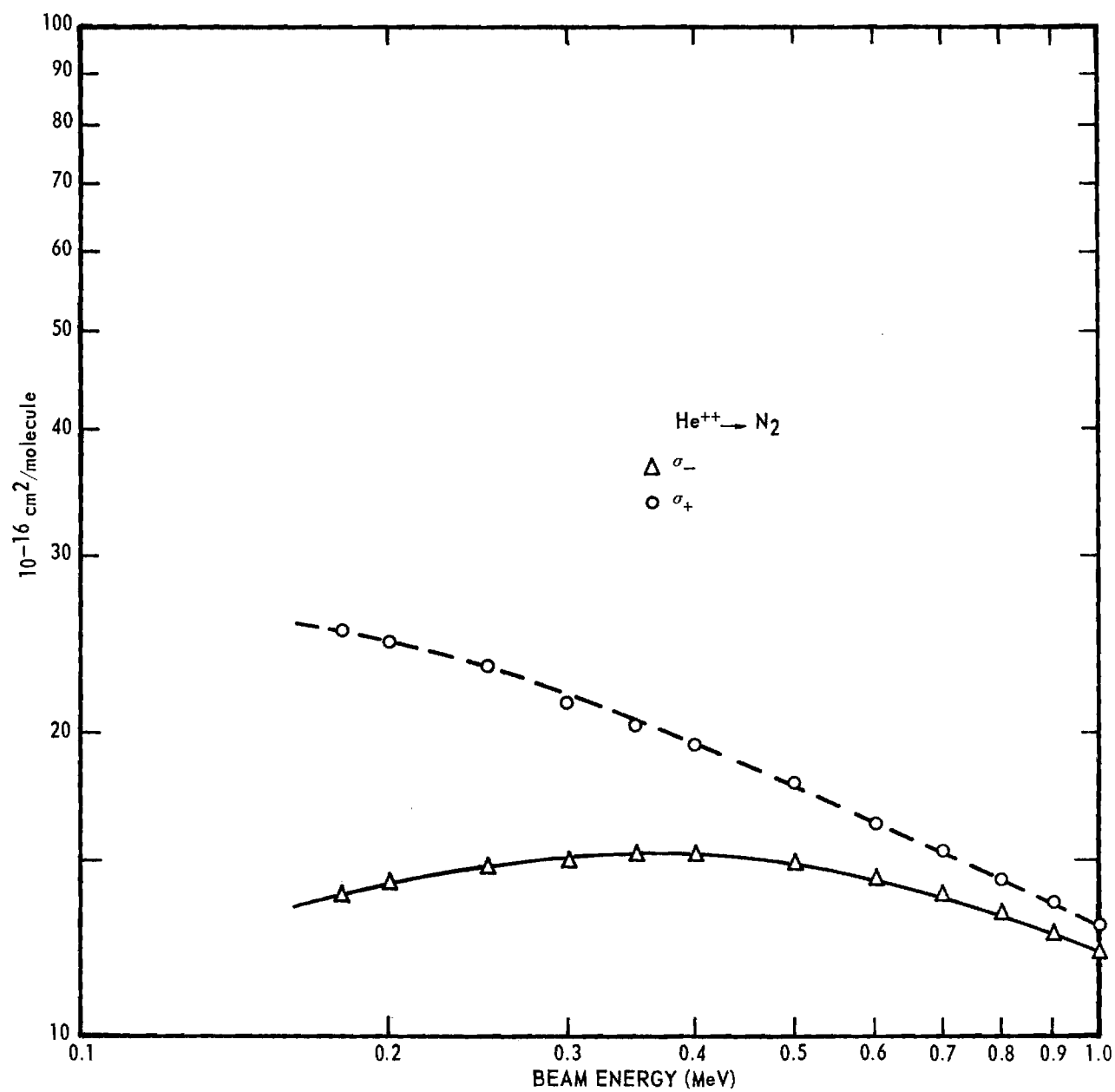


Figure 16. Total Apparent Cross Sections for Production of Positive Ions,  $\sigma_+$ , and of Free Electrons,  $\sigma_-$ , for  $\text{He}^{++}$  Ions Incident on Molecular Nitrogen.

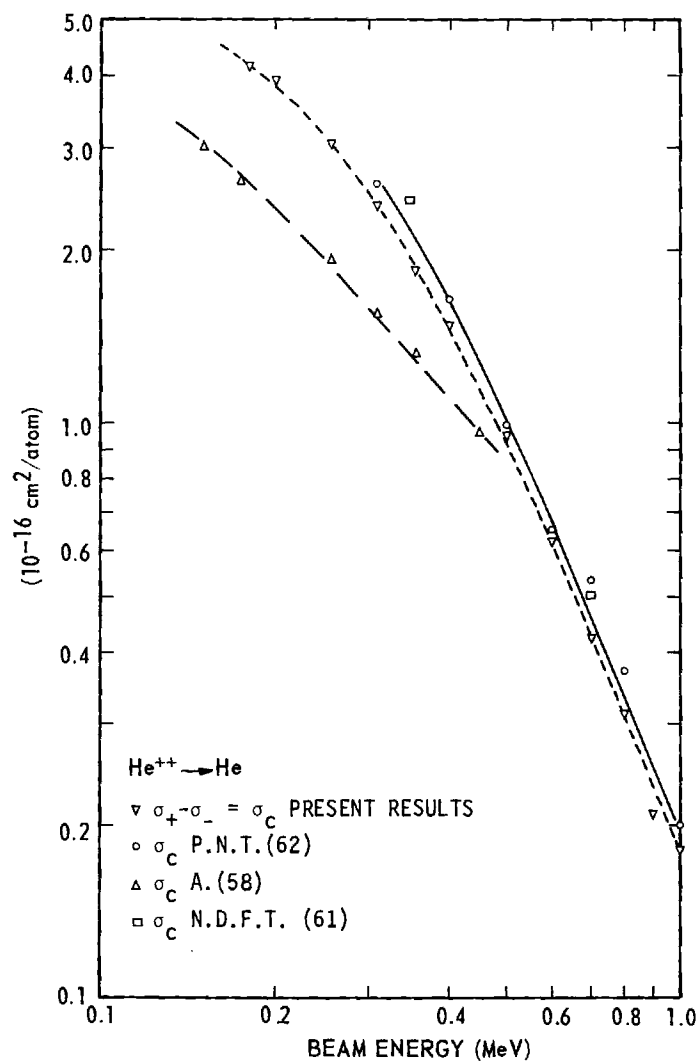


Figure 17.

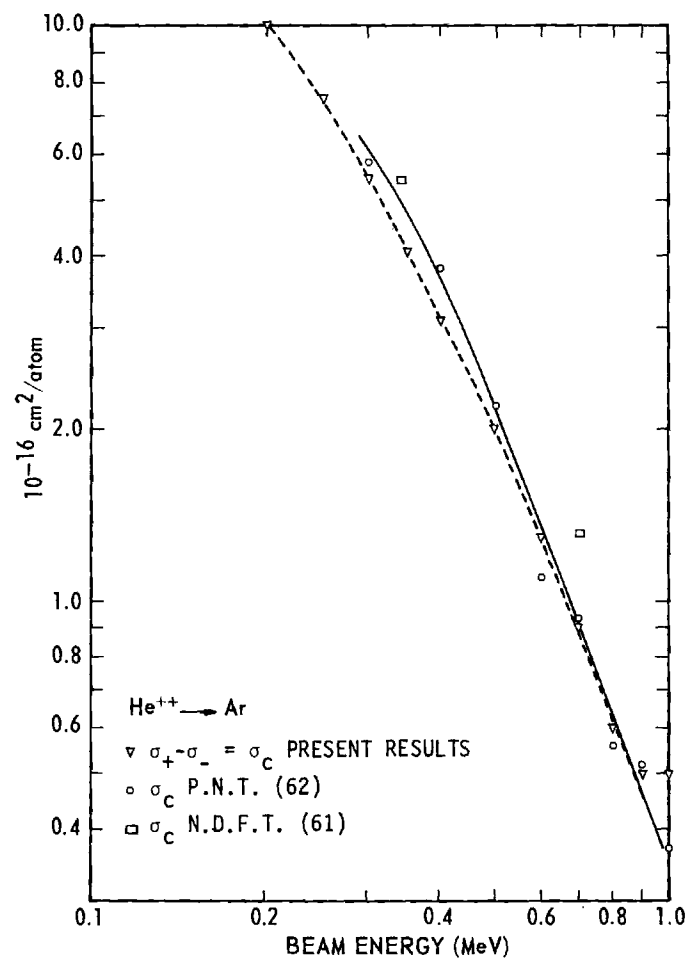


Figure 18.

Cross Correlation Between the Total Apparent Ion and Electron Production Cross Sections, and the Charge Changing Cross Sections for  $\text{He}^{++}$  Ions Incident on Helium (Fig. 17) and on Argon (Fig. 18). Key to References: P.T.N.(62), Pivovar, et al., (Reference 10); A(58), Allison, (Reference 22); N.D.F.T.(61), Nikolaev, et al., (Reference 14).

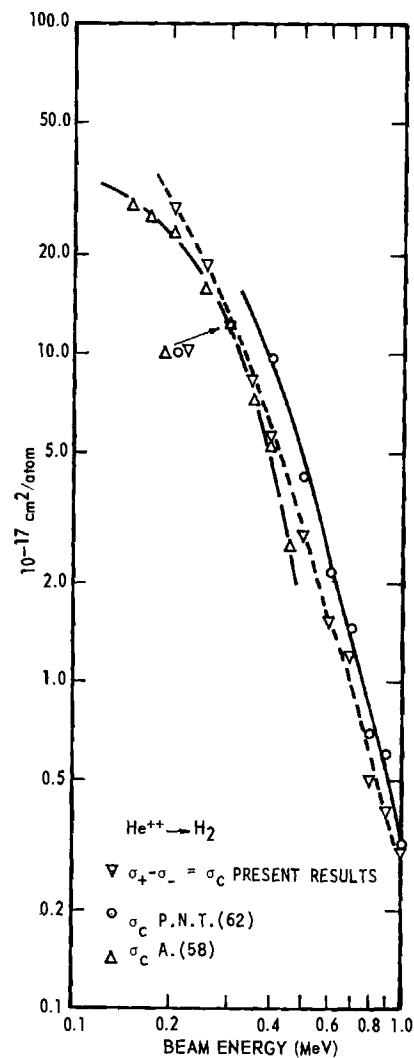


Figure 19.

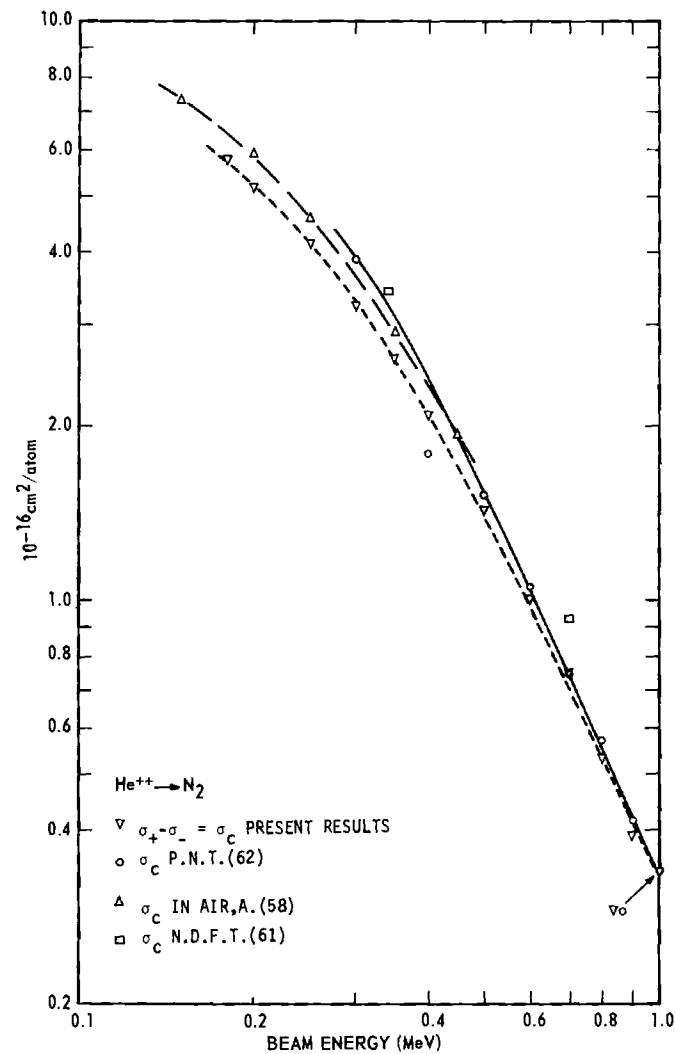


Figure 20.

Cross Correlation Between the Total Apparent Ion and Electron Production Cross Sections, and the Charge Changing Cross Sections for  $\text{He}^{++}$  Ions Incident on Molecular Hydrogen (Fig. 19) and on Molecular Nitrogen (Fig. 20). Key to References: P.T.N.(62), Pivovar, et al., (Reference 10); A(58), Allison, (Reference 22); N.D.F.T.(61), Nikolaev, et al., (Reference 14).

of the beam. Therefore, the  $\sigma_c$  determined from the above experiments involved measurements that were quite different from those of the present experiment, in which the net excess positive charge deposited in the gas by the fast beam was measured.

The cross section values measured in the present investigation are presented without correction for the Gaede effect (refer to Appendix III). Instead, the possible errors from this effect are incorporated into the error limits assigned to these results. The fractional accuracy of the difference cross sections is generally less than that of the individual cross sections. In the upper energy range ( $\sigma_+ - \sigma_-$ ) is fractionally small compared with either  $\sigma_+$  or  $\sigma_-$ , and, therefore, random errors in the differences are proportionately larger than in  $\sigma_+$  and  $\sigma_-$  individually. The systematic errors are, however, the same in both the difference and individual cross sections.

The indicated errors in the comparison results of Pivovar, et al.,<sup>10</sup> Allison,<sup>22</sup> and Nikolaev, et al.<sup>14</sup> were all about  $\pm 10$  percent. Each of these workers, however, employed a McLeod gauge as a pressure standard; consequently, there were some uncertainties with regard to systematic errors. In fact, from the comparison of the results of these workers, notably Pivovar and Allison, it is seen that they in some cases differ by more than 75 percent. The extent of this disagreement is significantly outside of their combined error limits.

It may be noted that the measurements made in this laboratory generally fall between those of Pivovar and of Allison, and the agreement generally improves for increasing energy. This is a surprising observation because random errors in  $\sigma_+$  and  $\sigma_-$  measurements are proportionately



larger in  $(\sigma_+ - \sigma_-)$ . In fact, for  $\text{He}^{++}$  on  $\text{H}_2$  the difference in  $\sigma_+$  and  $\sigma_-$  at 1 MeV is only about two percent and the random error in the difference is about  $\pm 3$  percent. The agreement with Pivovar at this energy therefore serves to indicate that  $\sigma_+$  and  $\sigma_-$  are relatively determined to better than one percent. This agreement provides strong confirmation of the validity of both the present total ion production and charge changing cross sections.

For the noble target gases He and Ar, it is noted that the agreement with Pivovar persists within 10 percent to the lowest projectile energies. However, for the molecular targets of  $\text{H}_2$  and  $\text{N}_2$ , the present results fall as much as 50 percent below those of Pivovar at 180 keV, which is outside of the combined error limits of these two experiments. It is seen in Figures 17-20 that Pivovar's results are higher in all the gases studied than the measurements of this laboratory. It is possible that a systematic error was present in Pivovar's results due to the entrance and exit channels on his collision chamber. In his experiment, which was described in Chapter II, the projectiles were passed through a gaseous target, the thickness of which directly entered the cross section calculation. Long narrow channels, comparable to the length of the collision chamber, of large pumping impedance were used to help confine the gas to the chamber. Because of the pressure gradient down the axis of these channels, the effective thickness of the target gas was not a simple quantity to evaluate, and perhaps led to a systematic error. Certainly, if this effective increase in the length of the collision chamber were not accounted for, the result would be a falsely large cross section measurement.

Finally, it is important to note that the departure from good agree-

ment with the results of Pivovar at low energies brings the present results into better agreement with those of Allison, which extend to an even lower energy.

The total apparent ion and electron production cross sections by fast incident neutral helium atoms, in the same four target gases, helium, argon, hydrogen, and nitrogen, are presented in Table 4 and Figures 21-24. Also shown for comparison are the similar measurements of Solov'ev, et al.<sup>7</sup> extending up to only 0.18 MeV.

As was discussed in Chapter II, Solov'ev's experiment is essentially the same as the present experiment. That is, he collected the slow residual collision products left in the gas by the passage of the fast beam. Specifically, he measured  $\sigma_+$  and  $\sigma_-$  in the same fashion as was done in this investigation. However, Solov'ev published only his  $\sigma_+$  results, for which the stated possible error was  $\pm 15$  percent. It is noted that the two sets of results are in rather good agreement, well within their combined error limits. For neutrals at these high energies, the probability is very small that the projectiles will capture electrons to form negative ions.<sup>36</sup> Therefore, the measured total apparent positive ion production cross section  $\sigma_+$  is identical to the total apparent ionization cross section  $\sigma_i$ . Similarly, the difference between the total apparent electron production cross section and the total apparent positive ion production cross section is just the total apparent stripping cross section  $\sigma_s$  for the fast neutrals. This difference is also plotted in each figure; for comparison there is also shown the total stripping cross sections of Allison,<sup>24</sup> of Barnett and Stier,<sup>12</sup> and the single stripping cross section of Pivovar, et al.<sup>11</sup> It is immediately evident that the present results are

Table 4. Apparent Cross Sections for Production of Positive Ions  $\sigma_+$  and Electrons  $\sigma_-$   
by an Incident Beam of  $\text{He}^0$   
(All Cross Sections are in Units of  $10^{-16} \text{ cm}^2/\text{molecules.}$ )

Projectile Energy (keV)	Helium		Argon		Hydrogen		Nitrogen	
	$\sigma_+$	$\sigma_-$	$\sigma_+$	$\sigma_-$	$\sigma_+$	$\sigma_-$	$\sigma_+$	$\sigma_-$
150	1.22	2.51	8.47	13.1	2.64	4.23	8.18	13.7
180	1.26	2.56	8.37	13.4	2.72	4.45	7.98	13.7
200	1.26	2.56	7.95	13.1	2.66	4.39	7.82	13.8
250	1.27	2.55	7.85	13.5	2.50	4.17	7.52	13.7
300	1.22	2.47	7.52	13.3	2.40	4.03	7.45	13.7
350	1.20	2.40	7.33	13.2	2.26	3.84	7.20	13.5
400	1.14	2.28	6.91	12.7	2.16	3.68	6.82	12.9
500	1.05	2.09	6.34	12.0	1.93	3.32	6.50	12.5
600	0.99	1.95	6.00	11.4	1.75	3.01	6.05	11.9
700	0.91	1.81	5.36	10.5	1.56	2.68	5.62	10.9
800	0.86	1.68	5.05	9.76	1.40	2.42	5.25	10.4
900	0.79	1.56	4.85	9.25	1.30	2.24	4.98	10.1
1000	0.73	1.43	4.26	8.24	1.17	2.01	4.60	9.46

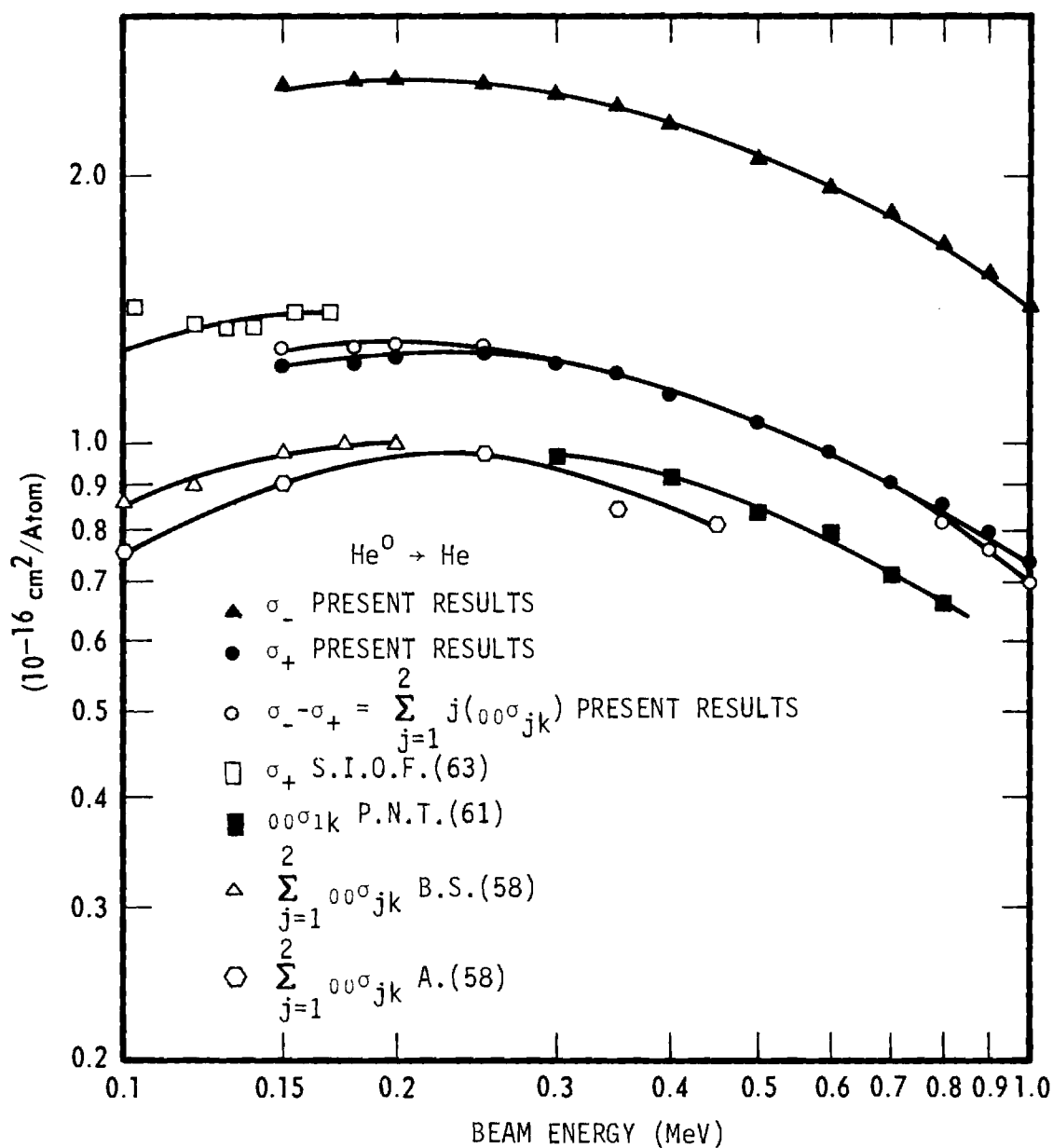


Figure 21. Total Apparent Positive Ion and Electron Production Cross Sections, and the Total Apparent Stripping Cross Sections, for Fast Neutral  $\text{He}^0$  Atoms Incident on Helium. Key to the Results of Other Investigators: S.I.O.F.(63), Solov'ev, et al., (Reference 7); P.T.N.(61), Pivovar, et al., (Reference 11); B.S.(58), Barnett and Stier, (Reference 12); A(58), Allison, (Reference 24).

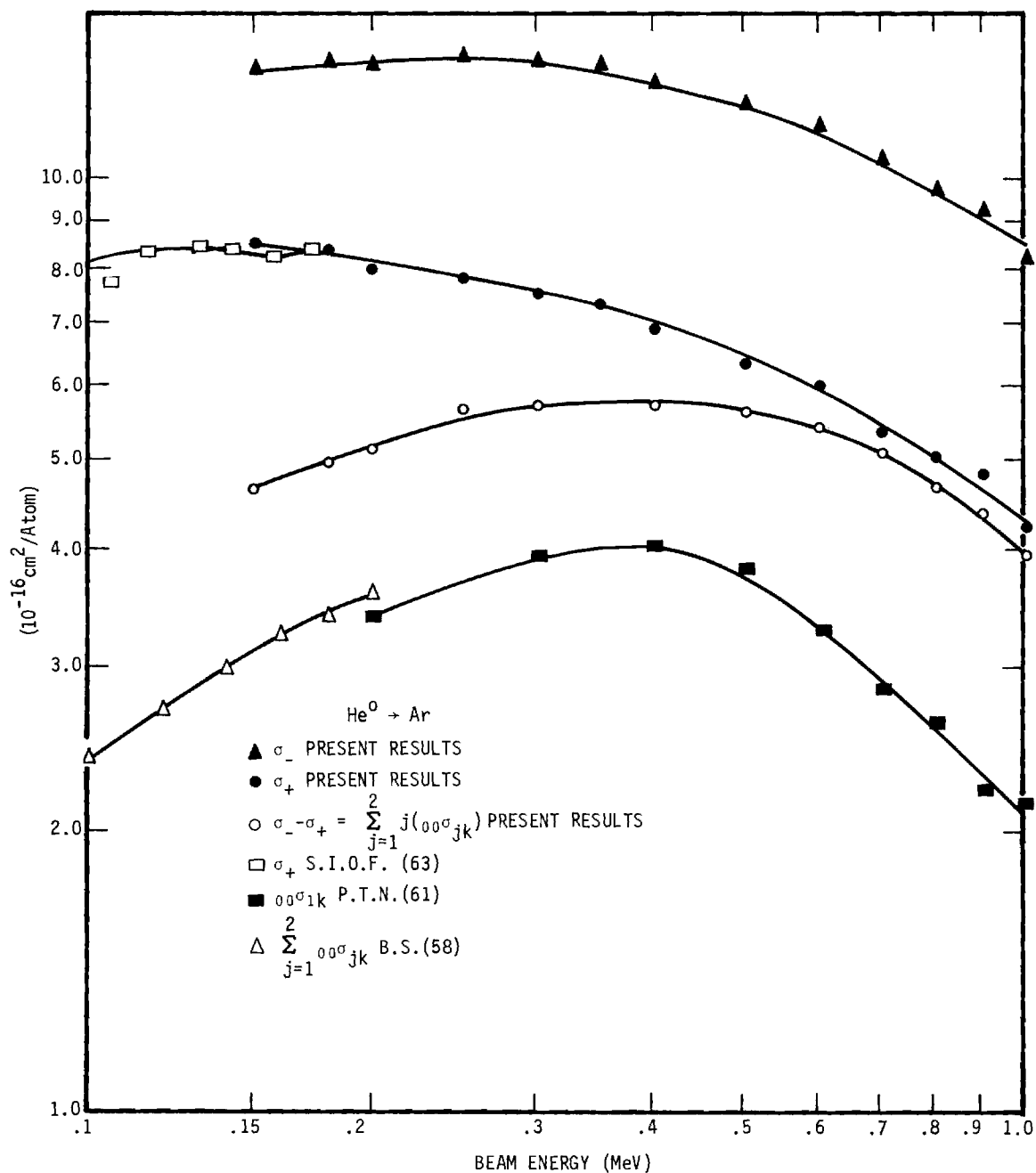


Figure 22. Total Apparent Positive Ion and Electron Production Cross Sections, and the Total Apparent Stripping Cross Sections, for Fast Neutral  $\text{He}^0$  Atoms Incident on Argon. Key to the results of other investigators:  
 S.I.O.F.(63), Solov'ev, et al., (Reference 7); P.T.N. (61), Pivovar, et al., (Reference 11); B.S.(58), Barnett and Stier, (Reference 12).

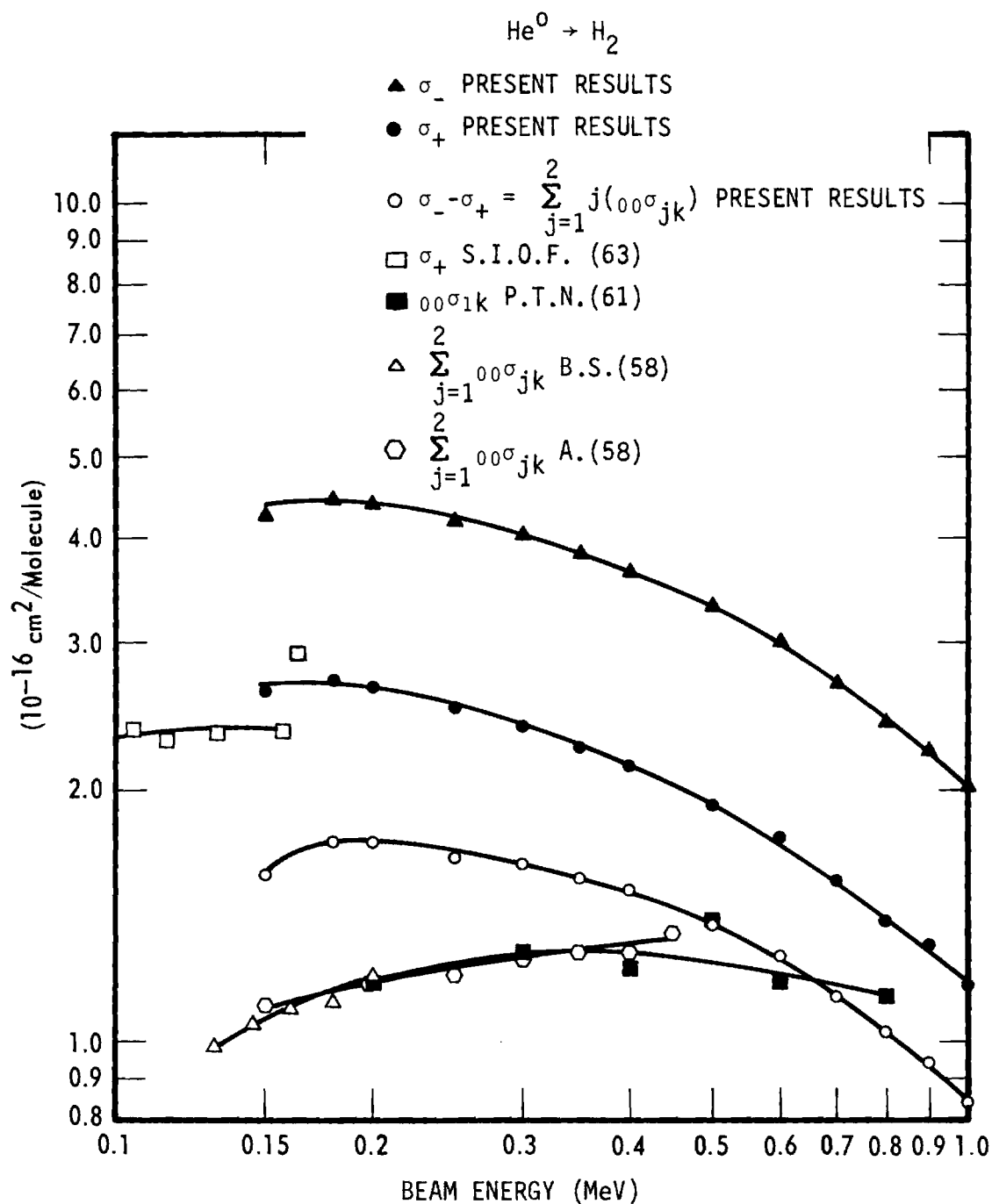


Figure 23. Total Apparent Positive Ion and Electron Production Cross Sections, and the Total Apparent Stripping Cross Sections, for Fast Neutral  $\text{He}^0$  Atoms Incident on Molecular Hydrogen. Key to the results of other investigators:  
 S.I.O.F.(63), Solov'ev, et al., (Reference 7);  
 P.T.N.(61), Pivovar, et al., (Reference 11);  
 B.S.(58), Barnett and Stier, (Reference 12);  
 A(58), Allison, (Reference 24).

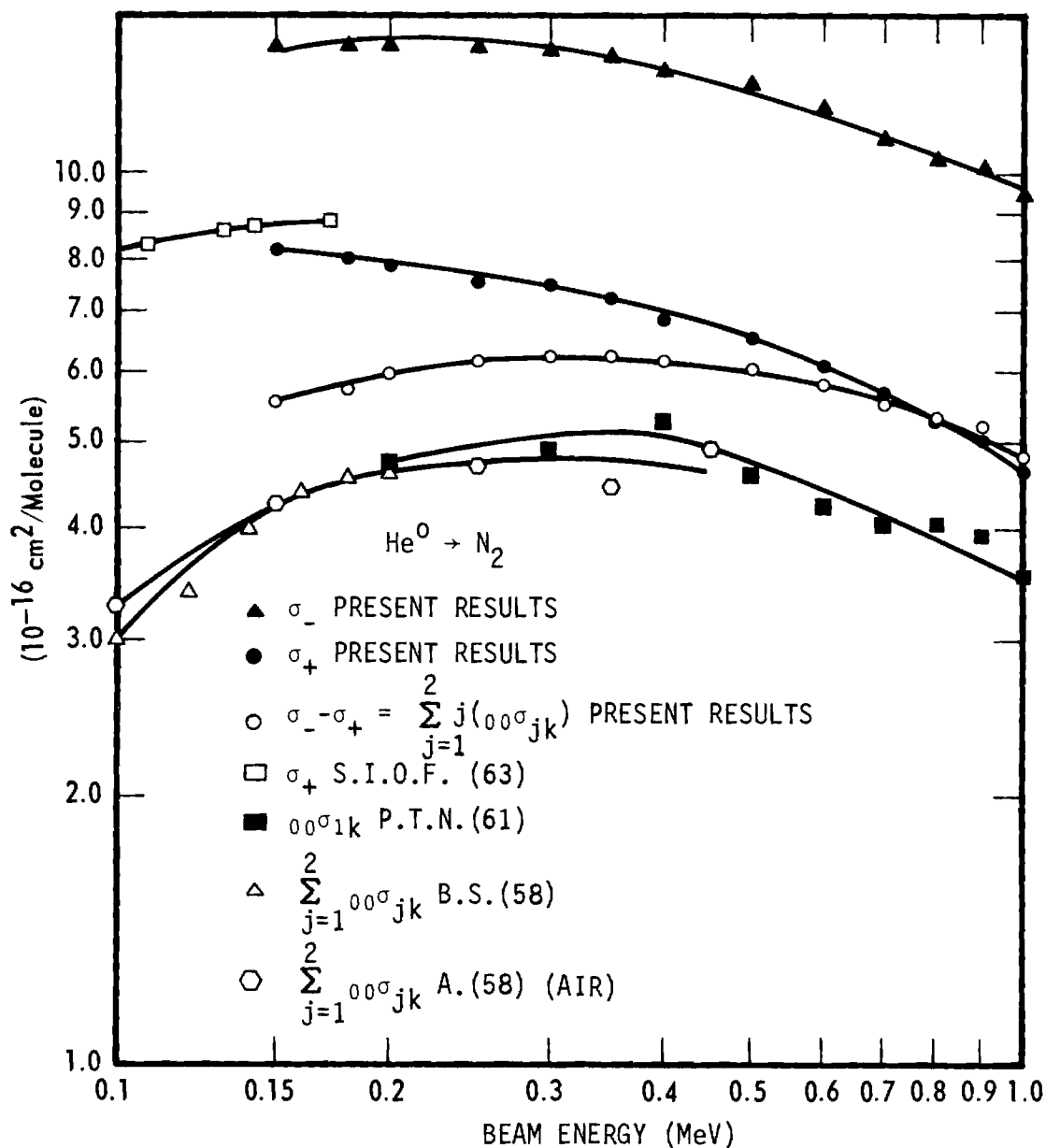


Figure 24. Total Apparent Positive Ion and Electron Production Cross Sections, and the Total Apparent Stripping Cross Sections, for Fast Neutral  $\text{He}^0$  Atoms Incident on Molecular Nitrogen.

Key to the results of other investigators:

S.I.O.F.(63), Solov'ev, et al., (Reference 7);

P.T.N.(61), Pivovarov, et al., (Reference 11);

B.S.(58), Barnett and Stier, (Reference 12);

A(58), Allison, (Reference 24).

systematically some 40 percent higher than those of the last three investigators, who are in fairly good agreement with each other. It should be noted, however, that the present result is not precisely the same physical quantity as theirs. Since in this investigation all of the electrons formed in the target were collected, the measured total apparent stripping cross section  $\sigma_s$  was the single-stripping plus twice the double-stripping cross section, i.e.,  $\sigma_s = \sum_{j=1}^2 j ({}_{00}\sigma_{jk})$ . (Recall that the unspecified subscript k denotes a summation over the full range of charge states it represents.) In contrast, Allison and Barnett have measured the total attenuation of the neutral fast beam by both single and double stripping, with no attempt to distinguish these; hence, their result is simply

$\sum_{j=1}^2 {}_{00}\sigma_{jk}$ . The observed differences then imply that

$$\sum_{j=1}^2 j ({}_{00}\sigma_{jk}) \approx 1.4 \sum_{j=1}^2 {}_{00}\sigma_{jk} \quad (19)$$

$${}_{00}\sigma_{2k} \approx 2/3 {}_{00}\sigma_{1k} \quad (20)$$

However, this inference is in contradiction to the separate findings of Allison<sup>23</sup> and Solov'ev, et al.<sup>7</sup> that  ${}_{00}\sigma_{2k}$  is not more than five percent of  ${}_{00}\sigma_{1k}$ . The agreement between the results of Pivovar and the other two workers, which is shown in Figures 21-24, also suggests that the double-stripping cross section is small.

It was mentioned in Chapter II that these  ${}_{00}\sigma_{1k}$  results of Pivovar



are rather suspect, for the following reasons. Both  ${}_{00}\sigma_{1k}$  for the  $\text{He}^0$  beam and  ${}_{20}\sigma_{1k}$  for the  $\text{He}^{++}$  beam were determined indirectly from the direct measurements of the charge changing cross sections for a  $\text{He}^+$  beam, namely  ${}_{10}\sigma_{2k}$  and  ${}_{10}\sigma_{0k}$ , combined with measurements of the equilibrium fractions  $F_{0\infty}$ ,  $F_{1\infty}$ , and  $F_{2\infty}$ . Pivovar assumed that all double electron capture and double stripping cross sections were negligible in order to drop terms from the equilibrium fractions expressions. This is clearly not justified, because even though those cross sections may be small ( $\leq$  five percent) they are multiplied in the equations by other very sizable cross sections. Nevertheless, he did make those assumptions to arrive at the following relations .

$${}_{20}\sigma_{1k} = {}_{10}\sigma_{2k} \frac{F_{1\infty}}{F_{2\infty}} \quad (21)$$

and

$${}_{00}\sigma_{1k} = {}_{10}\sigma_{0k} \frac{F_{1\infty}}{F_{0\infty}} \quad (22)$$

for which the experimental errors were  $\pm 24$  percent and  $\pm 34$  percent, respectively.

It should be noted that in a later paper,<sup>10</sup> Pivovar directly measured  ${}_{20}\sigma_{1k}$ , in Equation 21 above, using a  $\text{He}^{++}$  beam and obtained results that were as much as 40 percent larger than his own earlier determination. The conclusion to be drawn from this discussion is that even though the cross sections in Equation 21 were measured more accurately than those of Equation 22, the direct measurement of the cross section in Equation 21 changed the value some 30 to 40 percent. It appears quite likely, there-

fore, that the cross sections in Equation 22, with which the present investigation is concerned, may be in even greater error.

In light of the above facts it seems almost fortuitous that Pivovarov's results agree so well with those of Allison and Barnett, et al., both of which were believed to have been less than  $\pm 10$  percent in error.

The conclusions regarding the discrepancies in the variously measured stripping cross sections for  $\text{He}^0$  are the following:

1. two experiments that observe the residual slow collision products have measured  $\sigma_+$  and agree within ten percent;

2. in both of these experiments, checks on the equality of measuring efficiency in  $\sigma_-$  and  $\sigma_+$  were satisfactorily made (this will be further discussed for the present experiment);

3.  $\sigma_- - \sigma_+ = \sum_{j=1}^2 j (oo\sigma_{jk})$  was, therefore, accurately determined within  $\pm 3$  percent;

4. two experiments were performed elsewhere that directly observed the projectile beam after it had traversed the collision region, and their results for  $\sum_{j=1}^2 oo\sigma_{jk}$  agreed with each other within ten percent;

5. the  $\sum_{j=1}^2 j (oo\sigma_{jk})$  results were about 40 percent greater than the  $\sum_{j=1}^2 oo\sigma_{jk}$  results;

6. if both results were correct, then  $oo\sigma_{2k} \approx 2/3 oo\sigma_{1k}$ ; however, this was shown to be false. Therefore, the final conclusion is that

7. there is a basic measurement error, attributable to  $oo\sigma_{1k}$ , which is common to one or the other of the two types of experiments.

After thoroughly testing the present apparatus, it is believed that the results obtained with it are accurate within the quoted error limits. Therefore, the discrepancy remains unresolved.

As was discussed in Chapter III, a major concern in this experiment is the possibility that fast neutral beams, which were obtained through electron capture by fast singly charged ions in a gas cell, might be appreciably contaminated with atoms in metastable excited states. Tests were described, however, that gave no evidence for the presence of such metastable states in either  $\text{H}^0$  or  $\text{He}^0$  beams. An important further verification of the absence of the effects of excited states in the neutral  $\text{He}^0$  beam is found in the data of Figure 21 for He neutrals into He target gas. Since the target and projectile particles are identical in this case, the cross sections for the total apparent ionization of the target and the total apparent stripping of the projectile should be equal, provided that both are in the same initial atomic state. The latter is surely the ground state for the room temperature target gas atoms. It is evident in Figure 21 that  $(\sigma_- - \sigma_+)$  and  $\sigma_+$  are in fact equal within the experimental errors and the small deviations from complete agreement are probably not significant.

In Table 5 and in Figures 25-28 are shown the total apparent ion production cross sections  $\sigma_+$  and the total apparent electron production cross sections  $\sigma_-$  for  $\text{H}^0$  incident on He, Ar,  $\text{H}_2$ , and  $\text{N}_2$ , respectively. The difference cross sections  $(\sigma_- - \sigma_+)$  for these cases are also shown in the figures.

It should be noted that the energy range over which an  $\text{H}^0$  beam of satisfactory intensity could be obtained was restricted to 150 to 400 keV.

Table 5. Apparent Cross Sections for Production of Positive Ions  $\sigma_+$  and Electrons  $\sigma_-$   
by an Incident Beam of  $H^O$   
(All Cross Sections are in Units of  $10^{-16} \text{ cm}^2/\text{molecule.}$ )

Projectile Energy (keV)	Helium		Argon		Hydrogen		Nitrogen	
	$\sigma_+$	$\sigma_-$	$\sigma_+$	$\sigma_-$	$\sigma_+$	$\sigma_-$	$\sigma_+$	$\sigma_-$
150	0.40	1.1	3.0	6.9	0.91	1.9	3.0	6.6
180	0.39	1.1	2.9	6.6	0.85	1.7	2.8	6.1
200	0.39	1.0	2.9	6.7	0.82	1.6	2.7	6.2
250	0.35	0.95	2.5	6.0	0.71	1.4	2.2	5.3
300	0.31	0.80	2.1	5.2	0.62	1.2	1.9	4.5
350	0.29	0.75	1.9	4.8	0.54	1.1	1.9	4.5
400	0.27	----	1.8	4.6	0.50	1.0	1.7	4.3

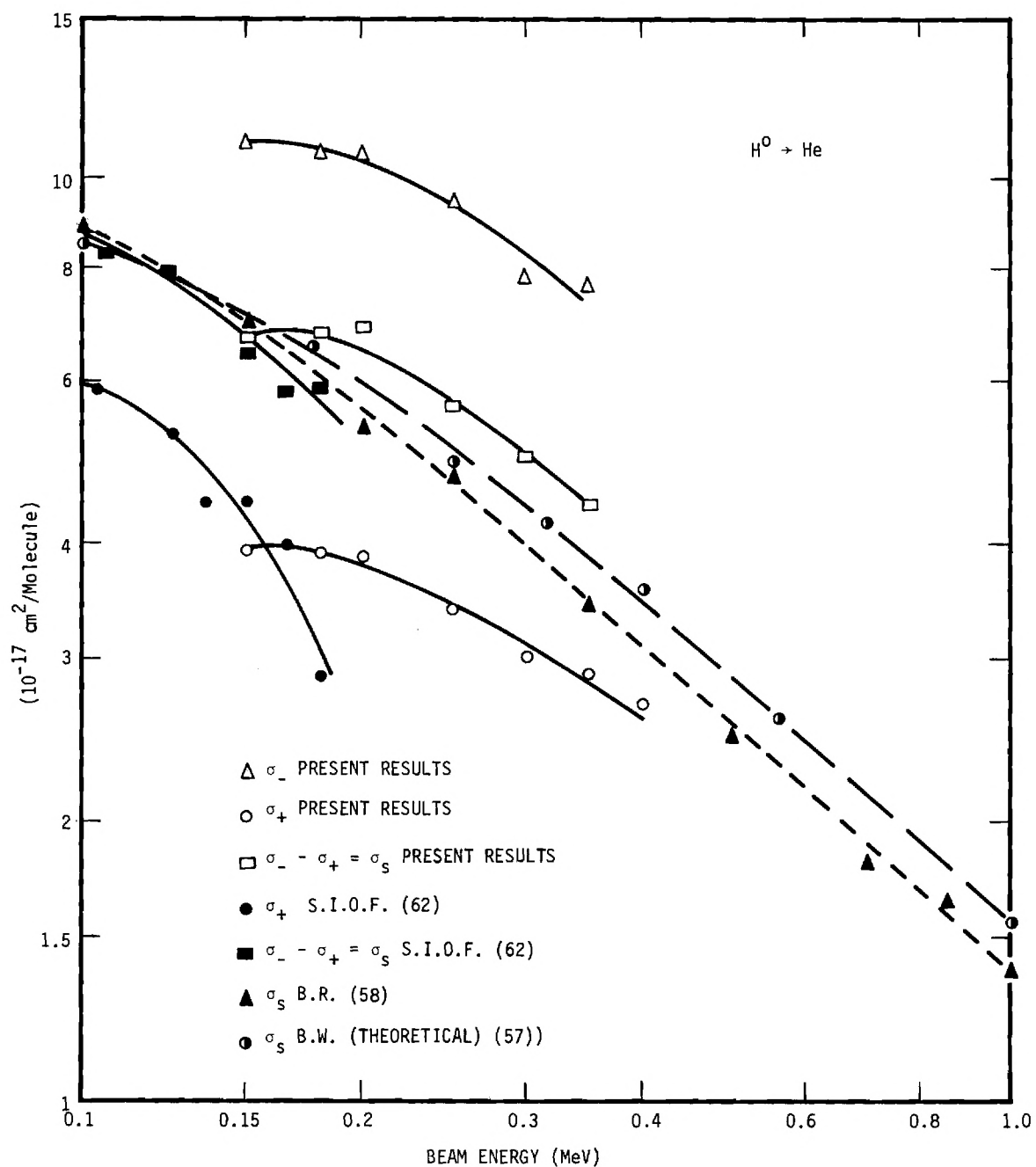


Figure 25. Total Apparent Positive Ion and Electron Production Cross Sections, and the Stripping Cross Sections, for  $H^0$  Atoms Incident on Helium. Key to the results of other investigators: S.I.O.F.(62), Solov'ev, et al., (Reference 8); B.R.(58), Barnett, et al., (Reference 13); B.W.(57), Bates, et al., (Reference 18).

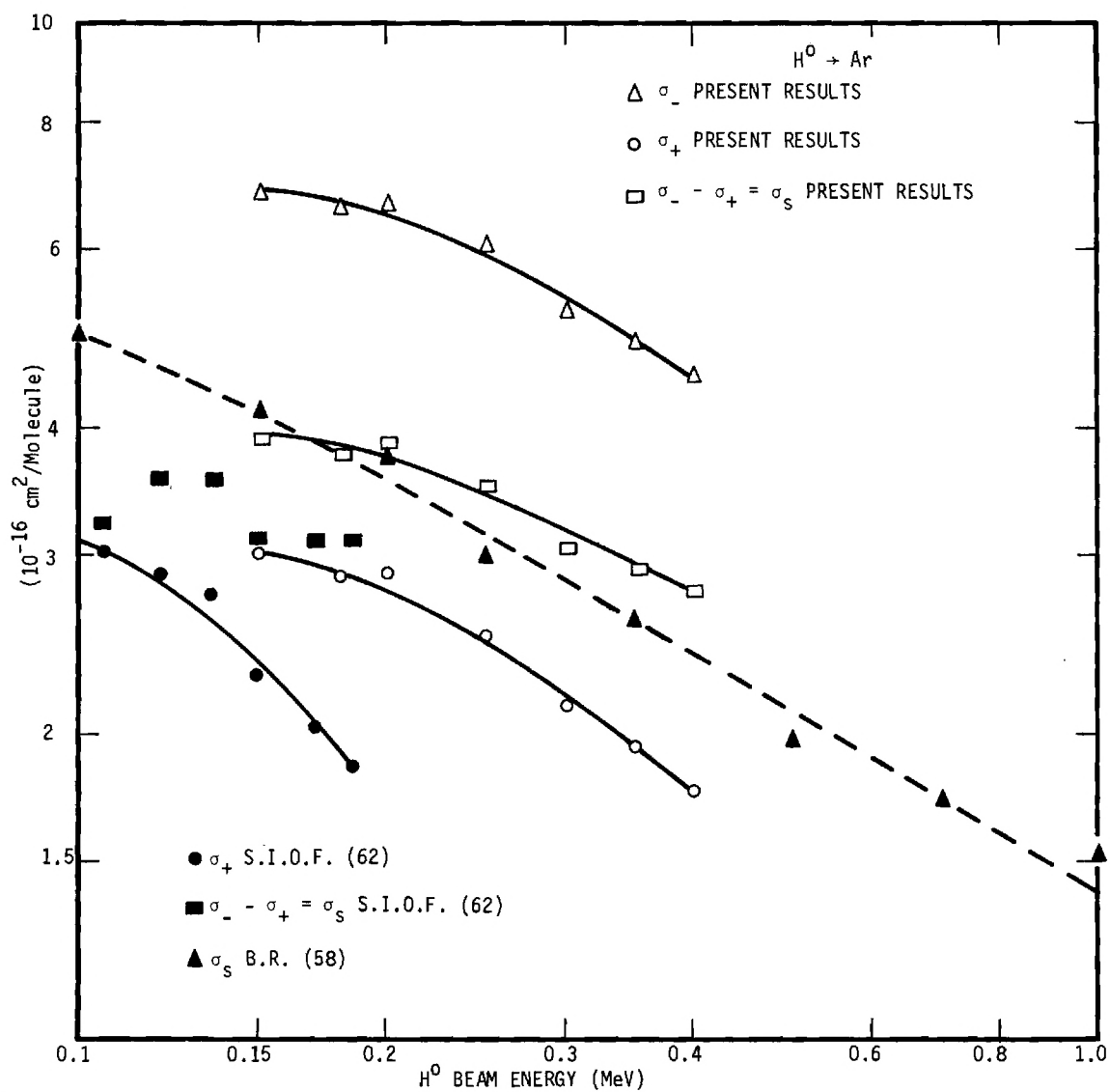


Figure 26. Total Apparent Positive Ion and Electron Production Cross Sections, and the Stripping Cross Sections, for  $H^0$  Atoms Incident on Argon. Key to the Results of other Investigators: S.I.O.F.(62), (Reference 8); B.R.(58), Barnett, et al., (Reference 13).

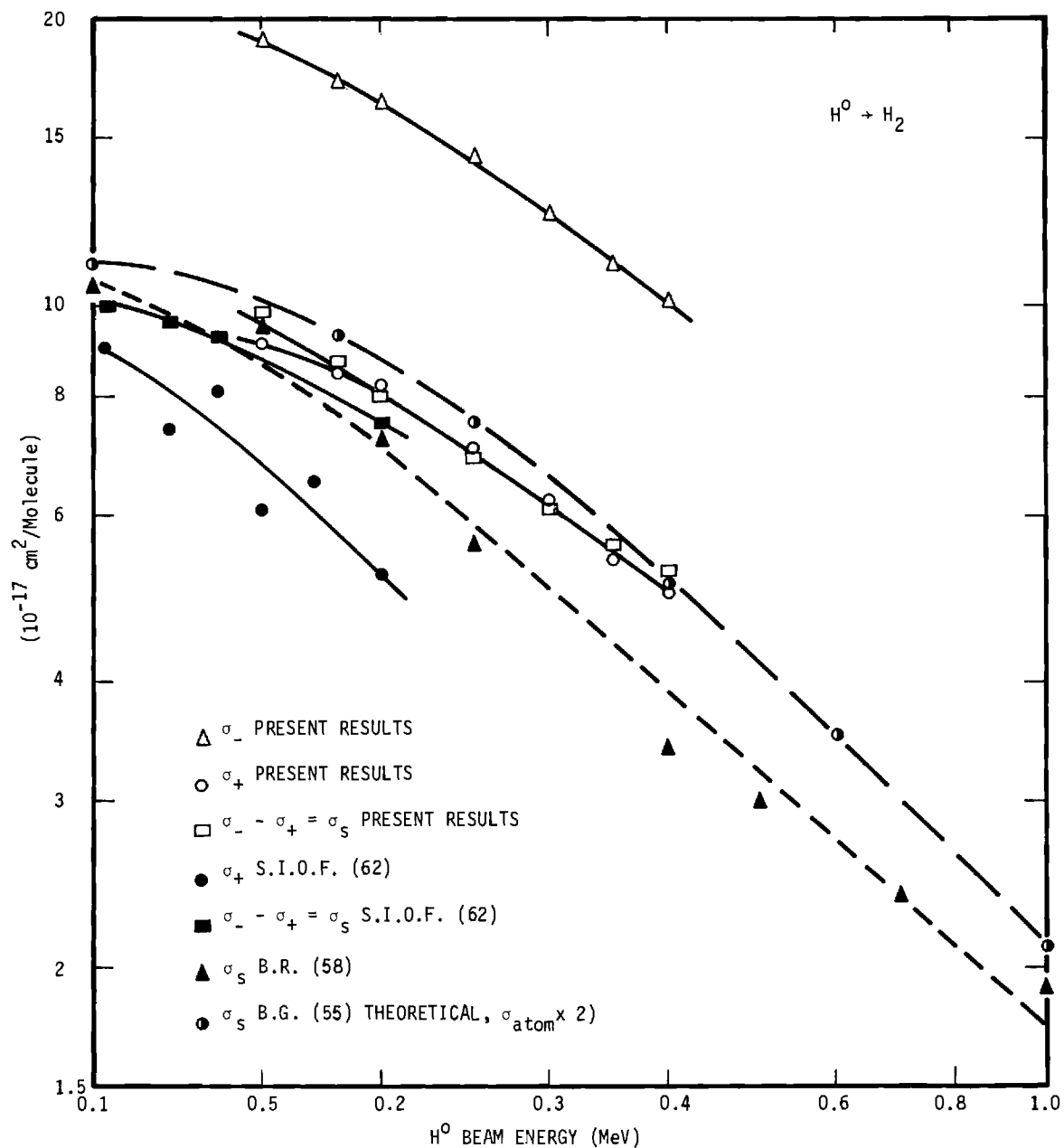


Figure 27. Total Apparent Positive Ion and Electron Production Cross Sections, and the Stripping Cross Sections, for  $H^0$  Atoms Incident on Molecular Hydrogen. Key to the Results of Other Investigators: S.I.O.F.(62), (Reference 8); B.R.(58), Barnett, et. al., (Reference 13); B.G.(55), Bates, et al., (Reference 19).

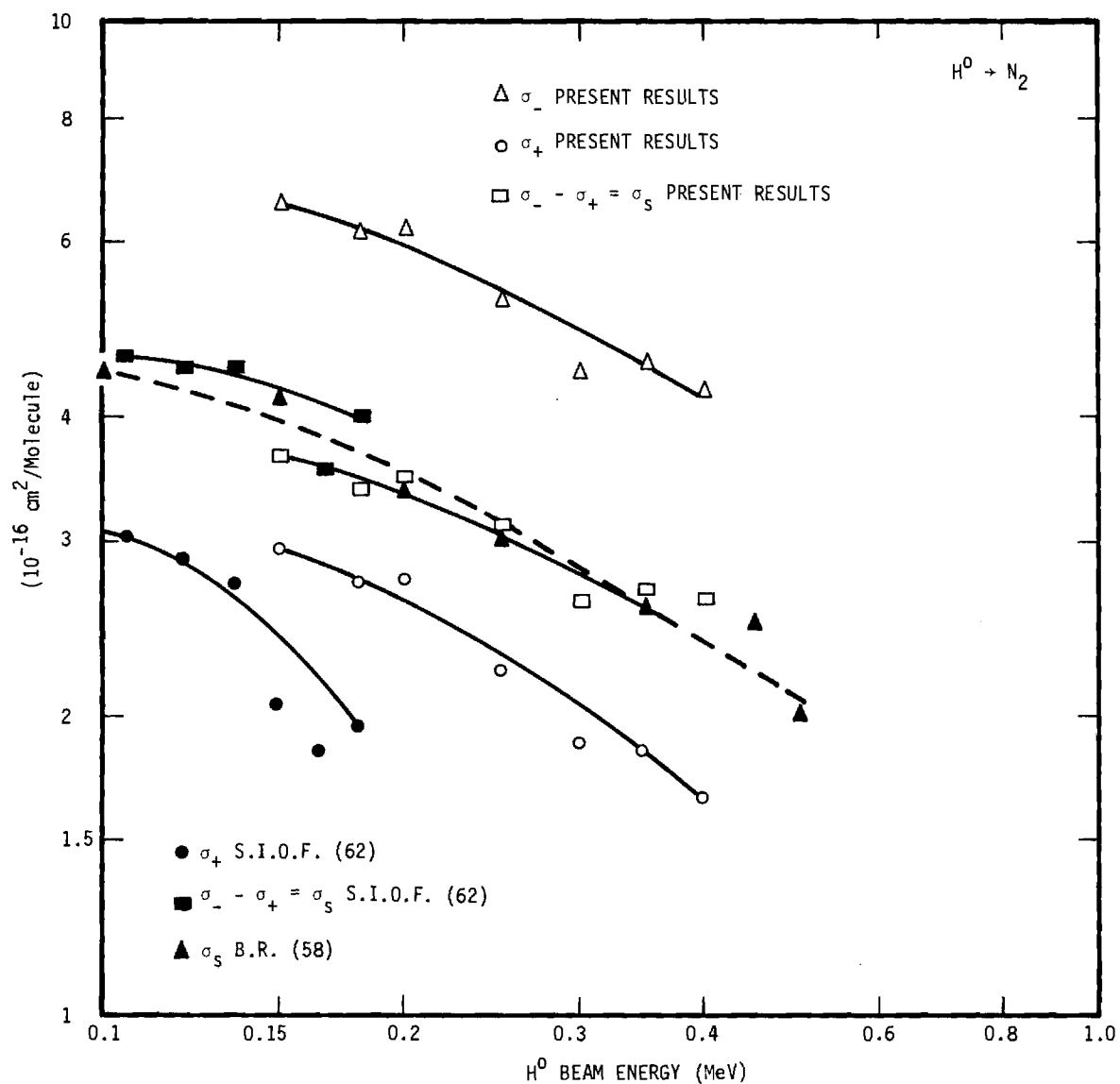


Figure 28. Total Apparent Positive Ion and Electron Production Cross Sections, and the Stripping Cross Sections, for  $H^0$  Atoms Incident on Molecular Nitrogen. Key to the Results of Other Investigators: S.I.O.F.(62), Solov'ev, et al., (Reference 8); B.R.(58), Barnett, et al., (Reference 13).

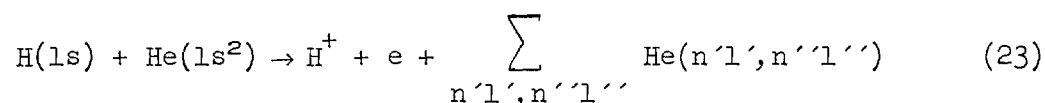


This restriction was due to the very rapid fall-off of the electron capture cross section of  $H^+$  with increasing energy. The sensitivity of the neutral beam detector was insufficient to maintain an acceptable signal-to-noise ratio with the beam intensities available above 400 keV. At 400 keV, the noise was  $\pm 8$  percent of the beam current and rapidly increased with higher energies. Also, about this same energy the electron and ion currents had decreased to the point that the noise was about  $\pm 6$  percent. It was clear that the only significant way to extend these measurements to higher energies was to obtain a larger beam current from the accelerator. It was considered more important, for the present however, to progress on to the next phase of the cross section measurements.

Shown for comparison in Figures 25-28 are the measurements of Solov'ev, et al.<sup>8</sup> for  $\sigma_+$  and  $(\sigma_- - \sigma_+)$ , in which the stated maximum errors were  $\pm 15$  percent. It is seen in the figures that these  $\sigma_+$  measurements are usually some 20 to 30 percent lower than the present values. However, with the exception of the hydrogen target, the results are still within the combined error limits of the two experiments. Reasons will be discussed later for the belief that the present  $\sigma_+$  results are more accurate than those of Solov'ev. Also, it is seen that the energy dependence of Solov'ev's  $\sigma_+$  is somewhat steeper than the present results. Since the difference cross section  $(\sigma_- - \sigma_+)$  is identical to the stripping cross section  $\sigma_s$  for the  $H^0$  projectile, a comparison is also made with the  $\sigma_s$  cross section measured by Barnett and Reynolds<sup>13</sup> in their fast beam attenuation experiment (discussed in Chapter II). It is seen that their value, which was indicated to be less than  $\pm 10$  percent in error, falls between

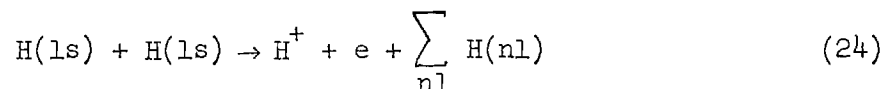
the present results and those of Solov'ev, in both absolute value and energy dependence.

For the target gases, helium and hydrogen (Figures 25 and 27), a comparison is also made with theoretical values of  $\sigma_s$ . Figure 25 shows the Bates and Williams<sup>18</sup> calculation of  $\sigma_s$  using the full Born approximation for the reaction



in which the summation includes an integration over the continuum. This calculated  $\sigma_s$  falls between the present and Barnett's result for  $\sigma_s$ , and, therefore, it is well within the error limits of these experiments. Also, the energy dependence of all three curves appears to be about the same above 250 keV.

A comparison is also shown in Figure 27 with the Bates and Grifing<sup>19</sup> calculation of  $\sigma_s$ , using the full Born approximation, for the stripping reaction of  $\text{H}^0$  on the atomic target  $\text{H}^0$



In this investigation, the target is molecular hydrogen  $\text{H}_2$ . It is reasonable to suppose, however, that in the stripping reaction a hydrogen target molecule is approximately equivalent to two hydrogen atoms. Therefore, for comparison with the present results in Figure 27, the calculated values for the atomic target have been multiplied by a factor of two. As

has been previously observed for other cases,<sup>19</sup> it is seen that this scaling procedure yields a cross section that is greater than any of the experimental values for  $\sigma_s$ . In fact, it is beyond the error limits of all the experimental results except those of the present experiment. However, since the hydrogen molecule is not exactly equivalent to two hydrogen atoms, the uncertainty in the scaling procedure does not allow any firm conclusion regarding the relatively better agreement of theory with the present results than with those of Barnett.

For convenience in comparing the relative sizes of the ion producing cross sections  $\sigma_+$  in the different target gases, Figures 29-31 each shows this cross section for all four target gases for projectiles of  $\text{He}^{++}$ ,  $\text{He}^0$ , and  $\text{H}^0$ , respectively. In all cases, the helium target yields the smallest  $\sigma_+$  followed by the molecular hydrogen target. It is seen that the ion producing cross section is uniformly larger in argon than in nitrogen for the  $\text{He}^{++}$  and  $\text{H}^0$  projectiles, while for  $\text{He}^0$ , the nitrogen cross section curve crosses the argon curve to become the higher one at the upper end of the energy range. However, no particular significance is attributed to this curve crossing. One can also see (by comparing the three figures) that the  $\sigma_+$  cross sections successively increase for the projectiles in the order of  $\text{H}^0$ ,  $\text{He}^0$ , and  $\text{He}^{++}$ , respectively.

Figures 32-34 are also summary figures, and each shows the electron production cross sections  $\sigma_-$  in the four target gases for the  $\text{He}^{++}$ ,  $\text{He}^0$ , and  $\text{H}^0$  projectiles, respectively. These figures show that  $\sigma_-$  increases for the target gases in the order helium, hydrogen, nitrogen, and argon, with the exception that argon falls below nitrogen for the case of the  $\text{He}^0$  projectile. It is seen also that the  $\sigma_-$  cross sections increase for

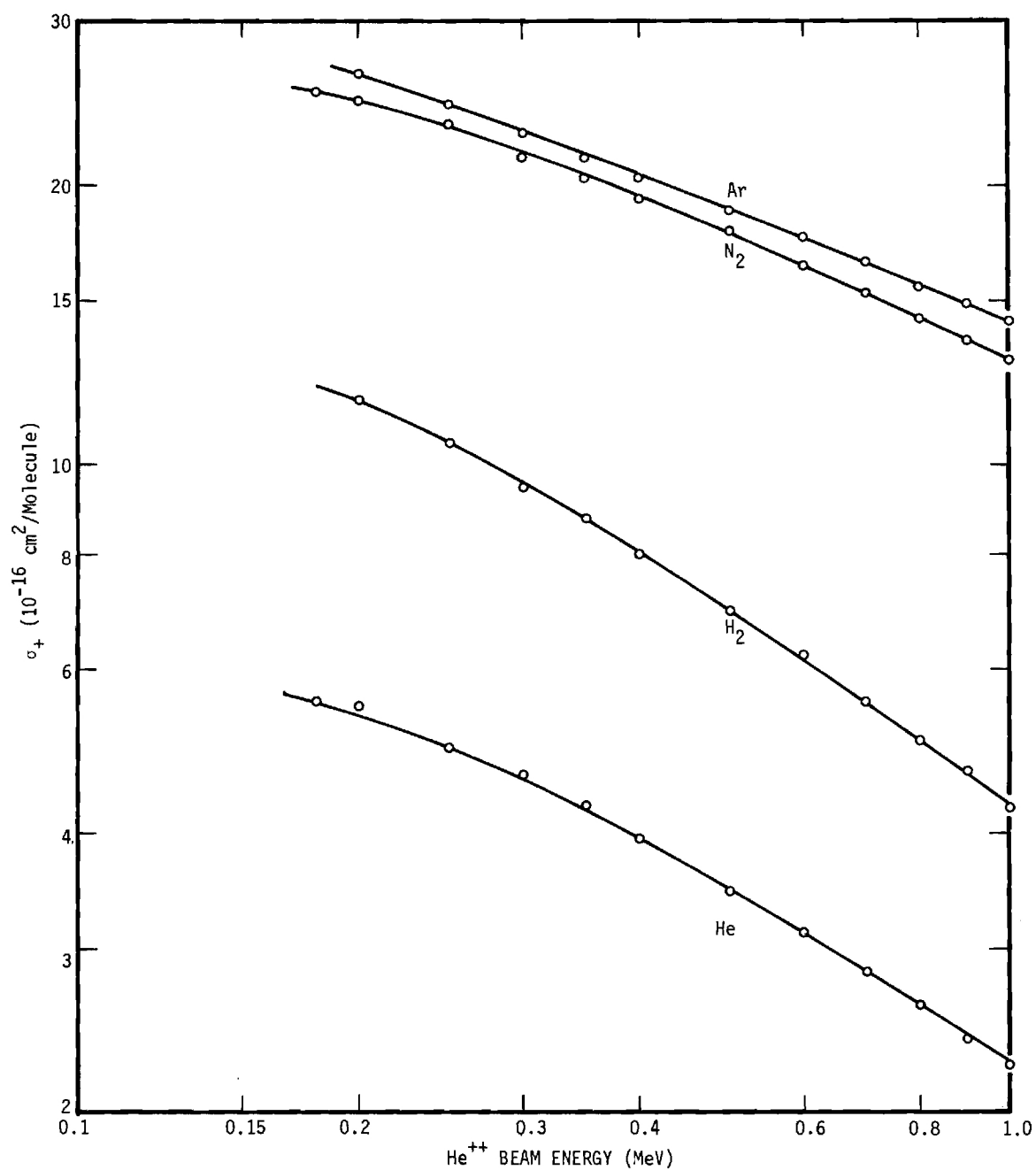


Figure 29. Total Apparent Cross Sections for the Production of Positive Ions of He, H<sub>2</sub>, N<sub>2</sub>, and Ar by Incident He<sup>++</sup> Ions.

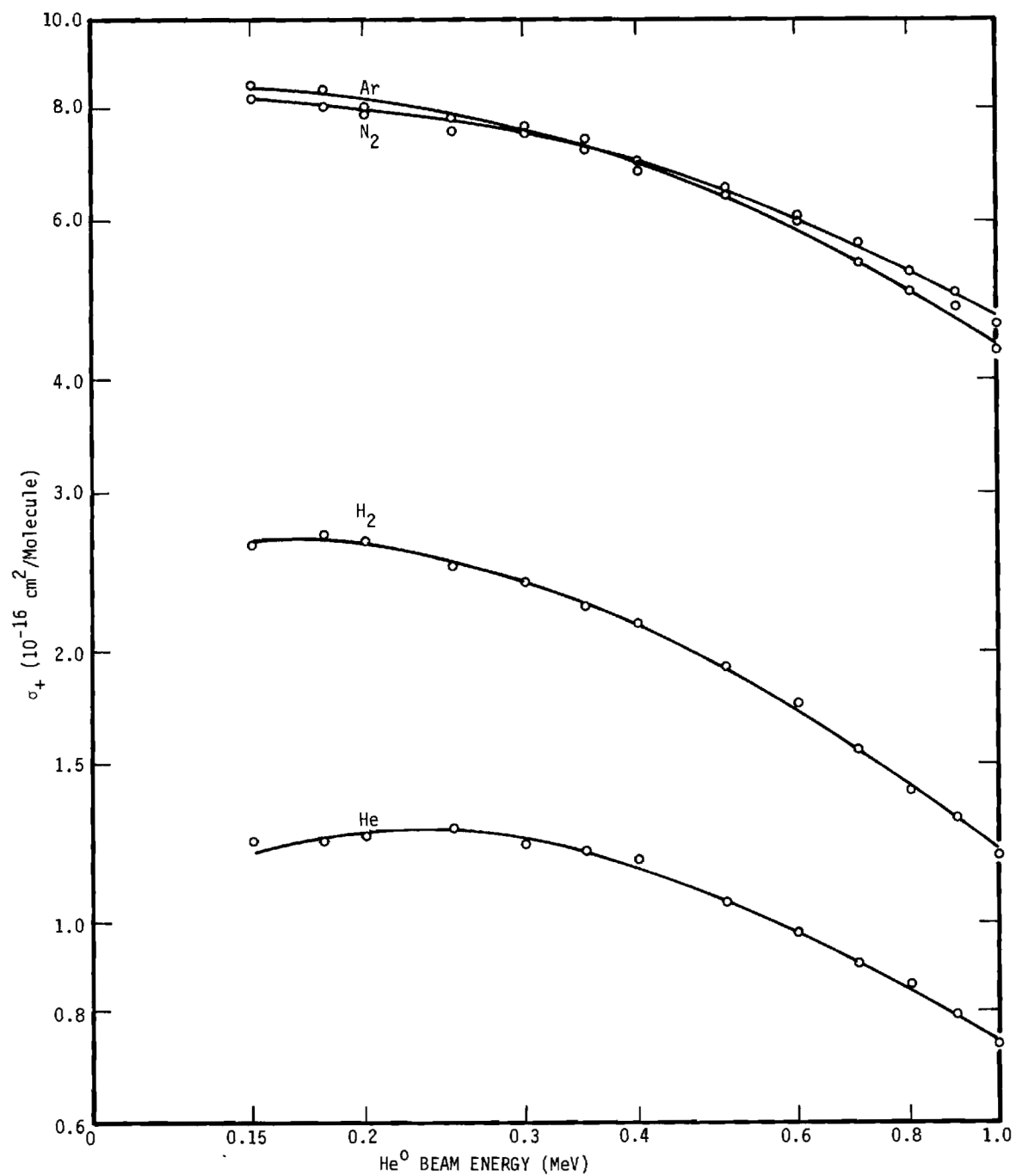


Figure 30. Total Apparent Cross Sections for the Production of He, H<sub>2</sub>, N<sub>2</sub>, and Ar Ions by Incident He<sup>0</sup> Atoms.

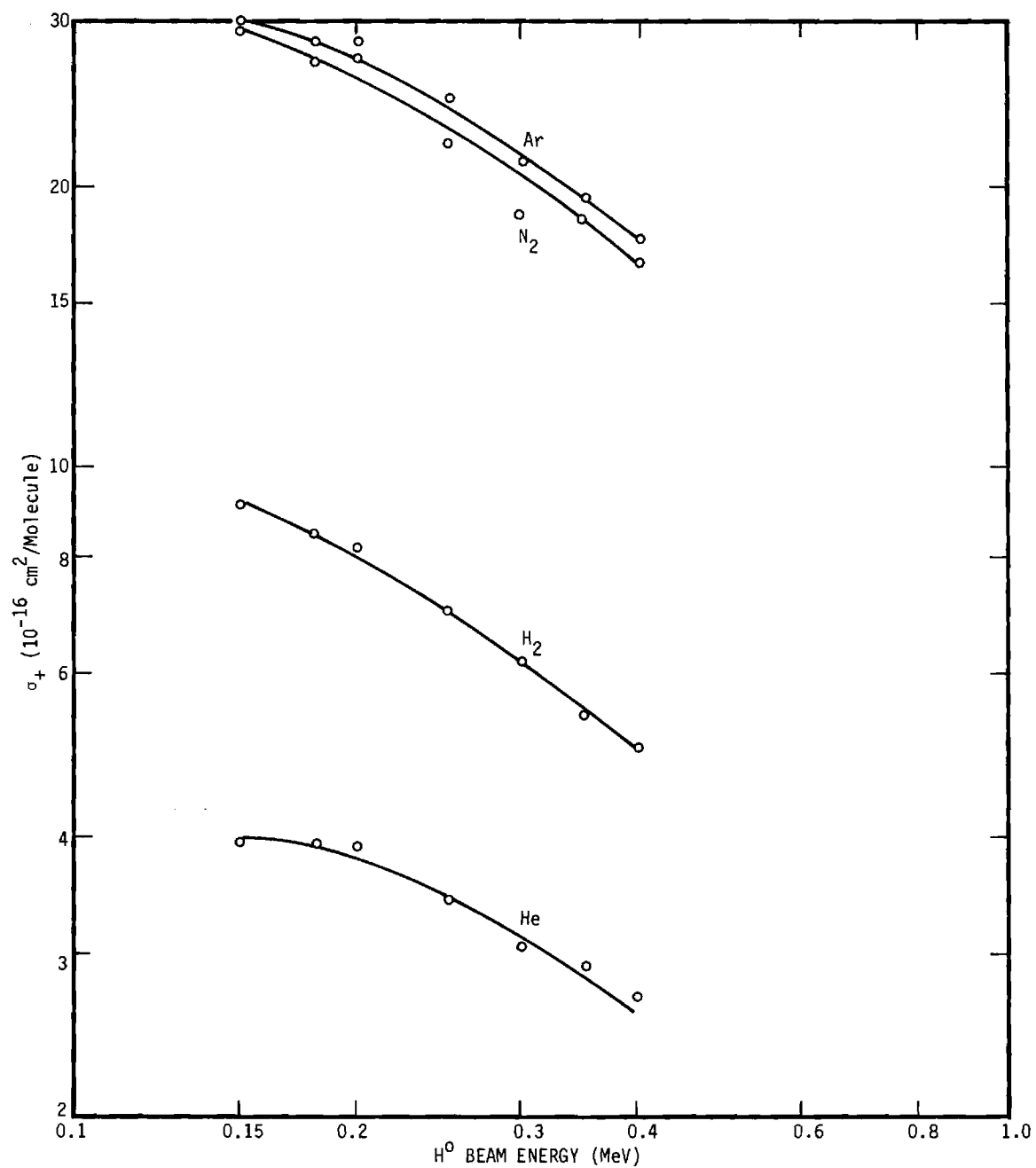


Figure 31. Total Apparent Cross Sections for the Production of Positive Ions of He, H<sub>2</sub>, N<sub>2</sub>, and Ar by Incident H<sup>0</sup> Atoms.

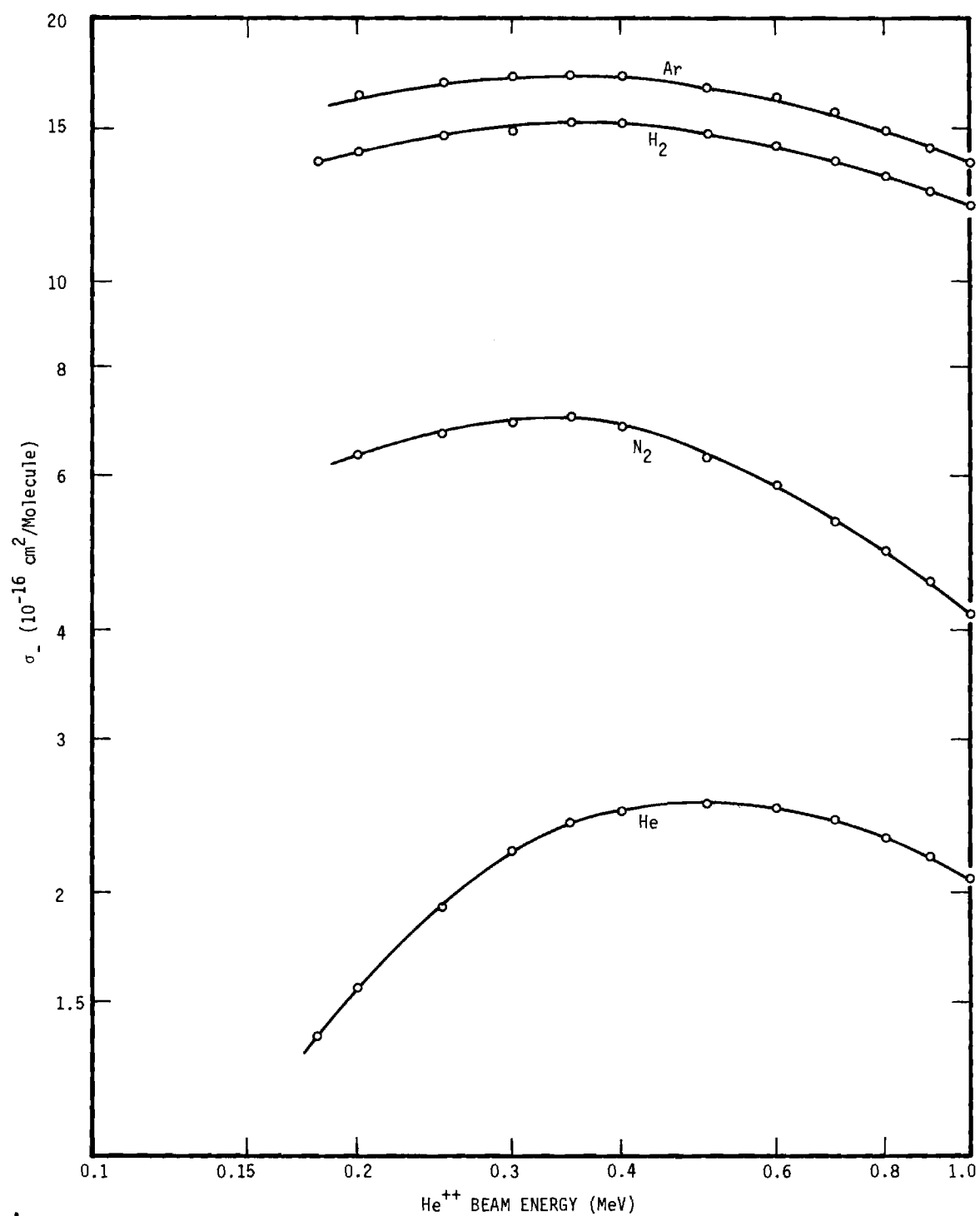


Figure 32. Total Cross Sections for the Production of Free Electrons in He, H<sub>2</sub>, N<sub>2</sub>, and Ar by the Impact of He<sup>++</sup> Ions.

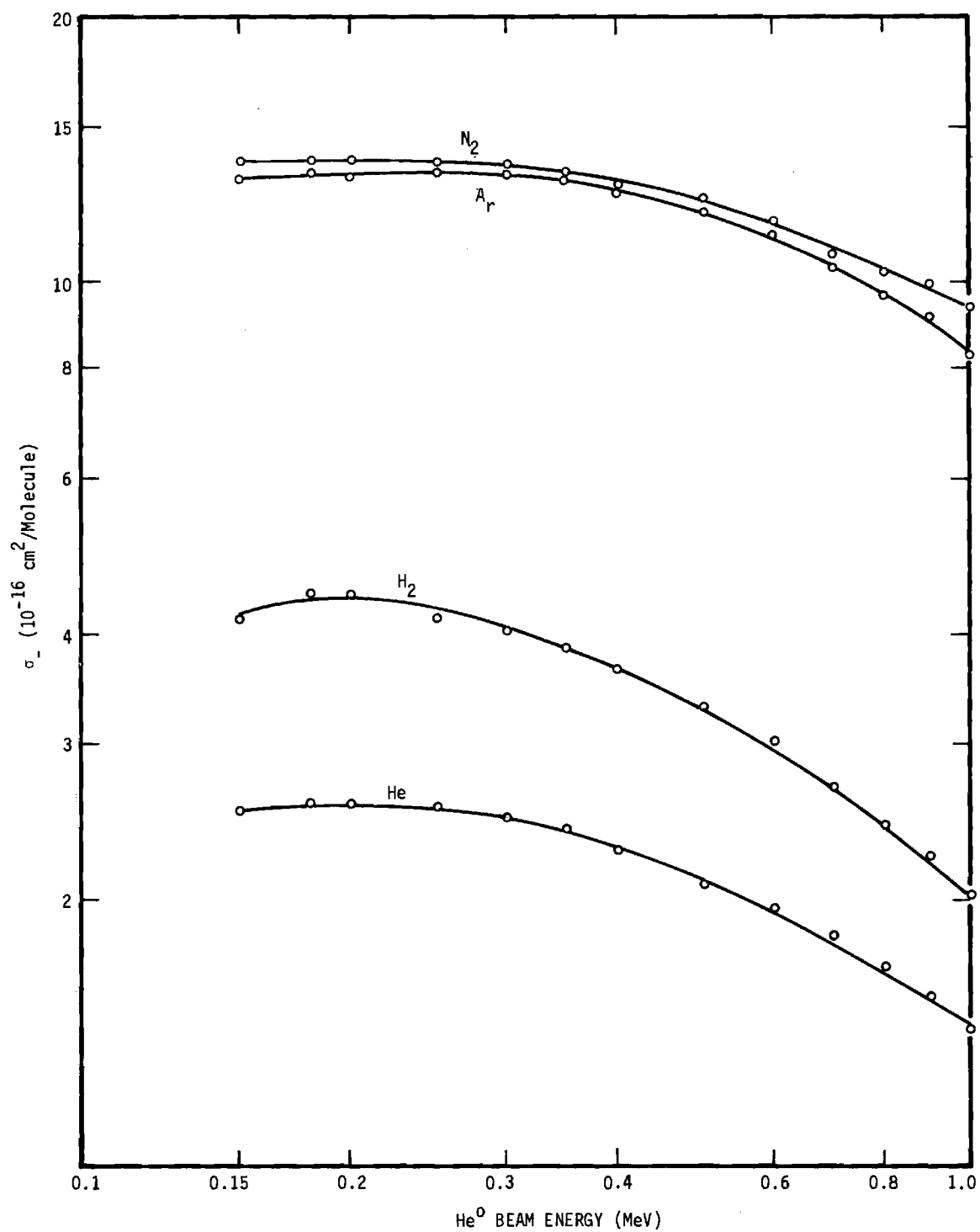


Figure 33. Total Cross Sections for the Production of Free Electrons in He,  $\text{H}_2$ ,  $\text{N}_2$ , and Ar by the Impact of  $\text{He}^0$  Ions.



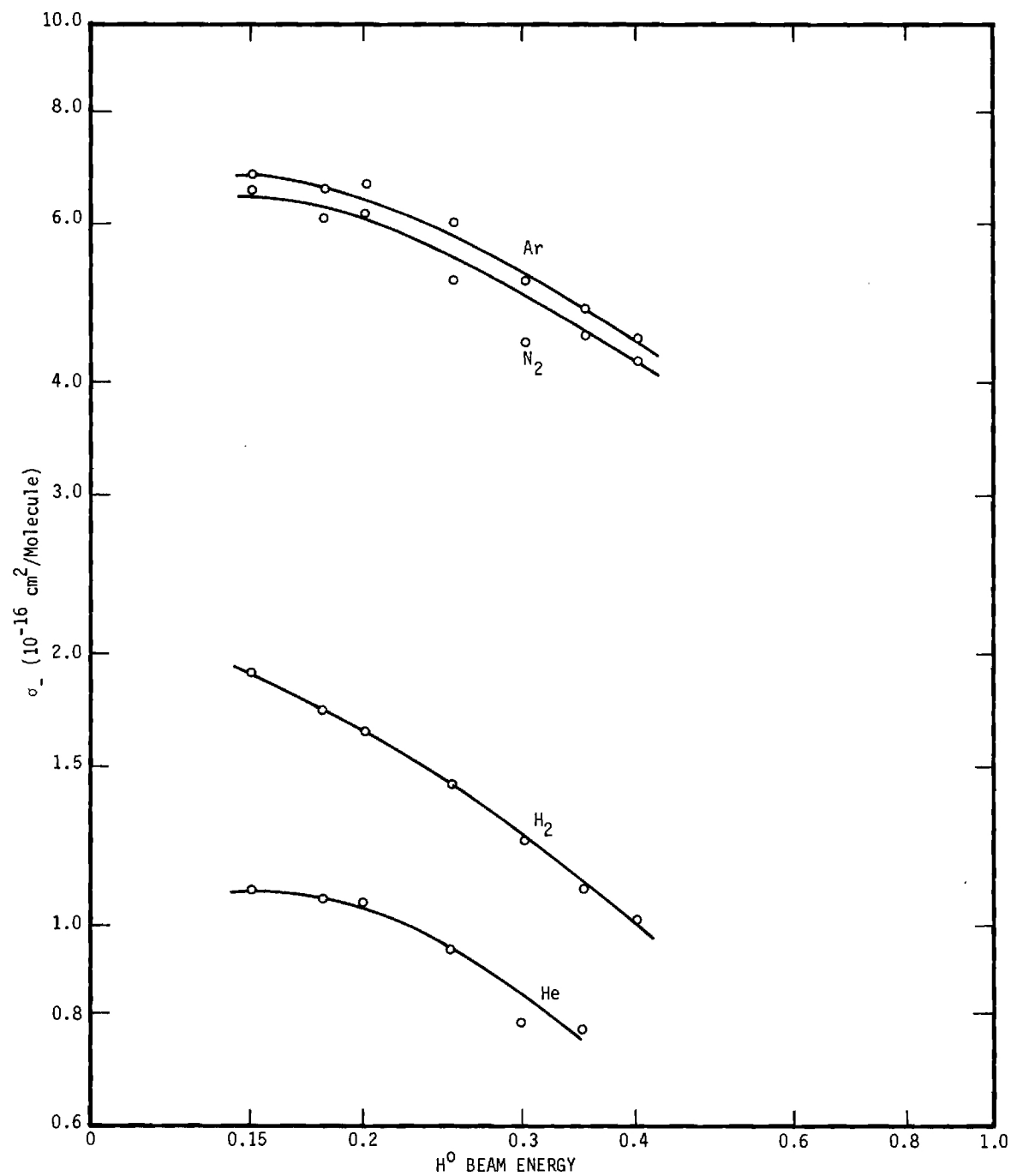


Figure 34. Total Cross Sections for the Production of Free Electrons in He, H<sub>2</sub>, N<sub>2</sub>, and Ar by the Impact of H<sup>0</sup> Atoms.

the projectiles in the order  $H^0$ ,  $He^0$ , and  $He^{++}$ , with the exception of  $He^{++}$  at energies less than 0.4 MeV for which  $\sigma_-$  falls off more rapidly for  $He^{++}$  than for the other projectiles, particularly for the He target. This indicates that the total apparent ionization cross section  $\sigma_i (= \sigma_-)$  for  $He^{++}$  incident on He peaks at a higher energy for this than for the other projectile-target combinations.

The next comparisons of interest are those between the experimental and theoretical results for the ionization cross sections. Of particular interest are those comparisons between the results obtained with various projectiles that are predicted by the form of the theory to be in agreement.

As is well known, ionization cross sections cannot be exactly calculated even for the simplest case of protons incident on hydrogen atoms, although the wave functions for the unperturbed H atom are known completely and analytically. An infinite set of coupled differential equations would have to be solved to obtain  $\sigma_i$  exactly, so approximate methods must be used.

One of the most useful approximations is that due to Born.<sup>37, 38</sup> The basic assumption in this approximation is that the potential energy of interaction is small, so that the interaction between the particles may be treated as a perturbation. A sufficient, but not necessary, condition, therefore, is that the interaction energy be much smaller than the total energy of the projectile. This condition is evidently obeyed for sufficiently fast projectiles.

Calculations of simple ionization cross sections in the full Born approximation have been made for only a few of the simplest cases. Among

these, the cases of interest for comparison purposes include those two previous calculations of the stripping reactions of  $H^0$  incident on  $He^0$  (Equation 23) and  $H^0$  (Equation 24); these reactions can be viewed either as stripping of the incident  $H^0$  or, conversely, ionization of the  $H^0$  by incident  $He^0$  and  $H^0$ , respectively. Other cases of interest include  $H^+$  incident on  $H^0$  (Reference 15) and  $He^0$  (Reference 17), and  $He^+$  incident on  $H^0$  (Reference 16). These theoretical values of the cross sections will be used for comparison with the absolute magnitudes and energy dependences of the measured values.

Before presenting the above comparisons, it is useful to consider a further approximation, developed by Bethe<sup>37, 38, 40</sup> which produces results with a simpler mathematical form. Cross sections calculated in the Bethe-Born approximation tend to the more general results of the full Born treatment for very high impact velocities. The main feature of the Bethe approximation is the assumption that there is very little contribution to the cross section for values of the projectile momentum change  $K$ , greater than a certain value  $K_0$ , which is much less than the maximum value allowed by the conservation laws. With this assumption, an integral over  $K$  that occurs in the formulation is terminated at the upper limit  $K_0$ . A factor  $\exp(iKz)$  in the integrand can then be expanded, and only the first term which produces a nonvanishing contribution to the integral need be retained for the case of very high impact velocities. With this approximation, the following result for a point charge projectile incident on a stationary target may be obtained.

$$\sigma_i = AZ^2 \frac{M}{E} \log_e \left[ \frac{BE}{M} \right] \quad (25)$$

where  $E$  is the kinetic energy of the incident ion,  $Z$  is the charge number of the incident ion, and  $M$  is its mass in units of the proton mass. The constants  $A$  and  $B$  are characteristic of the target atom and do not depend on the nature or the energy of the incident ion. Therefore, an empirical evaluation of  $A$  and  $B$  for a given target atom from experimental measurements of  $\sigma_i$  for any one type of projectile can be used in Equation 25 for two purposes: first, to extrapolate the measured  $\sigma_i$  for the given target atom and projectile to energies outside the experimental range in particular to higher energies, and second, to estimate  $\sigma_i$  for the given target atom and some other projectile with a different value of  $Z$  and/or  $M$ . Both of these purposes will be employed in the comparisons.

It is worthy of note that the quantities  $M$  and  $E$  appear in Equation 25 only in the ratio  $E/M$ , so that the expression predicts that various projectiles of equal  $Z$  but different  $M$  will have equal cross sections for equal velocities. This is a well known feature of the theory, which is also displayed by the full Born approximation.<sup>15, 37, 38</sup>

It should be emphasized that all of the discussion of Equation 25 above applied only to the cross sections for simple ionization events, in which the projectile ion suffers no change in its charge state. However, as was seen in Chapter II, the observed ionization cross sections  $\sigma_i$  are not restricted to these simple ionization events. In addition, the relationships discussed here should apply, strictly speaking, only to point-charge projectiles, i.e., to electrons or bare nuclei. An incident ion carrying bound electrons might, however, be expected to be equivalent in the simple ionization process to a partially screened point charge having an "effective" charge  $Ze$  lying somewhere between its actual net charge and

its nuclear charge. The value of  $Z$  for a given ion, and indeed the validity of the whole concept of an effective projectile charge, can for the present be evaluated only by experimental test. The concept will be useful only if  $Z$  for a given projectile ion can be shown to be independent of the target-atom type and of the collision energy, or at least asymptotically so at high energies.

The preceding discussion enumerated the following four separate types of comparisons to be made between the theoretical and experimental results:

1. comparison of absolute magnitudes and energy dependence;
2. comparison between cross section measurements that are predicted to be equal when the projectiles are scaled to be equicharge and equivelocity;
3. comparison of cross sections which are extrapolated by means of the constants  $A$  and  $B$  outside of the energy range of the measurement; and
4. comparison of the effective charge of various equivelocity projectiles.

In Figures 35-38 the total apparent ionization cross sections  $\sigma_i$  for  $\text{He}^{++}$ ,  $\text{He}^0$ , and  $\text{H}^0$  in the target gases hydrogen, helium, argon, and nitrogen are plotted together with the previously published results<sup>35, 39, 41-44</sup> for  $\text{H}^+$  and  $\text{He}^+$  that were measured in this laboratory. The energy axis is shifted a factor of four, according to Equation 25, to compare the hydrogen with the helium projectiles of equal velocity.

In order to compare the experimental results on molecular hydrogen targets with the theoretical predictions for atomic hydrogen, a scaling

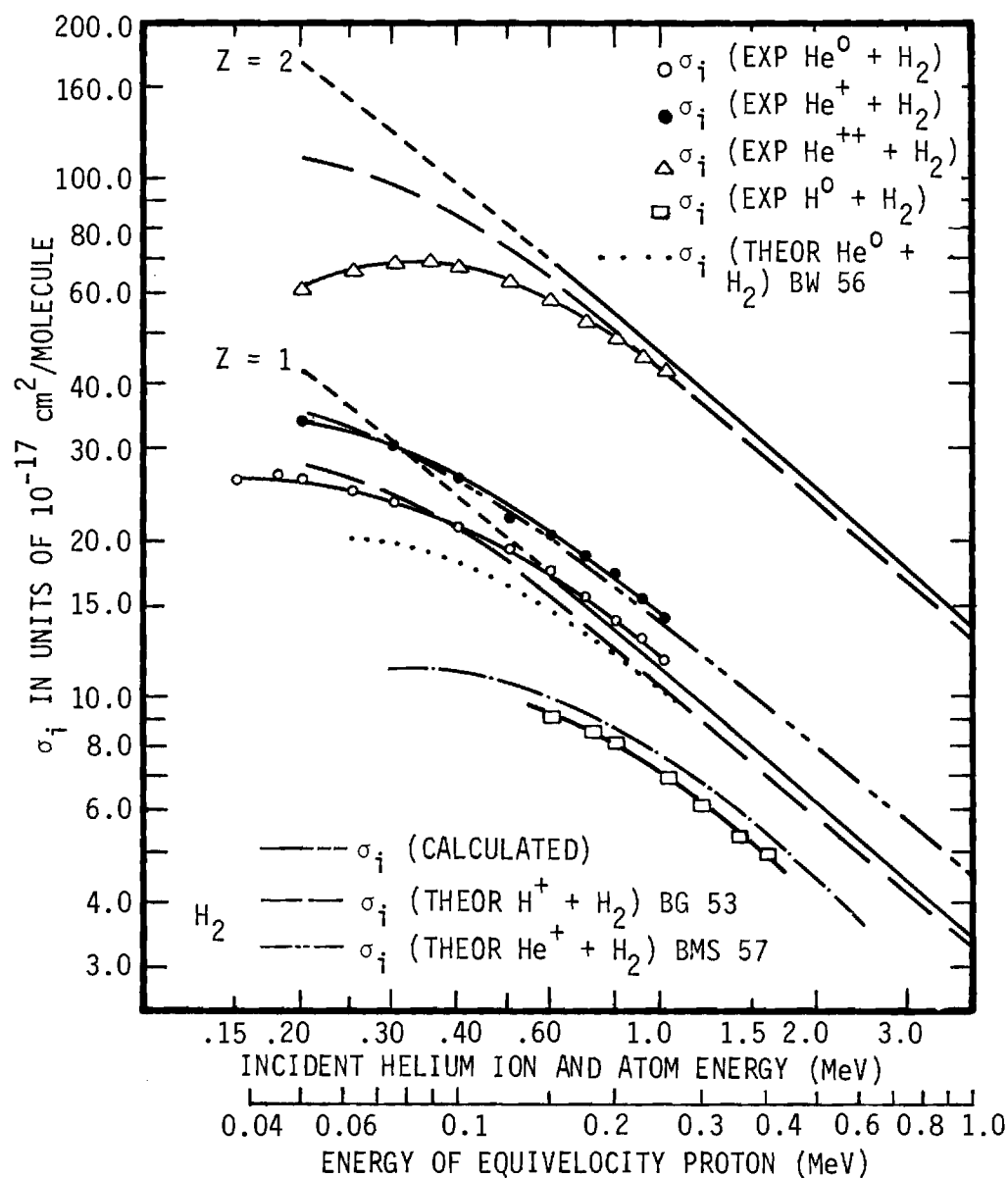


Figure 35. Total Apparent Ionization Cross Sections  $\sigma_i$  for H and He Ions and Atoms Incident on Molecular Hydrogen, Compared with the Calculated Curve:  $\sigma_i = AZ^2M/E \ln(BE/M)$  with A and B Evaluated from Corresponding  $\text{H}^+$  Data (Reference 34), for  $Z = 1$  and  $Z = 2$ . Also Shown Are Theoretical Calculations for Atomic Hydrogen Targets, Scaled to Molecular Hydrogen Targets, for Incident  $\text{H}^+$  (BG 53, Bates and Griffing, Reference 15) for  $Z = 1$  and  $Z = 2$ , for Incident  $\text{H}^0$  (BG 55, Bates and Griffing, Reference 19), for Incident  $\text{He}^+$  Ions (BMS 57, Boyd, Moiseiwitsch, and Stewart, Reference 16), and for Incident  $\text{He}^0$  Atoms (BW 56, Bates and Williams, Reference 18).

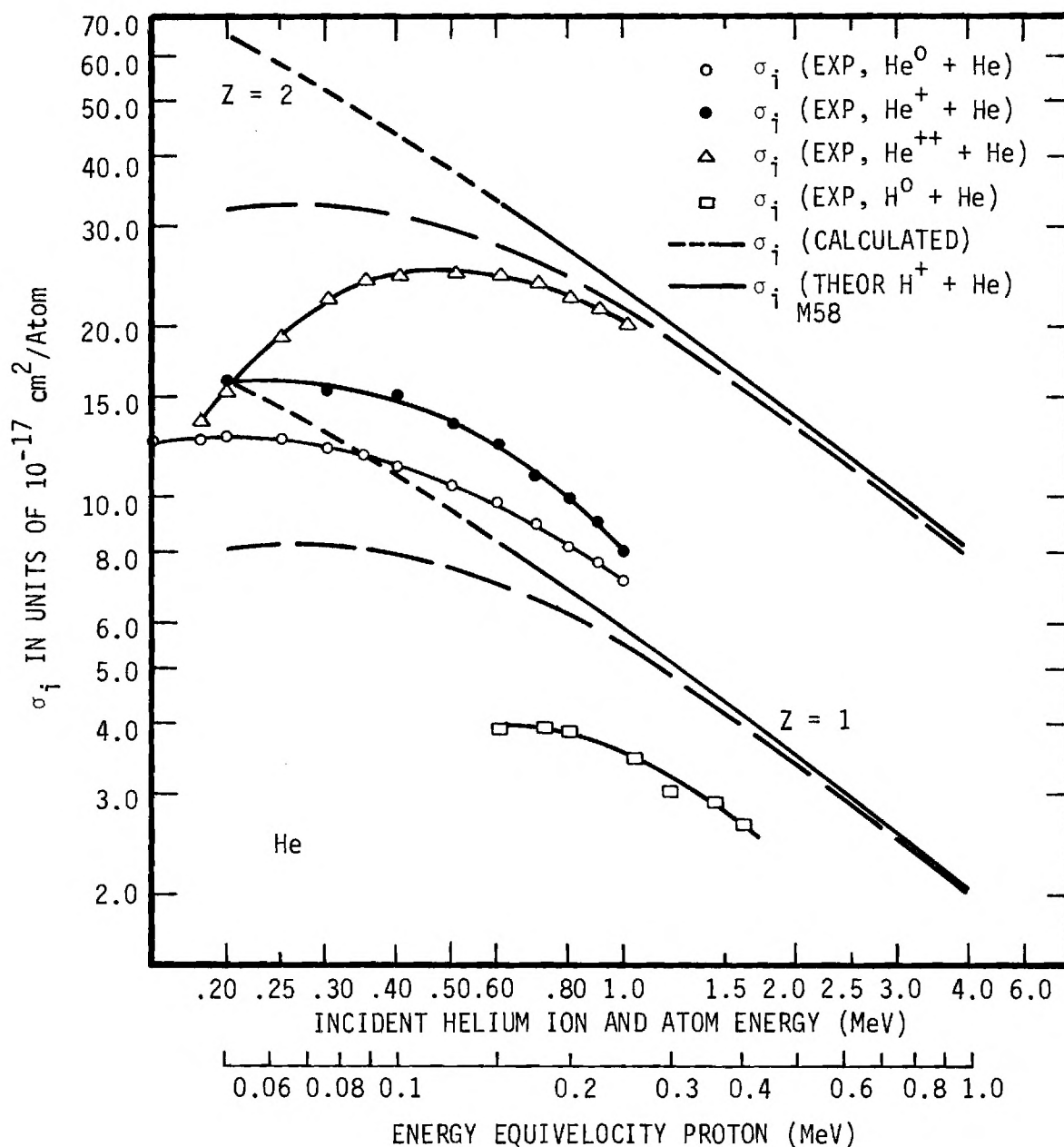


Figure 36. Total Apparent Ionization Cross Sections  $\sigma_i$  for H and He Ions and Atoms Incident on Helium, Compared with the Calculated Curve  $\sigma_i = AZ^2M/E \ln (BE/M)$  with A and B Evaluated from Corresponding Proton Data (Reference 34), for  $Z = 1$  and  $Z = 2$ . Also Shown Is the Theoretical Calculation for Equivelocity Protons on Helium (Reference 17) for  $Z = 1$  and  $Z = 2$ .

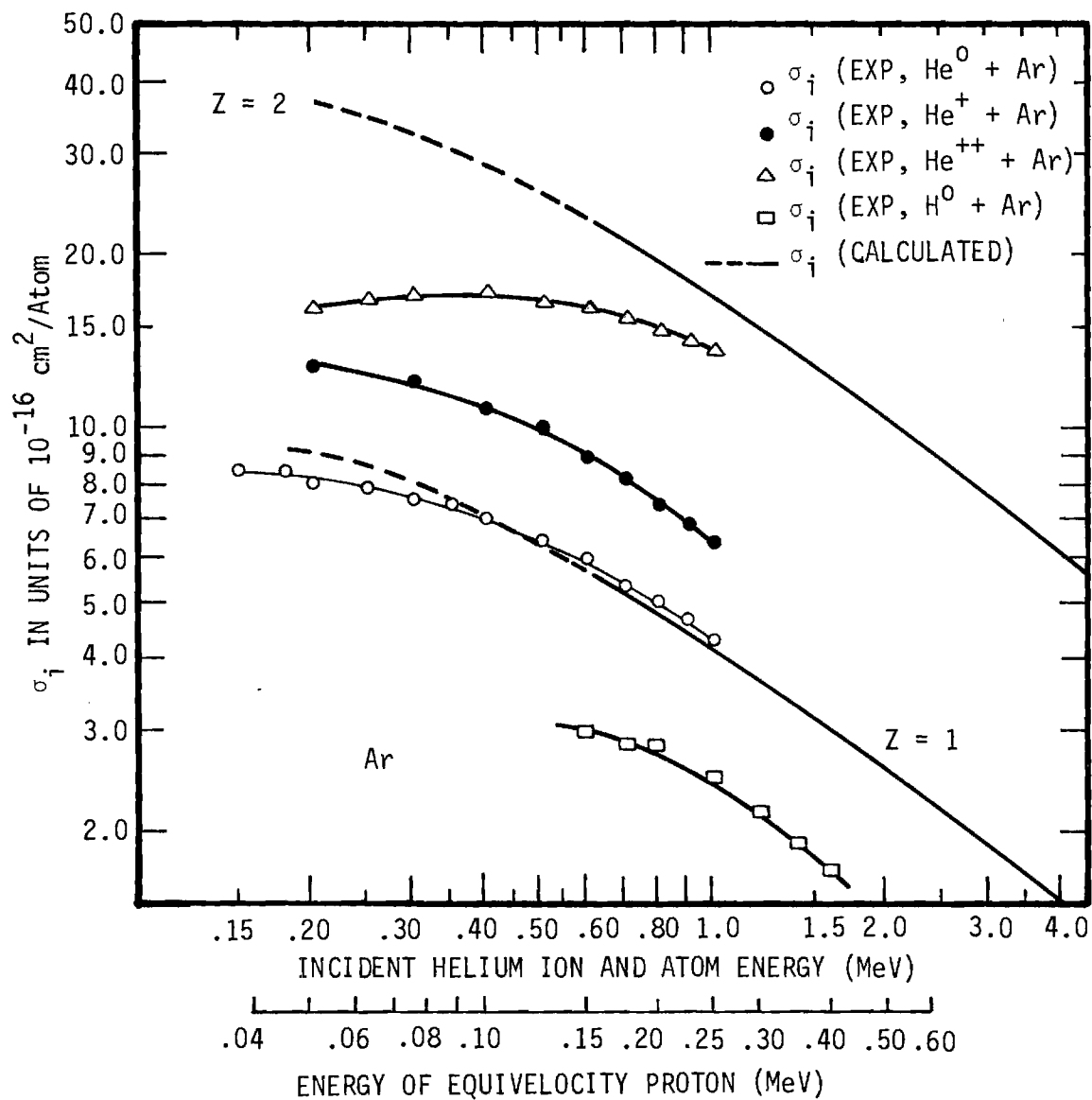


Figure 37. Total Apparent Ionization Cross Sections  $\sigma_i$  for H and He Ions and Atoms Incident on Argon, Compared with the Calculated Curve  $\sigma_i = [AZ^2M/E] \ln(BE/M)$  with A and B Evaluated from Corresponding Proton Data (Reference 34), for  $Z = 1$  and  $Z = 2$ .



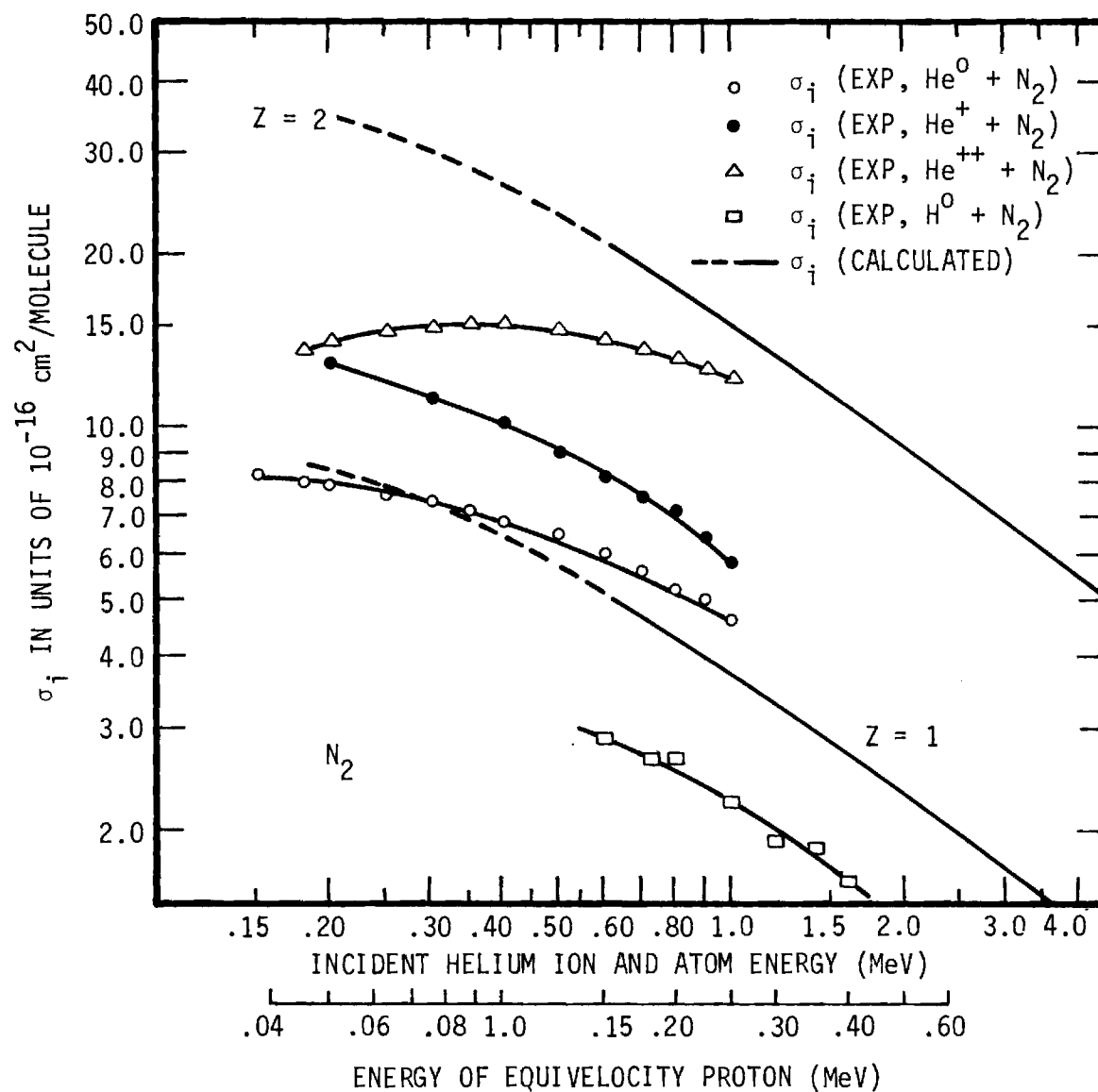


Figure 38. Total Apparent Ionization Cross Sections  $\sigma_i$  for H and He Ions and Atoms Incident on Molecular Nitrogen, Compared with the Calculated Curve  $\sigma_i = [AZ^2M/E] \ln(BE/M)$  with A and B Evaluated from Corresponding Proton Data (Reference 34), for  $Z = 1$  and  $Z = 2$ .

procedure was employed. This procedure, suggested by Bates and Griffing,<sup>15</sup> allows for the difference in ionization potential between the atomic and molecular targets. It was applied to the theoretical case of  $H^+$  incident on  $H^0$  to compare with the observed values in Figure 35. The solid portion of the  $Z = 1$  curves labeled "calculated" in each figure represents the plot of the proton results referred to as the "equivelocity proton energy" abscissa. The dashed portion of each "calculated" curve is extrapolated outside the data range by means of Equation 25. The curve labeled BG 53 is the calculation for  $H^+$  incident on  $H^0$  scaled from the atomic to the molecular case as discussed previously. It is seen that the agreement is rather good throughout the experimental energy range; the experimental results average about ten percent larger than the theoretical values. The energy dependencies of the two results are essentially the same.

The scaling procedure used for the preceding comparisons strictly applies only to a point charge projectile ion with no bound electrons. For projectiles with bound electrons, there are more terms in the interaction and the form of the dependence of the results on the projectile energy and ionization potential is consequently more complex.<sup>15</sup> It is not evident that the same simple scaling procedure should have any validity. Nevertheless, it was tried for  $He^+$ ,  $He^0$ , and  $H^0$  projectiles, and for the case of  $He^+$  incident on  $H_2$  good agreement was obtained.

The curve labeled BMS 57 in Figure 35 represents the theoretical calculation for  $He^+$  incident on  $H^0$ , scaled to  $H_2^0$  as previously discussed. It may be noted that the agreement with the estimated ionization cross sections from the  $He^+$  measurements is excellent. However, this agreement should be regarded with some reservation because the evaluation of  $\sigma_i$  for

the  $\text{He}^+$  projectile is complicated by the fact that the projectile can undergo both electron capture and stripping reactions. Therefore, in order to arrive at a value for  $\sigma_1$ , it was necessary to estimate the relative sizes of several cross sections.

The results for  $\text{He}^0$  and  $\text{H}^0$  scaled in the above manner, however, were lower than the experimental values by about 30 percent and 50 percent, respectively, and they are not shown in the figure. Instead, the results obtained by simply doubling the atomic cross sections are presented and are seen to be in substantially better agreement with experimental values. The curve in Figure 35 labeled BG 55 represents the theoretical value for  $\text{H}^0$  incident on  $\text{H}^0$  multiplied by a factor of two. It is seen to lie about ten percent above the measured values and to have essentially the same energy dependence. Also shown in this figure is the theoretical calculation of  $\text{He}^0$  incident on  $\text{H}^0$ , multiplied by a factor of two and labeled BW 56. This curve is about 14 percent below the measured values, and in the upper part of the energy range, as has been observed to be the usual case, the two results have about the same energy dependence.

Although no explicit calculation is available in this energy range for  $\text{He}^{++}$  incident on these four gases, the form of Equation 25 predicts that the proton measurements multiplied by  $Z^2 = (2)^2$  for  $\text{He}^{++}$ , and scaled to be equivelocity with  $\text{He}^{++}$ , should have the same cross section for sufficiently high velocity. The "calculated" curve in Figure 35 labeled  $Z = 2$  represents the proton results scaled in the above manner. It is observed that the  $\text{He}^{++}$  results demonstrate quite precisely the expected behavior, i.e., they are just four times the proton results, for

the higher energies used in this experiment. Also scaled according to Equation 25 is the theoretical calculation for  $H^+$  incident on  $H^O$ , scaled to  $H_2$ . It is also seen to provide good agreement with the observed values at the highest energies used in this investigation.

In Figure 36, the same type of experimental curves discussed in the preceding paragraphs is shown. The only available calculation for ionization of the helium target is shown as the curve labeled M 58 for incident  $H^+$ , and good agreement is obtained between the calculated and measured values. Both of these curves, scaled according to Equation 25 and labeled  $Z = 2$ , are seen to be in generally good agreement with the  $He^{++}$  measurements for the highest energies, particularly the theoretical curve.

For the heavier target gases, argon and nitrogen, shown in Figures 37 and 38, respectively, it is seen that the  $He^{++}$  results appear to be approaching the scaled proton results at some higher energy, perhaps two or three MeV.

The final comparison to be made with these measurements is to determine whether or not the concept of the effective charge is valid for the non-point charge projectiles. The requirement for this concept to be valid is that the cross section curve for the non-point charge projectile be uniformly separated from that of a true point charge projectile such as  $H^+$  or  $He^{++}$ , at least asymptotically so at high energies.

A comparison of the  $He^+$ ,  $H^O$ , and  $He^O$  results with the  $H^+$  results indicates that: the previously measured  $He^+$  curves are roughly about a factor of 1.5 above the  $H^+$  curves; the  $H^O$  curves are uniformly lower than the  $H^+$  curves by about a factor of 0.64 in the upper energy range; and the  $He^O$  curves are approximately equal to the  $H^+$  curves for both the

lightest and heaviest targets, i.e., hydrogen and argon, and are about a factor of 1.2 above the  $H^+$  results for the other two cases—this amount of variation is outside of the error limits for the  $He^0$  projectile. It is concluded, therefore, that  $He^+$  and  $H^0$  projectiles do possess an effective charge, according to Equation 25, of  $\sqrt{1.5} = 1.2$ , and  $\sqrt{0.64} = 0.80$ , respectively. However, it appears that this effective charge concept is not applicable to the  $He^0$  projectile.

### Conclusions

The experimental values of the total apparent cross sections for productions of ions,  $\sigma_+$  and of electrons,  $\sigma_-$ , were measured for the cases of  $He^{++}$ ,  $He^0$ , and  $H^0$  incident on the target gases He, Ar,  $H_2$ , and  $N_2$ .

For the cases involving  $He^{++}$  projectiles, the only comparison data that were available were total charge changing cross sections for the capture of electrons by the projectile, which were equivalent to the difference ( $\sigma_+ - \sigma_-$ ) in the present data. It was noted that the agreement was excellent, which provided a strong confirmation of the validity of both the apparent ion production and the total charge changing cross section measurements.

For the cases involving an atomic helium beam, comparison data were available for  $\sigma_+$  and were in reasonably good agreement. The present results for ( $\sigma_- - \sigma_+$ ) were seen to be about 40 percent greater than was expected from certain related results of the other investigators, which all involved the observation of the change in beam composition as it passed through the target gas. It is pointed out that one other investigator, who measured the residual slow collision products (as in the present experi-

ment) also obtained results that were some 40 percent greater than those referred to above. Unfortunately, these results, which were apparently in agreement with the present values, were not published and no response was received to a request for those data. It was concluded from the present results for  $\sigma_+$  that it was not very meaningful to define an "effective charge" for  $\text{He}^0$  that represented the charge of a hypothetical point-charge ion of the same mass, that has the same cross section for simple ionization at high energies.

The data for  $(\sigma_- - \sigma_+)$  obtained for the  $\text{H}^0$  projectile were usually in rather good agreement with the comparison data; however, the agreement of the present  $\sigma_+$  cross sections with the comparison values varied considerably among the various target gases. Also, in some cases the present and comparison results for  $\sigma_+$  displayed a considerably different energy dependence. Confidence in the present results for  $\sigma_+$  was considerably enhanced when it was noted that, for all four target gases, the  $\text{H}^0$  and  $\text{H}^+$  ionization cross sections,  $\sigma_i = \sigma_+$ , were displaced a constant amount from each other above about 300 keV. It appeared that this close correlation, although not expected a priori, would be highly unlikely to occur in all four target gases if there were serious random errors present in the results of the individual gases. It was, therefore, concluded that the excellent correlation was testimony to the accuracy of the present  $\sigma_+$  results for the  $\text{H}^0$  projectile.

From the form of the cross section in the Bethe-Born approximation (Equation 25), this constant offset in the  $\text{H}^0$  and  $\text{H}^+$  ionization cross sections implied that the "effective charge" concept could be applied to the

$H^0$  projectile. The calculated value of the effective charge was 0.80 e.

It is interesting to note that the "effective charge" concept was applicable to the hydrogen projectile  $H^0$  and the hydrogenic projectile  $He^+$ ; however, it was not deemed applicable to the  $He^0$  projectile in this experiment. No explanation of this observation is offered at present.

It was observed that generally good agreement was obtained between the experimental and theoretical cross sections, even those that were scaled from atomic to molecular hydrogen. It is concluded, therefore, that the theory pertaining to the high energy cross sections measured in this work is substantially correct for relative velocities above about  $5 \times 10^6$  m/sec ( $\approx 0.5$  MeV helium;  $\approx 0.1$  MeV hydrogen), and in some cases that the theory appears to be valid at lower velocities.

PART C



## CHAPTER VI

APPARATUS AND TECHNIQUES EMPLOYED IN THE MEASUREMENTS  
OF THE PARTIAL IONIZATION CROSS SECTIONSDiscussion of Some Fundamental Design Considerations  
for This Apparatus

In order to subdivide the individual cross sections that comprised the total apparent ion production cross section, into groups that correspond to the cross sections for the formation of ions of specified charge states, some type of ion spectrometer must be used. The initial concept of this spectrometer was predicted on the assumption that no significant fraction of the slow ions would be formed with initial kinetic energies in excess of perhaps 100 eV. The analyzer was to be mounted so as to sample at  $90^\circ$  to the direction of the fast beam. Its entrance slit was to be cut in the "active" ion collector plate of the parallel plate collision region. The electric field normally applied to sweep to the active plate all of the slow positive ions formed in a well defined collision volume, would simply sweep some of these ions into the spectrometer entrance slit. If the width of the slit were made an accurately known fraction of the length of the active plate, this same fraction of all the ions formed in the collision volume should be swept to the slit. It was intended that analysis and measurement of the ion stream through the slit would be made simultaneously with measurement of the total current collected to the plate. Comparison of the ratios of these currents to the

geometrical ratio would be a direct check on the collection efficiency of the analyzer, and the simultaneous measurement of the already well established total ion production cross sections would provide a continuous check on several of the more important factors in the measurement.

Before any detailed design was begun, however, further study was given to the adequacy of the underlying assumptions. The main aspects of these deliberations will be detailed below; the result was, however, a major decision to discard the concept of a fixed-angle spectrometer with a collection field in favor of a spectrometer that is movable in angle, and which samples with a narrow angular acceptance from a field-free collision region.

The principal technical reason for this change of plans was mounting evidence that a significant fraction of the recoil ions, particularly the multiply-charged recoil ions, are formed with substantial initial energies. Such energies would then require equally substantial values for the collection field voltages to assure that all of the ions formed in a well defined collision region would reach the spectrometer entrance slit. Furthermore, the details of the angular distribution of the initial motion could influence the transmission efficiency of the ion optics of the spectrometer and require the use of still higher collection fields. Quite apart from any other difficulties this might entail, a large collection field would have the serious disadvantage of distorting the initial energy distribution. The incident beam has a finite spatial width; thus recoil ions would be formed over a region across which the electrostatic potential varies, and they would be given variable amounts of energy by the field as they were accelerated to the slit. Thus, a recoil energy

spectrum analysis would be complicated by the use of a collection field.

It was felt that some indication that the ions possessed substantial recoil energies was shown in Figures 10 and 11. On very careful examination, it has been determined that the slow ion current collected to the "active" plate of the ion collection assembly (discussed in Chapter IV) as a function of the voltages applied to the plates does not really "saturate" and become constant until the equal plus and minus voltages approach 200 volts or more. The few percent increase between 100 volts and 200 volts was small enough to be partially masked by the random errors in a single test, but the pattern of the increase over a large accumulation of data was unmistakable. It was felt that this slight increase in ion current indicated that a small but significant fraction of the slow ions is formed with energies of more than 100 eV. It appeared that the fraction having energies above 200 eV was too small to have a significant effect on the accuracy of the total apparent ion production cross sections. However, from this observation it did not follow that a similarly small fraction of all of the multiply-charged ions formed also had energies less than 200 eV, if the multiply-charged ions represented only a small fraction of the total ion current in the first place. Indeed, there is much evidence to the contrary.

The energy and momentum conservation equations, that are applicable to the inelastic ionizing collisions of this experiment, can be used to give the relation between the energy imparted to the target  $T_2$  and the other important collision parameters, according to Afrisomov,<sup>45</sup> as follows:

$$T_2 = \frac{m_1 m_2 T_0}{(m_1 + m_2)^2} \left( \cos \theta \pm \sqrt{\cos^2 \theta - \frac{(m_1 + m_2) Q}{m_2 T_0}} \right)^2$$

where  $m_1$  and  $m_2$  are the projectile and target mass, respectively;  $T_0$  is the initial kinetic energy of the projectile;  $\theta$  is the recoil angle of the target, and  $Q$  is the inelastic energy loss by the collision partners. It should be noted that for a given recoil angle  $\theta$  the recoiling targets will in general have two different energy components and the more energetic ions will be found at smaller values of  $\theta$ . The existence of these two energy groups is another very important reason that one should be extremely careful, when using a collection field, to assure that both groups are efficiently collected. It is conceivable that an investigator that used weak to moderate collection fields (sufficient for the low energy ions) might overlook the presence of the energetic component.

Afrosimov and Federenko<sup>46</sup> have used a magnetic slow-ion analyzer which is rotatable about a field-free collision region and has a direction-defining collimator, to study the relative production of each slow ion charge state, differential in the recoil angle. The instrument had sufficient momentum resolution to provide a low resolution measurement of the recoil ion energy, and this was supplemented by a retarding potential feature for independent energy determinations. In studies of  $\text{Ne}^+$  and  $\text{Ar}^+$  ions up to 0.18 MeV in neon and argon targets, they found that quite appreciable fractions of the higher charge state recoil ions had initial energies of more than 200 eV. In fact, it was observed that virtually all of the  $\text{Ar}^{5+}$ , produced from an Ar target gas by incident  $\text{Ar}^+$  projec-

tiles, had energies greater than 1 keV. They remarked that earlier studies<sup>47</sup> made in their own laboratory of the same collision partners, with a fixed angle analyzer and a collection field such as we had contemplated, were significantly in error for the recoil ions that were more than triply charged, particularly when the mass of the projectile was of the same order as the target mass.

Morgan and Everhart<sup>48</sup> have also studied the energy distribution of the recoil ions in  $\text{Ar}^+$  on Ar collisions, at selected recoil angles that were well forward from  $90^\circ$ , corresponding to very hard collisions. They did indeed find recoil particles at these angles, particularly those of the higher charge states, with the energies of 1 keV and more expected for these angles. This particular paper gives no absolute figures on the intensities of the recoils, as a function of the recoil angle, to permit estimation of the relative contribution of such hard collisions to the total cross section, but it does verify that there are measurable numbers of recoils, particularly for the higher charge states, at these forward angles.

The evidence cited thus far for energetic recoil ions has in each case involved a heavy incident ion. The case of incident protons, which were used in the present experiment, has been studied with fixed-angle spectrometers using a collection field by Solov'ev, et al.<sup>49</sup> and by Wexler.<sup>9</sup> The measurements of Solov'ev, et al., cover energies only up to 0.18 MeV, while those of Wexler ranged from 0.80 to 3.75 MeV. Both groups have studied protons on He, Ne, Ar, and Kr targets. While their energy ranges do not overlap, a comparison of sorts can be made by extrapolation. There is an appearance of good agreement for the low charge states of the

slow ions, but this actually results from the fact that neither set of measurements was absolute. Solov'ev's group normalized to their own total ion production measurements, while Wexler normalized to previous measurements made in this laboratory on total ion production cross sections.<sup>41, 42</sup> The apparent agreement for the ions of low charge state thus really reflects only the rather good agreement between these two sets of total ion production measurements. Significantly, the agreement does not appear to be as good for some of the higher charge states of the recoil ion; in fact, for some cross sections, the extrapolated comparisons disagree by more than a factor of eight.

The suggested conclusion is that measurements of absolute or even only relative cross sections for the production of multiply charged slow ions, using a fixed angle spectrometer and relying on collection of the ions to the entrance slit by an electrostatic field, can be substantially in error in some circumstances. Therefore, it was considered essential to include the capability of a field-free angular measurement and yet not preclude the use of a collection field when desired. It is not indicated that either of these collection methods is individually sufficient for the general case, but rather that a combination of the two methods is necessary. A spectrometer movable in angle, capable of collecting within a well defined angular interval from a field-free collision region, would produce results differential in the recoil angle. Integration of the results over the recoil angles to get the total production cross section for a given charge state should be more reliable than the simpler measurement, because the ion collection efficiency would be purely geometrical.

However, when the recoil ion energies are low, collection difficulties are produced by weak stray fields in the chamber. Even though evidence has been presented for the presence of energetic recoil ions, the fact still remains that most ions<sup>46</sup> of lower charge states have energies of only a few electron volts, and their collection efficiency can be seriously disturbed by stray fields. Therefore, it appears that the use of a collection field to measure the cross sections leading to production of low energy ions, and the field-free collision environment to measure the cross sections for production of energetic recoils should be a satisfactory combination of techniques.

A Nier-type<sup>50</sup> 60° magnetic deflection spectrometer, with electrostatic preacceleration was selected for this investigation. Two of the advantages of this type of spectrometer are that it can be used to provide a charge-to-mass analysis of ions with a large range in energy, and that it will provide a momentum analysis of each charge state of the more energetic ions. One of the difficulties associated with this type of spectrometer is that the magnet is a potential source of stray fields in the vicinity of the collision chamber. However, the magnet can be shielded, even though it is sometimes difficult.

Also relevant to the overall design decision was the fact that it was desirable to construct this analyzer to be fully compatible with later evolution of a coincidence experiment, in which the final charge states of both of the partners from a single collision will be determined. Originally, the coincidence experiment had been conceived in terms of fixed-angle spectrometers and a collection field. As such, the results would still be subject to the same possible errors due to hard collisions as

described in the preceding discussion. An experiment with movable spectrometers, differential in both the scattering and the recoil angles, would avoid this difficulty, while producing a more detailed result of intrinsic interest. In addition, if there is sufficiently good angular resolution, the inelastic energy loss in each collision is unambiguously determined from these two angles. The only atomic collision coincidence experiments that have been published thus far have in fact been designed with emphasis on study of details of the inelastic energy loss.<sup>51-53</sup> While the primary interest in the program of this laboratory will be in the measurement of cross sections, it was concluded that a doubly-differential apparatus would be of sufficiently greater general utility as to represent the clearly preferable choice.

Thus, the new apparatus was designed to perform measurements that are differential in the recoil angle and have sufficient momentum resolution to provide a moderate resolution scan of the energy spectra of the recoil ions.

The general mechanical quality of this apparatus, such as the machining, the precision rotation bearings, and the number of adjustments provided, are all directly connected with the aiming accuracy of the fast beam, the recoil ion spectrometer, and a future fast beam spectrometer. In the present investigation of the angular distribution of the recoil ions, it was desirable to have an angular resolution of about  $\pm 0^\circ 30'$  which, in the geometry of the spectrometer collimator, necessitates the use of rather narrow apertures (of the order of 0.020 inch). Since the size of the collision region viewed by the spectrometer is defined by the intersection of the beam and spectrometer collimators, it is important to



maintain a high degree of aiming precision as the spectrometer is rotated in angle.

The later evolvement of a coincidence experiment through the addition of a fast beam spectrometer will place considerably greater requirements on the accuracy and constancy of the aiming of the spectrometers. In fact, more than twice as great an angular resolution will be required of each spectrometer for the determination of inelastic energy losses. Consequently, the accuracy with which they must be aimed at a common point in the beam path, as they are rotated in angle, is correspondingly increased. The apparatus used to achieve this general level of aiming accuracy is described in the following sections.

#### General Description of Apparatus

An overall view of the new apparatus is shown in Figure 39. The apparatus is connected to the electrostatic beam analyzer following the gas cell by means of a flexible bellows, which permitted alignment with the beam emerging from the analyzer. In the new apparatus the beam was passed through a collimating cone and into the collision chamber in which it underwent ion producing collision with the target gas. Also inserted into the collision chamber was the incident beam detector and the slow ion collimator cone of the spectrometer, both of which were mounted such that they could be rotated about a fixed point in the collision region. The spectrometer, which was rigidly connected to the slow ion collimator, employed a system of electrodes for ion acceleration and focusing and an electromagnet to analyze the ion beam. An electron multiplier was employed for the detection of the ions as they emerged from the analysis

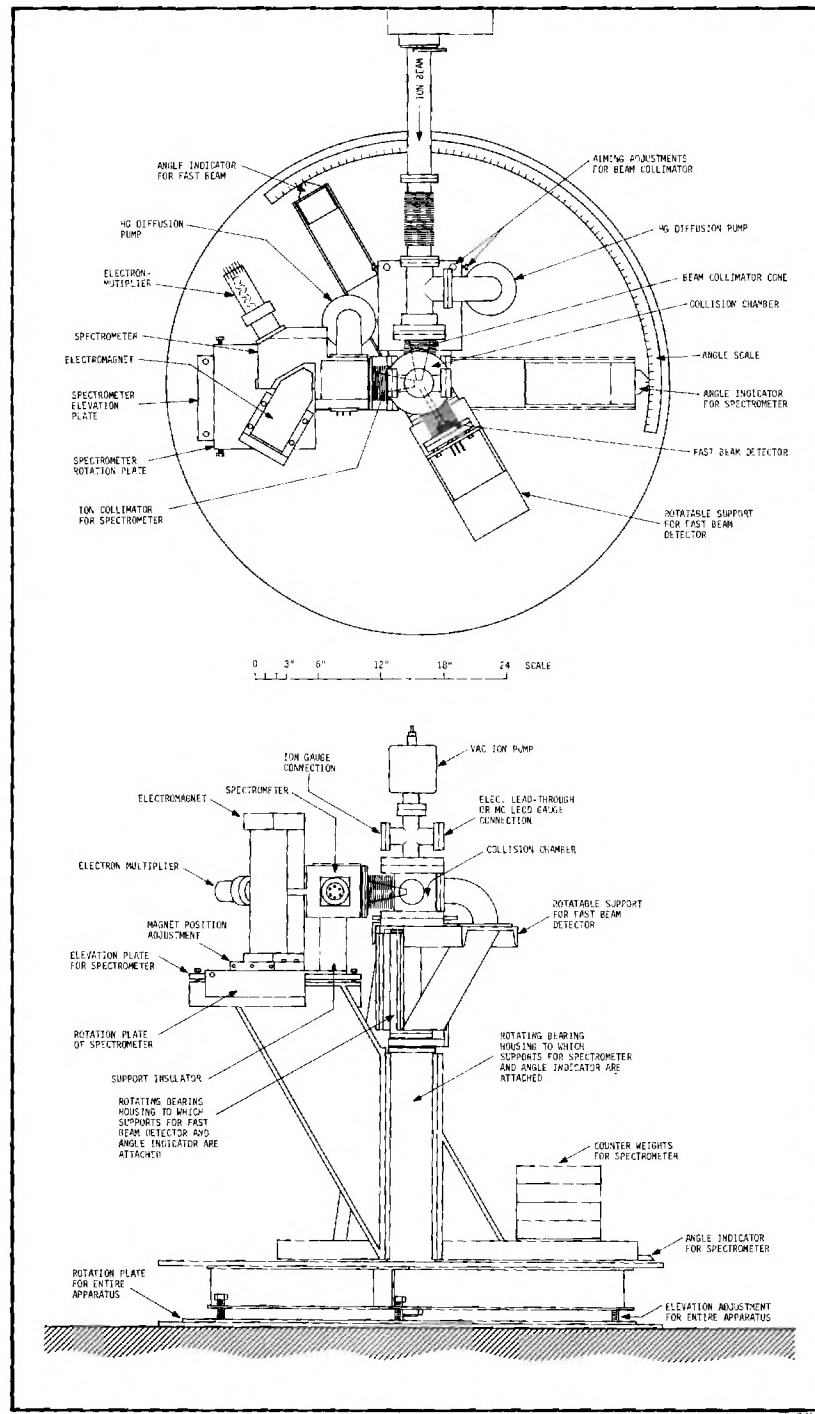


Figure 39. Overall Drawing of Apparatus Employed for the Measurements of Partial Cross Sections.

region.

All of the components mentioned thus far are mounted on supports (shown in Figure 39) that are mechanically attached to a vertical support column, or spindle, whose axis passes through the center of the collision chamber. The lower end of the spindle is securely seated and locked in a machined housing located in the center of the tripod base that supports the entire apparatus. The supports for the beam detector and slow ion spectrometer are rigidly bolted to separate bearing housings, each of which rotates on ultra-precision bearings about the common spindle. (In this experiment, however, the rotation feature of the fast beam detector was not used except to assure that the detector was centered in the  $\theta = 0^\circ$  position.) On the side of the bearing housing opposite the spectrometer there is located a second support which serves two purposes. First, it provides a mechanical attachment for an angle indicator for the spectrometer. The angle scale, which is divided into five minute increments, is mounted near the circumference of the large diameter steel plate which, itself, is bolted to the top of the tripod base. The second purpose of the support is that it provides a position for a spectrometer counterweight. Even though calculations indicate that the 200 pound weight of the spectrometer is insufficient to produce a significant deflection of the spindle, the precision to be required on the coincidence experiment is more easily guaranteed if the spectrometer is counterbalanced.

There are two complete sets of alignment adjustments. Those referred to as internal adjustments are the vertical and horizontal adjustments located on the supports for the beam collimator, the beam detector, and the slow ion analyzer. These adjustments and the precision machining

in this apparatus are to assure that these components rotate in the same plane (normal to the spindle axis) and about the same point (within 0.001 inch) in the collision region. The procedure for attaining this alignment is described in Appendix IV.

The second set of adjustments referred to as external adjustments are located on the base of the apparatus and are the adjustments used for alignment of the apparatus with the Van de Graaff beam. The jack screws in each leg of the tripod provide elevation and tilt, and the angular rotation of the apparatus is accomplished by means of a jack screw in a separate rotation plate, which is located beneath the plate on which the tripod rests.

The entire apparatus, with the exception of the tripod base, was constructed from nonmagnetic materials.

#### The Beam Collimator

For the purpose of the present discussion, a more detailed view of the beam and slow ion handling system is shown in Figure 40.

The beam emerging from the electrostatic analyzer following the gas cell entered the apparatus at the top right portion of the figure and passed through the collimator, through the collision chamber, and into the detector.

The beam collimator has provisions for three apertures. The first aperture position is in the flange connection between the bellows and the "T-shaped" pipe to which the two-inch cold-trapped mercury diffusion pump is attached. However, on the basis of the results obtained in the old apparatus, which were previously discussed, it was decided that a two slit

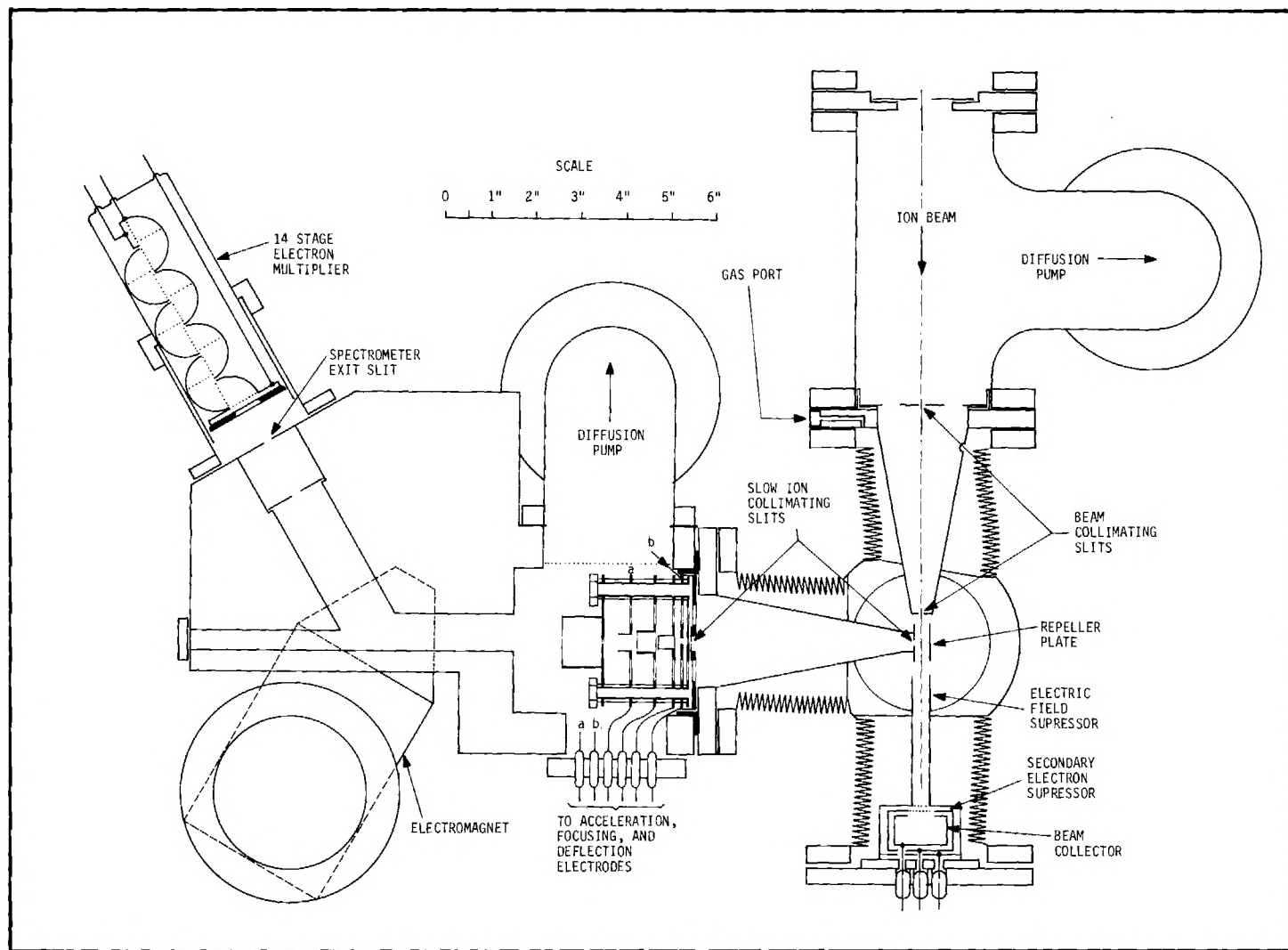


Figure 40. Detailed Drawing of Collision and Analysis Regions.

collimator would be sufficient for the present work. Therefore, the first aperture of the collimator through which the beam passed was located in the base of the "beam collimator cone," and the second was in the narrow end of the cone which protruded into the chamber.

All the apertures were machined in small brass "buttons" of 0.40 inch diameter and about 0.005 inch thick in the end with the aperture. The first collimating aperture was of 0.025 inch diameter and the button was fitted in a three-inch diameter plate located in the base of the cone. Six holes of  $5/8$  inch diameter removed most of the metal in this mounting plate to provide good pumping speed at the small end of the cone which contained the final 0.035 inch diameter aperture. However, it was found necessary (as will be discussed) to drill a 0.20 inch hole in the base of the collimator cone in order to provide sufficient pumping speed in the collision chamber. With this arrangement, it was observed that when the collision chamber was evacuated, the pressure in the entrance to the collimator was about  $4 \times 10^{-7}$  Torr, as measured on a Veeco (RG-75K) ionization gauge; when the chamber was filled with the target gas to a pressure of about  $1 \times 10^{-4}$  Torr, the pressure at the collimator entrance was less than  $5 \times 10^{-6}$  Torr. It will later be demonstrated that this collimator pressure is sufficiently low so that charge changing collisions by the beam are unimportant in this investigation.

The difficulties associated with fast electrons in the beam were not as important in this as they were in the old apparatus, because here the electron current was not to be measured, and hence the fast electrons were collected in only the beam detector. Therefore, the only errors these electrons could cause were either through ionization of the target

gas, or by being collected with the beam. It was demonstrated in the old apparatus that even when the collimator was poorly aligned the fraction of electrons in the beam corresponded to considerably less than one percent. It is generally true, as will be shown in later figures, that electrons, regardless of their energies, have ionization cross sections less than those of the ions in this (0.15 to 1.00 MeV) energy range. The conclusion is that the fast electrons will not cause any appreciable error in the measurements.

#### The Beam Detector

As the beam emerged from the small end of the collimator cone, it passed through the target gas, with which the collision chamber was filled, for about one inch before it entered the beam detector. The purpose of the short path in the target gas was to minimize the change in beam composition, through charge changing collisions, before the beam passed the relatively short (0.025 inch) portion of the path viewed by the spectrometer collimator.

The design of the beam detector was determined primarily by the desire to maintain the collision region as free of stray fields as possible. It is generally acknowledged<sup>54</sup> that one of the most effective schemes for the measurement of the current delivered by a high energy beam of particles is to trap the beam in a deep cup in which the entrance aperture subtends a small solid angle at the beam impact point. The purpose of the small solid angle is to minimize the probability that a particle ejected by the beam impact will escape the detector. Since, however, the emission of particles such as secondary electrons and sputtered target atoms does not fol-

low an isotropic distribution, it is difficult to associate the size of the solid angle with the efficiency with which these particles are contained in the detector. To further increase the efficiency of containment, an appropriately biased suppression grid or electrode is normally employed.

Both the small solid angle and the suppression grid were used in the present detector. It is obvious at once, however, that the electric field from the voltage applied to a grid in the detector might very well penetrate into the collision region and thereby cause an appreciable change in the transmission of the spectrometer collimator. In order to minimize the disturbance of the conditions in the collision region, a long narrow entrance tube was provided on the entrance to the detector to suppress the penetration of the electric field.

The detector is shown in Figure 40. The beam passes down the rather long grounded entrance tube and through the grid which is spot welded to its base. Immediately following this grid is the suppression grid, which is followed by the beam collector. It was found that a suppressor grid potential in excess of about -15 volts was sufficient to cause the measured beam current to saturate. A potential of about -30 volts was used for these measurements. The current to the electric field suppressor tube was measured and found negligible compared to the beam current.

The current from the beam detector was measured by means of a Keithley (Model 410) pico-ammeter. However, on the occasions when the analyzed ion counts (discussed in the following) were accumulated over periods of several minutes, it was difficult to estimate the average beam current over that period. This difficulty was avoided by integrating the signal



over the measurement period through use of a dc voltage-to-frequency converter (Dymec Model DY 2210). This V-to-F converter was connected to the recorder output of the pico-ammeter and was adjusted to produce about 1000 pulses per second for full scale deflection of the pico-ammeter. These pulses were then fed into a 100 kC scaler, and in this manner the integrated beam current over a given period of time could be determined.

#### The Collision Chamber

The collision chamber was constructed from thick-walled stainless steel tubing and is attached to the beam collimator, the beam detector, and the spectrometer collimator by means of three welded stainless steel bellows. These bellows are welded to the chamber on one end and on the other end of each is welded a rotatable flange (for use with aluminum gaskets). The 20° offset in the side of the chamber, through which the beam collimator protrudes, was designed to allow the maximum angular rotation of the spectrometer before either of the two collimators would contact the chamber wall and thus stop the rotation. The analyzer rotation was further increased by permitting the chamber itself to rotate, as described in the following paragraphs. Both the top and bottom covers of the chamber are removable six-inch diameter Con-Flat flanges (for use with copper gaskets) manufactured by Varian Associates. The bottom flange had a 3/8 inch diameter hole drilled one inch deep into a boss in its center. A matching hole was drilled in the top of the spindle on which the bottom flange of the chamber rests. A slightly undersized stainless steel pin was fitted into these two holes to keep the vertical axis of the chamber aligned with the spindle axis. This retaining pin was loose enough to permit the cham-

ber to rotate into equilibrium about its vertical axis under the influence of the bellows forces as the spectrometer was rotated.

On the top flange to the chamber was mounted a rotatable cross fitting, which was also manufactured by Varian Associates. The three flanges of this cross were employed to connect such things as an ionization gauge (Veeco RG-75K) or a McLeod gauge (CEC GM 110), an electrical feed through, and an eight liter-per-second Vac-Ion pump (Varian 911-5000) to the collision chamber.

It should be recalled that one of the prime concerns with this collision chamber and the spectrometer collimator was to minimize the presence of stray fields. The beam detector was designed with this in mind, and it should be noted that only metal gaskets are used on the collision chamber. Elastomer gasket materials such as neoprene and Buna-N have been observed<sup>55</sup> to outgas substantial quantities of hydrocarbons which, it was feared, would coat such critical surfaces as the spectrometer collimating apertures. If these insulating deposits were allowed to form and acquire an electrostatic charge, a stray field would be established, which probably would disturb the transmission of the collimator, particularly for the low energy ions. A further advantage of the stainless steel chamber with metal gaskets was that it could be heated, which helped remove condensable deposits on the surfaces. The heating to temperatures around 110°C was accomplished by means of a number of heating tapes which were wrapped around the chamber and the adjacent components.

It should also be noted that cold-trapped mercury diffusion pumps were used and for the same reasons as given above. Even with well designed cold traps, some creepage of the pumping fluid of oil diffusion pumps is

usually observed,<sup>56</sup> because oil wets all trap surfaces and, therefore, can migrate along the surface into the system. However, mercury does not wet stainless steel, the material of which the present traps were constructed, consequently the mercury does not creep.<sup>56</sup> It should be noted, however, that even if mercury did creep into the system, a thin conducting film of mercury is clearly preferred over that of oil.

There is still one source of stray fields that has not been discussed yet, and that is contact potentials between dissimilar metals in the chamber. To minimize the effect of this, the entire collision chamber, flanges, collimators, apertures, and the beam detector, were rhodium plated. Rhodium was chosen because it is a noble metal that does not oxidize or amalgamate. Therefore, should a substantial quantity of mercury get into the chamber, it could very simply be cleaned off of the surfaces.

A Vac-Ion pump, which operates by ionizing and "gettering" the gas, was employed to directly evacuate the collision chamber prior to the measurement of cross sections. With this and the diffusion pumps on the beam collimator and the spectrometer working, the chamber pressure was about  $3 \times 10^{-7}$  Torr after bake-out, as measured on an ionization gauge. However, the Vac-Ion pump employed a 1000 gauss magnet, which had a substantial fringe field in the collision chamber. Therefore, this pump was not operated during cross section measurements, and the magnet was removed from the vicinity of the chamber. Even without the aid of the Vac-Ion pump, a satisfactory low background pressure of  $1 \times 10^{-6}$  Torr was obtained. However, before the previously mentioned 0.20 inch hole was drilled into the collimator base, the equilibrium pressure was about  $1 \times 10^{-5}$  Torr, which, as will be seen later, is about ten percent of the target gas pressure.

The target gas was obtained from a standard high pressure cylinder. It was first passed through a high pressure regulator and then through a vacuum regulator, which, because it was more sensitive to small pressure fluctuations, considerably improved the pressure regulation. Next, the gas was passed through a copper coil immersed in a dry ice and acetone mixture ( $-79^{\circ}\text{C}$ ) which served to remove some of the condensable impurities. Following this cold trap, the gas was passed through an Edwards metering valve and into an adapter that screwed into the base flange of the beam collimator. This flange contained a radial hole  $1/16$  inch in diameter (shown in Figure 40) that made a right angle turn and emerged from the flange face next to the base of the cone. Following this route, the target gas emerged inside the collision chamber.

#### The Spectrometer

Two different types of measurements, which required different collimator extensions, were performed with this spectrometer. The first measurements involved the use of a field-free collision region and observation of the angular distribution of the recoil ions. The second type of measurement involved the collection with an electric field of the ions formed along a portion of the beam path, regardless of their original directions of recoil.

The two different collimator extensions that were used in these measurements are shown in Figure 41 and Figure 42. These two figures are photographs of the collision chamber with the top removed. In each figure can be seen the beam collimator cone protruding into the left side of the chamber and diametrically opposite is the entrance to the beam detector.

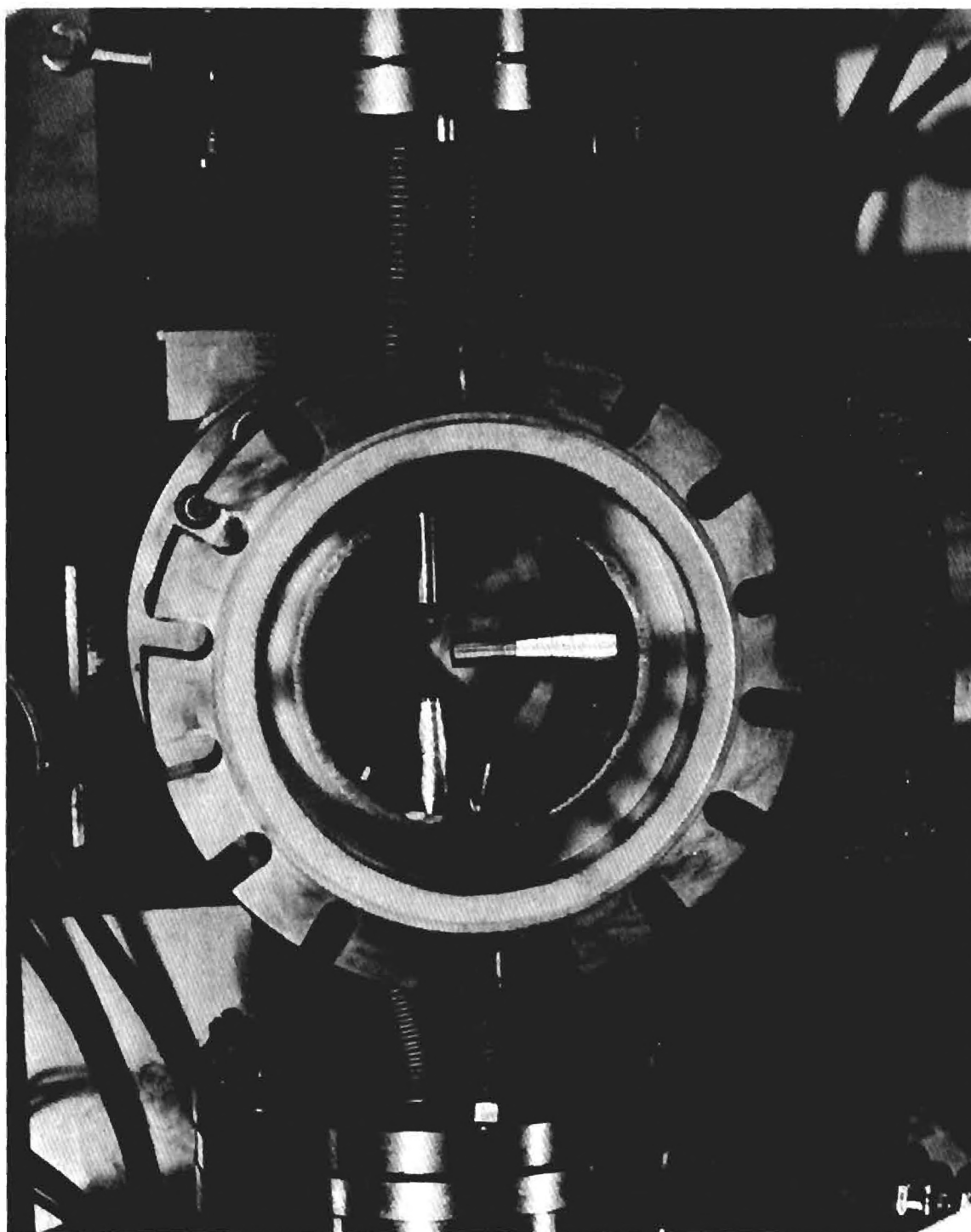


Figure 41. Plan View of the Field-Free Collision Region.

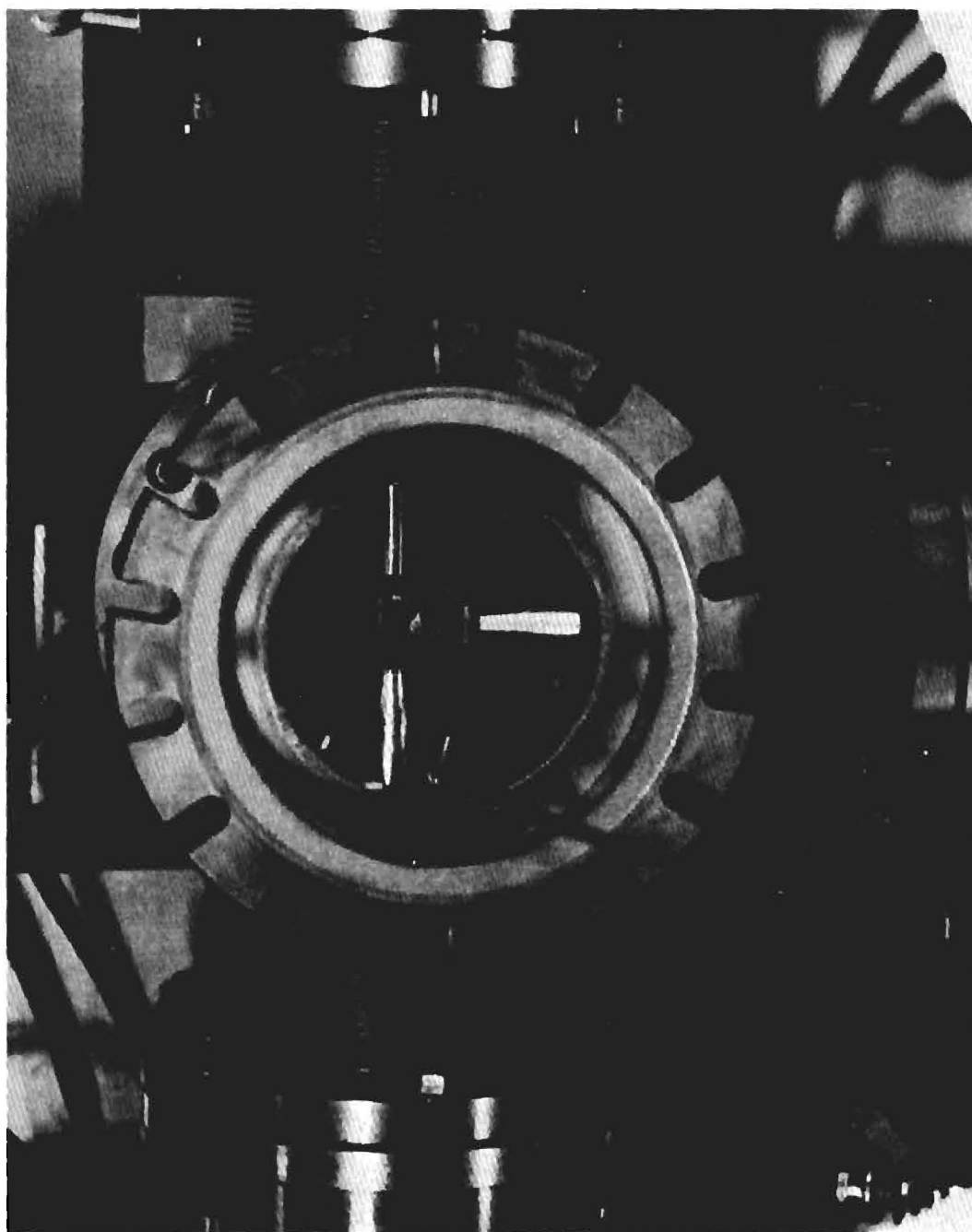


Figure 42. Plan View of Collision Region with Repeller Electrode Installed.

The only difference in the two figures is the attachment on the spectrometer collimator. The simple cylindrical extension in Figure 41 is a rhodium plated aperture ( $0.025 \times 0.040$  inch tall) that was used for the field measurements of the angular distribution of the recoiling ions. The more complicated attachment on the collimator in Figure 42 is the repeller electrode which is shown in greater detail in Figure 43. This electrode was used for the measurement of the cross sections for the production of  $\text{He}^+$  ions and, separately, of  $\text{He}^{++}$  ions regardless of their original directions of recoil.

The actual electrode to which the repeller potential was applied was a thin (0.010 inch) sheet of phosphor bronze that was shaped to wrap around three sides of the beam path. It was attached with insulating spacers to the grounded aperture extension which was fitted into the end of the cone.

The second aperture of the collimator was in the first electrode of the spectrometer, which was located in a recess in the base of the cone. It was anticipated that a greater angular resolution than  $\pm 0^\circ 30'$ , which was obtained with the present apertures, would be required in later experiments. Therefore, provisions were made to mount a separate and smaller aperture  $1/16$  inch in front of the present aperture.

The recess, in which the electrode structure was mounted, was machined concentric and parallel to the small end of the collimator cone that contained the entrance aperture button. Also located in this recess were four drilled and tapped holes and four accurately milled holes. Into the tapped holes were screwed four rods of about four-inch length on which the analyzer accelerating and focusing electrode structure was mounted.

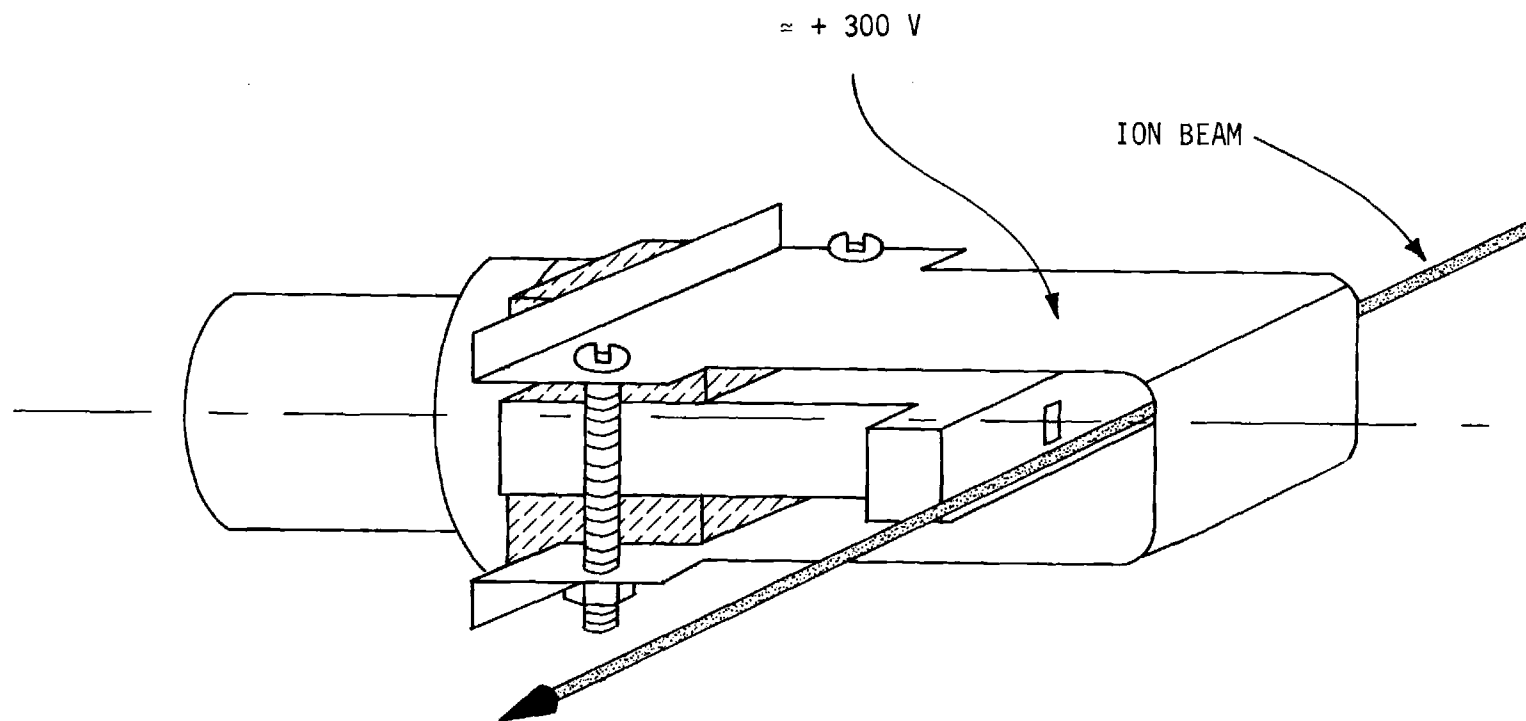


Figure 43. Isometric Drawing of Repeller Electrode.



The electrodes were separated from each other and the mounting rods by a series of machined Supramica insulators. The alignment of these electrodes with the collimator axis was obtained by assembling the entire structure on four jig rods that were inserted into the milled holes in the collimator base. Once the structure was assembled and lock nuts had been placed on the mounting rods, then the jig rods were removed.

The basic focusing geometry of this electrode structure was designed from the information presented in Terman's Radio Engineer's Handbook.<sup>57</sup> The entire electrode structure (shown in Figure 40) consists of six elements which serve to accelerate and focus the beam before it is passed into the spectrometer vacuum enclosure, which itself is at the full acceleration voltage. The first element was a thin (0.010 inch) rhodium plated disc that contained a 1/16 inch diameter aperture and was electrically grounded. It served as the second collimating aperture and to prevent the electric fields from the following acceleration electrodes from penetrating into the field-free region of the collimator.

The second element of the lens system was a rhodium-plated centering electrode. Its function was to center the beam in the electrode structure that followed (if by some chance the jig alignment was not adequate). This electrode consisted of two insulated halves that could be used individually to push or pull the beam from side to side, or both halves could be used together to retard the beam. The latter feature could be used to furnish information on the energy of the recoiling ions. Tests showed, however, that the jig alignment of the assembly was sufficient, and therefore the centering feature of this electrode was not employed. In fact, both sides were operated at ground potential to minimize the field penetration of the

following acceleration and focusing electrode into the region of the second collimator aperture.

The geometry of the following two electrodes was selected according to the information and evaluation of focusing characteristics presented by Terman,<sup>57</sup> according to which this lens could be used to focus the beam at any location between the last electrode and the end of the spectrometer. The third element, which comprised the first half of the focusing lens, was 0.25 inch in diameter and 0.35 inch long, and the second half of the lens (the fourth electrode) was 0.45 inch in diameter and also of 0.35 inch length. The latter electrode established the terminal acceleration of the lens system, which was typically one to two kilovolts.

The next element (fifth electrode) was similar in design to electrode number two and provided a convenient means of deflecting the beam after it had been accelerated and focused.

The primary function of the sixth electrode was to serve as the entrance aperture to the magnetic analyzer geometry, i.e., this electrode was located at the focal point of the magnet and, therefore, its aperture served as an object of the focusing magnetic field. The size of this aperture, which was one of the primary determinants of the spectrometer resolution, was 0.10 inch in diameter. This value was selected because it was slightly larger than the diameter of the unfocused beam at that location and yet it was smaller than the width of the spectrometer exit slit (to be discussed). Thus, it served as an acceptable upper limit on the beam diameter as it entered the magnetic analyzer.

The last electrode also marks the beginning of the electric field-free region of the magnetic selector of momentum/charge. To serve this

function, it must, because of protruding points at ground potential in the rest of the assembly, have a "shroud" on the back side of the electrode.

The beam diverging from a focus at the final slit of the electrode assembly passed through a Nier-type  $60^\circ$  sector magnetic field,<sup>50</sup> which re-focused it on the  $1/8$  inch wide exit slit of the spectrometer. The magnetic focusing, however, was only in the plane of Figure 40; there was no focusing in the vertical plane. In order to allow for the lack of vertical focus, the spectrometer collimator and the hole through which the beam passed in route to the exit slit were so designed that the beam would not strike any surface before the exit slit, even if there were no focusing.

In Figure 40 is shown a  $1/4$  inch baffle that precedes the exit slit. The purpose of this baffle was to reduce the transmission, through the exit slit to the detector, of detuned beam components that were reflected from the walls.

The  $60^\circ$  deflection geometry had a five-centimeter radius of curvature in the magnetic field. A current of 1.1 amperes was required in the magnet coil to supply the 1.8 kilogauss field necessary to analyze a one kilovolt  $\text{He}^+$  ion.

A rather low resolving power, about ten, was used in this experiment because the interest in the present work was not in high resolution, but rather in the attainment of flat-topped peaks as the analyzed ion beam was swept across the exit slit. This mode of operation required the use of a rather wide exit slit and a corresponding sacrifice of resolution. The resolving power of ten was, however, more than adequate for the present work. As will be demonstrated later, the focusing ability of this instrument is sufficient to produce a resolving power of 50 if the  $1/8$  inch

exit slit were replaced with a  $1/32$  inch slit, and the resolving power could be approximately doubled, to 100, by using a smaller ( $1/32$  inch) slit in the end of the collimating cone.

In order to minimize the fringe field in the vicinity of the "field-free" regions of the collision chamber and the spectrometer collimator, a  $3/8$  inch thick mild steel plate was mounted about  $5/8$  inch from the pole face of the magnet. With this shield, the fringe field (normal to the ion path) with 1.8 kilogauss in the magnet gap, was less than one gauss in the collision chamber and less than two gauss in the collimator. Although the magnet would supply a field greater than eight kilogauss, later tests on the recoil energy of the ions demonstrated that large fields were unnecessary and, therefore, only small fields were used in order to minimize the fringing into the collision chamber.

With the full accelerating potential on the spectrometer vacuum housing, it was necessary to insulate it from all the grounded components that were connected to it. The magnet was insulated by two  $1/64$  inch sheets of Teflon which were inserted in the gap between the magnet and spectrometer housing.

The grounded collimator cone was insulated from the spectrometer housing by means of two accurately ground alumina spacers, which are shown as wide black lines in Figure 40. One spacer was used to align the collimator axis parallel to the axis of the spectrometer, and the other was used to assure that these two axes were the same.

A two-inch cold-trapped mercury diffusion pump was used to evacuate the spectrometer, from which it was insulated by a thin ( $1/16$  inch) Nylon washer. With this pumping arrangement (shown in Figure 40) the spec-

trometer pressure was maintained at less than  $8 \times 10^{-7}$  Torr (as measured on a Veeco RG-75K ionization gauge) even when the collision chamber was filled to the working pressure with target gas. In order to increase the pumping speed to the region behind the first aperture of the collimator, all of the electrodes that were solid discs were perforated by six  $5/8$  inch diameter holes, and the two deflection electrodes had four somewhat larger holes drilled in them. A calculation, based on the conductances of the collimator and electrodes, indicated that a pressure drop of about 100 could be expected between the collision chamber and small end of the cone.

As an extra precaution, to decrease the penetration of the acceleration fields through these pumping holes into the field-free collimator, a very thin grid (rhodium plated) was spot-welded across the holes. This grid was 97 percent transparent and the wire was about 0.002 inch in diameter. Therefore, the grid was expected to serve as a good equipotential surface and to have a negligible pumping impedance. Such a grid was also used to cover the pumping port on the side of the spectrometer; it was intended to prevent the grounded elbow to the pump from disturbing the field inside the spectrometer.

#### The Ion Detector

Mounted on the end of the spectrometer and spaced about one inch from the exit slit was a 14 stage copper-beryllium electron-multiplier detector (DuMont SPM-03-314).

This multiplier permitted the detection of individual ions that passed through the spectrometer. In Figure 40 it is seen that an ion entering the multiplier strikes the first of a series of 14 curved metallic

(CuBe) surfaces; these are referred to as dynodes. When the ion strikes the first dynode, secondary electrons are ejected; they are swept by an electric field to the next dynode where the process of secondary emission is repeated. Thus the electrons multiply in number as they are swept down the series of dynodes by successively higher positive voltage. The current gain of the present tube was estimated to be greater than  $10^6$  electrons/ion.

In this experiment, it was desirable to detect the analyzed ions with an efficiency of around 99 percent. The achievement of such a high efficiency required that about 99 percent of all incident ions eject at least one secondary electron from the first dynode. It was explained by Deitz<sup>58</sup> that the expected frequency distribution for producing  $n$ ,  $n = 0, 1, 2, \dots$ , secondary electrons is given by the Poisson distribution  $(\gamma^n/n!) \exp(-\gamma)$ , where  $\gamma$  is the average secondary emission coefficient. In the same paper, he verified that this was a good approximation to the actual situation. Therefore, according to the above distribution, it is necessary that  $\gamma = 5$  in order that 99 percent of all the ions eject at least one secondary electron. The relation between the mass and energy of an ion to the secondary emission coefficient for typical multiplier surfaces has been demonstrated by Akishin,<sup>59</sup> and according to the figures he presented, an ion energy considerably greater than ten keV is required to attain  $\gamma = 5$  for the light helium ions. Therefore, to achieve these ion energies, a high postanalysis voltage was employed to accelerate the ions into the detector. However, this entire acceleration voltage was not wanted across the multiplier because the secondary emission coefficient by electrons, which determined the gain of the detector, peaked around 300 to 400 electron volts; consequently, a potential difference greater than

about 400 volts per dynode, which implies an overall detector voltage of about 6500 volts, would produce a decrease in detector gain. Therefore, the circuit which is shown in Figure 44 was arranged to drop a variable fraction of the postanalysis acceleration voltage across the detector.

As is indicated in Figure 44, the postanalysis acceleration potential into the first dynode was supplied directly from the high voltage source. The ten henry coil and the  $0.005 \mu\text{F}$  capacitor were installed to filter out high frequency switching transients from the rectifiers in the supply. Normally about a five kilovolt drop was maintained across the multiplier resistor string, which established a 350 volt interdynode potential. The remainder of the accelerating voltage was dropped across the lower variable resistor string, which, of course, was comprised of high voltage and high power resistors. Because of the limit on the voltage and power ratings in commercially available resistors, it was necessary to choose these values such that only a few tenths of a milliamp passed through the resistor string.

The two paralleled capacitors (500 pF and one  $\mu\text{F}$ ) were installed for the purpose of bypassing the noise at the end of the dynode string to ground, rather than permit it to be coupled into the signal circuit. The 500 pF capacitor was used because it was suggested that it had better high frequency qualities than the large capacitor.

When the electron avalanche initiated by the incoming ion reaches the anode of the tube, a current pulse is passed through the 100 k $\Omega$  load resistor, which develops the voltage pulse that is passed by the isolation capacitor into the preamplifier. Following the preamplifier, the signal was passed through an amplifier (Oak Ridge National Laboratory, Model ALD)

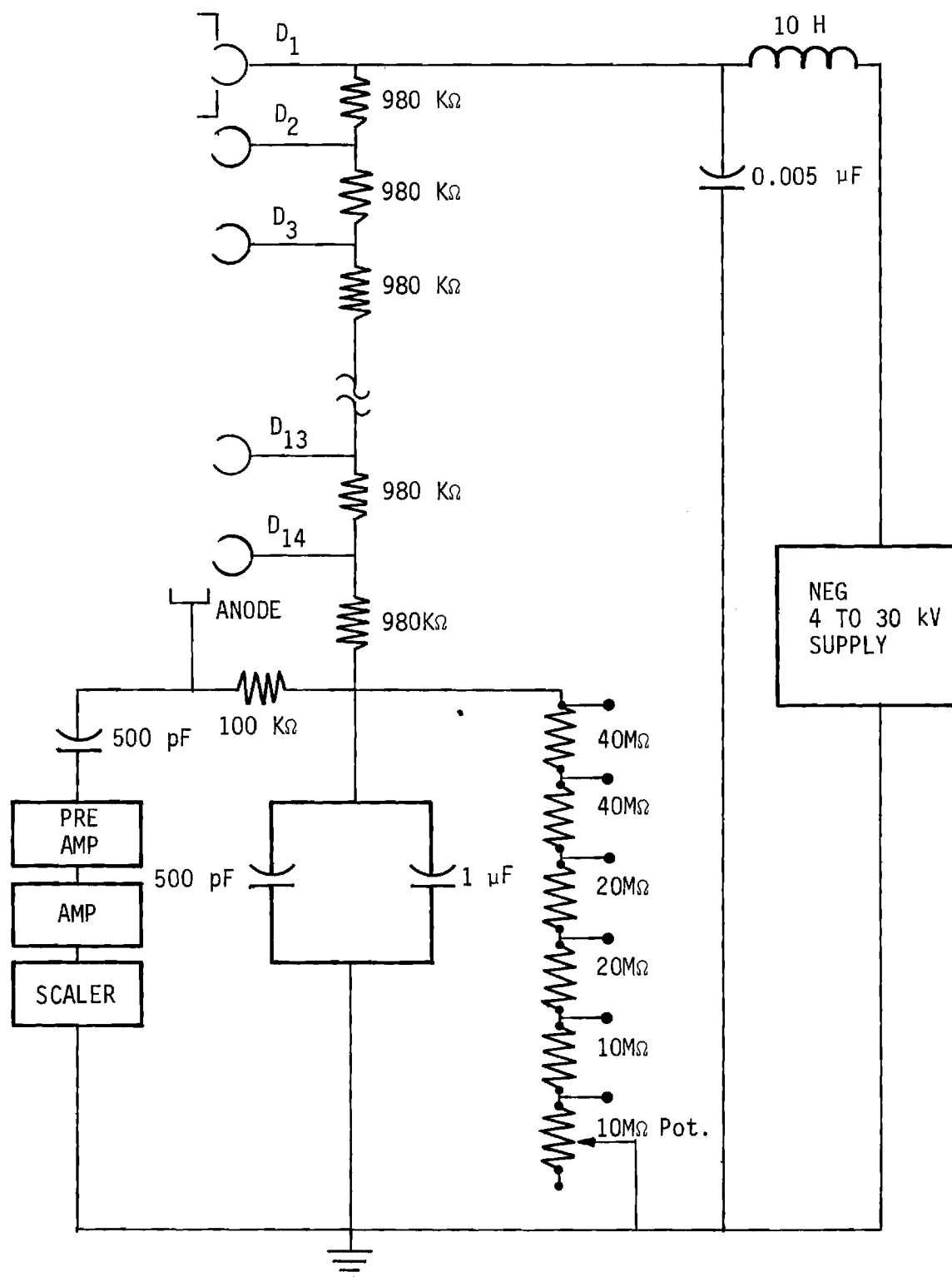


Figure 44. Wiring Diagram of Particle Multiplier.



and into a scaler (Systron-Donner 1034) in which the individual pulses were recorded.

CHAPTER VII  
EXPERIMENTAL PROCEDURES FOR THE MEASUREMENT  
OF PARTIAL IONIZATION CROSS SECTIONS

Evaluation Tests of Apparatus

Prior to the measurements of cross sections the performance of the new apparatus was evaluated. In order to facilitate this procedure, the repeller electrode was used in the collision chamber to provide a substantial ion current through the spectrometer.

The projectile-target combination of protons incident on helium was selected because of its simplicity, i.e., the only two likely charge states of the target are  $\text{He}^+$  and  $\text{He}^{++}$ .

To begin this series of tests, the proton beam was passed through the helium gas and into the detector, then the spectrometer was adjusted to produce a maximum count rate in the multiplier circuit.

Test 1. Determination of the optimum gain of the multiplier. This was accomplished by using the high voltage power supply to establish a ten kilovolt acceleration into the first dynode. The lower resistor string (Figure 44) was used to vary the voltage drop across the multiplier from about two to seven kilovolts. In this fashion, the response curve of Figure 45 was obtained. It should be noticed that the counting rate appeared to saturate above about five kilovolts, i.e., about 350 volts per dynode. Therefore, in this experiment a multiplier voltage of around 5.5 kilovolts was chosen.

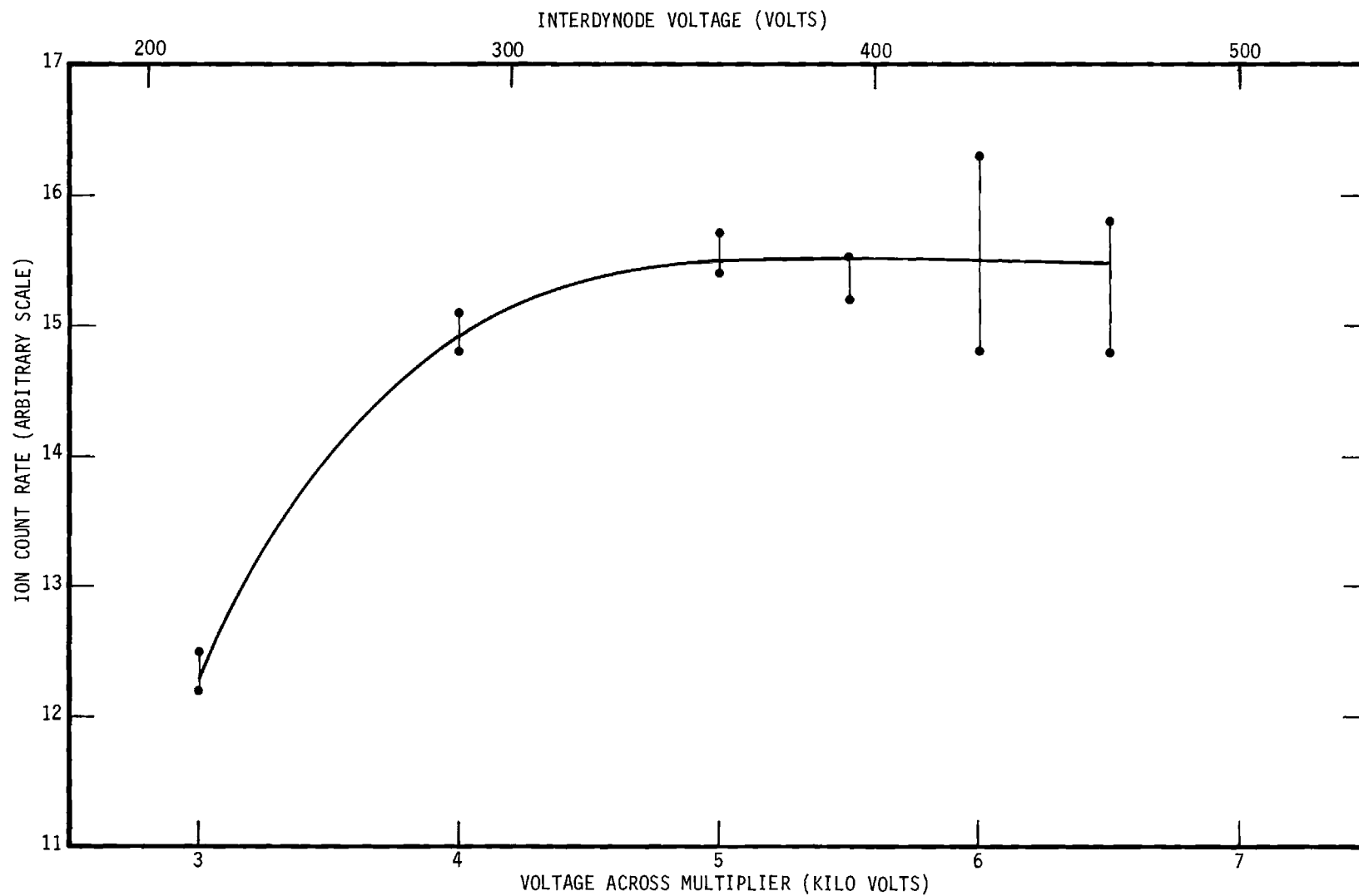


Figure 45. Response of Ion Count Rate of Multiplier to Interdynode Voltages.

Test 2. Evaluation of the response of the multiplier count rate to the ion accelerating voltage. It was of particular interest to demonstrate that the ion counting efficiency was near 100 percent. For the reasons discussed in Chapter V, it was believed that when the ion acceleration potential reached a sufficiently high value to produce an average secondary yield of five or more electrons per incident ion, then the detection efficiency would be approximately 100 percent. It was also desirable to demonstrate that under the above conditions the signal pulses were clearly separated in amplitude from noise pulses.

The above two conditions are related and were tested in the following manner. For a series of increasing values of the acceleration voltage into the multiplier, pulse height spectra were obtained through the use of the pulse height discriminator on the amplifier. It was found that the noise was usually negligible compared to the signal, even when the lowest discriminator settings were used. Unfortunately the low discriminator settings necessary to include the smallest signal pulses (those pulses corresponding to  $\gamma = 1$  on the first dynode) were unreliable and some scatter was obtained in the data. However, it was found (even with that discriminator setting) that as the acceleration voltage was increased, the count rate also increased up to a point and thereafter remained constant as the voltage was further increased. This saturation in count rate was interpreted to indicate that all of the real signal pulses were above that discriminator setting and therefore equal and near 100 percent detection efficiency was obtained at the acceleration voltages for which the count rate saturated. In this manner, Figure 46 was obtained for both helium ions. It should be noticed that, although the acceleration poten-

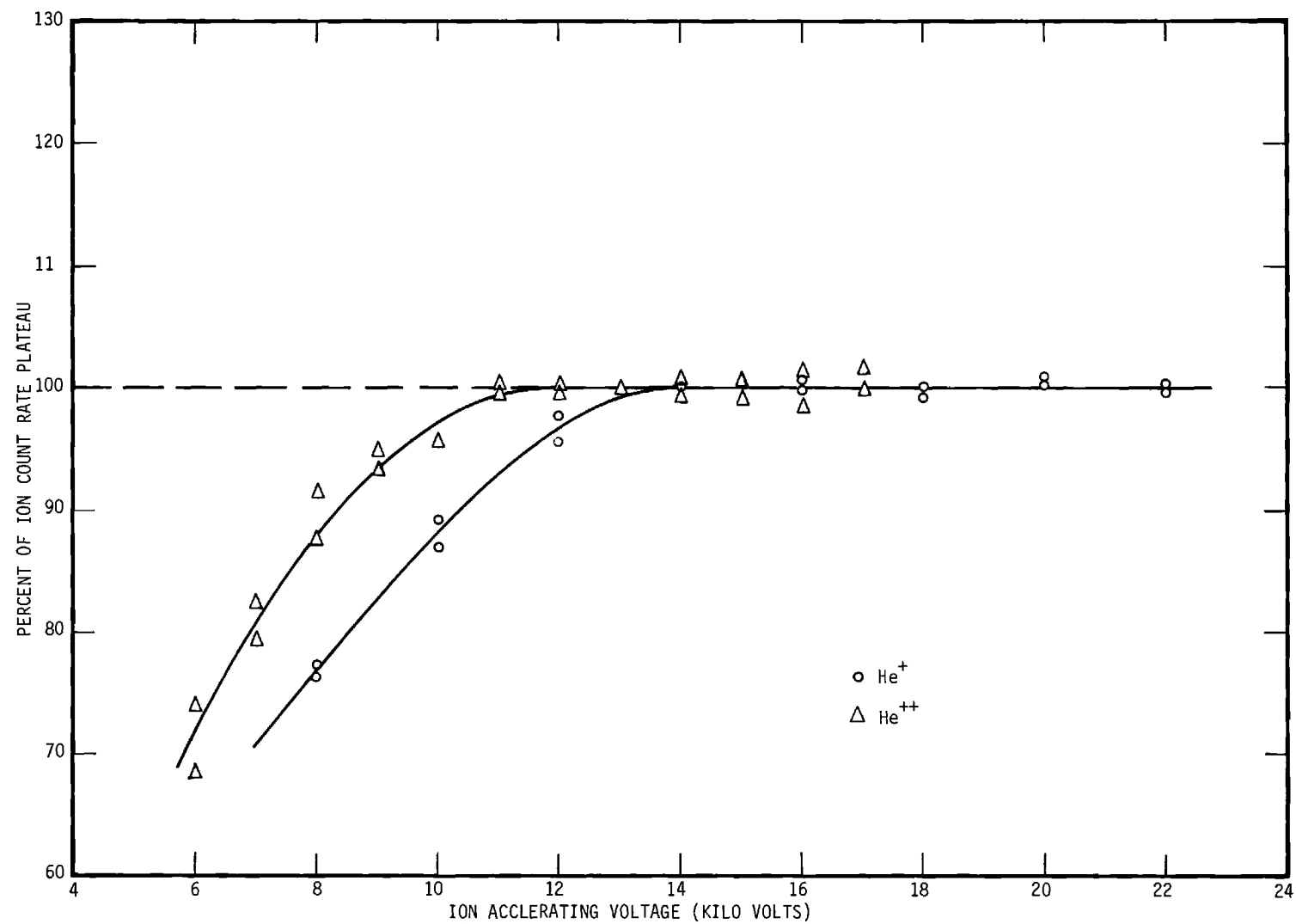


Figure 46. Response of Multiplier Ion Count Rate to Ion Acceleration Voltage.

tial at which the  $\text{He}^{++}$  saturated was 12 kV, its energy was 24 keV, and therefore greater than the 14 keV energy for which  $\text{He}^+$  saturated. The saturation curves were not extended beyond 22 kV at this time because at that point the noise was observed to being a rapid increase. The curves of Figure 8 were taken before the large one  $\mu\text{F}$  capacitor was added in parallel to 500 pF bypass capacitor shown in Figure 44. The later addition of the large capacitor served to reduce the noise at 20 kV by a factor greater than 50, which permitted the extension of the saturation plateaux up to about 25 kV for  $\text{He}^+$  and about 21 kV for  $\text{He}^{++}$ . However, at 25 kV the noise again became comparatively large ( $\frac{\text{sig}}{\text{noise}} \approx 8$ ) and, indeed, great care was required in providing adequate insulation between the various circuit elements in order to even reach the total 30 kV acceleration potential without electrical discharges. For the preceding reasons, a postanalysis acceleration voltage of around 16 to 18 kV was selected for the helium ions in this investigation.

Test 3. The purpose of this test was to determine the optimum acceleration and focusing voltages of the spectrometer. This test was performed separately with the repeller electrode and with the rhodium plated aperture for field-free measurements in the collision chamber.

Without a repeller field it was found that optimum focusing and transmission occurred for about 800 volts acceleration, i.e., the profile of the count rate, as the beam was magnetically swept across the 1/8 inch exit slit of the spectrometer, was flat topped. For this condition, the potential on the focus electrode was about 150 volts. It was found that flat-topped peaks were maintained for spectrometer potentials up to and including 1700 volts; such a profile is shown in Figure 47 for 1100 volts

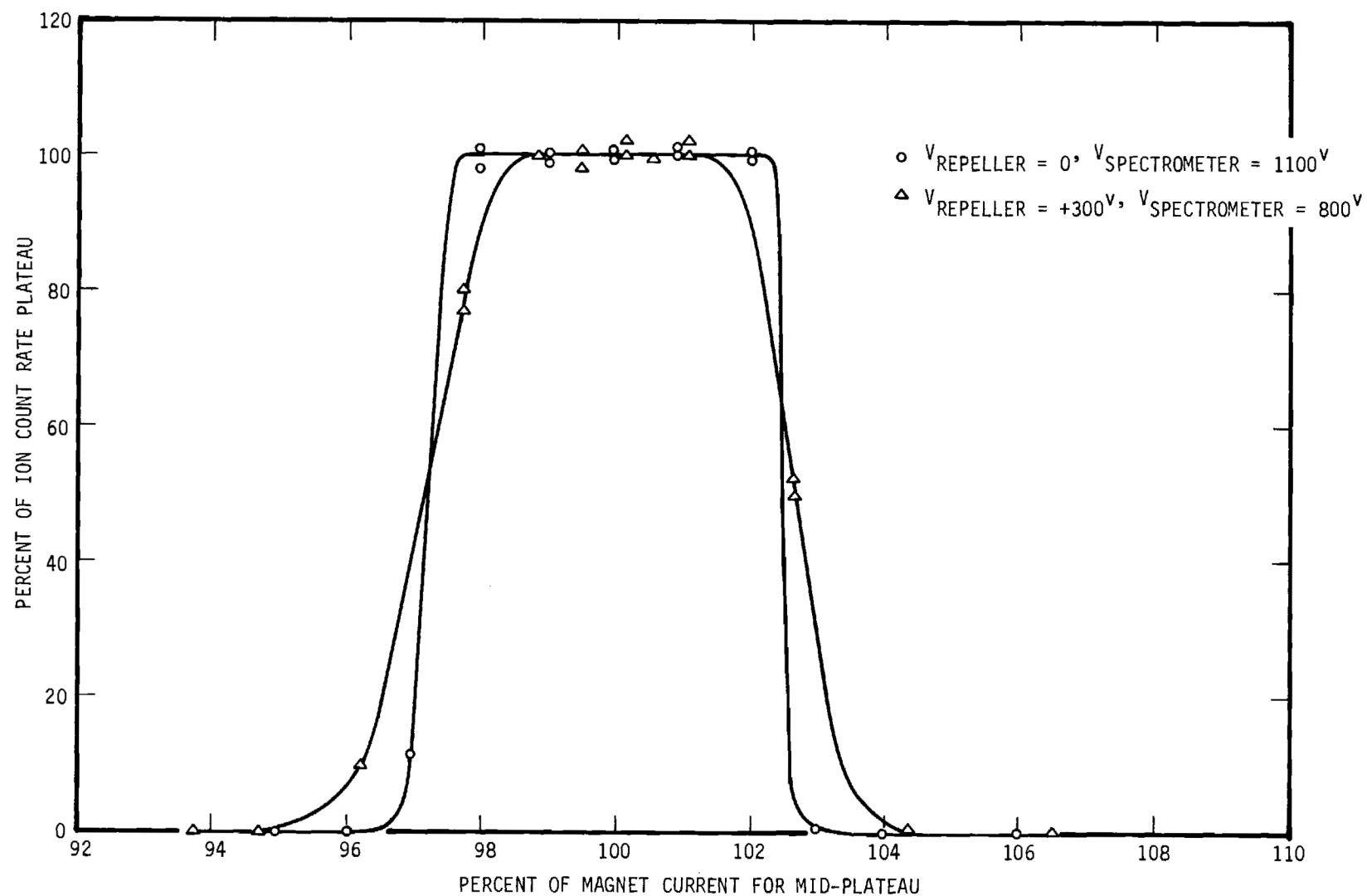


Figure 47. Profile of Count Rate as Beam Was Swept Across the Spectrometer Exit Slit.

acceleration.

When the repeller field was applied, which gave the ions substantial energies, the focusing conditions were different. It was found that optimum focusing was obtained for a ratio of repeller potential  $V_r$  to spectrometer potential  $V_a$  such that

$$1/4 \leq \frac{V_r}{V_a} \leq 1/3$$

A count rate profile is shown in Figure 47 for this case also. It should be noted that the flat top is somewhat narrower than that of the zero repeller potential case. This is believed to be due to the increased difficulty in focusing energetic ions.

Test 4. When the repeller electrode was used, it was necessary to know at what voltage it should be operated to insure equal collection efficiencies for all ions. Figure 48 shows the relation between the ion count rate to the repeller potential for both helium ions with all the previously discussed parameters properly tuned. The occurrence of saturation in count rate versus repeller field was interpreted to indicate that the repeller field was sufficiently strong to cause both  $\text{He}^+$  and  $\text{He}^{++}$  ions to very nearly follow the lines of electric force to the collimator aperture. Therefore, the only requirement to assure equal collection efficiencies for these ions was a sufficiently large collection field, which was apparently satisfied above about 300 volts on the repeller; a value of 350 volts was selected for this work, which dictated a spectrometer potential of 1000 to 1400 volts.



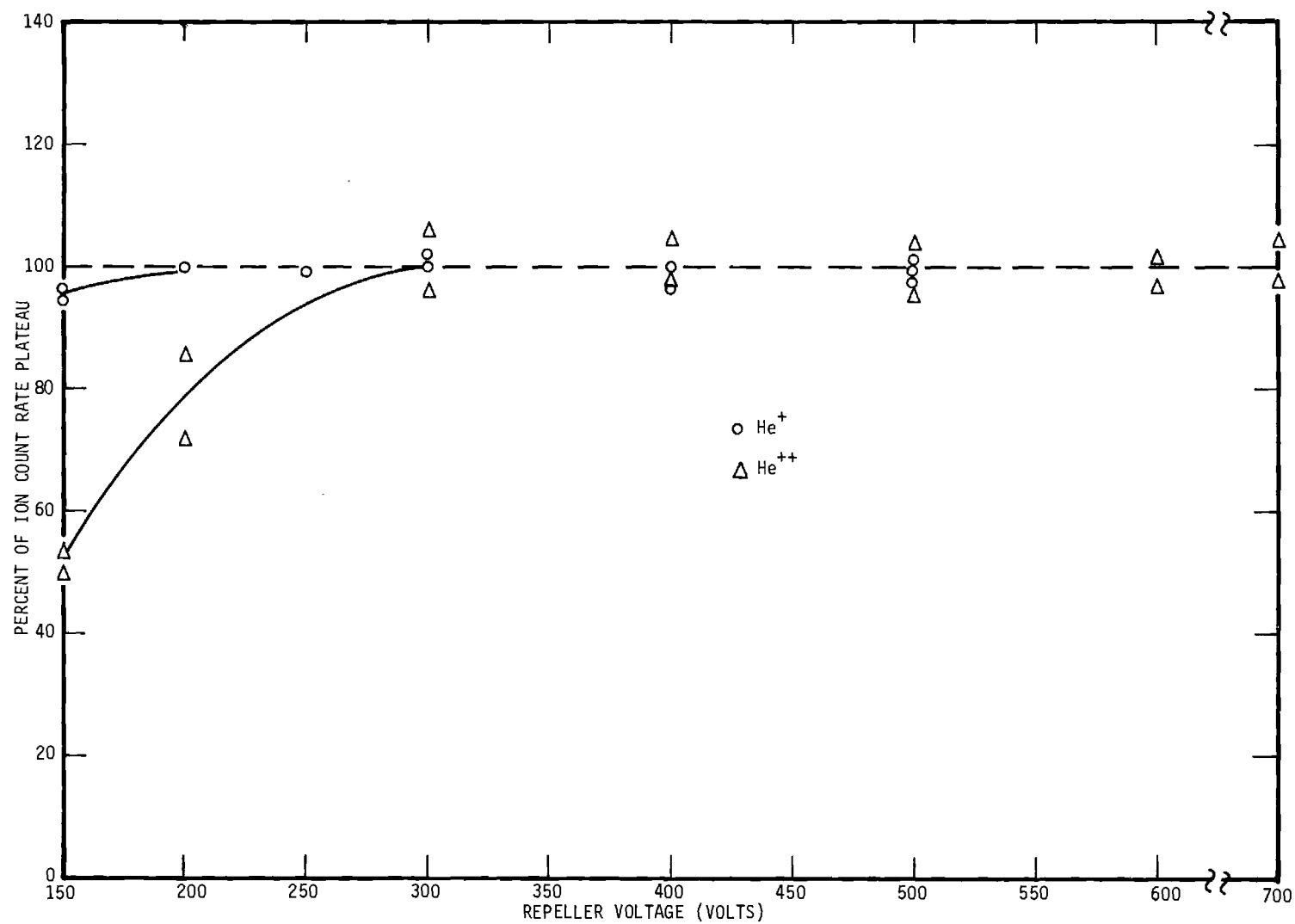


Figure 48. Response of Ion Count Rate of Multiplier to Repeller Voltage.

Test 5. This test was to determine the pressure range over which thin-target conditions existed. The quantity plotted on the ordinate of Figure 49 is proportional to the measured cross section for production of these two helium ions. Therefore, from the figure it is seen that the measured cross sections are constant as the target gas pressure (indicated by an ionization gauge) is increased up to a value of about  $2 \times 10^{-4}$  Torr.

Test 6. It was necessary to determine whether or not a significant fraction of the two helium ions, which were formed by the beam collisions with the target gas, underwent secondary charge changing collisions in the gas before they entered the evacuated collimator. Of particular concern was the resonance charge exchange process ( $\text{He}^+ + \text{He} \rightarrow \text{He} + \text{He}^+$ ), which could completely destroy the  $\text{He}^+$  recoil angular distribution, and it is expected to be the largest charge changing process operative at these ion energies of around 200 eV (imparted by the repeller electrode). In addition, it was necessary to determine the effect of the pressure in the collimator on the ion abundances.

The test designed to detect the resonance process was based on the following reasoning. The  $\text{He}^+$  ions that are formed in the gas receive an acceleration to the collimator aperture by the repeller field. The energy that the ion had acquired when it arrived at the collimator was proportional to the distance through which it traveled in the repeller field. If there were no charge changing collisions experienced by the ion in traveling from the point of creation in the beam to the collimator, then the average ion energy would correspond to the acceleration potential at the beam axis. The energy spread about this value would correspond to the spatial width of the beam in the repeller field, and it should be approxi-

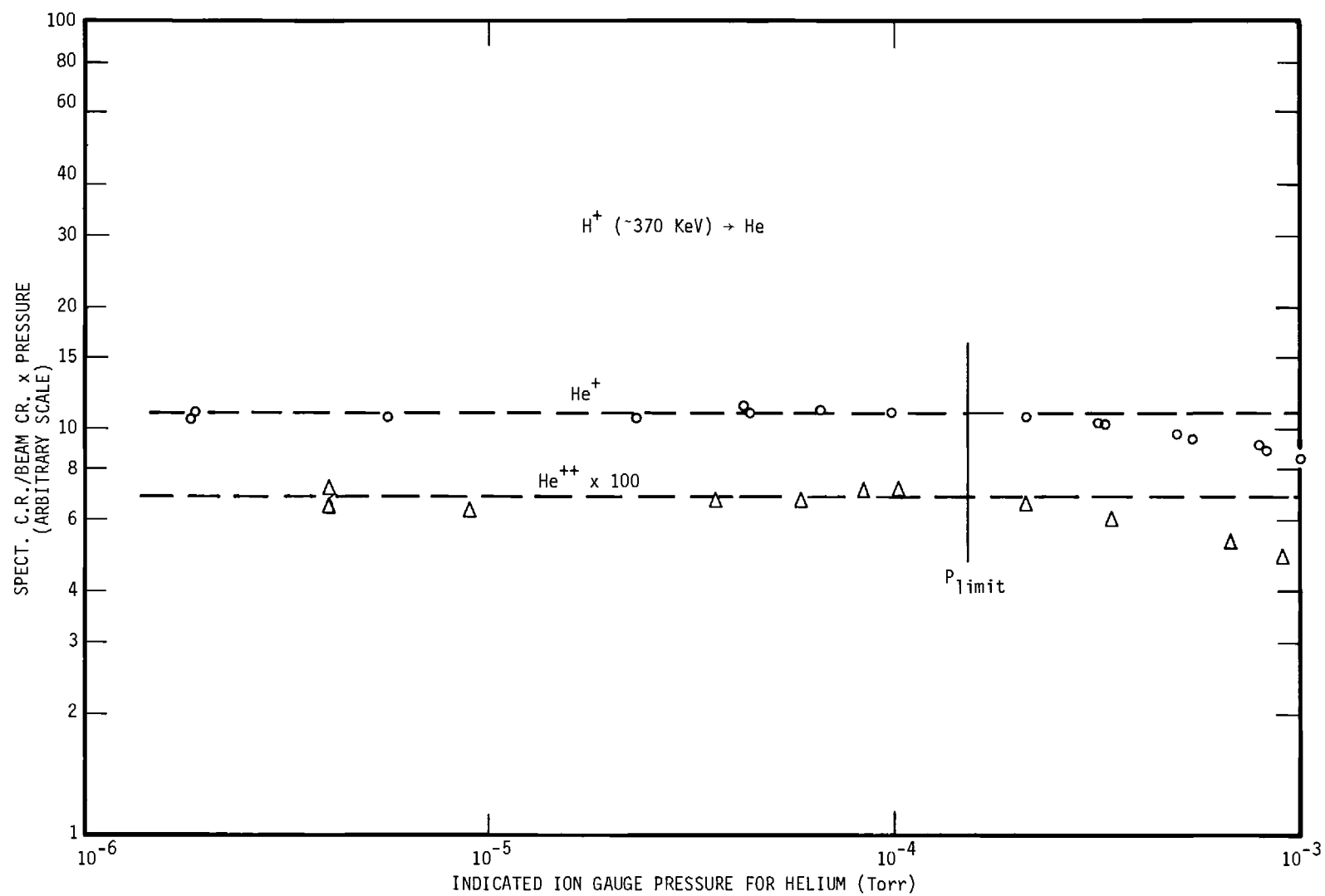


Figure 49. Limiting Pressure for Thin-Target Conditions.

mately symmetric. When a low acceleration potential is used in the spectrometer, the profile of the ion peak (count rate) at the exit slit should be directly related to the energy spread of the ions emerging from the collision chamber.

If resonance charge exchange did play an important part, however, some of the original  $\text{He}^+$  ions would be neutralized at some point between the beam and the collimator, and the newly created  $\text{He}^+$  ion would be accelerated on to the collimator. These new ions would be different in at least two respects from the original ions. First, they would not have the angular distribution characteristic of the high energy beam collision, and second, their energy acquired from the repeller field would be less because of the shorter distance through which they were accelerated.

As was previously mentioned, the importance of resonance charge exchange in this experiment is that it destroys the angular distribution of the recoil ions; however, the test for the presence of this effect was based on the energy difference of the ions. Specifically, evidence for this effect would be found in the energy profile of the ion peak at the exit of the spectrometer. If the peak were skewed to low ion energies as the target gas pressure was increased, then the presence of resonance charge exchange would be considered affirmed.

As the test was performed and the pressure was varied over the range from about  $5 \times 10^{-6}$  to  $5 \times 10^{-4}$  Torr, no evidence was found for the secondary charge changing collisions in the collision chamber.

The same type of test was employed to detect charge changing collisions in the collimator. If, for example, the  $\text{He}^+$  were neutralized in the

collimator, it would not reach the detector, of if it were converted to  $\text{He}^{++}$ , its energy would be about one-half that of the  $\text{He}^{++}$  ions which originated in the collision chamber. The neutralization of  $\text{He}^+$  would manifest itself in a reduction of peak height, and the change of  $\text{He}^+$  to  $\text{He}^{++}$  would cause the ion peak to be skewed.

The indicated test was performed by varying the pressure in the spectrometer (and therefore the collimator) by about a factor of 20 with no noticeable effect on the ion peaks.

The conclusions from this series of tests are as follows:

(1) a constant and equal fraction of the two helium ions formed in the target gas are repelled into the spectrometer by  $V_r \geq 300$  volts, and  $V_a$

adjusted to satisfy the condition that  $1/4 \leq \frac{V_r}{V_a} \leq 1/3$ ;

(2) maximum detector gain is obtained for about 350 volts interdynode potential;

(3) constant and near 100 percent detection efficiencies are obtained for both ions for postanalysis acceleration (acceleration into the detector) in excess of about 15 kilovolts, and

(4) no significant effect from charge changing collisions in either the collision chamber or the collimator is present in this experiment in the collision chamber pressure range  $5 \times 10^{-6}$  to  $5 \times 10^{-4}$  Torr.

#### Procedures for Relative Cross Section Measurements

Prior to any measurements, the collision chamber and spectrometer were evacuated to about  $5 \times 10^{-7}$  Torr. When this was attained, the Vacuum pump was turned off and its magnet was removed. Normally the chamber pressure would equilibrate around  $1.5 \times 10^{-6}$  Torr with only the two mer-

cury diffusion pumps operating.

The  $H^+$  beam would then be directed into the chamber and the beam detector. The current was measured directly on a Keithley (Model 410) pico-ammeter, the output of which was used to drive a Dymec (DY-2210) voltage-to-frequency converter, which in turn produced pulses at a rate proportional to the signal on the recorder output of the pico-ammeter. These pulses were counted on a 100 KC scaler. (Checks were made to assure that the output of the V-to-F converter was not sensitive to the high frequency modulations of the Van de Graaff beam.)

Next, the target gas was admitted to the chamber and the pressure was set at  $1 \times 10^{-4}$  Torr, as indicated on the ionization gauge. It was noted, in contrast to the total apparent cross section experiment, that in this work the operation of the ionization gauge did not affect the measurements. This was due to the gauge being mounted on one of the horizontal arms of the "cross" on the top of the chamber. In such a mounting configuration, it would be difficult for ions from the gauge to reach the collision region.

When the repeller field was used, its potential was normally set by means of batteries after the target gas was admitted into the chamber.

The next step was to tune the spectrometer and detector. The spectrometer voltage was furnished and adjusted to about 1000 volts by means of a Hamner (Model N-413, 0-5kV) high voltage and highly regulated supply. The magnet current was obtained from a Harrison (Model 6263A) 10 amp, 18 volt current supply. The postanalysis acceleration potential was adjusted to about 18 kV by means of a Sorensen (Model 5030-4) 30 kV supply. The interdynode potential was set at approximately 350 volts.

When the magnetic field was used to scan the charge-to-mass spectrum, it was found that the only observable peaks were at  $q/m = 1/4$  ( $\text{He}^+$ ), and  $1/2$  ( $\text{He}^{++}$ ). However, early in the testing stages of the apparatus, small peaks were observed that corresponded to heavier ions such as  $\text{H}_2\text{O}^+$  and  $\text{N}_2^+$ , but these diminished as the collision chamber vacuum improved.

With the preceding arrangement, the output pulses from the multiplier were passed through the preamplifier and amplifier and into the 100 mc scaler.

The procedure described thus far applies to both collection with and without the repeller field.

When the field-free collision arrangement was employed, the spectrometer was rotated about the collision region. It was expected that the more energetic recoil ions would have a rather distinct angular dependence. However, as the spectrometer was rotated from about  $92^\circ$  to within less than  $70^\circ$  of the beam direction, no angular dependence was observed—the ion count rate remained constant. It was then observed that the count rate slowly decreased with time. A series of tests indicated that this difficulty was associated with surface charging problems which were affecting the ion transmission. An attempt to clean the rhodium surfaces of the beam and spectrometer collimators with emery paper and acetone produced no noticeable effect.

It was suggested, on the belief that low energy electrons would be attracted to and neutralize any positively charged surface in the collision region, that this difficulty might be remedied by operating a filament in the chamber. Although this did not prove to be the case, some important information on the ion energies was obtained from that test.

The test was the following. A filament was suspended near the top of the collision chamber (about two inches from the collision region). When it was operated at about two microamperes emission, the ion count rate in the spectrometer decreased by a factor of about 100. This was believed to be due to recoil ions being attracted to the negative potential which was produced by the electron space charge around the filament. Next, a self-biasing resistor was installed in the filament circuit such that an emission of two microamperes raised the dc filament potential to about plus two volts. This procedure would also raise the potential of the space charge region. It was observed that in this arrangement the ion counting rate of the spectrometer did not change, which indicated that the space charge potential was not now sufficient to influence the ions.

The surprising conclusion drawn from this test is that virtually all of the ions created from the helium target by the proton beam had energies less than about two electron volts (perhaps considerably less). With ions of such low energy, the angular distribution could be substantially distorted by surface potentials in the millivolt range, but even so, it might have been supposed that some sort of distorted angular distribution would be observed. However, Everhart<sup>60</sup> recently pointed out that the effects of the thermal motion of the target atoms are sufficient to substantially broaden even a rather sharp angular distribution. Adapting the results of his analysis to the present energy range and collision pairs, indicates that the half-width of the peak (due to thermal motion alone) would be 10° to 20° or more for recoil angles around 90°. Therefore, from the observation in this investigation that the helium ion energies are very low ( $\ll 2$  eV) and from Everhart's analysis, it is not



surprising that no angular distribution was observed.

The conclusion, based on the preceding observations, is that a detectable angular distribution will be obtained in the total energy spectrum of a given ion only for those collision partners for which there is substantial energy transfer (at least several electron volts).

The Rutherford scattering expression<sup>61</sup> indicates that the energy transfer to the target is proportional to the square of the product of the atomic numbers of the collision partners. Therefore, in order to produce an appreciable energy transfer, a heavy projectile-target combination should be used.\* With this last observation, the search for an angular distribution for the recoil ions was discontinued for the  $H^+$  on He projectile-target combination.

The results of the preceding tests demonstrated that satisfactory results could be obtained with the repeller field for this particular collision combination. It should be noted that this conclusion is not valid for every projectile-target combination.<sup>46</sup> In fact, the attempts at field-free measurements were necessary in order to prove that a collection field could be efficiently employed for the total ion collection. With this conclusion, therefore, the repeller electrode was installed and used to obtain the cross sections for production by protons of  $He^+$  and  $He^{++}$  ions, irrespective of their recoil angles.

With the apparatus tuned as previously described, the spectrometer was set at an angle near  $90^\circ$  with respect to the beam direction. The ion

---

\* In confirmation of this conclusion, a very pronounced angular distribution has been obtained in this apparatus, at the time of this writing, by other investigators who used the relatively heavy neon on argon projectile-target combination.

count rate was measured as the spectrometer and the attached repeller electrode were rotated several degrees about this position. As expected for these low energy ions, there was no noticeable change in count rate over this angular range, and the spectrometer returned to the  $90^\circ$  position for the remainder of the measurements.

A check was made to assure that the counting rates of the electronics were linear over the wide range employed in this experiment. It was found that the ALD amplifier became nonlinear for a random pulse rate exceeding  $2 \times 10^4$  counts per second.

The  $\text{He}^+$  peak was first tuned in the spectrometer and both this count rate and the count rate produced by the V-to-F converter, which was proportional to the beam current, were accumulated simultaneously over several ten-second intervals, as set on the scaler-timers.

This procedure was repeated at each incident beam energy throughout the range of the experiment. It should be noted that the tuning of the spectrometer was not altered in an energy scan. This was done to more accurately determine the energy dependence of the cross sections. After one complete sweep of the energy range, the  $\text{He}^{++}$  peak was tuned and the measurement procedure was repeated.

At the conclusion of the above, the collision chamber was evacuated and the background contribution to the  $\text{He}^+$  and  $\text{He}^{++}$  peaks was evaluated. It was found that the background contribution to the  $\text{He}^+$  peak was about 0.02 percent and the contribution to the  $\text{He}^{++}$  was about 40 percent. This large contribution to the  $\text{He}^{++}$  peak was about thirty times the normal background noise level (including that of the  $\text{He}^+$  peak). From the measurements with the chamber filled with target gas, it was observed that

the  $\text{He}^+$  ions were about one hundred times more abundant than those of the  $\text{He}^{++}$ . On this basis, it was concluded that the 40 percent background contribution to the  $\text{He}^{++}$  peak was not  $\text{He}^{++}$ , but some other ion with a  $q/m = 1/2$ , such as  $\text{H}_2^+$ . It was concluded that a very probable source of such an ion was the  $\text{H}^+$  beam itself. It had been observed that when the beam was directed into the collision chamber, the indicated background pressure had a sustained increase of almost  $1 \times 10^{-6}$  Torr. This was believed to be due to the evolvment of deposited hydrogen from the detector, under beam impact conditions.

The He target gas pressure employed was about  $1 \times 10^{-4}$  Torr (uncorrected ionization gauge reading) and the observed  $\text{He}^{++}$ , as was mentioned was about a hundred times less intense than  $\text{He}^+$ . Therefore, if the  $\text{H}_2$  gas liberated from the beam detector had an ionization cross section comparable to that of helium (which it does),<sup>34</sup> then the presence and magnitude of the  $\text{H}_2^+$  background peak is explained. The  $\text{H}^+$  peak was not observed because it was about a factor of 50 less intense than that of  $\text{H}_2^+$  and, therefore, was not distinguishable from the noise. However, in the measurement procedure, the  $\text{H}_2^+$  peak was observed to determine its stability and energy dependence, then its contribution at each energy was subtracted from the  $\text{He}^{++}$  peak. In the above manner, the relative cross sections for the production of  $\text{He}^+$  and  $\text{He}^{++}$  were evaluated throughout the energy range from 0.15 to 1.00 MeV. That is, the present experimental results determined both the energy dependencies

$$_{10}\sigma_{j1}(\text{He}^+) \propto f_+(E) \quad (26)$$

and

$${}_{10}\sigma_{j2} (\text{He}^{++}) \propto f_{++}(E) \quad (27)$$

of the individual cross sections, as well as

$$\frac{{}_{10}\sigma_{j1} (\text{He}^+)}{{}_{10}\sigma_{j2} (\text{He}^{++})} = k(E) \quad (28)$$

where  $k(E)$  is a function of the beam energy.

#### Calculation of the Absolute Cross Sections

In order to determine the above cross sections absolutely, it is only necessary to determine either  ${}_{10}\sigma_{j1} (\text{He}^+)$  or  ${}_{10}\sigma_{j2} (\text{He}^{++})$  absolutely at one energy.

This procedure can be accomplished through use of a relation discussed in Chapter II. Namely, that the total apparent ionization cross section  $\sigma_i$  is the weighted sum of the individual cross sections, e.g.,

$$\sigma_i = {}_{10}\sigma_{j1} (\text{He}^+) + 2 {}_{10}\sigma_{j2} (\text{He}^{++}) \quad (29)$$

Substitution of Equation 28 into Equation 29 yields

$${}_{10}\sigma_{j2} (\text{He}^{++}) = \frac{\sigma_i}{2 + k(E)} \quad (30)$$

The one value chosen for  $\sigma_i$ , from which the absolute values of  ${}_{10}\sigma_{j1} (\text{He}^+)$  and  ${}_{10}\sigma_{j2} (\text{He}^{++})$  may be determined at any energy, is that mea-

sured in this laboratory at an energy of 1.00 MeV by Hooper.<sup>34</sup> This energy was chosen because the charge exchange cross section is negligible, and the total apparent ion production cross section  $\sigma_+$  measured by Hooper should be simply the total apparent ionization cross section  $\sigma_i$ .

The normalization procedure for obtaining the absolute cross sections was performed and the results are presented in Chapter VIII.

## CHAPTER VIII

## EXPERIMENTAL RESULTS FOR PARTIAL IONIZATION CROSS SECTIONS

Present Results and Comparison with Other Experimental Data

The absolute cross sections for the production of  $\text{He}^+$  and  $\text{He}^{++}$  ions by  $\text{H}^+$  and electrons are shown in Table 6 and Figure 50. The solid triangles represent the present results over the proton energy range from 0.15 to 1.00 MeV. One point which was previously discussed should now be reemphasized and that is that only one energy point (1 MeV) was used to normalize the relative cross sections in order to obtain these absolute values. Both the absolute separation and slopes of these two cross sections are characteristic of the present data only and in no way reflect the normalization procedure.

The present data give an excellent fit to a straight line on a log-log plot throughout the energy range investigated. The data, therefore, correspond to an expression of the form

$$\sigma = A E^{-c} \quad (31)$$

where  $E$  represents the proton energy. These two cross sections can then be represented as

$${}_{10}\sigma_{j1}(\text{He}^+) = 2.07 E^{-0.75} \times 10^{-17} \text{ cm}^2/\text{atom} \quad (32)$$

Table 6. Cross Sections for Production of  $\text{He}^+$  and  $\text{He}^{++}$  Ions  
in Helium Gas by Incident Protons

Proton Energy (keV)	Measured Relative Cross Section $\frac{10\sigma_{j1}}{10\sigma_{j2}}$	Calculated Absolute Cross Sections ( $10^{-18}$ cm <sup>2</sup> /atom)	
		$10\sigma_{j1}$	$10\sigma_{j2}$
150	90.7	88.0	0.970
200	106	71.8	0.678
300	143	51.0	0.356
400	177	42.9	0.242
500	199	35.0	0.176
600	215	31.4	0.146
700	239	27.3	0.114
800	254	24.8	0.0977
900	274	22.7	0.0828
1000	283	20.7	0.0732

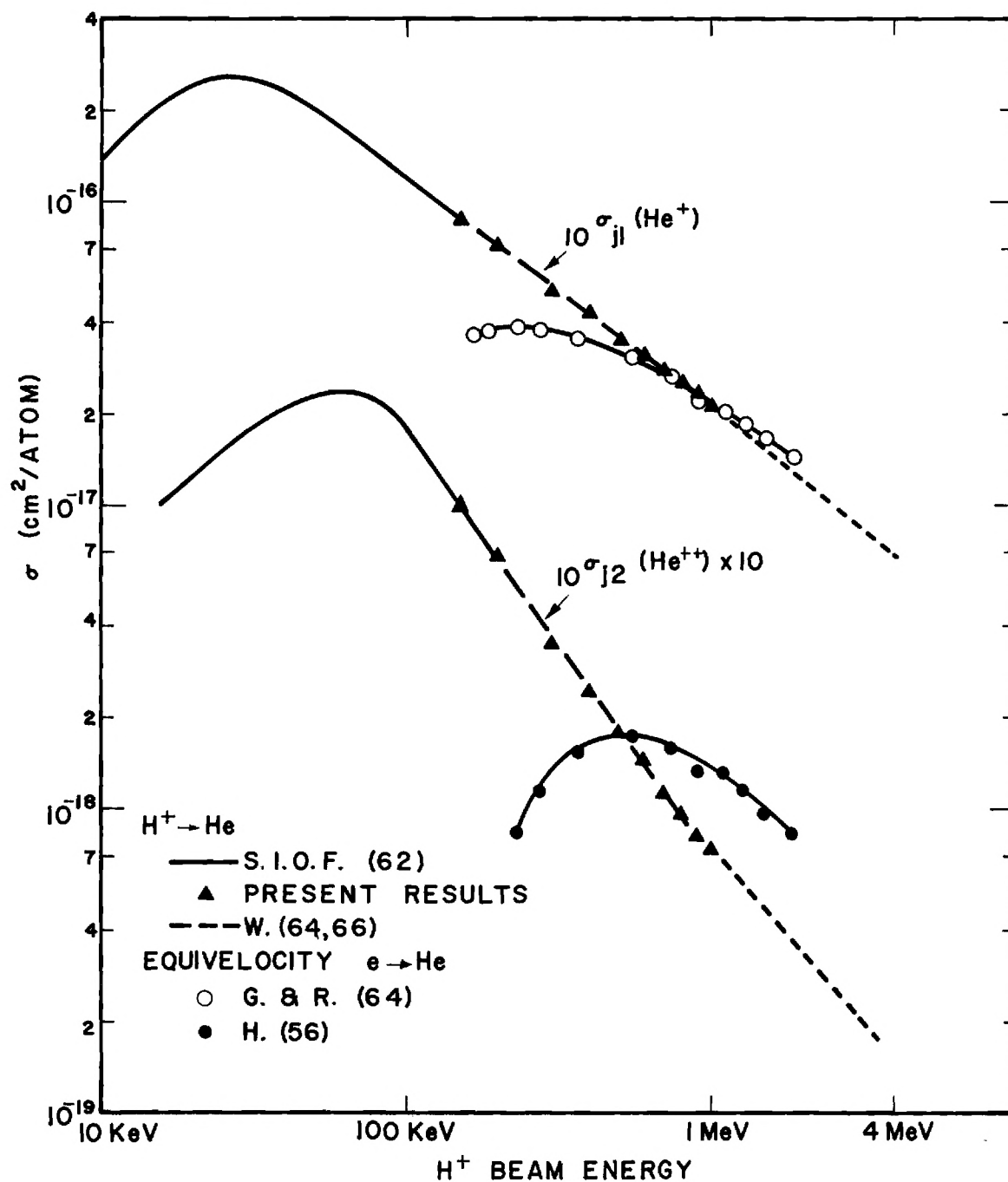


Figure 50. Partial Cross Sections for Production of  $\text{He}^+$  and  $\text{He}^{++}$  Ions by Incident Protons. Key to the Results of Other Investigators: S.I.O.F.(62), Solov'ev, et al., (Reference 8); W.(64, 66), Wexler (Reference 9); G. & R.(64), Golden, et al., (Reference 62); H.(56), Harrison, (Reference 63).



$${}_{10}\sigma_{j2} (\text{He}^{++}) = 0.71 E^{-1.37} \times 10^{-19} \text{ cm}^2/\text{atom} \quad (33)$$

Shown for comparison with the present results are the proton data of Solov'ev, et al.<sup>8</sup> below 180 keV and that of Wexler<sup>9</sup> above 0.80 MeV. It is seen that excellent agreement is obtained with the overlapping measurements below 180 keV; in fact, the data are essentially the same. For comparison with the data above 0.80 MeV, it should be noted that Wexler also measured only relative cross sections and normalized these to the same  $\sigma_i$  measurements of Hooper<sup>34</sup> that were used in the present experiment. One can regard this as normalization of only the  ${}_{10}\sigma_{j1} (\text{He}^+)$  cross section, because at 1 MeV energy the  ${}_{10}\sigma_{j2} (\text{He}^{++})$  is only 0.35 percent of the  ${}_{10}\sigma_{j1} (\text{He}^+)$  cross section. Therefore, the present  $\text{He}^+$  measurements and those of Wexler are in forced agreement at the 1 MeV energy point. Consequently, the only comparison to be made between the two measurements of the  ${}_{10}\sigma_{j1} (\text{He}^+)$  cross section is in the energy dependence, which Wexler observed to be slightly steeper (about  $E^{-0.82}$ ) than the present value of  $E^{-0.75}$ .

The comparison between the present results for  $\text{He}^{++}$  and those of Wexler does not reflect the normalization procedure, and their absolute agreement is significant. Here also the energy dependencies are slightly different: Wexler's results demonstrate an  $E^{-1.2}$  dependence as compared with the present value of  $E^{-1.4}$ .

One very significant point should be made regarding the experimental apparatuses used by Solov'ev and Wexler. Both of these investigators used electrometers to measure their ion currents and certainly there was

no ion discrimination involved, in possible contrast to the electron multiplier detector employed in the present experiment. Even though tests had indicated that the electron multiplier was also being operated without ion discrimination, it was very gratifying to receive apparent verification of this fact in the form of excellent agreement on the measured cross section values among these several laboratories.

Also shown for comparison purposes are the cross sections for production of these two helium ions by electrons that are of the same velocity as the protons. If one recalls the discussion of the Bethe-Born approximation of Chapter V, it was pointed out that so far as simple ionization events by point charge projectiles were concerned, the cross section depended only on the charge and velocity of the projectile. Therefore, the simple ionization cross sections should be equal for equivelocity protons and electrons. It is seen in Figure 50 that this prediction is fulfilled for  $10\sigma_{j1}(\text{He}^+)$  at proton energies above about 1 MeV. However, for the more violent collisions that produce  $\text{He}^{++}$ , there is a substantial difference in the electron and proton cross sections even for the highest energies shown. This discrepancy is believed significant because there is considerable agreement ( $\pm 5$  percent) on these electron cross sections by other investigators,<sup>64,65,66</sup> and those that disagree<sup>67</sup> are usually higher and, consequently, in worse agreement with the proton results.

A recent literature search failed to reveal any quantum mechanical calculations pertaining to collisions of this nature, and a "classical" Gryzinski-type<sup>68</sup> calculation produced results in poor agreement with the present results, both in absolute magnitude and energy dependence. Speci-

fically, the calculated proton cross sections at 1 MeV are more than a factor of two greater than the experimental values, and the two results are diverging with increasing energy in this range.

At the conclusion of the preceding experiment, the Van de Graaff accelerator was not scheduled to be used for two days. Consequently, this time period was used to make some preliminary measurements on the partial cross sections for the production of argon ions by impact with fast electrons. The cross sections for the first six argon ions were measured. However, only the cross sections for the first four ions were considered reliable ( $\pm 50$  percent), simply because insufficient time was available to thoroughly test and tune the apparatus for this ion species.

The argon results are presented in Table 7 and Figure 51. The same type of comparison cross sections as in the previous figure are shown with the argon results. The data of Solov'ev, et al.<sup>8</sup> are presented for energies up to 180 keV and those of Wexler<sup>9</sup> for energies above 0.80 MeV.

It should be noted that the results of both these investigators agree rather well with the present results with the exception of  $10\sigma_{j3}$  ( $\text{Ar}^{3+}$ ) by Solov'ev. It is seen that this cross section is about a factor of eight greater than the value predicted by extrapolating Wexler's  $10\sigma_{j3}$  ( $\text{Ar}^{3+}$ ) curve to this energy and about a factor of ten less than the value indicated by the present measurements. The extent of this disagreement is clearly outside of the  $\pm 15$  percent error of Solov'ev and the  $\pm 20$  percent quoted by Wexler.

Also shown for comparison are the cross sections for production of these argon ions by equivelocity electrons. These electron results are in substantially better agreement with the proton cross sections in argon than

Table 7. Preliminary Cross Sections for Production  
of  $\text{Ar}^{n+}$ ,  $n = 1, 2, 3$ , and 4 in Argon Gas by  
Incident Protons

Proton Energy (keV)	Absolute Cross Sections ( $10^{-17} \text{ cm}^2/\text{atom}$ )			
	$10^{\sigma_{j1}}$	$10^{\sigma_{j2}}$	$10^{\sigma_{j3}}$	$10^{\sigma_{j4}}$
180	37	4.6	1.2	0.11
400	30	2.1	0.56	0.09
600	19	1.1	0.30	0.08

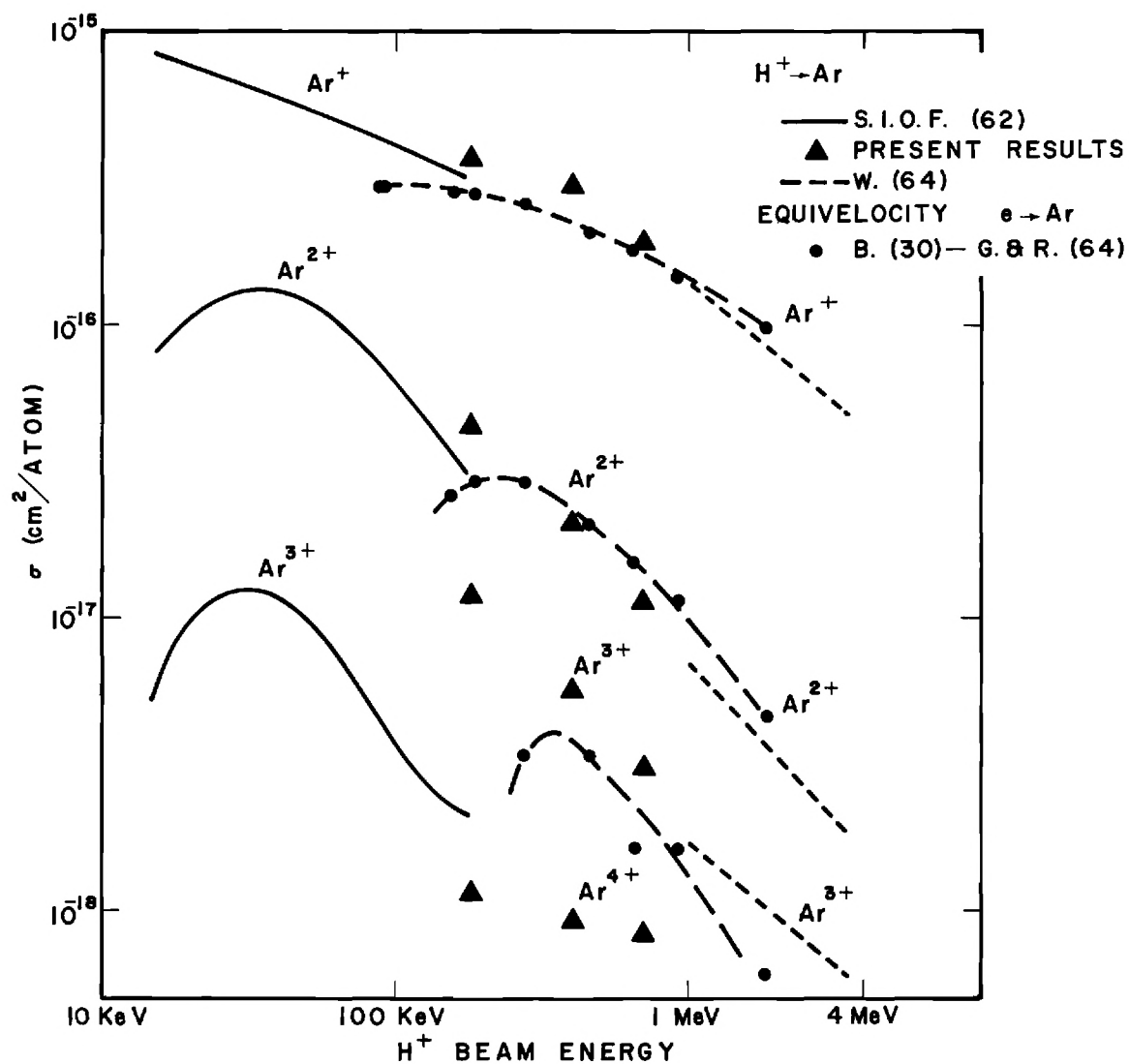


Figure 51. Partial Cross Sections for Production of  $\text{Ar}^{n+}$  ( $n = 1, 2, 3$ , and 4) by Incident Protons. Key to the Results of Other Investigators: S.I.O.F.(62), Solov'ev, et al., (Reference 8); W.(64), Wexler (Reference 9); B.(30), Bleakney (Reference 69) - Normalized to G. & R. (64), Golden, et al., (Reference 62).

they were in helium. Perhaps this indicates that the Born approximation is satisfied at a lower energy for heavy targets, such as argon, than for the light helium targets.

#### Discussion of Errors

In this experiment the assignment of error limits is simplified because only relative cross sections were measured. The only significant source of error is in the relative collection and detection efficiencies of the two helium ions, and it was the purpose of the series of tests in the beginning of the previous chapter to assure that these efficiencies were equal. Because most of the possible sources of systematic relative errors lie in the evaluation of these tests, the final assignment of error limits is necessarily somewhat subjective.

It is the judgment of the author that the maximum error in the relative magnitudes of these two helium cross sections is not more than  $\pm 10$  percent, and the error is probably not more than  $\pm 4$  percent.

In order to assign error limits to the absolute cross sections, it is necessary to include the  $\pm 6$  percent (probable) error in the  $\sigma_1$  measurement of Hooper used for normalization. It should be noted that no consideration was given to the Gaede effect (Appendix III) in the error assigned to  $\sigma_1$ , and for helium this is believed to cause a zero to  $+ 3$  percent error. Thus, it is estimated that the probable error in the absolute cross sections for production of  $\text{He}^+$  and  $\text{He}^{++}$  is less than  $+ 13$  to  $- 10$  percent, most of which is due to the normalization procedure.

### Conclusions

The experimental results of this investigation demonstrated that the helium ions produced in helium gas, by the passage of a beam of protons in the energy range from 0.15 - 1.00 MeV, were of energies considerably less than two electron volts. The effects of thermal motion of the target molecules and the very small stray fields in the collision region were sufficient to cause the angular distribution of the low energy recoil ions to appear to be isotropic. It was concluded that these low energy helium ions were collected with equal efficiencies by the repeller field.

The results of the evaluation tests and cross section measurements indicated that the electron multiplier was operated without ion discrimination and with nearly 100 percent detection efficiency.

The results for the cross sections for production of the two helium ions by protons were in excellent agreement with those of other investigators. However, the comparison cross sections for  $\text{He}^{++}$  production by electron impact, scaled according to the Born approximation, failed to produce agreement with the proton results within the combined experimental errors. The extent of this disagreement suggests a deficiency in the application of the Born approximation to the case of double ionization of helium by protons and electrons. Although there are serious discrepancies among the results for the production of variously charged argon ions by fast protons, it appears that the scaled electron cross sections are generally in better agreement than was observed for the case of the helium target.

## APPENDICES



## APPENDIX I

## DETERMINATION OF THE NEUTRAL BEAM INTENSITY

The neutral beam detector, described in Chapter IV, is an assembly which totally traps the beam and has three functions, i.e., provisions to make the following three observations: (1) net current of the beam  $I_i$ ; (2) secondary emission current from the beam target foil  $I'_i$ ; (3) total power of the beam  $P$ , through observation of the temperature rise of the target foil by means of a thermocouple.

The calibration scheme depends on calibration of the beam power  $P$  in terms of the net current  $I_i$ , using a single charged ion beam, whose intensity is directly measurable absolutely by function (1), and applying this calibration to the neutral beam. The secondary emission current  $I'_i$  can then be calibrated for the neutral beam in terms of the beam power  $P$ , so that either  $I'_i$  or  $P$  can be used for measurement of the neutral beam intensity, as is convenient.

The only critical assumption is that the beams of neutral and charged particles deposit equal amounts of energy in the target foil. This assumption was verified by the direct measurements of Mahadevan,<sup>70</sup> in which he found, for heavier projectiles such as Ne at energies above about 2 keV, that ions and atoms deposited equal amounts of energy into the metallic surface. Evidence was also presented that the equality of energy deposition was reached at lower energies for lighter projectiles. Therefore, the assumption that essentially the full power of both the

ionic and atomic beams is deposited thermally in the foil, for the energy range under investigation, is clearly justified. To further substantiate this assumption, it has been shown for the  $H^+$  and  $He^+$  ion beams that the thermocouple emf is directly proportional to the beam power, independent of the beam energy, throughout the range of beam energy and intensity utilized in this experiment. Figure 52 shows the relationship of the thermocouple emf to beam power in the case of the  $He^+$  projectile at two different energies.

Because of the beam fluctuations, it was essential that the calibration of any one function in terms of another be accomplished by simultaneous observations of both functions. With the physical arrangements employed, it was possible to observe  $I_i$  and  $I'_i$  simultaneously and to observe  $I'_i$  and  $P$  simultaneously, but unfortunately it was not possible to observe  $I_i$  and  $P$  simultaneously. A simultaneous observation of  $I_i$  and  $P$  would have required that the nano-voltmeter be "floated" off ground as part of the input circuit of the electrometer which measured the total net current. This arrangement was unsuitable because the resultant pickup, stray currents, and capacitance thus introduced into the electrometer input circuit rendered its readings quite meaningless. Similarly, a switching arrangement to switch rapidly from one connection scheme to another, so as to eliminate an intermediate calibration step in terms of the secondary emission current  $I'_i$ , proved to be unworkable for essentially the same reasons. Therefore, a slightly more indirect procedure than that indicated above was required. The detector was first connected to observe  $I_i$  and  $I'_i$ , and  $I'_i$  was calibrated in terms of  $I_i$  for the ion beam at a given energy. The connections were then changed to observe  $I'_i$  and  $P$ , and  $P$  was calibrated in terms of

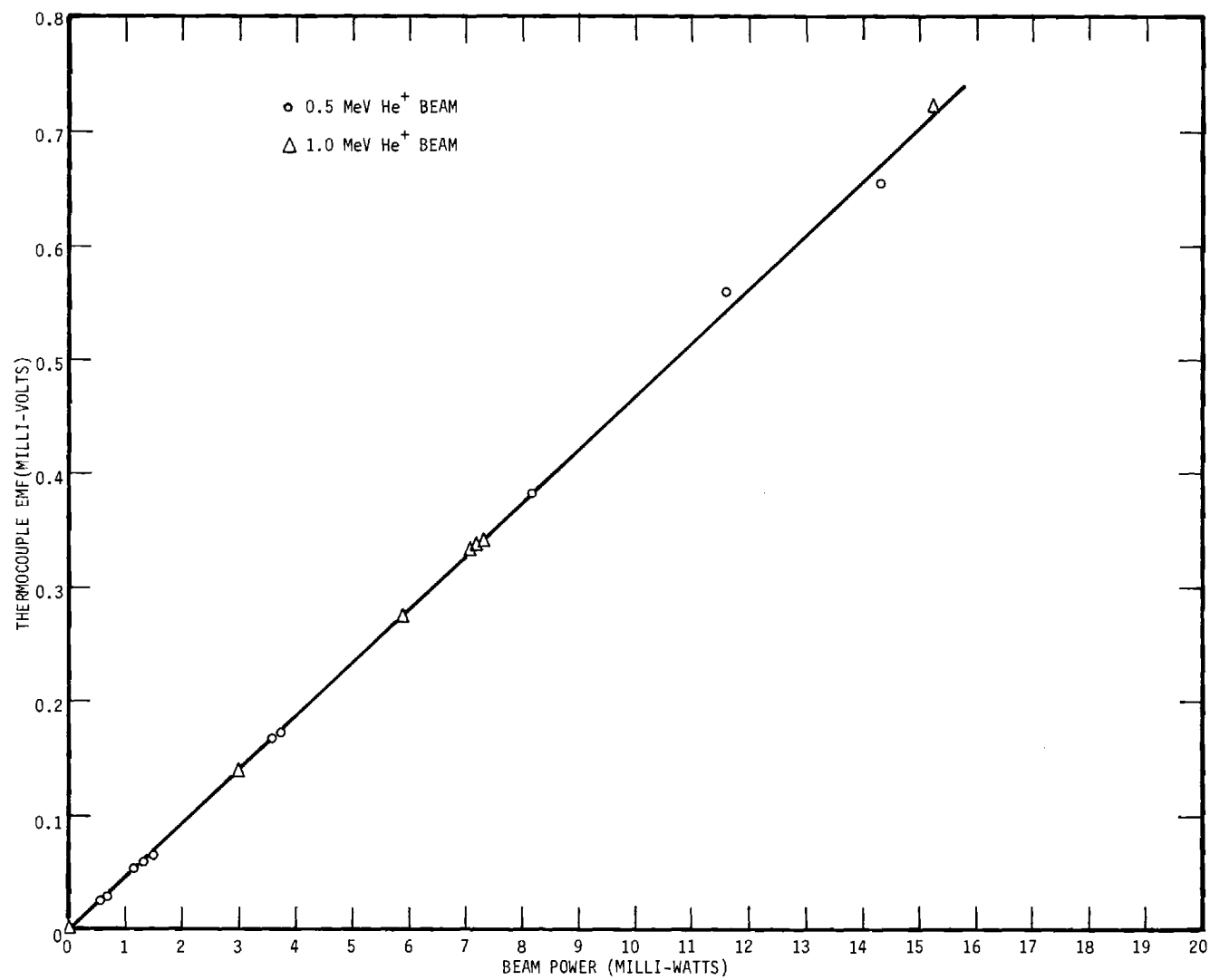


Figure 52. Response of the Thermocouple of the Neutral Particle Detector to the Impinging Beam.

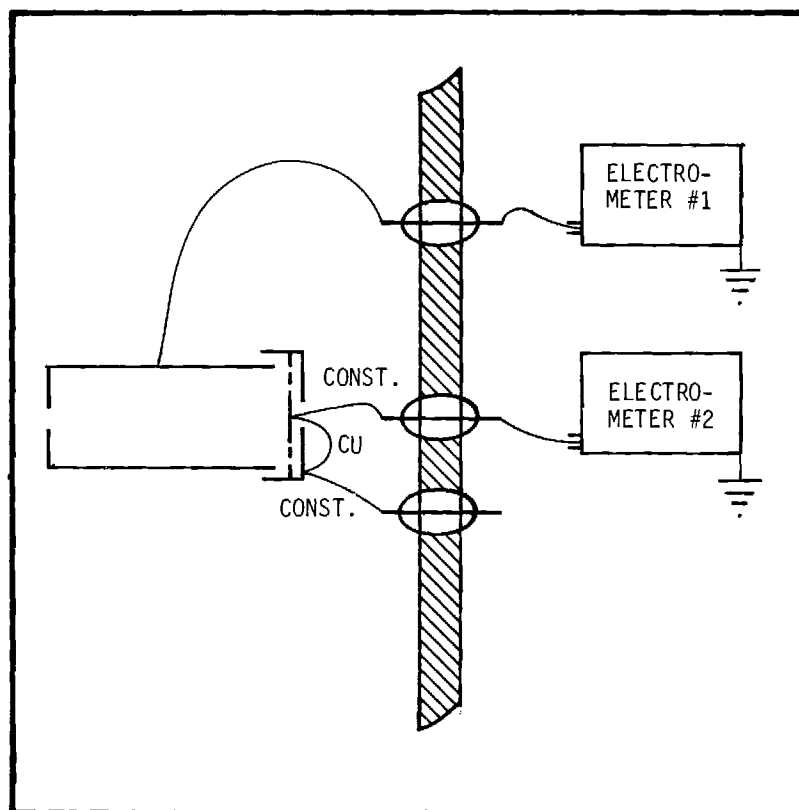
$I'_i$ , again using the same ion beam. This procedure was repeated at several energies throughout the energy range, to verify that, even though the calibration of  $I'_i$  was energy dependent, that of  $P$  was not. (The calibration of  $I'_i$  was also time dependent as the surface condition of the foil changed, but it was verified that the calibration of  $P$  was stable within about ten percent over periods of many weeks operation. However, the calibration of  $P$  was performed daily.) The established calibration of  $P$  was then assumed applicable to the neutral beam, as previously explained.

On the rather rare occasions when it was desired to use the secondary emission function for measurement of the neutral beam, its calibration was checked several times per day and separately at each value of the beam energy against the established calibration of the beam power. Note that no assumptions are made about the relative calibration of  $I'_i$  for ions vs. atoms, or about the energy dependence of the calibration.

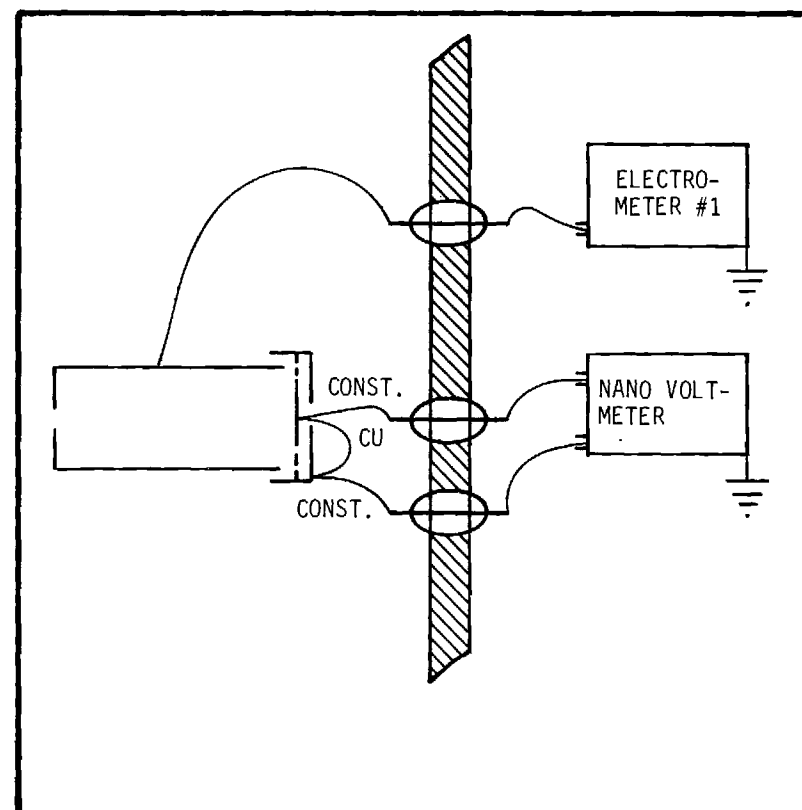
Figure 53a is a block diagram of the electrical connections for the simultaneous observation of  $I_i$  and  $I'_i$ , using two Keithley (Model 410) electrometers.

The reading of electrometer number 1 was the secondary emission current  $I'_i$  and that of electrometer number 2 was the net beam current plus the secondary emission current,  $I_i + I'_i$ .  $I_i$  and  $I'_i$  were always of the same order of magnitude. For  $H^+$  beams,  $I_i$  was about half  $I'_i$ , and for  $He^+$  beams,  $I_i$  was about one-quarter  $I'_i$ . Therefore,  $I'_i$  was never a small difference between two nearly equal readings. In this manner,  $I'_i$  was calibrated in terms of  $I_i$  as

$$I'_i = \gamma I_i \quad (34)$$



(a)



(b)

Figure 53. Schematic Diagram of Electrical Connections Employed in the Calibration of the Neutral Beam Detector.

where  $\gamma$ , the constant of proportionality, is the effective secondary emission coefficient for the singly charged ion beam on this copper foil at this given energy.

Figure 53b is a diagram of the electrical connections for simultaneous observation of  $I'_1$  and P, using electrometer number 1 and a Keithley (Model 149) nano-voltmeter for observation of the thermocouple emf. These observations yield the relation between the secondary emission current, which will be designated as  $I''_1$  (because it may be different in magnitude from the former  $I'_1$ ) and the emf  $\epsilon_1$  at a single energy value,

$$I''_1 \propto \epsilon_1 \quad (35)$$

which in itself is not very useful. Figure 52 demonstrated that the emf  $\epsilon_1$  was proportional to the beam power, which is a product of the beam current and the accelerator voltage  $I_1 V$ . Therefore, to derive some useful information from this set of observations, they should all be combined to produce a relationship between the beam power and the emf. This objective can be accomplished by use of Equation 34 and the accelerator voltage to relate Equation 35 to the total beam power  $I_1 V$  as

$$V \left( \frac{I''_1}{\gamma} \right) \propto \epsilon_1 \quad (36)$$

which is valid for all energies and currents used in this experiment. It should be noted that the  $I'_1$  contained in the expression for  $\gamma$  cannot be

cancelled with the  $I_i''$ , because even though they represent the same type of current, they were measured at different times and may, therefore, be unequal in magnitude.

A more useful form of Equation 36 for the measurement of the neutral beam is

$$\frac{E_i I_i''}{e\gamma} \propto \epsilon_i \quad (37)$$

in which  $E_i$  is the energy of the singly charged ion beam and  $e$  is the charge of an electron.

Finally, to determine the "particle current" of the neutral beam (the number of atoms per second  $N_a$  striking the foil target) it was only necessary to make two measurements and to use Equation 37. The measured quantities were the emf  $\epsilon_a$  generated in the thermocouple by the atomic beam, and the energy  $E_a$  of the atomic beam. With this information, one can write

$$\frac{N_a E_a}{\left[ \frac{I_i'' E_i}{e\gamma} \right]} = \frac{\epsilon_a}{\epsilon_i} \quad (38)$$

and

$$N_a = \frac{\epsilon_a}{E_a} \left[ \frac{E_i I_i''}{\epsilon_i \gamma e} \right] \text{const.} \quad (39)$$

Thus  $N_a$  (atoms/sec) is expressed in terms of measurable quantities and the electron charge  $e$ . This expression was written in terms of the energy  $E_i$

and charge  $e$  rather than simply the accelerator voltage  $V$  because, when substituted into the cross section expressions, the charge  $e$  cancels.

The bracketed term is a constant in Equation 39 and, like the  $I'_i$  in Equation 36, the energies  $E$  should not be cancelled. As such, Equation 39 is valid over the entire energy range of this experiment, even though the calibration was performed at only one energy  $E_i$ .



## APPENDIX II

## DETERMINATION OF APPARENT CROSS SECTIONS

## FROM EXPERIMENTAL OBSERVABLES

In this section expressions for the apparent cross sections  $\sigma_-$  and  $\sigma_+$ , the total cross section for the production of negative and positive charges, respectively, will be developed in terms of experimental observables.

Consider a parallel, monoenergetic beam of  $N_p$  projectiles per second to be directed through a chamber filled with the target gas of density  $m$ . The number of free electrons per second  $N_-$  produced along a length  $L$  of the beam path by the passage of the beam may be expressed as

$$N_- = mL N_p \sigma_- \quad (40)$$

where  $\sigma_-$  is the effective cross sectional area of the target molecule for the production of electrons. Specifically,  $\sigma_-$  is the cross section for production of one electron plus twice the cross section for production of two electrons plus three times the cross section for production of three electrons, etc. Thus  $\sigma_-$  is referred to as the apparent cross section for electron production. It is assumed that the number density  $m$  is sufficiently low such that no target molecule is shielded by another, and that no projectile undergoes more than one collision.

The application by means of parallel plate electrodes of a sufficiently strong transverse electric field to this collision region will result in the collection of all the free electrons on one electrode and all of the slow positive ions on the other. This collection of  $N_-$  electrons per second produced a current

$$I_- = eN_- \quad (41)$$

where  $e$  is the charge of an electron.

Simultaneously, the ionizing beam was collected and measured. In this part of the experiment the projectiles used were  $\text{He}^{++}$ ,  $\text{He}^0$ , and  $\text{H}^0$ . For the charged projectile,  $\text{He}^{++}$ , the measurement consisted of stopping the beam in a deep Faraday cup which produced a current  $I_p$ , where

$$I_p = 2eN_p \quad (42)$$

For the atomic projectiles  $\text{He}^0$  and  $\text{H}^0$ , the "neutral current"

$$I_n = eN_p \quad (43)$$

was determined as described in Equation 39 of Appendix I.

Thus we have expressions that permit the evaluation of  $N_p$  for both ionic and atomic beams. These are Equations 42 and 43, respectively. Substitution of Equations 41 and 42 into 40 yields

$$[\sigma_-]_{\text{He}^{++}} = \frac{2}{mL} \frac{I_-}{I_p} \quad (44)$$

In order to obtain the corresponding equation for the atomic beams, substitute Equation 41 and 43 into 40. One obtains

$$[\sigma_-]_{\text{He}^0, \text{H}^0} = \frac{1}{mL} \frac{I_-}{I_n} \quad (45)$$

A similar analysis applied to the measurement of the slow positive ions leads to the following results:

for  $\text{He}^{++}$  projectiles

$$[\sigma_+]_{\text{He}^{++}} = \frac{2}{mL} \frac{I_+}{I_p} \quad (46)$$

and

for  $\text{He}^0, \text{H}^0$  projectiles

$$[\sigma_+]_{\text{He}^0, \text{H}^0} = \frac{1}{mL} \frac{I_+}{I_n} \quad (47)$$

Thus the apparent cross sections for production of electrons  $\sigma_-$  and positive ions  $\sigma_+$  are presented in terms of measurable quantities. The composition of these cross sections is investigated in detail in Chapter II.

## APPENDIX III

THE USE OF A McLEOD MANOMETER TO MEASURE  
GAS PRESSURES BETWEEN  $10^{-2}$  AND  $10^{-5}$  TORRIntroduction

The classical instrument that has stood, since its invention in 1874, as the absolute standard of pressure measurement for gas pressure in the range from 1 to  $10^{-6}$  Torr, is the McLeod manometer.

The accuracy of this instrument was almost unchallenged until a few years ago when investigations uncovered several systematic errors associated with its customary mode of operation. To date, it appears that the evaluation of these errors is still unsure. This is evidenced by the fact that the National Bureau of Standards has not been willing for some time to calibrate any vacuum gauges below about one Torr. However, even with the knowledge of the existence of these errors, it was felt, at the beginning of this work, that the McLeod gauge was still the best calibration standard available, although at present it seems that more investigators are turning to the recently developed capacitance manometer for an absolute pressure standard. However, since the McLeod gauge was used as the primary standard of the present work, the following discussion will be limited to this instrument. The operating principle, the major associated errors, the gauge preparation, and the actual method of operation will be described.

### Operating Principle of the McLeod Gauge

Basically this is an instrument that isolates a rather large volume of gas at the pressure to be measured and compresses it through a large and known volume ratio by means of a rising column of mercury that acts as a piston. As the gas is compressed, it exerts a downward force on the mercury column. At a suitable compression, the height of this mercury column is compared with that of a like column which has not compressed any gas. This offset in mercury columns along with the compression ratio yields the desired pressure.

In this investigation, a Model GM-110 McLeod gauge manufactured by Consolidated Vacuum Corporation was used as the primary standard. This gauge was originally equipped with 0.535 mm diameter capillaries by the manufacturer. As will be discussed later under the heading "Systematic Errors," these capillaries were found to be unsatisfactory and were replaced by 1.00 mm diameter capillaries.

In order to obtain the "McLeod gauge equation," one may start with the assumption that Boyle's law will apply to this situation. Thus

$$P_i V_i = P_f V_f \quad (48)$$

where  $P_i$  and  $V_i$  are the pressure of the gas and volume of the gauge, respectively, before the gas is compressed.  $P_f$  and  $V_f$  denote those same quantities after the compression. The quantity of interest is, of course,  $P_i$  the initial gas pressure.

$V_i$  for this gauge is 2185 cm<sup>3</sup>

$$V_f = \frac{\pi d^2}{4} H$$

where  $d = 1.00$  mm is the compression capillary diameter and  $H$  is shown on Figure 54;  $P_f \equiv \Delta h$  is also shown in Figure 54. With this information then, Equation 48 becomes the "McLeod gauge equation"

$$P_i = \frac{\frac{\pi d^2}{4} H \Delta h}{V_i} \quad (49)$$

$$= 3.906 \times 10^{-7} H \Delta h$$

for this gauge. Here,  $P_i$  is in Torr when  $H$  and  $\Delta h$  are expressed in mm. For future reference, this pressure will be denoted simply as  $P$ .

The conventional method of operating the McLeod gauge is to run the mercury up in the capillaries until  $H = \Delta h$ , this simplifies the reading procedure. However, as will be discussed later under the heading of "Systematic Errors," a more reliable determination of pressure is usually possible when a series of different compressions of the sample gas is made. This is accomplished by raising the mercury in the capillaries to several different heights and measuring  $H$  and  $\Delta h$  at each position. A position in the vicinity of  $\Delta h = H$  is usually included in these measurements. This procedure is referred to here as the "multiple - compression - mode" of operating a McLeod gauge.

#### Systematic Errors

The chief systematic errors inherent in even a well constructed

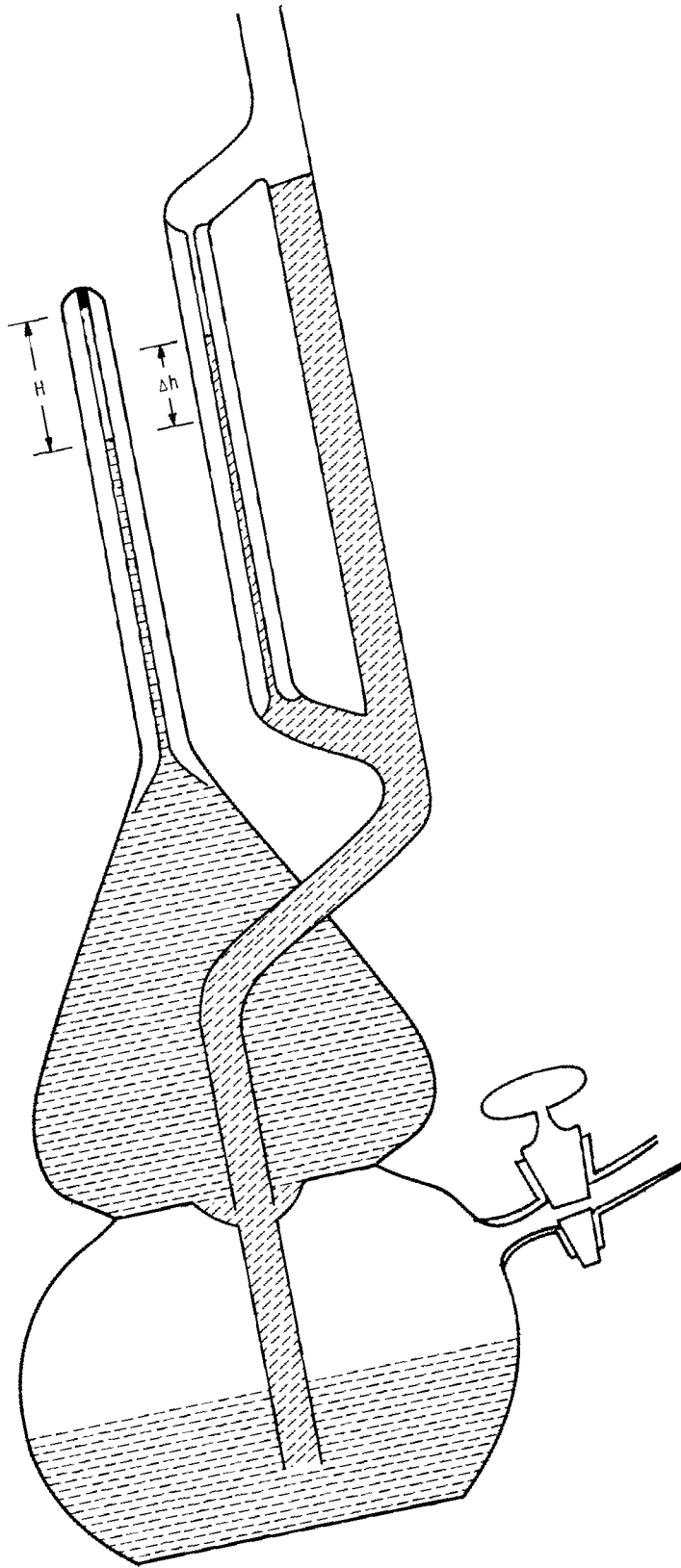


Figure 54. McLeod Gauge.

McLeod gauge are the result of:

- (1) departures from Boyle's law;
- (2) nonuniform capillary depression; and
- (3) the presence of a cold trap in the tabulation between the

manometer and the system whose pressure is to be measured.

Each of these effects will now be examined with the purpose in mind of either eliminating or correcting for them.

#### 1. Departures from Boyle's Law

The McLeod gauge equation presumes that the gas obeys Boyle's law; the behavior of a real gas at low pressure is more closely approximated by Van der Waal's equation, which takes account of the finite size of the molecules and certain of the forces between them. The relative error introduced by assuming that the gas obeys Boyle's law has been computed by Jansen and Venema.<sup>71</sup> They found this error for all the gases used in this work to be less than 0.1 percent for pressures up to 400 Torr in the compression capillary. In the present research, the pressure in the closed capillary did not exceed about 50 Torr; therefore, this error may be neglected.

There is a further reason that use of Boyle's law may not accurately describe the gas sample in the manometer. During the pressure measurement cycle, this gas may be partially adsorbed and desorbed on the walls of the gauge.

An especially alarming consideration is the following. If a monolayer of gas adsorbed on the spherical bulb of a McLeod gauge, one liter in volume should rapidly desorb, the pressure in the gauge would increase by  $10^{-2}$  Torr. Therefore, for less than one percent error at  $10^{-4}$  Torr,



the number of molecules adsorbed must be stable to  $10^{-4}$  of a monolayer.<sup>72</sup>

Thus this sorption effect appears to be a potential source of a large error.

Kreisman<sup>73</sup> has performed three separate tests in an attempt to detect this sorption effect. The following description of these tests was taken from his own report.

Another possible source . . . [of error] . . . is temporary adsorption of the gas during its compression into the fine-bore, closed-end capillary. However, tests made with gases having different adsorption properties showed no noticeable effects.

A direct experimental search for adsorption effects in the McLeod gauges is made in the following way: with a fixed amount of gas in the closed McLeod gauge system, a measurement is made with both gauges simultaneously and the pressures recorded. Next, the top of the closed capillary of one of the gauges is cooled with dry ice or liquid nitrogen. If there are gas molecules adsorbed on the capillary wall, cooling the wall will decrease their tendency to desorb. When the mercury is removed from the gauges, a lower system pressure should be obtained due to the molecules remaining on the capillary wall. If the gas pressure is again measured with the uncooled gauge, the lower pressure should be evident. The experiment was carried out with the lower pressure gauge being cooled and showed no indication of the adsorption.

Adsorption of gas by the walls of the McLeod gauge compression bulb can be measured in the following way: After a pressure measurement has been made with the gauge, the gas compressed into the top of the closed-end capillary is trapped there by freezing some of the mercury in the capillary. The remainder of the mercury is lowered to a point just above the bulb cutoff level. Any gas adsorbed by the compression bulb walls should desorb at the lower pressure obtained. If the mercury is now raised in the bulb, any desorbed gas will be trapped between the rising mercury and that frozen in the capillary tube. The volume and pressure of the desorbed gas can be measured and the amount of desorbed gas can be determined. This experiment, carried out with nitrogen under conditions that were not ideal, indicated that the amount of nitrogen desorbed by the large compression bulb of the low pressure McLeod gauge was less than one percent of the total gas originally admitted to the gauge.

The somewhat surprising conclusion from Kriesman's work is that these sorption effects are not important in a "clean" high vacuum McLeod

gauge.

It appears then that we are justified in using the ideal gas law to derive the McLeod gauge equation, given here as Equation 49.

## 2. Nonuniform Capillary Depression

Of the three chief sources of error previously listed, it is the capillary depression error that the investigator is most likely to notice. In fact, in the beginning of the present experiment this was the cause of some very obvious and intolerable errors.

Capillary depression is caused by the forces of interaction between the mercury and glass wall of the capillary. The normal mercury depression as calculated for clean glass capillaries of 1.0 mm diameter is 11 mm. This is quite appreciable compared to the mercury depression produced by the compressed gas in the closed capillary, which is about 22 mm for a typical initial pressure of  $2 \times 10^{-4}$  Torr. It is reasonable to expect then that additional interaction of the mercury with the forces due to local impurities on the glass capillaries might radically alter the normal capillary depression and, because this is such a large portion of the total depression, it would result in a substantial error in the pressure determination.

The test employed in this work to detect nonuniform capillary depression is as follows. The gauge was evacuated to about  $5 \times 10^{-7}$  Torr and the mercury was raised in the capillaries and the 8.0 mm diameter side arm. At this low pressure  $\Delta h$  should be essentially zero except in the last three or four centimeters of compression. This left more than 15 cm of capillary over which the mercury in both capillaries should be the same height. In this region then the mercury was raised in intervals of

a centimeter or less and was allowed to rest at each position until the level ceased to change, which usually required several minutes. At each position the level of the mercury in both capillaries and the side arm was measured. In this test a Gaertner (M 911) cathetometer was used to measure the menisci positions. The smallest reading on its vernier was 0.05 mm. It could be expected that the mercury in the relatively large side arm would be the least sensitive to wall effects. For this reason, it was used as the reference against which the mercury levels of two capillaries were plotted to show the depression of the menisci levels in the capillaries as a function of mercury position.

With the 0.535 mm diameter capillaries with which the gauge was originally equipped, the levels in both capillaries varied rather badly, and furthermore, the interesting quantity  $\Delta h$  varied from +10 mm to -1 mm with the sign of the slope changing several times. This test was repeated four or five times and in each the procedure was varied, but always with similar results. These variations in operating procedures will be discussed later.

A decision was based on the above results to replace the 0.535 mm capillaries with 1.0 mm diameter capillaries. This was accomplished and the preceding test was repeated. This time the mercury in the two capillaries rose smoothly and there were no systematic variations. The mercury in the open capillary appeared to ride slightly lower than that of the closed capillary, about 0.1 to 0.2 mm. When the pressure to be measured is so low that this offset,  $\Delta h_d$ , is appreciable compared to  $\Delta h$  or  $H$ , then one must correct for it.

A test of the above type, however, may not be sufficient to evaluate

$\Delta h_d$  for operational pressure measurements. During the pressure measurement, the conditions above the mercury in the closed capillary are different from those in the open capillary, due to the radically different gas pressure.

A good way of evaluating  $\Delta h_d$  during the pressure measurement is the following: a test sample of gas is compressed in the gauge, and  $H$  and  $\Delta h$  are recorded as usual. However, instead of the normal McLeod gauge equation

$$P = KH\Delta h \quad (49)$$

where  $K = 3.906 \times 10^{-7}$

the depression error  $\Delta h_d$  is inserted and the equation becomes

$$P = KH (\Delta h - \Delta h_d) \quad (50)$$

where  $(\Delta h - \Delta h_d)$  is the true depression due to the pressure. Equation 50 may be rearranged to give

$$\Delta h = \frac{P}{KH} + \Delta h_d \quad (51)$$

Thus a plot of  $\Delta h$  versus  $1/H$  would give a straight line of slope  $P/K$  and intercept on the  $\Delta h$  axis of  $\Delta h_d$ . Of course, if  $\Delta h_d$  is a function of  $H$ , then Equation 51 will not produce a straight line.

The test was performed on the modified gauge, with 1.00 mm diameter capillaries, and the graph of Equation 51 is presented as Figure 55.

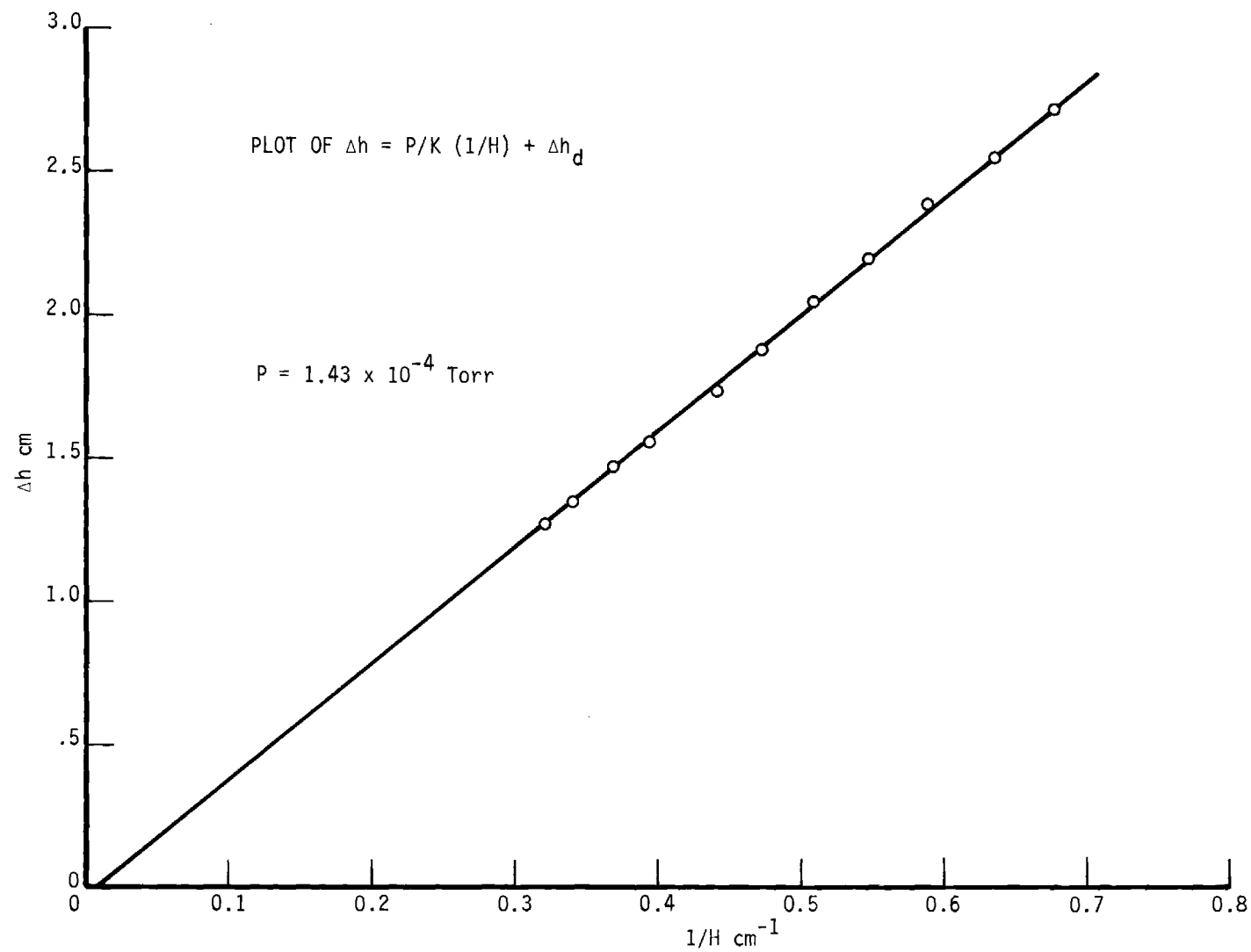


Figure 55. Plot of Modified McLeod Gauge Equation for this Gauge.

Out of eleven positions of the mercury, each being carefully read one time, the maximum deviation of any point from the straight line was less than 1.3 percent. The line drawn through these points intersected  $\Delta h$  at  $\Delta h_d = -0.30 \pm 0.05$  mm.

The conclusion is that there is no appreciable dependence of  $\Delta h_d$  on  $H$ , and that  $\Delta h_d$  is only important when

$$\Delta h \leq 100 \Delta h_d \quad (52)$$

or

$$H \leq 100 \Delta h_d \quad (53)$$

For this modified McLeod gauge,  $\Delta h_d$  causes less than one percent error for pressures above  $3 \times 10^{-4}$  Torr. However,  $\Delta h_d$  might be an unstable quantity and must be frequently checked.

### 3. Errors Due to the Cold Trap

The third and sometimes largest source of systematic error arises from the use of a cold trap.

A cold trap is normally placed between the gauge and the system whenever it is desirable to prevent the flow of mercury into the system or to prevent condensable gases from entering the McLeod gauge. When this is done, two significant errors will be introduced. One is caused by thermal transpiration and the other by the Gaede effect.

Thermal Transpiration. Rusch and Bunge<sup>74</sup> have dealt with this problem. This effect is caused by temperature differences between the various parts of the system and may result in pressure differences even between parts that have a common temperature.

At high pressures, when the mean free path of the gas molecules is small compared to the dimensions of the tube connecting the warm and cold regions, the pressure will be the same everywhere. This is because the gas-gas collisions predominate over the gas-wall collisions. For the other extreme of very low pressures, in which the mean free path is very long compared to the tube dimensions, the regions of common temperature will still have common pressure; however, the regions of different temperature will have different pressures,<sup>74</sup> because the gas-wall collisions are now predominant.

Between these two extremes are cases in which there will be a pressure difference between the warm and cold places which depends on the dimensions of the connecting tubulation. The effect can be particularly serious with regard to a cold trap where there are large temperature gradients along relatively narrow tubes. Even if the portions of the system on both sides of the trap are at equal temperatures, there can be a net pressure difference if the conductances of the tubes from the cold region of the trap to the two warm regions on either side are unequal.

Rusch and Bunge<sup>74</sup> have demonstrated that errors attributable to this effect can rise to ten percent. However, they were able to essentially eliminate these errors by proper dimensioning of the trap or by using a symmetric trap.

In the present experiment, the traps used were not made strictly in accordance with the suggested design of Rusch and Bunge. However, from information presented in their paper, it appears that our traps should produce considerably less than one percent error in the pressure range below  $1 \times 10^{-3}$  Torr. Other considerations, during the time before

we were aware of the present effect, led to a trapping arrangement that used two asymmetrical traps "back-to-back," which, of course, produced a symmetrical trapping arrangement. Thus, despite the design of the individual traps, the final arrangement did comply strictly with the suggestions of Rusch and Bunge, and the errors produced by thermal transpiration should now be negligible.

Gaede Effect. The error produced in this case is due to mercury vapor streaming from the McLeod gauge reservoir through the connecting tubulation to the cold trap. The diffusing mercury molecules undergo collisions with, and impart momentum to, the molecules of the gas under measurement. This momentum has a component directed away from the manometer. Thus, this mercury and trap arrangement functions as a diffusion pump. The result is that the pressure of the gas to be measured would be lower in the McLeod gauge than it would be in the system supplying the gas. Hence, the measurement of pressure would be falsely low.

In his paper in which he described his invention of the mercury diffusion pump, in 1915, Gaede<sup>75</sup> presented an analysis of this effect, and even gave warning to the users of McLeod gauges that cold traps would cause errors. However, it appears from the lack of mention of this effect in subsequent literature until 1962<sup>76, 77</sup> that his warning went unheeded. In recent years, similar treatments have been presented by several investigators. Principal among these were Ishii and Nakayama,<sup>76</sup> Meinke and Reich,<sup>77</sup> and Vries and Rol.<sup>78</sup> The only analysis that differed substantially from Gaede's was that based on kinetic theory by Takaishi.<sup>79</sup> The treatment presented here is not radically different from those mentioned above.



To describe this process mathematically, consider a stationary cloud of mercury vapor in a tube whose diameter is large compared to the mean free path of the molecules. Into one end of the tube a gas is introduced, whose pressure is much lower than that of the mercury. These gas molecules flow into the mercury by the process of ordinary diffusion. This diffusion can be described by the equation

$$j = - D_{12} \frac{dn}{dx} \frac{\text{molecules}}{\text{cm}^2 \text{ sec}} \quad (54)$$

in which  $j$  is the flux of molecules into the mercury,  $D_{12}$  is the diffusion coefficient for the diffusion of gas against mercury, and  $dn/dx$  is the density gradient of the gas. When this diffusion takes place in the tubulation between the McLeod gauge and the cold trap, in which the mean free path is comparable to the tube dimensions, the process will be slowed by the finite impedance of the tube. Denote the inhibiting factor by  $f$  and write

$$j = - f D_{12} \frac{dn}{dx} \quad (55)$$

However, in practice the mercury vapor is not stationary but moves with a net velocity  $u$  from the gauge to the trap, which acts as a sink. If it were not for the diffusion just described, this flow of mercury would sweep  $nu$  gas molecules per  $\text{cm}^2$  per second back to the trap, in a tube of zero impedance. However, wall effects retard this process by a factor which, it is argued, is precisely the same inhibiting factor  $f$  appearing in Equation 55.

In the stationary state these two processes are equal in magnitude and one may write

$$nuf = - f D_{12} \frac{dn}{dx} \quad (56)$$

Thus, the inhibiting factor  $f$  cancels out in the final relation. Since the density,  $n$ , is proportional to pressure,  $p$ , this equation becomes

$$\frac{dp}{p} = - \frac{u}{D_{12}} dx \quad (57)$$

Integration over the length of tube,  $L$ , from gauge to trap yields

$$\ln \frac{p \text{ (trap)}}{p \text{ (gauge)}} = \frac{uL}{D_{12}} \quad (58)$$

The velocity  $u$  of the mercury is related to the conductance  $C$  of the tubulation through

$$u = \frac{C}{\pi r^2} \quad (59)$$

in which  $r$  is the radius of the tube.

The following equation for  $C$ , which is applicable in the molecular flow region, is given by Dushman.<sup>80</sup>

$$C = 3.048 \times 10^4 \frac{r^3}{L} \sqrt{\frac{T}{M}} \quad (60)$$

This expression is applicable to a cylindrical tube for which  $L > 100 r$ . When the tube length  $L$  and radius  $r$  are given in cm, then  $C$  has the units of  $\text{cm}^3/\text{sec}$ .  $T$  is the temperature ( $^{\circ}\text{K}$ ) and  $M$  is the molecular weight of the gas.

However, in the operating temperature range of this laboratory ( $23^{\circ} - 28^{\circ}\text{C}$ ), the vapor pressure of mercury is not sufficiently low to be clearly in the molecular flow region. Dushman<sup>81</sup> gives a multiplicative correction factor,  $C'/C$ , which is in the vicinity of 0.97 for this temperature range. Substituting Equations 59 and 60 and  $C'/C$  into Equation 58 yields

$$\ln \frac{p(\text{trap})}{p(\text{gauge})} = 3.048 \times 10^4 \frac{r}{\pi D_{12}} \sqrt{\frac{T}{M}} \frac{C'}{C} \quad (61)$$

In this experiment  $r = 0.4$  cm and for mercury  $M = 200$ . Since  $D_{12}$  is inversely proportional to pressure and there is an abundance of data at atmospheric pressure from which  $D_{12}$  can be evaluated, the quantity

$\frac{D_{12}(1 \text{ at}) \times 760}{P_{\text{Hg}}}$  will be calculated. With this expression Equation 61

becomes

$$\frac{p(\text{trap})}{p(\text{gauge})} = \exp \left[ 0.361 \frac{P_{\text{Hg}} \sqrt{T(^{\circ}\text{K})}}{D_{12}(1 \text{ at})} \right] \frac{C'}{C} \quad (62)$$

The diffusion coefficient  $D_{12}(1 \text{ at})$  was calculated from the expression given by Dushman,<sup>82</sup>

$$D_{12}(1 \text{ at}) = \frac{4 (v_{\text{Hg}}^2 + v_g^2)^{\frac{1}{2}}}{3\pi n (\delta_{\text{Hg}} + \delta_g)^2} \quad (63)$$

for the case in which the mercury vapor pressure is large compared to the real gas pressure. The  $g$  subscripts refer to the real gas whose pressure is to be determined,  $v$  represents the average velocity of the molecules,  $n$  the number density at one atmosphere and  $\delta$  is the molecular diameter. All of the quantities with the exception of the  $\delta$  are computed in an obvious manner, and for this reason these values, which were computed from viscosity measurements,<sup>83</sup> are shown in Table 8.

Table 8. Molecular Diameters ( $\delta$ )  
(Units of  $10^{-8}$  cm)

Temp ( $^{\circ}$ C)	$\delta_{H_2}$	$\delta_{He}$	$\delta_{N_2}$	$\delta_{Ar}$	$\delta_{Hg}$
24	2.70	2.18	3.73	3.62	5.12
26	2.71	2.18	3.73	3.62	5.10
28	2.71	2.18	3.72	3.61	5.09
30	2.70	2.18	3.72	3.61	5.07

Equation 62 was evaluated for  $H_2$ ,  $He$ ,  $N_2$ , and  $Ar$  in the temperature range from  $22^{\circ}$  to  $28^{\circ}$ C. It was also evaluated for  $Ne$ ,  $CO$ , and  $O_2$  between  $24^{\circ}$  and  $26^{\circ}$ C. These results are plotted in Figure 56, and these calculated errors due to the Gaede effect seem to be substantial. However, it should be noted that these errors are at their maximum values, because it was assumed in the derivation of Equation 62 that the pressure of the real gas was negligible compared to the mercury vapor pressure. In the present work using  $He^{++}$  projectiles, this was a reasonable assumption because the real gas pressure was always less than a few percent of the mercury vapor pressure, which was about  $2.5 \times 10^{-3}$  Torr. However, the low cross sections

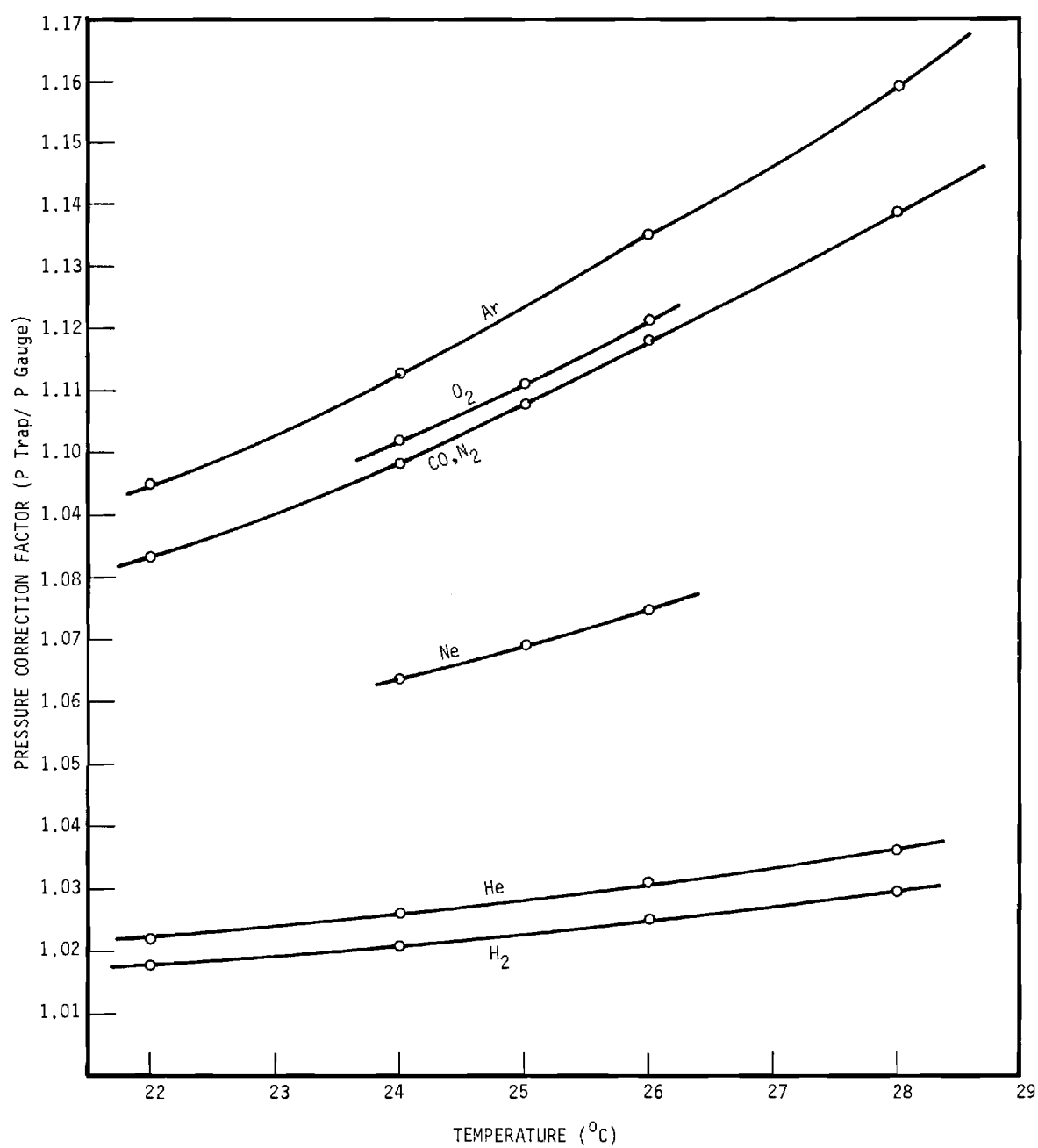


Figure 56. Indicated McLeod Gauge Correction Factor for Gaede Effect.

for the neutral projectiles necessitated the use of higher gas pressures, sometimes as high as  $1 \times 10^{-3}$  Torr. As the percentage of the real gas pressure rises the Gaede effect decreases, although not in direct proportion. Therefore, in the present experiment it seems that the error would be larger for  $\text{He}^{++}$  projectiles than for  $\text{H}^{\circ}$  and  $\text{He}^{\circ}$ . Existing experimental measurements<sup>62, 76-78, 84-87</sup> of this effect are not in close agreement, although they are usually within + 5 and - 50 percent of these calculated values. At present the reasons for these discrepancies are not obvious.

An investigation of this effect was undertaken in this laboratory by Thomas.<sup>87</sup> His procedure was to compare the pressure as indicated by a McLeod gauge, operated in the multiple-compression-mode, with that of a capacitance manometer. Although this McLeod gauge was not the same as the one used in the present experiment, the calculated Gaede effect was of the same order of magnitude. The pressure range investigated was from about  $1 \times 10^{-4}$  to  $5 \times 10^{-3}$  Torr. At the lower pressures, i.e., less than about  $4 \times 10^{-4}$  Torr, he did observe that the pressures indicated on the two instruments sometimes differed. However, the difference was always in the wrong sense for it to be ascribed to the Gaede effect. Thomas attributed this to errors in the capacitance manometer for such low pressures. Above the pressure of  $4 \times 10^{-4}$  Torr there appeared no evidence for the existence of the Gaede effect or systematic errors in either of the two manometers. However, as mentioned previously, in this pressure range above  $4 \times 10^{-4}$  Torr, the assumption that the real gas pressure is negligible compared to that of the mercury vapor is no longer valid, and consequently the Gaede effect should be less than those values indicated

in Figure 56. Thomas has suggested that the reason he did not observe the Gaede effect is because his McLeod gauge was "dirty." That is, the gauge and mercury are old and perhaps contaminated with adsorbed gases and no recent attempt has been made to clean either. Specifically, the surface of the mercury from which the vaporization takes place was visibly dirty and hence the rate of evaporation would be inhibited. If one recalls, the working mechanism that produces this effect is the evaporation and condensation of the mercury from the reservoir and on the cold trap, respectively. It is therefore evident that the Gaede effect will be reduced in proportion to the reduction in the evaporation rate of the mercury.

The above suggestion is perhaps substantiated by the work of Utterback,<sup>86</sup> who used what would be classified as a "clean" gauge. His technique was nominally the same as that of Thomas, and he did observe the effect. Furthermore, it appeared to be of about the expected magnitude.

However, Utterback's results are somewhat suspect because he did not observe the predicted pressure dependence, i.e., the effect he observed was a constant, independent of pressure, over the entire range investigated, which extended up to about  $2.5 \times 10^{-3}$  Torr. It should be noted, however, that other investigators<sup>84</sup> did observe the expected pressure dependence.

From the foregoing considerations it appears quite likely that the Gaede effect does exist and may produce substantial errors in the measurement of pressure. However, it is not felt that the magnitude of this effect has been sufficiently substantiated at this time to be used as a correction factor. Rather, it is felt that for the purpose of the present

investigation, the critical parameters such as temperature, tube dimensions, and indicated pressure should be recorded. If one wishes to consider the cleanliness of the gauge, perhaps it is even important to note that it was connected to the system by means of a greased stopcock. Such quantities as the gauge cleanliness would be extremely difficult to evaluate. However, the other quantities mentioned are explicitly accounted for in the theory.

The purpose in recording such parameters would be twofold. First, it would at most allow an absolute correction of the data if ever the magnitude of this effect is established; and second, at the least, it would allow some other investigator to make a more meaningful comparison to the present results. The latter would be accomplished by noting from these parameters in which gauge the effect is expected to be greatest, and relatively how much greater.

#### Preparation of the McLeod Gauge for Pressure Measurement

Upon receipt of this gauge from the manufacturer, it was rinsed in the following sequence with acetone, distilled water, concentrated nitric acid (approximately 30 seconds in the capillaries), and distilled water. After each rinsing the liquid was removed and deposited in a reservoir by evacuation. Following the final rinse with distilled water, the gauge was placed in its operating location and connected to the high vacuum system. When a vacuum of about  $1 \times 10^{-6}$  Torr was attained, the gauge was heated to approximately  $100^{\circ}\text{C}$  for several hours by means of a hot air gun. At the completion of this procedure it was estimated that the gauge vacuum was about  $1 \times 10^{-7}$  Torr. Next, the McLeod gauge was valved off from the



high vacuum system and the existing gauge vacuum was utilized to "draw" the triple-distilled mercury through a connecting tube and into the gauge reservoir.

Following the installation of the mercury, the gauge was returned to the system vacuum and heating was resumed for several hours. During this time the capillaries were maintained at a higher temperature ( $\sim 75^\circ - 100^\circ\text{C}$ ).

The purpose in this final heating was to remove residual gases such as water vapor and carbon dioxide from the gauge. A higher temperature bake would have been desirable; however, no facilities were available that would enable this to be done in a controlled manner.

Alpert<sup>88</sup> observed, in heating a McLeod gauge to  $400^\circ\text{C}$ , that as many as 30 monolayers of water vapor and substantial quantities of  $\text{N}_2$  and  $\text{CO}_2$  are released from the glass surfaces.

Aside from the glass walls outgassing, Kriesman,<sup>73</sup> in a very detailed study of the McLeod gauge, observed that the mercury itself outgassed. Several days under high vacuum conditions were required for the outgassing to cease. He then back-filled the gauge to several  $\times 10^{-3}$  Torr with dry  $\text{N}_2$  or Ar and sealed it off overnight. He concluded that the readings before and after this storage period indicated that under these conditions neither the mercury nor the glass adsorbed any significant amount of this dry  $\text{N}_2$  or Ar.

#### Operational Procedure

In the present research, the pressure range of interest is between  $5 \times 10^{-5}$  and  $2 \times 10^{-3}$  Torr, and a description of the measurement proce-

ture follows. In order to minimize the amount of capillary surface exposed to gas, the mercury is left in the fully raised position when the gauge is not in use, after first evacuating to about  $1 \times 10^{-7}$  Torr. Several minutes before the gauge is to be used, the traps are cooled to liquid nitrogen temperature so that all the condensable vapors will be removed from the connecting tube between the mercury surface in the side arm and the trap. The mercury is then lowered into the reservoir. The gas to be measured is slowly admitted into the vacuum system and thereby into the McLeod gauge. Several minutes are allowed for pressure equilibrium to be reached. Then, by admitting dry nitrogen into the reservoir, the mercury is allowed to rise. This must be done slowly so that the gas undergoing compression will remain in thermal equilibrium with the rest of the gauge. If the gas is allowed to heat, a falsely high pressure will be indicated. To insure that this did not occur, the mercury was allowed to rest several minutes before the reading was made.

Care should be taken to allow the mercury to approach its rest position only by rising. This insures that the rest position of the mercury meniscus is not affected by the electrostatic charge on the glass wall. This charge<sup>71</sup> is produced by the friction between the mercury and glass if the mercury is allowed to overshoot and then must be lowered to the desired rest position.

Most investigators advocate tapping of the capillaries before the reading is taken. In the McLeod gauge used by Jansen and Venema<sup>71</sup> it was demonstrated that

Tapping against the capillary tubes enables the mercury meniscus to reach the most stable position, corresponding to the average position of a large number of positions formed

during experiments without tapping.

The results clearly show that, although the average difference in height,  $\Delta h$ , is almost the same with and without tapping, the average error in one observation with tapping is much smaller than without.

This was not observed to be the case with the gauge used in this work. In fact, with tapping, a lower pressure was indicated than without tapping. This was attributed to the observation that the closed capillary was attached on one end only, and because of this it would have larger amplitudes of vibration than the comparison capillary. Moreover, sometimes the closed capillary would resonate and the mercury would rise above its equilibrium position. When this occurred, it would seldom completely recover because of the frictional forces previously described. Consequently, for readings with this gauge, the capillaries were not tapped.

After the mercury was allowed to remain in its rest position for several minutes, the menisci levels were read by means of a cathetometer. Following this, the mercury was allowed to compress the gas further and the levels were again read. This was repeated for three or four measurements. If the sequence of these measurements indicated a trend toward higher or lower pressure, they were plotted to determine the  $\Delta h_d$  correction factor (refer to previous discussion under the subheading of nonuniform capillary depression).

When the gauge was operated in this fashion, the pressure from one sequence of measurements to the next was usually reproducible within one percent. Although after the gauge had been used for several days the individual data points, as shown in Figure 55, would begin to scatter three or four percent from the straight line, this was remedied by return-

ing the gauge to high vacuum and heating it with a hot air gun for an hour or two.

### Conclusions

It was found that, if great care were taken and the operating procedure outlined in the preceding paragraphs was followed, then the random errors in this gauge could be reduced to less than one percent in the pressure range from  $5 \times 10^{-5}$  to  $2 \times 10^{-3}$  Torr.

In consideration of the systematic errors, it was concluded that the effect of thermal transpiration was negligible due to the symmetrical trapping arrangement. The other major systematic error, which is due to the Gaede effect, appears to be significant if one judges from either the theoretical calculations or the experimental results. The poor agreement among the experimental results, however, has caused some investigators to doubt that this effect has been properly evaluated.

In the present investigation, it was felt that the calculated Gaede effect was based on well established quantities, such as conductances, diffusion coefficients, etc. and was probably very nearly correct in the assumed pressure range and for clean mercury. Evidence in support of this opinion exists in the form of data taken by Meinke and Reich<sup>84</sup> who have paid close attention to satisfying all of these assumptions. It seems that one such confirmation of this effect should outweigh several less ambitious attempts that either measure less than the full predicted effect or no effect at all. In particular, it seems that once the full effect has been observed, then the investigators that measure a lesser effect are only demonstrating that their apparatus failed in some capa-

city to satisfy the assumptions of the calculation. Unfortunately, these convictions do not serve any useful purpose so far as correcting for this effect in the present McLeod gauge is concerned.

If one recalls the work of Thomas<sup>87</sup> for a rather dirty gauge in which no Gaede effect was observed and contrasts it to the work of Meinke and Reich<sup>84</sup> for a clean gauge, in which the full effect was observed, then one should realize the magnitude of the Gaede effect for the present moderately clean gauge could fall anywhere in between these two extremes. On this basis for the systematic error bracket on these pressure measurements, it seems only reasonable to choose the lower one to correspond to no Gaede effect and the upper one to correspond to the full effect as indicated by the curves of Figure 56.

Assigning the systematic errors in the above fashion and allowing a plus or minus one percent for random errors, then one has for the gases used in the present experiment the following total errors in pressure measurements:

Gas	The indicated pressure is from
H <sub>2</sub>	1 percent high to 3 percent low
He	1 percent high to 4 percent low
N <sub>2</sub>	1 percent high to 12 percent low
Ar	1 percent high to 14 percent low

Rather than attempt to correct the measured cross sections for these pressure errors, they will simply be added to the other errors to determine the overall error limits of this experiment.

## APPENDIX IV

## ALIGNMENT OF ANGULAR ROTATION MECHANISM

Prior to the measurements of the angular distribution of the recoils, it was necessary to align the apparatus such that the spectrometer would rotate about a fixed point in the ion beam.

The tools employed for alignment purposes were an engineers transit, a three meter rod to which was taped a 15-inch scale divided into 1/100 inch increments, and a  $\pi$  tape.

The alignment procedure was the following.

1. The spindle axis was adjusted to be vertical. This adjustment was accomplished by utilizing the precision machined features of the apparatus. When the precision spindle seat was turned in the base tripod, a flat surface was also turned on the large diameter steel base plate on which the angle scale was to be mounted. Hence, if the machined surface on the base plate is leveled, then the spindle is vertical. Utilizing this feature, the three meter rod and machinist scale were positioned approximately vertical at several locations around the circumference of the base plate. At each location, the elevation was determined with the aid of the transit, and the indicated adjustments were made by the jack screws in the tripod legs. After such a series of successive leveling approximations, it was estimated that the spindle was aligned within one minute of angle from the vertical.

2. The top and bottom flanges of the collision chamber were re-

moved and a machined (conical) pointer was fitted into a precision 0.375 inch hole (on axis) in the top of the spindle. The tip of the pointer defined the position of intersection of the line of sight through the spectrometer collimator and the fast beam collimator.

3. The transit was set up about five feet from the collision chamber (far enough for good focus, yet close enough for good magnification), approximately on the beam axis. The transit telescope was leveled and focused on the tip of the pointer in the collision chamber. Next, the beam collimator was adjusted to coincide with the axis defined by the transit telescope and the pointer, and the adjustments were locked.

The following step, which was later employed for the determination of the angle between the fast beam and the spectrometer, was to tilt the telescope downwards so that its axis swept out the vertical plane defined by the spindle axis and the transit axis. When the cross-wires of the telescope were focused on the outer edge of the large diameter base plate (on which the angle scale was mounted), a mark was made at the intersection of the cross-wires.

4. The transit was moved, readjusted and sighted through the "straight-through" port on the spectrometer. The rotation angle of the spectrometer was not important as long as it was near  $90^\circ$ . The vertical and horizontal adjustments on the spectrometer support were used, along with the horizontal displacement adjustment on the transit, to align the spectrometer axis with the axis defined by the telescope and pointer.

Next, the telescope was tilted downwards as previously described, and a mark was made on the edge of the base plate.

5. The  $\pi$  tape was then placed around the circumference of the base

plate and the plate diameter was measured to within 0.01 percent.

6. The angle scale, which was etched on a machined strip of aluminum of accurately known radius, was then mounted at the prescribed radius on the base plate. This was accomplished by measuring radially inwards from the edge of the plate with a micrometer.

7. The final measurement was the determination of the linear distance between the two marks made on the edge of the base plate in steps 3 and 4. This distance together with the known diameter of the plate permitted the calculation of the angular separation of the beam collimator and the spectrometer collimator. The angle pointer (mounted on the end of the counter weight support) was then adjusted to the calculated angle on the angle scale.

Thus, the alignment procedure was completed. It was estimated, on the basis of the accuracy of the individual alignment steps, that each collimator was aligned with 0.002 inch of the rotation axis, and the angular determination was within  $0^{\circ} 02'$  at  $90^{\circ}$ .



## BIBLIOGRAPHY\*

1. H. S. W. Massey and E. H. S. Burhop, Electronic and Ionic Impact Phenomena, (London: Oxford University Press, 1956).
2. S. K. Allison, Rev. Mod. Phys., 30, 1137 (1958).
3. S. K. Allison and M. Garcia-Munoz, Atomic and Molecular Processes, edited by D. R. Bates, (New York: Academic, 1962).
4. N. V. Fedorenko, Usp. Fiz. Nauk 68, 481 (1959); [English Transl.: Soviet Phys.-Usp. 2, 526 (1959)].
5. E. W. McDaniel, Collision Phenomena in Ionized Gases, (New York: John Wiley and Sons, Inc., 1964), Chap. 6.
6. V. S. Nikolaev, Usp. Fiz. Nauk 85, 679 (1965); [English Transl.: Soviet Phys.-Usp. 8, 269 (1965)].
7. E. S. Solov'ev, R. N. Il'in, V. A. Oparin, and N. V. Fedorenko, Zh. Eksperim. i Teor. Fiz. 45, 496 (1963); [English Transl.: Soviet Phys.-JETP 18, 342 (1964)].
8. E. S. Solov'ev, R. N. Il'in, V. A. Oparin, and N. V. Fedorenko, Zh. Eksperim. i Teor. Fiz. 42, 659 (1962); [English Transl.: Soviet Phys.-JETP 15, 459 (1962)].
9. S. Wexler, J. Chem. Phys. 41, 1714 (1964) and 44, 2221 (1966).
10. L. I. Pivovarov, M. T. Novikov, and V. M. Tubaev, Zh. Eksperim. i Teor. Fiz. 42, 1490 (1962); [English Transl.: Soviet Phys.-JETP 15, 1035 (1962)].
11. L. I. Pivovarov, V. M. Tubaev, and M. T. Novikov, Zh. Eksperim. i Teor. Fiz. 41, 26 (1961); [English Transl.: Soviet Phys.-JETP 14, 20 (1962)].
12. C. F. Barnett and P. M. Stier, Phys. Rev. 109, 385 (1958).
13. C. F. Barnett and H. K. Reynolds, Phys. Rev. 109, 355 (1958).

---

\* Abbreviations used herein conform to those found in the American Institute of Physics Style Manual (1965).

## BIBLIOGRAPHY (Continued)

14. V. S. Nikolaev, I. S. Dmitriev, L. N. Fateeva, and Y. A. Teplova, Zh. Eksperim. i Teor. Fiz. 40, 989 (1961); [English Transl.: Soviet Phys.-JETP 13, 695 (1961)].
15. D. R. Bates and G. Griffing, Proc. Phys. Soc. (London) A66, 961 (1953).
16. T. J. M. Boyd, B. L. Moiseiwitsch, and A. L. Stewart, Proc. Phys. Soc. (London) A70, 110 (1957).
17. R. A. Mapleton, Phys. Rev. 109, 1166 (1958).
18. D. R. Bates and A. Williams, Proc. Phys. Soc. (London) 70, 306 (1957).
19. D. R. Bates and G. W. Griffing, Proc. Phys. Soc. (London) 68, 90 (1955).
20. P. M. Stier and C. F. Barnett, Phys. Rev. 103, 896 (1956).
21. J. B. Hasted, Physics of Atomic Collisions, (London: Butterworth and Co., Ltd., 1964) Chap. 3.
22. S. K. Allison, J. Cuevas, and P. G. Murphy, Phys. Rev. 102, 1041 (1956).
23. S. K. Allison, Phys. Rev. 109, 76 (1958).
24. S. K. Allison, Phys. Rev. 110, 670 (1958).
25. V. S. Nikolaev, I. S. Dmitriev, L. N. Fateeva, and Y. A. Teplova, Zh. Eksperim. i Teor. Fiz. 40, 989 (1961); [English Transl.: Soviet Phys.-JETP 13, 695 (1961)].
26. E. S. Solov'ev, R. N. Il'in, V. A. Oparin, and N. V. Fedorenko, Zh. Eksperim. i Teor. Fiz. 41, 26 (1961); [English Transl.: Soviet Phys.-JETP 15, 459 (1961)].
27. Ibid. 45, 496 (1963); JETP 18, 342 (1964).
28. R. A. Langley, Total Cross-Sections for the Production of Positive Ions and Electrons by Helium Ions in Gaseous Targets, Unpublished Ph.D. Thesis, Atlanta: Ga. Inst. of Tech. (1963).
29. S. T. Butler and R. M. May, Phys. Rev. 137, A10 (1965).
30. A. H. Gabriel and D. W. O. Heddle, Proc. Roy. Soc. (London) 258, 124 (1960).

## BIBLIOGRAPHY (Continued)

31. H. C. Brinkman and H. A. Kramers, *Proc. Acad. Sci. Amsterdam* 33, 973 (1930).
32. D. Jaacks, B. Van Zyl, and R. Geballe, *Phys. Rev.* 137, A340 (1965).
33. V. V. Afrosimov and N. V. Fedorenko, *Zh. Techn. Fiz. (USSR)* 27, 2557 (1957); [English Transl.: *Soviet Phys.-Tech. Phys.* 2, 2391 (1957)].
34. J. W. Hooper, Ionization Cross Sections for Protons Incident on Helium, Neon, Argon, Hydrogen, Nitrogen, Oxygen and Carbon Monoxide in the Energy Range 0.15-1.10 MeV, Unpublished Ph.D. Thesis, Atlanta: Ga. Inst. of Tech. (1961).
35. J. W. Hooper, D. S. Harmer, D. W. Martin, and E. W. McDaniel, *Phys. Rev.* 125, 2000 (1962).
36. E. W. McDaniel, Collision Phenomena in Ionized Gases, (New York: John Wiley and Sons, Inc., 1964), Chap. 8.
37. N. F. Mott and H. S. W. Massey, The Theory of Atomic Collisions, (Oxford: Oxford University Press, 1952), 2nd ed.; Atomic and Molecular Processes, edited by D. R. Bates (New York: Academic Press, Inc., 1962); E. H. S. Burhop, in Quantum Theory, edited by D. R. Bates (New York: Academic Press, Inc., 1961), Vol. I; T. Y. Wu and T. Ohmura, Quantum Theory of Scattering (Englewood Cliffs, New Jersey: Prentice-Hall, Inc., 1962).
38. E. W. McDaniel, Collision Phenomena in Ionized Gases (New York: John Wiley and Sons, Inc., 1964) Secs. 6-11-D and 6-16-A.
39. D. W. Martin, R. A. Langley, D. S. Harmer, J. W. Hooper and E. W. McDaniel, *Phys. Rev.* 136, A385 (1964).
40. H. A. Bethe, *Ann. Physik* 5, 325 (1930).
41. J. W. Hooper, E. W. McDaniel, D. W. Martin, and D. S. Harmer, *Phys. Rev.* 121, 1123 (1961).
42. E. W. McDaniel, J. W. Hooper, D. W. Martin, and D. S. Harmer, Proceedings Fifth International Conference on Ionization Phenomena in Gases, Munich 1961, (Amsterdam: North-Holland Pub. Co., 1962), Vol. I, p. 60.
43. D. W. Martin, R. A. Langley, J. W. Hooper, D. S. Harmer, and E. W. McDaniel, Proceedings Third International Conference on the Physics of Electronic and Atomic Collisions, London 1963, (Amsterdam: North-Holland Pub. Co., 1964), p. 679.

## BIBLIOGRAPHY (Continued)

44. R. A. Langley, D. W. Martin, D. S. Harmer, J. W. Hooper, and E. W. McDaniel, Phys. Rev. 136, A379 (1964).
45. V. V. Afrosimov and N. V. Fedorenko, Zh. Techn. Fiz. (USSR) 27, 2546 (1957); [English Transl.: Soviet Phys.-Tech. Phys. 2, 2378 (1957)].
46. V. V. Afrosimov and N. V. Fedorenko, Zh. Techn. Fiz. 27, 2546 and 2557 (1957); [English Transl.: Soviet Phys.-Tech. Phys. 2, 2378 and 2391 (1957)].
47. N. V. Fedorenko and V. V. Afrosimov, Zh. Techn. Fiz. 26, (1956); [English Transl.: Soviet Phys.-Tech. Phys. 1, 1872 (1956)].
48. G. H. Morgan and E. Everhart, Phys. Rev. 128, 667 (1962).
49. E. S. Solov'ev, R. N. Il'in, V. A. Oparin, and N. V. Fedorenko, Zh. Eksperim. i Teor. Fiz. 42, 659 (1962); [English Transl.: Soviet Phys.-JETP 15, 459 (1962)].
50. A. O. Nier, Rev. Sci. Instr. 18, 398 (1947); W. E. Stephens and A. L. Hughes, Phys. Rev. 45, 123 (1934); W. E. Stephens, Phys. Rev. 45, 513 (1934); and J. A. Hipple, J. Appl. Phys. 13, 551 (1942).
51. E. Everhart and Q. C. Kessel, Phys. Rev. Letters 14, 247 (1965).
52. Q. C. Kessel, A. Russek, and E. Everhart, Phys. Rev. Letters 14, 484 (1965).
53. V. V. Afrosimov, Y. S. Gordeev, M. N. Panov, and N. V. Fedorenko, Zh. Techn. Fiz. 34, 1613, 1624, and 1637 (1964); [English Transl.: Soviet Phys.-Tech. Phys. 9, 1248, 1256, and 1265 (1965)].
54. J. B. Hasted, Physics of Atomic Collisions, (London: Butterworth and Co., Ltd., 1964), p. 130.
55. G. Lewin, Fundamentals of Vacuum Science and Technology, (New York: McGraw-Hill, Inc., 1965), p. 170.
56. Ibid., p. 137.
57. F. E. Terman, Radio Engineer's Handbook, (New York: McGraw-Hill Book Co., Inc., 1943), pp. 322-340.
58. L. A. Dietz, Rev. Sci. Instr. 36, 1763 (1965).

## BIBLIOGRAPHY (Continued)

59. A. L. Akishin, Soviet Phys.-Usp. 66, 113 (1958).
60. Q. C. Kessel and E. Everhart, Phys. Rev. 146, 16 (1966).
61. R. D. Evans, The Atomic Nucleus, (New York: McGraw-Hill Book Co., Inc., 1955) Appendix 5b.
62. D. Rapp, P. Golden, Lockheed Missiles and Space Co. Report 6-74-64-12, "Total Cross-Sections for Ionization and Attachment on Gases by Electron Impact, I. Positive Ionization." April 20, 1965.
63. H. Harrison, The Experimental Determination of Ionization Cross Sections of Gases under Electron Impact, (Washington, D. C.: Catholic University of America Press, 1956).
64. W. Bleakney and L. G. Smith, Phys. Rev. 49, 402 (1936).
65. D. D. Briglia and D. Rapp, Bull. Am. Phys. Soc. 11, 69 (1966).
66. M. H. Mittleman, Phys. Rev. Letters 16, 498 (1966).
67. H. E. Stanton and J. E. Monohan, Phys. Rev. 119, 711 (1960).
68. M. Gryzinski, Phys. Rev. 138, A336 (1965).
69. W. Bleakney, Phys. Rev. 36, 1303 (1930).
70. P. Mahadevan, J. K. Layton, A. R. Comeaux, and D. B. Medved, J. Appl. Phys. 34, 2810 (1963).
71. C. G. J. Jansen and A. Venema, Vacuum 9, 219 (1959).
72. P. H. Carr, Vacuum 14, 37 (1964).
73. W. S. Kriesman, Geophysics Corp. of America, Technical Report 61-19-N, 63, (Dec. 1961).
74. M. Rusch and O. Bunge, Zh. Techn. Physik 13, 77 (1932).
75. W. Gaede, Ann. Physik 46, 357 (1915).
76. H. Ishii and K. I. Nakayama, Trans. of the Eighth Nat. Vac. Symp. (London: Pergamon Press, 1962) Vol. 1, p. 519.
77. C. Meinke and G. Reich, Vakuum Technik 11, 86 (1962).
78. A. E. deVries and P. K. Rol, Vacuum 15, 135 (1965).

## BIBLIOGRAPHY (Concluded)

79. T. Takaishi, Trans. Faraday Soc. 61, 840 (1965).
80. S. Dushman, Scientific Foundations of Vacuum Technique, (New York: John Wiley and Sons, 1962) 2nd. ed., p. 88.
81. Ibid., p. 107.
82. Ibid., p. 67.
83. Ibid., p. 33.
84. C. Meinke and G. Reich, Vakuum Technik 12, 79 (1963).
85. E. W. Rothe, J. Vac. Sci. Technol. 1, 66 (1964).
86. N. G. Utterback and T. Griffith, Jr., Rev. Sci. Instr. 37, 866 (1966).
87. E. W. Thomas, Annual Technical Status Report No. 2, Project B-2021 of the Ga. Inst. of Tech., U.S.A.E.C. Contract No. AT-(40-1)-2591, (Dec. 1, 1966).
88. D. Alpert, Handbuch der Physik 12, Springer Verlag (1958).

## VITA

Lawrence Jackson Puckett was born in Claxton, Georgia on September 28, 1938. He is the son of Mr. and Mrs. Osbourne Puckett. On June 25, 1960 he was married to Anne Wilson Dukes, from Columbia, South Carolina. A daughter, Anne Lynne, and a son, David Lawrence, were born on February 25, 1962, and April 16, 1963, respectively.

Mr. Puckett attended public schools in Augusta, Georgia, where he was graduated from the Academy of Richmond County in 1956. He received the degrees of Bachelor of Science in Physics from the Virginia Military Institute in 1960, and a Master of Science in Physics from the Georgia Institute of Technology in 1962.

During the summers of 1960 and 1962, he was employed as a physicist by E. I. DuPont de Nemours and Company at the Savannah River Plant. Since the fall of 1962, he has been employed as a graduate research assistant with the Engineering Experiment Station of the Georgia Institute of Technology.

Mr. Puckett is a member of the American Physical Society and of Sigma Xi.

## ERRATA

Page

94 Figure 32.

Curve labeled " $H_2$ " should be labeled " $N_2$ ";

Curve labeled " $N_2$ " should be labeled " $H_2$ ".

101 Figure 35.

Add to figure legend this curve identification:

Alternate long dash, single dot,  $\sigma_i$  (Theor.  $H^O + H_2$ ) BG 55.



TECHNICAL REPORT

SCATTERING OF  $\text{He}^+$  IONS BY NOBLE GASES  
AT HIGH ENERGIES

By G. O. Taylor, Jr.  
D. W. Martin  
E. W. Thomas



USAEC Document Number  
ORO-2591-42

Contract No. AT-(40-1)-2591

U. S. Atomic Energy Commission  
Oak Ridge, Tennessee

September



School of Physics  
GEORGIA INSTITUTE OF TECHNOLOGY  
Atlanta, Georgia

GEORGIA INSTITUTE OF TECHNOLOGY  
School of Physics  
Atlanta, Georgia

TECHNICAL REPORT

SCATTERING OF  $\text{He}^+$  IONS BY NOBLE GASES  
AT HIGH ENERGIES

By

G. O. Taylor, Jr.  
D. W. Martin  
E. W. Thomas

USAEC Document No.  
ORO-2591-42

Contract No. AT-(40-1)-2591

U. S. Atomic Energy Commission  
Oak Ridge, Tennessee

3 September 1969

## PREFACE

This report summarizes the results and the apparatus and techniques used in the course of studies conducted under Contract AT-(40-1)-2591 from the U. S. Atomic Energy Commission. This report covers the work performed to June 1, 1969, and is identical to the text of a thesis entitled "Scattering of  $\text{He}^+$  Ions by Noble Gases at High Energies" which was submitted by George O. Taylor, Jr. to the faculty of the Georgia Institute of Technology in partial fulfillment of the requirements for the degree of Doctor of Philosophy in the School of Physics. Having completed all other requirements, he will be awarded this degree at the June, 1970, commencement of the Georgia Institute of Technology.

Mr. B. W. Griffiths, Mr. D. E. Troyer, and Mr. F. T. Richie assisted in the operation of the equipment during the later portions of this work.

The results of this work were presented at the Sixth International Conference on the Physics of Electronic and Atomic Collisions at the Massachusetts Institute of Technology, Cambridge, Massachusetts, July 28 - August 2, 1969. The text of this paper was published in the Abstracts of Papers in this meeting which has been published by The M.I.T. Press, Cambridge, Massachusetts. It is planned to submit an article detailing the apparatus, techniques, results, and comparisons, both with theory and with other experiments, to the Physical Review for publication. The thesis contains a far more detailed treatment of the experimental

apparatus and of the tests used to evaluate the apparatus than would be permissible in a journal article.

None of the work on optical excitation cross section measurements conducted under this same contract is included in this report.

## TABLE OF CONTENTS

PREFACE . . . . .	Page ii
LIST OF TABLES. . . . .	vi
LIST OF ILLUSTRATIONS . . . . .	vii
ABSTRACT. . . . .	x
Chapter	
I. INTRODUCTION . . . . .	1
II. BASIC CONCEPTS OF HIGH ENERGY TWO BODY COLLISIONS . . . . .	6
Definition of Differential Scattering Cross Sections . . . . .	7
Coordinate Transformation. . . . .	16
Validity of Classical Scattering . . . . .	18
Classical Scattering . . . . .	20
Charge Changing Theories . . . . .	28
III. SCATTERING EXPERIMENTS AT HIGH ENERGIES. . . . .	36
Previous Experiments . . . . .	38
N. V. Fedorenko E. Everhart L. I. Pivovar V. V. Afrosimov	
Present Experiment . . . . .	50
IV. APPARATUS AND TECHNIQUES OF MEASUREMENT. . . . .	52
Source of Projectiles. . . . .	52

## TABLE OF CONTENTS (Concluded)

	Page
Description of Scattering Apparatus. . . . .	55
Mechanical Construction	
Alignment Procedures	
Vacuum System	
Electronics	
Evaluation of Detection Systems. . . . .	87
Scattered Particle Analyzer	
Measurement and Monitoring of Projectile Beam	
Techniques of Measurement. . . . .	100
Errors in Measurement. . . . .	108
V. EXPERIMENTAL RESULTS . . . . .	113
Differential Scattering Cross Sections . . . . .	113
Charge State Fractions . . . . .	127
Angular Dependence	
Energy Dependence	
VI. CONCLUSIONS. . . . .	142
APPENDICES	
A. GEOMETRICAL FACTOR IN SCATTERING EXPERIMENT. . . . .	145
B. CALIBRATION OF CAPACITANCE MANOMETER . . . . .	155
BIBLIOGRAPHY. . . . .	159

## LIST OF TABLES

Table		Page
1.	Experimental Work of N. V. Fedorenko's Group . . . . .	39
2.	Experimental Work of E. Everhart's Group . . . . .	43
3.	Experimental Work of L. I. Pivovarov's Group . . . . .	46
4.	Experimental Work of V. V. Afrosimov's Group . . . . .	49
5.	Typical Values for Statistical Errors. . . . .	109
6.	Energy Dependence of $P_n$ for $\text{He}^+ + \text{He}$ . . . . .	136
7.	Energy Dependence of $P_n$ for $\text{He}^+ + \text{Ne}$ . . . . .	137
8.	Energy Dependence of $P_n$ for $\text{He}^+ + \text{Ar}$ . . . . .	138
9.	Heights of Intersections and Peaks of $P_n$ Compared with Statistical Theory . . . . .	141

## LIST OF ILLUSTRATIONS

Figure		Page
1.	Scattering Geometry for Infinitesimal Element of Incident Beam . . . . .	9
2.	Two Points Which Satisfy the Condition $\omega(x_1) = \omega(x_2)$ . . . . .	12
3.	Scattering of Projectile by Center of Force. . . . .	22
4.	Apparatus. . . . .	56
5.	Main Support Shaft . . . . .	57
6.	Interior of Collision Chamber. . . . .	60
7.	Top of Collision Chamber . . . . .	62
8.	Cross Sectional View of Top of Collision Chamber. . . . .	64
9.	Collimation of Incident and Scattered Beam . . . . .	66
10.	Schematic of Scattering Apparatus. . . . .	68
11.	Silicon Surface Barrier Detector . . . . .	71
12.	Two-Dimensional Motion Assembly for Silicon Detector . . . . .	72
13.	Scattered Projectiles Versus Pressure. . . . .	78
14.	Wiring Schematic . . . . .	80
15.	Pulse Shapes and Maximum Counting Rates. . . . .	83
16.	Wiring of E.M.I. #6256S Photomultiplier. . . . .	85
17.	Side View of Scattered Particle Analyzer . . . . .	88
18.	Scattered Particles Versus Deflection Voltage. . . . .	90
19.	Scattered Particles Versus Vertical Position of Detector. . . . .	92



## LIST OF ILLUSTRATIONS (Continued)

Figure		Page
20.	Pulse Height Spectra for Scattered Ne Particles. . . . .	93
21.	Pulse Height Spectrum for Scattered He Particles . . . . .	94
22.	Horizontal Profile of Scattered Beam in Detector Plane . . . . .	96
23.	Vertical Profile of Scattered Beam in Detector Plane. . . . .	98
24.	Calibration of Photon Count Rate Against Projectile Beam Using Ionization Gauge. . . . .	104
25.	Differential Scattering Cross Sections Versus Angle for $\text{He}^+$ + Ar with Incident Energy of 208 keV . . . . .	114
26.	Differential Scattering Cross Sections Versus Angle for $\text{He}^+$ + Ar with Incident Energy of 418 keV . . . . .	115
27.	Differential Scattering Cross Sections Versus Angle for $\text{He}^+$ + Ar with Incident Energy of 627 keV . . . . .	116
28.	Differential Scattering Cross Sections Versus Angle for $\text{He}^+$ + He with Incident Energy of 400 keV . . . . .	117
29.	Differential Scattering Cross Sections Versus Angle for $\text{He}^+$ + He with Incident Energy of 600 keV . . . . .	118
30.	Differential Scattering Cross Sections Versus Angle for $\text{He}^+$ + Ne with Incident Energy of 400 keV . . . . .	119
31.	Reduced Cross Sections for Scattering of $\text{He}^+$ + Ar. . . . .	123
32.	Differential Scattering Cross Sections Versus Energy for $\text{He}^+$ + Ar at a Scattering Angle of $4^\circ$ . . . . .	125
33.	Fraction of Scattered Beam in Charge State n Versus Scattering Angle for $\text{He}^+$ + Ar with Incident Energy of 208 keV . . . . .	128
34.	Fraction of Scattered Beam in Charge State n Versus Scattering Angle for $\text{He}^+$ + Ar with Incident Energy of 418 keV . . . . .	129
35.	Fraction of Scattered Beam in Charge State n Versus Scattering Angle for $\text{He}^+$ + Ar with Incident Energy of 627 keV . . . . .	130

## LIST OF ILLUSTRATIONS (Concluded)

Figure		Page
36.	Fraction of Scattered Beam in Charge State $n$ Versus Scattering Angle for $\text{He}^+ + \text{He}$ with Incident Energy of 400 keV . . . . .	131
37.	Fraction of Scattered Beam in Charge State $n$ Versus Scattering Angle for $\text{He}^+ + \text{He}$ with Incident Energy of 600 keV . . . . .	132
38.	Fraction of Scattered Beam in Charge State $n$ Versus Energy for $\text{He}^+ + \text{He}$ . . . . .	133
39.	Fraction of Scattered Beam in Charge State $n$ Versus Energy for $\text{He}^+ + \text{Ne}$ . . . . .	134
40.	Fraction of Scattered Beam in Charge State $n$ Versus Energy for $\text{He}^+ + \text{Ar}$ . . . . .	135
41.	Umbra and Penumbra Regions in Scattering . . . . .	146
42.	Finite Dimensions of Incident Beam . . . . .	153
43.	Calibration of Capacitance Manometer . . . . .	157

## ABSTRACT

The scattering of  $\text{He}^+$  projectiles by impact on the noble gases, He, Ne, and Ar, was investigated in the energy range 120 to 830 keV under single collision conditions. Specifically, the experiment measured as a function of angle in the range one to eight degrees the total differential scattering cross section as well as the differential scattering cross sections for scattering without change of charge, for scattering with charge transfer, and for scattering with electron stripping. Also, the fraction of particles in a particular charge state was measured as a function of energy at fixed scattering angle.

A Van de Graaff accelerator furnished a monoenergetic beam of ions from 120 to 1000 keV. Two circular holes of diameter 0.025 inch collimated the beam entering the collision region, where the target gas pressure was typically one micron. Particles scattered through an angle  $\theta$  were collimated by a two-slit geometry, whose angular resolution was approximately 10 minutes of arc, passed through a parallel plate electrostatic deflector for charge sorting, and counted individually with a silicon surface barrier detector. At the energies of the present experiment, this detector has an efficiency of 100 percent. The primary projectile beam in the collision chamber was monitored continuously by detecting the collisionally induced photon emission from the target with a photomultiplier. The photon emission was calibrated in terms of beam current by a preliminary experiment in which a Faraday cup was temporarily placed in the incident beam path through the collision chamber.

The sum of the differential cross sections for scattering  $\text{He}^0$ ,  $\text{He}^+$ , and  $\text{He}^{2+}$  through an angle  $\theta$  was equal to the measured total differential cross section. The absolute error associated with the total differential cross section is  $\pm 23$  percent, the random error is estimated to be  $\pm 10$  percent. This total differential cross section was found to equal the theoretical differential scattering cross section based on a classical calculation using a screened Coulomb type potential. Thus, the scattering of the particles in these close encounters is determined by the mutual nuclear repulsion and may be adequately described by classical mechanics. The four differential scattering curves were parallel over the angular range investigated, indicating that  $P_n$ , the fraction of particles in a particular charge state  $n$ , was independent of the scattering angle. This result is consistent with theory and with experiments performed at slightly lower energies.

There was excellent agreement for the energy dependence of  $P_n$  in all three target gases with data at lower energies. The random error in  $P_n$  is estimated to be  $\pm 10$  percent. For the resonant case  $\text{He}^+ + \text{He}$ , it was found that  $P_0$ , the fraction of scattered particles which had picked up an electron during the collision, could be fitted in the investigated energy range by a semi-empirical equation if a damping factor in the equation was properly adjusted. Also, good agreement was found when comparing  $P_n$  with the predictions of a statistical theory.

## CHAPTER I

### INTRODUCTION

The investigation of differential scattering in atom collisions offers an excellent means of studying the connection between the electronic states of a diatomic system and its collision properties. For many years both experiments and theory focused attention primarily on total cross sections and ignored the details of angular distributions. However, more recently studies of differential scattering have revealed a great deal of interesting structure in the cross sections for various collisional processes which were previously unexpected and unsought.<sup>1</sup> Such studies have shown that many inelastic processes remain important down to surprisingly low energies, even close to threshold energies. The result of these developments is the beginning of a collisional spectroscopy of diatomic systems quite comparable to optical spectroscopy in richness of structure and variety of features that can be observed with similar potentialities for revealing information about the electronic structure and interactions of the transient molecular system formed during the collision.<sup>1</sup>

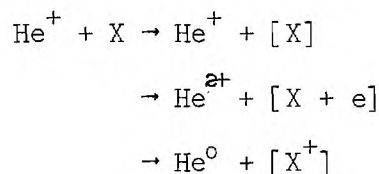
A theoretical task in the following years will be to develop understanding of these features and of the underlying principles in order that empirical evidence obtained from experiments can be converted into reliable information about interatomic potentials and other interaction parameters which can be used for a variety of predictive purposes. This

development of an empirical and phenomenological framework will be closely connected with the development of methods for a purely theoretical explanation.

One of the most striking measurements of differential scattering is contained in the studies of elastic collisions for  $\text{He}^+$  ions with He, Ne, and Ar atoms at low energies (10 to 600 eV).<sup>2,3</sup> These data contain a surprising wealth of information which appears in the form of structure superimposed on the smoothly varying differential scattering cross sections. Structure measurement has also been observed in the differential scattering as a function of angle of heavy noble gas ions by noble gas atoms at an energy of 50 keV.<sup>4</sup> Other workers have reported structure in differential scattering cross section curves, but these studies have been primarily at low energies.<sup>5,6,7</sup>

The one feature which distinguishes the measurements just mentioned from earlier measurements of differential scattering cross sections (prior to 1960) is the fine angular resolution. This improvement was possible because of more sensitive and more stable detection systems.

The present measurements were undertaken to closely examine the scattering of a relatively simple system, the  $\text{He}^+$  ion, in a high energy region. This work complements the low energy work of Lorents and Aberth,<sup>2,3</sup> and the two sets of data are linked through intermediate energies (10 to 200 keV) by the work of the group at the University of Connecticut.<sup>8,9</sup> The following reactions were investigated



where the target X was the noble gases He, Ne, and Ar. The charge state and the angle of scatter of the projectile were measured (in the range one to eight degrees) over the energy range from approximately 150 to 830 keV. The state of the target atom after the collision was unknown; thus, it was impossible to distinguish elastic from inelastic collisions even when the projectile did not change its charge state. The analysis of experimental data is complicated by contributions of inelastic processes; however, Firsov<sup>10</sup> has shown that classical ideas can be used to analyze inelastic scattering of primary ions whose energies are in the keV region if the ratio of the inelastic energy loss to the kinetic energy of the particle is small. Data from other laboratories<sup>11,12</sup> indicate this condition is clearly met in the present experiment.

The present work was undertaken to measure the differential scattering cross sections for  $\text{He}^+$  ions in an energy and angular range hitherto not examined. The data show that, within the investigated range, the interaction potential can be approximated very well by a screened Coulomb potential of the form

$$U(r) = U_{\text{coul}}(r) e^{-r/c_B} \quad (1)$$

where  $U_{\text{coul}}(r)$  is the Coulomb potential,  $r$  is the separation of the two nuclei, and  $c_B$  is the screening length.

$$c_B = \frac{a_0}{[Z_1^{2/3} + Z_2^{2/3}]^{1/2}} \quad (2)$$

where  $a_0$  is the Bohr radius. This potential, equation (1), has been dis-



cussed by Bohr,<sup>13</sup> who suggested the screening length,  $c_B$ . For the present experiment

$$c_B = 2.975 \times 10^{-9} \text{ cm for an He target}$$

$$c_B = 2.124 \times 10^{-9} \text{ cm for an Ne target}$$

$$c_B = 1.823 \times 10^{-9} \text{ cm for an Ar target}$$

The differential scattering curves were closely examined for structure superimposed on the smoothly varying cross section curves. Structure was not observed in the measured cross sections, and an upper bound was placed on the magnitude of any structure existing in the investigated range.

In the present experiment the fraction  $P_n$  of the total scattered projectiles in each particular charge state  $+ ne$ , where  $e$  is the electron charge, was measured as a function of energy and scattering angle. These fractions were found to be independent of the scattering angle over the entire energy range investigated, a result which is consistent with earlier work at lower energies of Fuls, et al.<sup>8</sup> Ziembra, et al.,<sup>9</sup> have measured the charge state fractions as a function of energy to 150 keV at fixed angle for the same projectile-target combinations as investigated in the present experiment. The present data agree very well with these earlier measurements.

The fraction of the total beam undergoing charge transfer (the charge transfer probability) has shown a very interesting oscillation for the resonant case  $\text{He}^+ + \text{He}$  when plotted as a function of energy (between approximately 10 and 200 keV) at fixed scattering angle.<sup>8</sup> This oscillatory behavior has been explained, in part, by the theoretical work of Bates and McCarroll.<sup>14</sup> The present measurements agree very well



in the investigated energy region with a semi-empirical relation suggested by Everhart<sup>15</sup> if the damping factor is appropriately chosen. The physical origin of such a damping effect is discussed both by Lichten<sup>16</sup> and by Marchi and Smith.<sup>17</sup>

Other general features for all target gases in the  $P_n$  versus energy curves are discussed in terms of the statistical theory advanced by Rusek.<sup>18,19</sup> This phenomenological theory gives good agreement with experiment even though the theory is based on assumptions of doubtful validity.

In this thesis the fundamental concepts of a two body collision at high energies are discussed. The true differential scattering cross section is defined and its relation with the measured differential scattering cross section developed. Relevant portions of classical and quantum mechanical scattering theory are also presented.

A brief resumé of other closely related experiments is given. Here the practical limitations of the other experiments are considered, thus providing a basis for comparison of the apparatus and techniques of the present experiment.

The mechanical construction of the apparatus, the tests which were performed to evaluate this equipment, and the methods and techniques used to accumulate the data are then discussed. Also, the errors associated with this work are considered.

The results of these measurements are presented in graphical form, in comparison with other experiments and with available theories.

## CHAPTER II

## BASIC CONCEPTS OF HIGH ENERGY TWO BODY COLLISIONS

Heavy particle collisions in which the projectile has an energy of hundreds of keV and where the scattering is through an angle of one degree or more have very small impact parameters. The deflection of the projectile is dominated primarily by the interaction between the two nuclei. The potential energy function of this interaction closely approximates a shielded Coulomb form. The final charge state of the scattered particle, on the other hand, depends largely on the interaction of the electrons and is reasonably independent of forces which control the nuclear scattering.<sup>20</sup>

Differential scattering cross sections measured in the hundreds of keV energy region can be compared with theoretical differential scattering cross sections evaluated from classical theory with the Coulomb force between the nuclei modified by a factor due to the electron screening. Classical theories, however, are unable to make predictions about the effect of charge changing processes on the scattered beam. Predictions concerning the fractions of the scattered beam in particular charge states employ either quantum mechanical approximations or use a statistical approach.

Recently, structure has been observed on the smoothly varying differential scattering cross section<sup>2,3,4</sup> (as predicted by a Coulomb type potential) when plotted as a function of angle. One explanation

of this structure presents a molecular complex picture of the collision,<sup>1</sup> while an alternate explanation that has been advanced is the concept of collective oscillations in the electron shells.<sup>21</sup> The molecular complex picture has been much more successful in explaining experimental data and will be considered below.

This chapter gives a background for the comparison of the experimental results with theory. A true differential scattering cross section will be defined and its relation to the measured differential scattering cross section developed. The measured differential scattering cross section is measured in the laboratory-fixed reference frame, whereas theoretical treatments are always developed in the center-of-mass reference frame. To connect these two different reference frames, the kinematical transformations between them are given. Then classical scattering theory will be discussed. The validity of the classical approach is considered, followed by a brief description of classical scattering where the question of extracting information about interaction potentials will be discussed. The final section of this chapter will outline the theoretical approaches which have been advanced to explain the distribution of charge states of the scattered particles.

#### Definition of Differential Scattering Cross Section

The discussion of this section follows the work of Thomas<sup>22</sup> and of Filippenko.<sup>23</sup> Begin by considering a single particle traveling along the x axis incident on a target of density  $N_t$ . Assume that there are sufficiently few targets, so that the projectile is scattered only once.

The probability of scatter into the infinitesimal solid angle

$d\omega = \sin\theta \, d\theta \, d\chi$ , while traversing the infinitesimal path length  $dx$  is

$$P = \frac{d\sigma}{d\omega}(\theta, \chi) N_t \, d\omega \, dx . \quad (3)$$

$\frac{d\sigma}{d\omega}(\theta, \chi)$  is a proportionality constant having the dimensions of area per particle steradian and is defined to be the true differential scattering cross section. It depends on the scattering angles  $(\theta, \chi)$  illustrated in Figure 1.

Let the beam of projectiles have a volume density  $N_p$ , and each particle a velocity  $v$ . The infinitesimal cross sectional area of the projectile beam is  $dA$ . The number of projectiles scattered per unit time into the infinitesimal solid angle,  $d\omega$ , from the "point volume,"  $dx dA$  will be

$$d\eta(\theta, \chi) = (v N_p dA) P = v N_p N_t \frac{d\sigma}{d\omega}(\theta, \chi) \, d\omega dA dx . \quad (4)$$

Experiments measure the particles scattered into a finite solid angle. Let  $dN$  be the number of particles per second scattered into the finite solid angle,  $\omega$ , from the infinitesimal "point volume element,"  $dx dA$

$$dN(\theta, \chi) = \int_{\omega} d\eta(\theta, \chi) = v N_p N_t dA dx \int_{\omega} \frac{d\sigma}{d\omega}(\theta, \chi) \, d\omega . \quad (5)$$

To proceed further assume that  $\frac{d\sigma}{d\omega}$  varies smoothly and slowly over the finite solid angle  $\omega$ . Make the approximation

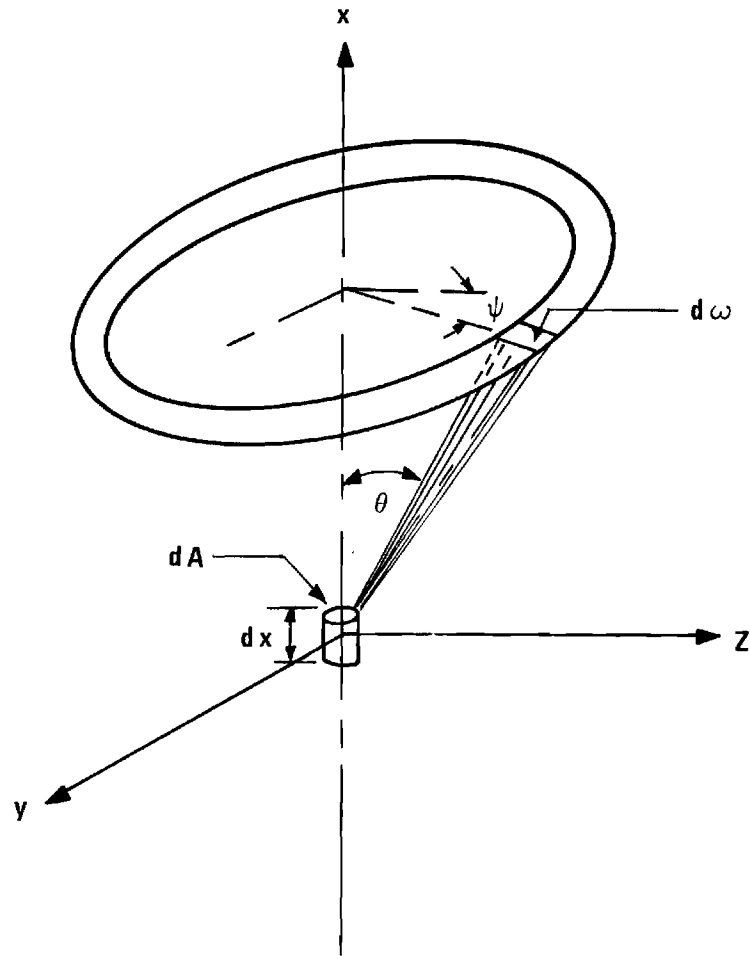


Figure 1. Scattering Geometry for Infinitesimal Element of Incident Beam.

$$\int \frac{d\sigma}{d\omega} d\omega \approx \overline{\frac{d\sigma}{d\omega}} (\theta, \chi) \omega . \quad (6)$$

$\overline{\frac{d\sigma}{d\omega}} (\theta, \chi)$  is the mean differential scattering cross section over the solid angle  $\omega$ . This approximation has the effect of smearing the scattering angle  $(\theta, \chi)$ ; contributions to  $\overline{\frac{d\sigma}{d\omega}}$  now are received from  $\theta$  to  $\theta + \Delta\theta$ ,  $\chi$  to  $\chi + \Delta\chi$ . This gives not only an average differential scattering cross section but also an average scattering angle which will be observed by the notation  $(\bar{\theta}, \bar{\chi})$ .

This assumption (henceforth referred to as Approximation I) is the fundamental limit in attempting to deduce differential scattering cross sections from experimental data. It is especially bad at very small scattering angles where there is quite rapid variation of the scattering cross section with angle. (The scattering here is still from a "point volume.")

Using this approximation, equation (5) becomes

$$dN(\bar{\theta}, \bar{\chi}) = v N_p N_t dA dx \overline{\frac{d\sigma}{d\omega}} (\bar{\theta}, \bar{\chi}) \omega . \quad (7)$$

In reality the detection system views a finite volume of beam,  $\iint dA dx$ , and the particles actually entering the detection system per second are

$$N(\bar{\theta}, \bar{\chi}) = \iint dN = v N_p N_t \iint \overline{\frac{d\sigma}{d\omega}} (\bar{\theta}, \bar{\chi}) \omega dA dx . \quad (8)$$

Next, make the approximation (Approximation II)

$$\iint \frac{d\sigma}{d\omega} (\bar{\theta}, \bar{\chi}) \omega dA dx \approx \overline{\frac{d\sigma}{d\omega} (\bar{\theta}, \bar{\chi})} \iint \omega dA dx . \quad (9)$$

The effect of this approximation is twofold. It tends to smooth out variations in the cross section and also to smear (to a greater extent than the first approximation) the definition of the angle  $(\bar{\theta}, \bar{\chi})$ . Both approximations become particularly bad at small angles.

To consider the effect of these approximations, take two points along the beam axis,  $x=x_1$  and  $x=x_2$ , so located with respect to the slits defining the scattered beam that these points satisfy the requirement  $\omega(x_1) = \omega(x_2)$ . Such a pair of points is shown in Figure 2. Then, from equation (5) (dropping both Approximations I and II for the moment)

$$dN_{x=x_1}(\theta, \chi) = \text{const.} \int_{\omega} \frac{d\sigma}{d\omega}(\theta, \chi) d\omega , \quad (10a)$$

and

$$dN_{x=x_2}(\theta, \chi) = \text{const.} \int_{\omega} \frac{d\sigma}{d\omega}(\theta, \chi) d\omega . \quad (10b)$$

Although the regions of integration are of identical size in these cases, the integrands are different;  $\theta$  for point  $x_1$  is smaller than  $\theta$  for point  $x_2$ . Hence, contributions to the scattered beam from a "point volume," and thus contributions to the total scattered beam  $N = \iint dN$ , depend not only on the magnitude of the solid angle but also on the point on the axis from which the scattering takes place.

Actually,

$$N = \iint dN = \text{const.} \iiint \frac{d\sigma}{d\omega} d\omega dA dx .$$

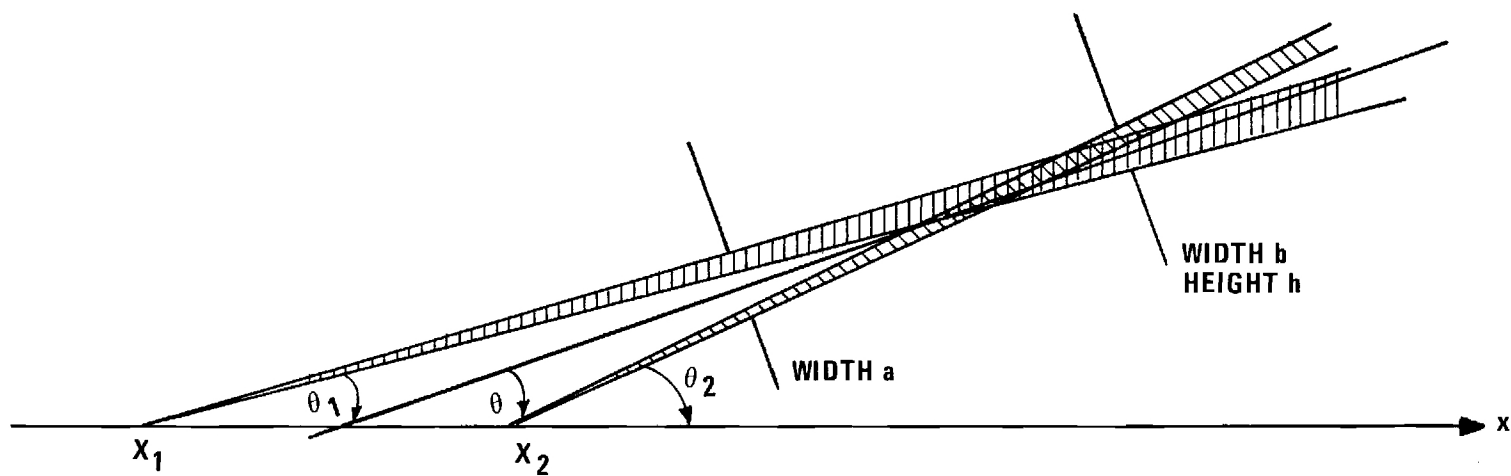


Figure 2. Two Points Which Satisfy the Condition  $\omega(x_1) = \omega(x_2)$ .



Approximation I relaxes the first integration giving

$$N = \text{const.} \iiint \overline{\frac{d\sigma}{d\omega}} \omega dA dx ,$$

while the second approximation allows the scattering cross section to be taken outside the volume integral.

Applying these approximations, equation (8) becomes

$$N(\bar{\theta}, \bar{\chi}) = v N_p N_t \overline{\frac{d\sigma}{d\omega}(\bar{\theta}, \bar{\chi})} \iiint \omega dA dx . \quad (11)$$

$N(\bar{\theta}, \bar{\chi})$  is the number of particles per unit time scattered into the angle  $(\bar{\theta}, \bar{\chi})$ .  $v N_p A$  represents the number of projectiles per unit time. Let  $N_o = v N_p A$  be the total intensity of the incident beam.

$$N(\bar{\theta}, \bar{\chi}) = \frac{N_o}{A} N_t \overline{\frac{d\sigma}{d\omega}(\bar{\theta}, \bar{\chi})} \int \omega dA dx . \quad (12)$$

Rearranging equation (12)

$$\overline{\frac{d\sigma}{d\omega}(\bar{\theta}, \bar{\chi})} = \frac{N(\bar{\theta}, \bar{\chi})}{N_o} \frac{1}{N_t} \frac{1}{\frac{1}{A} \int \omega dA dx} . \quad (13)$$

In Appendix A it is shown that, under most circumstances,

$$\int \omega dA dx \approx A \int \omega dx$$

is a very good approximation. Thus,

$$\overline{\frac{d\sigma}{d\omega}}(\bar{\theta}, \bar{\chi}) = \frac{N(\bar{\theta}, \bar{\chi})}{N_0} \frac{1}{N_t} \int \frac{1}{\omega dx} . \quad (14)$$

This is the equation which is used to evaluate an experimental value for the differential scattering cross section.

In a scattering experiment a beam of projectiles (the beam having a finite, but small, cross sectional area) is scattered by a target gas of low density at room temperature. If these particles have an axis, they are randomly oriented, and the experiment averages over any resulting azimuthal dependence, producing axial symmetry (see Figure 1). This experiment, as do most scattering experiments, moves the detector only in the x-o-z plane which holds  $\chi$  constant,  $\chi=0$  (ignoring the uncertainty in  $\chi$  due to previous approximations). Therefore, the  $\chi$  dependence will no longer be explicitly shown.

To simplify the notation which is used, the following changes will be made:

$$\overline{\frac{d\sigma}{d\omega}}(\bar{\theta}, \bar{\chi}) = \frac{d\sigma}{d\omega}(\theta) ;$$

$$N(\bar{\theta}, \bar{\chi}) = N(\theta) .$$

Hereafter,  $\frac{d\sigma}{d\omega}(\theta)$  will refer to the measured differential scattering cross section. Thus,

$$\frac{d\sigma^n}{d\omega}(\theta) = \frac{N^n(\theta)}{N_0} \frac{1}{N_t} \frac{1}{G(\theta)} \quad (15)$$

where

$$G(\theta) = \int \omega dx$$

is the geometrical factor discussed in Appendix A.

The superscript  $n$  denotes the charge state of the scattered particles and also the corresponding differential scattering cross section.

Equation (15) is a quantity that may be measured experimentally.  $\frac{d\sigma}{d\omega}(\theta)$  is the measured differential scattering cross section and is dependent upon the scattering apparatus; the relation of this measured to true differential scattering cross section is primarily dependent on two approximations stated in equations (6) and (9). Without exception the errors associated with making these approximations become large at small  $\theta$ , so that it is in this region that the largest discrepancy between the measured and the true differential scattering cross sections are to be found. The present measurements are in the angular range from approximately one to eight degrees, and in this range the approximations are not bad. Therefore, the measured is essentially equal to the true differential scattering cross section.

The total differential scattering cross section,  $\frac{d\sigma^T}{d\omega}(\theta)$  is the sum of the differential scattering cross section for electron capture,  $\frac{d\sigma^0}{d\omega}(\theta)$ , for electron stripping,  $\frac{d\sigma^{2+}}{d\omega}(\theta)$ , and for scattering without change of charge,  $\frac{d\sigma^+}{d\omega}(\theta)$ .

$$\frac{d\sigma^T}{d\omega}(\theta) = \frac{d\sigma^0}{d\omega}(\theta) + \frac{d\sigma^{2+}}{d\omega}(\theta) + \frac{d\sigma^+}{d\omega}(\theta) \quad (16)$$

Another important quantity in the present experiment is the fraction of the scattered beam in a particular charge state.  $P_n$  represents the fraction of the scattered particles in charge state  $n$ .

$$P_n = \frac{\frac{d\sigma^n}{d\omega}(\theta)}{\frac{d\sigma^T}{d\omega}(\theta)} = \frac{N^n(\theta)}{N^T(\theta)} \quad (17)$$

### Coordinate Transformation

The experimental value for the differential scattering cross section as measured in laboratory coordinates is given by equation (15). The theoretically predicted differential scattering cross section,  $\frac{d\sigma}{d\Omega}(\Theta)$ , is in the center of mass (C.M.) reference frame.  $\Theta$  is the scattering angle, and  $d\Omega$  is the element of solid angle in the center of mass frame. The reasons for using the C.M. reference frame will be discussed in the next section of this chapter.

The same number of projectiles must be scattered into a given element of solid angle  $d\omega$  in the laboratory as are scattered into the corresponding element of solid angle  $d\Omega$  in the C.M. system.

$$\frac{d\sigma}{d\omega}(\theta) d\omega = \frac{d\sigma}{d\Omega}(\Theta) d\Omega$$

or

$$\frac{d\sigma}{d\omega}(\theta) = \frac{d\Omega}{d\omega} \frac{d\sigma}{d\Omega}(\Theta) . \quad (18)$$

The ratio of corresponding solid angles is given by<sup>24</sup>

$$\frac{d\Omega}{d\omega} = \frac{[\gamma'^2 + 2\gamma' \cos \Theta + 1]^{3/2}}{1 + \gamma' \cos \Theta} , \quad (19)$$

where

$$\gamma' = \gamma \sqrt{\frac{E_{cm}}{E_{cm} - Q}} \quad (20)$$

and

$\gamma = m/M$ .  $m$  is the mass of the projectile;  $M$  is the mass of the target.  $E_{\text{cm}}$  is the energy associated with the relative motion in the center of mass reference frame.

$$E_{\text{cm}} = \frac{E_{\text{lab}}}{1 + \gamma} \quad (21)$$

$Q$  is the inelastic energy loss.

Equation (18) transforms the cross sections, but it is also necessary to transform the angle appropriate for the transformed cross section. This transformation equation is given by

$$\tan\theta = \frac{\sin\Theta}{\gamma' + \cos\Theta} . \quad (22)$$

The ratio  $Q/E$  is very small, so that  $\gamma' \approx \gamma$  is a very good approximation. The value of  $Q/E$  is discussed below. Hence, using this approximation, equations (18) and (22) perform the necessary transformation to compare theoretical and experimental differential scattering cross sections.

Equations (18) and (19) are correct only for infinitesimal solid angles  $d\omega$  and  $d\Omega$ . No difficulty arises in the use of these equations if the theoretical differential scattering cross section,  $\frac{d\sigma}{d\Omega}(\Theta)$  is transformed into the laboratory frame of reference and comparisons between theory and experiment are made in laboratory coordinates. However, additional errors, much like those discussed in the previous section, are introduced if this transformation is used to take the experimentally measured cross section  $\frac{d\sigma}{d\omega}(\theta)$  to the C.M. frame for comparison. All com-

parisons of the present measurements are made in laboratory coordinates.

### Validity of Classical Scattering

The interaction between two atoms during a collision can be approximately represented by the potential energy function,

$$U(r) = \frac{Z_1 Z_2 e^2}{r} e^{-r/c_B} . \quad (23)$$

The first factor is the Coulomb potential energy function between two nuclei of charges  $Z_1 e$  and  $Z_2 e$ . The exponential factor modifies the Coulomb potential function to allow for the electron screening. (This equation, as well as all equations presented will utilize the c.g.s. system of units.) Bohr<sup>13</sup> has discussed this potential function in detail and suggested a screening length (based on an estimate of the charge distribution within the atom by an appropriate statistical procedure such as developed by Thomas<sup>28</sup> and Fermi<sup>29</sup>).

$$c_B = \frac{a_0}{[Z_1^{2/3} + Z_2^{2/3}]^{1/2}} \quad (2)$$

where  $a_0$  is the radius of the first orbit in hydrogen,  $0.53 \times 10^{-8}$  cm. The potential function, equation (23), will henceforth be referred to as the Bohr potential.

Many authors<sup>25,26,27</sup> have discussed the validity of classical theory in describing the differential scattering cross section. The general results of these considerations give two conditions that must be satisfied for classical theory to adequately describe the differential

scattering cross section. These conditions are (1) the de Broglie wavelength,  $\lambda$ , of the projectile must be negligible when compared with any significant dimension of the scattering center, and (2) the collision must be well defined within the limits of the uncertainty principle.

The first condition requires that

$$\lambda \ll c$$

or

$$\lambda \ll D$$

where  $c$  is the screening length and  $D$  the collision diameter.

The collision diameter is the distance of closest approach which is energetically possible and is given by

$$D = \frac{Z_1 Z_2 e^2}{\frac{1}{2} m_r v^2} \quad (24)$$

where  $m_r$  is the reduced mass. ( $m_r = \frac{mM}{m+M}$ ,  $m$  is the mass of the projectile, and  $M$  is the mass of the target.)  $D$  is considered to be a good measure of the effective size of the scattering center if  $D/c$  is small.

The second condition may be restated in a different form, namely, that the deflection of the projectile must not be obscured by the spread of the wave packet. Bohr<sup>13</sup> has shown that, for the screened potential, equation (23), the lower limit of the scattering angle for the validity of classical mechanics is

$$\Theta^* \approx \frac{\lambda}{2\pi c_B}$$

Applied to the circumstances of the present experiment ( $\text{He}^+ + \text{Ar}$  at 400 keV);  $\lambda = 2.3 \times 10^{-12}$  cm,  $c_B = 1.8 \times 10^{-9}$  cm,  $D = 13.6 \times 10^{-12}$  cm,

and  $D/c_B = 0.0075$ .  $\Theta^* = 0.12$  degrees while the smallest angle in the measurements was approximately 0.8 degrees. Thus, these conditions are satisfied, and it is reasonable to expect classical theory to adequately describe the scattering. This expectation is verified by the data of this experiment.

Although no general quantum mechanical solution has been worked out for the potential function of equation (23), the solution in the Born approximation for this potential is known.<sup>13,30</sup> When the appropriate validity criteria are examined,<sup>13,25</sup> a very interesting fact emerges;<sup>26</sup> namely, the solution for particles heavier than electrons is valid only for angles less than  $\Theta^*$ . Since the classical solution is valid for angles greater than this limit, the two methods are valid in mutually exclusive angular ranges.<sup>26</sup>

### Classical Scattering

The following resumé of classical scattering theory follows the discussion found in many texts.<sup>27,31,32</sup> Consider a narrow beam of particles (each of mass  $m$  and traveling with a velocity  $v$  in the  $x$  direction) incident on a single target of mass  $M$  which is initially stationary. It is well known<sup>31</sup> that, if this problem is formulated in the center of mass (C.M.) reference frame, the relative motion of the projectile-target combination is equivalent to the motion of a single particle of reduced mass,  $m_r$ , acted on by a fixed scattering center. Furthermore, so long as only a central force field is considered, the scattering lies in a plane.<sup>32</sup>

The angle of scatter for each projectile is determined uniquely by energy and angular momentum of the particle.<sup>31</sup> The impact parameter,



$b$ , defined as the perpendicular distance between the scattering center and the incident velocity (see Figure 3) is directly related to the angular momentum. Thus, the scattering angle,  $\Theta$ , is determined once the energy and the impact parameter of the particle are known. The scattering angle is given by the equation<sup>32</sup>

$$\Theta = \pi - 2 \int_{r_0}^{\infty} \frac{dr}{\Phi(r)} \quad (25)$$

where

$$\Phi(r) = \sqrt{\frac{r^2}{b^2} \left[ 1 - \frac{U(r)}{E_{cm}} \right] - 1} . \quad (26)$$

$r$  is the magnitude of the vector describing the position of the projectile relative to the scattering center;  $r_0$  is the distance of closest approach (the largest real root of  $\Phi(r) = 0$ );  $U(r)$  is the interaction potential (assumed to be a central potential only); and  $E_{cm}$  is the C.M. energy of the collision.  $\Theta$  is the scattering angle of both  $m$  and  $M$  in the center of mass reference frame.

If  $N'_0$  is the number of projectiles per  $\text{cm}^2$  per second, then  $N'_0(2\pi b db)$  will be the number of projectiles that are incident on the scattering center with impact parameter in the range  $b$  to  $b + db$ . After scattering, these particles will travel in the angular range  $\Theta$  to  $\Theta + d\Theta$  with respect to the direction of the incident beam; the number scattered per second into this angular ring will be

$$N'_0(2\pi \sin \Theta d\Theta) \frac{d\sigma}{d\Omega}(\Theta) .$$

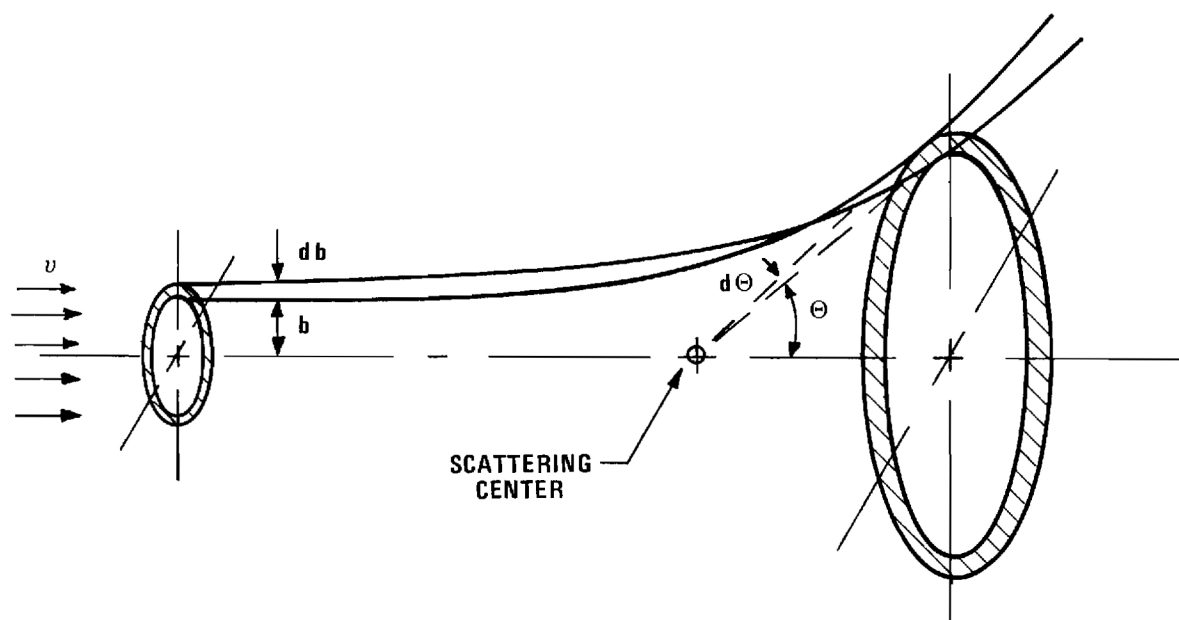


Figure 3. Scattering of Projectile by Center of Force.

$\frac{d\sigma}{d\Omega}(\Theta)$  is a quantity having the dimensions of area per steradian; it is the differential cross section for elastic scattering in the C.M. frame of reference. Figure 3 illustrates this situation. Thus,

$$|N_0'(2\pi b db)| = |N_0'(2\pi \sin \Theta d\Theta) \frac{d\sigma}{d\Omega}(\Theta)|$$

or

$$\frac{d\sigma}{d\Omega}(\Theta) = \frac{b}{\sin \Theta} \left| \frac{db}{d\Theta} \right|. \quad (27)$$

The impact parameter,  $b$ , is a function of the energy and the scattering angle related through equations (25) and (26),  $b = b(\Theta, E_{cm})$ . In general,  $b(\Theta, E_{cm})$  cannot be expressed in an analytic form; however, numerical solutions for the impact parameter are possible.

The total scattering cross section is given by

$$\sigma(\Theta) = \int_0^\pi 2\pi \frac{d\sigma}{d\Omega}(\Theta) \sin \Theta d\Theta \quad (28)$$

where it is assumed there is no azimuthal dependence.

Differential scattering cross sections provide information about the interaction potential, for it is this potential energy function that is responsible for the scattering. Basically, there are two ways to deduce the potential function from the measured cross section. One is to compare directly the measured values with calculations from arbitrarily assumed potential functions. The second is to deduce the potential energy function from the measured value.

Firsov<sup>33</sup> has shown how the potential (assuming a spherically symmetric function) can be deduced from differential scattering data at

fixed energy. This technique consists of two steps. First, the differential scattering cross section data are used to find the angular dependence of the impact parameter. The next step is to find the potential energy as a function of the separation distance. This technique has been applied to experimental data.<sup>34</sup>

F. Smith<sup>35</sup> points out that, if experimental data were absolutely accurate and extended over the full angular range from 0 to  $\pi$  at a fixed energy, no ambiguity would exist in extracting the potential by the Firsov method. However, experimental limitations place a boundary on the angular range, the resolution, and the accuracy of measurements. Hence, F. Smith<sup>35</sup> developed a single inversion technique to extract the potential function which combined data over a wide range of energy and angle. With this method it is, in principle, possible to estimate the potential function numerically, but Smith<sup>20</sup> states that, due to scatter in data, the procedure is somewhat ambiguous. He found it more profitable to fit curves using simple, physically plausible, potential functions.

In the present experiment the impact parameter was very small so that the first estimate of the interaction potential giving rise to the scattering force between the projectile and the target is simply the Coulomb potential between the bare nuclei. The Coulomb potential is

$$U(r) = \frac{Z_1 Z_2 e^2}{r} . \quad (29)$$

Upon substitution of this potential into equations (25) and (27), the classical Rutherford scattering cross section is obtained.

$$\frac{d\sigma}{d\Omega}(\Theta) = \left(\frac{D}{4}\right)^2 \frac{1}{\sin^4\left(\frac{\Theta}{2}\right)} \quad (30)$$

$D$ , the collision diameter, was previously discussed. Also, from the  $\Phi(r)$  equation a relation for the distance of closest approach can be obtained.

$$r_0 = \frac{D}{2} \left(1 + \frac{1}{\sin \frac{\Theta}{2}}\right) \quad (31)$$

The effect of the screening of the nuclei by the orbital electrons has been ignored. Several ways have been suggested to include this effect. One of the simplest is to consider the Bohr potential function mentioned above.

$$U(r) = \frac{Z_1 Z_2 e^2}{r} e^{-r/c_B} \quad (23)$$

The exponential factor modifies the pure Coulomb potential to simulate the effect of the electron screening. The extent of the electron screening is measured by  $c_B$ , the screening length, given by equation (2).

The differential scattering cross section for this screened potential energy function has been numerically calculated and presented in tabular form.<sup>26,36</sup> Also, these calculations have been compared with experimental results.<sup>8,37</sup>

O. B. Firsov<sup>38</sup> has made calculations with another potential function

$$U(r) = \frac{Z_1 Z_2 e^2}{r} \chi \left( \left[ Z_1^{2/3} + Z_2^{2/3} \right]^{\frac{1}{2}} \frac{r}{a} \right) \quad (32)$$

where  $\chi$  is the Fermi-Thomas shielding function.<sup>39</sup>

Both the Bohr and the Firsov potentials have shown good agreement with experimental work.<sup>34</sup> Lindhart, et al.<sup>40</sup> have considered the scattering by several types of potentials--the two potentials just discussed as well as a Lenz-Jensen potential and a power law potential. The effect of these potential functions is to modify the pure Coulomb potential to simulate the effect of electron screening. At high impact velocities, i.e., very close distances of approach, the screening effect introduced in each of these potentials reduces to the "pure" Coulomb potential. The entire development (regardless of the potential function used) is for elastic collisions. However, the present experiment does not, in fact cannot, truly distinguish elastic from inelastic events.

Subsidiary measurements, to be described in Chapter IV, with the present equipment indicate the average inelastic energy loss,  $Q$  (at any fixed scattering angle in the present range), to be small. These particular observations were not very sensitive and could only set an upper limit on  $Q$  of less than 15 percent of the incident energy. More direct measurements<sup>11,12</sup> of the inelastic energy loss in high energy heavy particle collisions show  $Q/E$  to be actually less than 0.01. Therefore, since the inelastic energy loss is such a small percentage of the projectile energy, it is reasonable to compare the measured total differential scattering cross section with the theoretical cross section based on elastic scattering. Firsov<sup>10</sup> has shown the validity of such consideration, and Smith<sup>20</sup> refers to such high energy scattering, where  $Q/E$  is very small, as quasielastic scattering.

As seen in equation (27) the impact parameter,  $b$ , is closely re-

lated to the differential scattering cross sections. While the impact parameter is not directly measured (see equation (15)), it is closely related to observables. In the semi-classical limit<sup>1</sup>

$$\begin{aligned} b &\simeq b(\Theta, E_{\text{cm}}, Q) \\ \Theta &\simeq \Theta(b, E_{\text{cm}}, Q) . \end{aligned}$$

In recent years such relations have been used to analyze experimental data in order to correlate various observed processes with particular impact parameters.<sup>1</sup> However, it has been necessary to assume a potential energy function to obtain the connection between  $b$  and  $\Theta$ .

Certain expansions have been developed which have proven very valuable in the comparison and analysis of experiments.<sup>35</sup> These are

$$\tau \equiv E_{\text{cm}} \Theta(b, E_{\text{cm}}) = \tau_0(b) + \frac{1}{E_{\text{cm}}} \tau_1(b) + \frac{1}{E_{\text{cm}}^2} \tau_2(b) + \dots \quad (33)$$

and a reduced cross section

$$\rho \equiv \Theta \sin \Theta \frac{d\sigma}{d\Omega}(\Theta, E_{\text{cm}}) = \rho_0(\tau) + \Theta \rho_1(\tau) + \Theta^2 \rho_2(\tau) + \dots \quad (34)$$

Smith<sup>35</sup> suggests plotting experimental data in terms of  $\rho$  versus  $\tau$ . In such graphs small angle scattering data can be effectively compared over wide spans of energy.<sup>20</sup> Also, particular features occurring in a limited range of  $\tau$  can be recognized as being associated with a given impact parameter and distance of closest approach, even if the actual values of these distances are not known.

### Charge Changing Theories

Investigations of the scattering of  $\text{He}^+$  ions on various noble gas targets have discovered very interesting oscillatory behavior.<sup>8,41</sup> This behavior, which is most pronounced in the resonant case,  $\text{He}^+ + \text{He}$ , has been observed in the energy range from 0.4 to 200 keV. At low energies ( $\approx 1$  keV) the oscillatory behavior also exhibits an angular dependence, but the oscillation becomes independent of scattering angle (if  $\theta \geq 4^\circ$ ) above 25 keV.

This oscillatory behavior was exhibited in the following manner.<sup>42</sup> The scattered particles were observed at a fixed angle, under single collision conditions. The fraction of the  $\text{He}^+$  ions which was neutralized by electron capture varied with the energy of the projectile, showing pronounced maxima at certain energies. A most interesting feature was that the maxima are equally spaced when  $P_0$  was plotted against the reciprocal of the velocity.<sup>42</sup>

These oscillations in the electron capture probability can be interpreted by means of the following qualitative picture.<sup>15</sup> As the  $\text{He}^+ + \text{He}$  system collides, it is assumed that the system can be described by the normalized sum of only two wave functions of  $\text{He}_2^+$ . These are  $\chi_g$  and  $\chi_u$ , functions of even and odd symmetry, respectively. The energies associated with these states are  $E_g$  and  $E_u$ . The "instantaneous-time dependencies" of these states are different, being  $\exp - (iE_g t/\hbar)$  and  $\exp - (iE_u t/\hbar)$ . During the collision these wave functions get in and out of phase with an "instantaneous-beat frequency"  $(E_g - E_u/\hbar)$  which is a function of internuclear separation  $r$ . The beat frequency increases as the particles approach, reaches a maximum as they pass close to one another, and then decreases as they re-



cede. Since  $\chi_g$  is even and  $\chi_u$  is odd, it is evident in adding them that the extra electron is on one side of the molecule when the two are in phase and on the other side when they are out of phase. Thus, the occurrence of charge transfer depends on whether the collision time is an integral or half-integral number of "instantaneous-beat frequency" periods.

The impact parameter method (I.P.M.) has been used to put the above qualitative discussion on a more formal basis being used, with various extensions, to explain charge transfer data.<sup>15,42,43</sup> The relevant portions of the I.P.M. will be outlined as it applies to the resonant  $\text{He}^+ + \text{He}$  case. Structure definitely appears in the non-resonant cases,<sup>8</sup> and the same general theoretical scheme is applicable,<sup>43</sup> with suitable modifications.

The impact parameter method assumes that the nuclei move in classical orbits, and quantal perturbation theory is applied to determine the transition probability from one electron state to another.<sup>43</sup> Further, it is assumed (for the symmetrical case  $\text{He}^+ + \text{He}$ ) that only two states of  $\text{He}_2^+$  are needed to describe the system;<sup>43</sup> excitation to other states is ignored. Also, the adiabatic assumption has been made that the electron wave functions at any instant are the same as they would be if the two nuclei were stationary at the same internuclear distance,  $r$ .<sup>15</sup> This last assumption has been modified both by Lichten<sup>16</sup> and by Bates and McCarroll.<sup>14</sup>

From these approximations it has been shown that<sup>14</sup>

$$P_0 = \sin^2 \left\{ \pi \frac{J(r_0)}{h} - \pi \beta(v, r_0) \right\} \quad (35)$$

where

$$J(r_0) = 2 \int_{r_0}^{\infty} (E_g - E_u) \frac{r}{\sqrt{r^2 - r_0^2}} dr, \quad (36)$$

and  $(E_g - E_u)$  is the energy difference between the adiabatic symmetric and antisymmetric states of the molecule,  $\text{He}_2^+$ .  $\beta(v, r_0)$  is a phase term which changes slowly compared to the first term.

Equation (35) has the same form as developed initially by Bates, et al.<sup>44</sup> and used by Ziemba and Russek<sup>43</sup> in discussing  $\text{He}^+ + \text{He}$  data, the principal difference being the term,  $\beta$ .  $\beta$  is a phase correction which arises in taking account of the transitional energy of the active electron. At low energies, theory predicts that  $\beta$  approaches zero, in which case equation (35) reduces to exactly the same form as developed earlier.<sup>44</sup>

The energy difference has been approximated by<sup>15</sup>

$$E_g - E_u = A e^{-r/\kappa} \quad (37)$$

with  $A = 130$  eV and  $\kappa = 0.422\text{\AA}$ . (This expression is valid for  $\text{He}^+ + \text{He}$ .) It is obtained from the molecular state curves of Lichten<sup>16</sup> or numerically from calculations by Phillipson.<sup>45</sup> Substituting equation (37) into (36), the integration can be performed analytically yielding

$$J(r_0) = A r_0 K_1 \left( \frac{r_0}{\kappa} \right) \quad (38)$$

where  $K_1$  is the first-order modified Bessel function of the second kind.

At higher energies<sup>43</sup>

$$r_0 K_1 \left( \frac{r_0}{K} \right) \approx K$$

Since the angular dependence of  $P_0$  is contained in  $J(r_0)$ , this last statement shows that, at high energies, the probability of charge exchange is independent of scattering angle and a function of energy only. This assertion agrees with the present data (Figures 33 and 37), not only for the resonant case of  $\text{He}^+ + \text{He}$ , but also for the non-resonant cases. This angular independence was observed also by Ziemba, et al.<sup>9</sup> when using  $\text{He}^+$  projectiles at 25 keV with  $\theta \geq 4^\circ$ .

Experimental data can be represented closely by the semi-empirical equation<sup>42</sup>

$$P_0 = K_0 \left( \frac{1}{v} \right) + K_2 \left( \frac{1}{v} \right) \sin^2 \left[ \frac{\pi \langle E' a \rangle}{v h} - \beta \right] \quad (39)$$

where  $K_0$  and  $K_2$  are slowly varying functions of the reciprocal velocity.  $E'$  is the interaction energy associated with the oscillation, and  $(a)$  is the distance over which the collision occurs.  $K_2$  is a damping function whose origin has been discussed by different authors.<sup>16,17</sup> Notice that if  $K_0 = 0$  and  $K_2 = 1$ , equation (39) has the same form as equation (35).

Lichten<sup>16</sup> proposes that damping arises in the deviation from adiabatic behavior which leads to a breakdown of the two-state approximation. It is proposed, based on the uncertainty principle, that the total wave function for the system must include a mixture of electronic states lying in a band very close to the states involved. The effect of mixing additional states destroys the interference, thus damping the oscillations. Marchi and Smith<sup>17</sup> propose a different reason for the damping, showing

that a two-state theory, even when properly formulated, would show a damping effect as a result of the interference of two scattering amplitudes that have different magnitudes at the scattering angle.

The values of  $\langle E'a \rangle$  and  $\beta$  are determined empirically from a plot of reciprocal velocity versus  $P_0$ .<sup>42</sup> The period  $T$  of one cycle of electronic oscillation is

$$T = \frac{a}{v_{n+2}} - \frac{a}{v_n} = \frac{h}{E}$$

where  $v_n$  and  $v_{n+2}$  are velocities of the projectile at the  $n^{\text{th}}$  and  $(n+2)^{\text{th}}$  maxima of the reciprocal velocity versus  $P_0$  curve. It was assumed that this period could be set equal to Plank's constant,  $h$ , divided by the interaction energy,  $E'$ , associated with the oscillation.

$$\langle E'a \rangle_n = \frac{h}{\frac{1}{v_{n+2}} - \frac{1}{v_n}}.$$

$\langle E'a \rangle$  can be determined experimentally in this manner. Since neither  $E'$  nor  $(a)$  are precise concepts, the brackets indicate an effective value of this quantity. Certainly the collision begins and ends gradually so that a fixed  $(a)$  is an over-simplification; also, the interaction energy varies with nuclear separation. For the case  $\text{He}^+ + \text{He}$ , Lockwood and Everhart<sup>42</sup> find that values  $\langle E'a \rangle = 102 \text{ eV} \cdot \text{\AA}$  and  $\beta = 0.23\pi$  fit their low energy experimental results with  $K_2 = \text{constant}$ . Figure 38 shows that this equation fits the present data between 150 and 1000 keV very well if  $K_2 \neq 1$ , but rather  $K_2 = 1.729 \times 10^8/v$  when  $v$  is the projectile velocity in cm/sec.

Further extensions of the I.P.M. treatment center around the determination of the energy difference ( $E_g - E_u$ ). The adiabatic representation has been used by many authors with the impact parameter method, but it is necessary to modify the adiabatic hypothesis in the neighborhood of an avoided crossing of the potential energy curves by making a particular linear combination of two adiabatic states. This method is satisfactory, but it is unclear how to construct the basic linear combinations in general situations where several states may be interacting.<sup>16</sup> Lichten has suggested the use of diabatic states which can be approximately described by molecular orbital considerations. These diabatic states which are constructed from a set of molecular orbital wave functions,<sup>16</sup> have the property of running smoothly through crossing points.

Lichten<sup>46</sup> has given a theoretical interpretation of inelastic atomic collisions. This work rests on two basic assumptions: molecular states can be used in the analysis of atomic collisions, and electrons are emitted from discrete states of the system. The agreement between this model and experiment in details of energy loss, fast electron spectra, and positions of critical internuclear distances is most impressive.<sup>46</sup> F. T. Smith<sup>47</sup> recently reexamined the equations of the general Born-Oppenheimer model for molecular problems. These results, which he refers to as the standard diabatic representation, have the properties called for in the work of Lichten.

As the projectile energy increases ( $\approx 1$  MeV), the recoil velocities of the nuclei become large compared with electronic velocities. Under these conditions, i.e., when the collision time is short compared with electron orbit time, the large momentum transfer between the nuclei is

not transmitted to the electrons, and the nuclei will become stripped of all electrons,<sup>16</sup> emerging from the collision fully ionized. The present measurements show that this condition is approached by the scattered projectile as seen in Figures 38 through 40. Under these conditions one would expect some high energy approximation (such as the Born approximation) to adequately describe the electron stripping process. While the Born approximation calculations have been applied to total cross sections, the results of the approximation for differential scattering cross sections have not been published; hence, comparisons between experiment and theory cannot be made at present.

A purely statistical theory was advanced several years ago by Russek.<sup>18,19</sup> This theory assumed that as the ion and atom collide a relatively small amount of kinetic energy of relative motion is transferred to the electrons. This energy is assumed to be distributed statistically among the outer-shell electrons, and the probability that any given number of electrons acquire more than the ionization energy is computed by statistical analysis. This ionization mechanism is analogous to the evaporation of molecules from a heated liquid.

This theory was initially designed for heavy particle interaction and gives good agreement with experiment in predicting both the height of intersections ( $P_n \times P_m$ ) and of the peaks ( $P_n$ ) of the ionization probability curves.<sup>9,37</sup> Further approximations, which were more difficult to justify,<sup>48</sup> were necessary to connect the probability curves with the angle of scatter. The statistical theory has been extended to apply to cases where any number of electrons (from 2 to 8) are contained in the outer shell.<sup>19</sup> In Chapter V, this theory is compared with data from the

present experiment. The agreement between theory and experiment can be seen in Table 9.

This statistical model as originally proposed is inconsistent with the shell structure of atoms and the discrete, sharp nature of auto-ionizing states. The statistical aspects of the theory have been improved and made more comprehensive,<sup>49</sup> such that the theory is now consistent with the concept of autoionizing transitions.<sup>50,51</sup>

## CHAPTER III

## SCATTERING EXPERIMENTS AT HIGH ENERGIES

The first experimental measurements of differential scattering cross sections in the high energy range for atomic ions incident on atoms were performed in 1954 and 1955 by Fedorenko<sup>52</sup> and by Everhart.<sup>\*53</sup> After initial studies of differential scattering, these groups subsequently pursued somewhat different types of investigations. Fedorenko<sup>54</sup> turned generally to total cross section measurements, whereas Everhart<sup>9</sup> measured primarily electron capture and stripping associated with large angle scattering. (It is interesting that these two groups after following their different routes would perform coincidence experiments at almost the same time.<sup>11,55</sup>)

In the mid-sixties Pivovarov<sup>\*37,56-58</sup> measured differential scattering cross sections for heavy ion-atom collisions. This work ranged to considerably higher energies than other measurements.

Measurements with which Fedorenko was associated, but not as the principal investigator, have more recently been conducted by V. V. Afrosimov.<sup>4,21,59</sup> This work was undertaken to confirm a proposed model explaining results from coincidence experiments.<sup>21</sup> These differential scattering cross sections show very interesting behavior.<sup>4,21,59</sup>

The work of these four groups constitutes the experimental data on differential scattering cross sections in the keV energy range. However,

---

\* In the present chapter the groups will be referred to by the name of the principal investigator, e.g., Fedorenko's group and Everhart's group.



it is necessary to mention the results of one other research team, Lorents and Aberth,<sup>2,3</sup> for their results at lower energies gave impetus to the present investigation. Gilbody<sup>60,61</sup> has also made important contributions to the study of scattering of atomic systems; however, his work will not be discussed because it is not directly connected to the present measurements.

Lorents and Aberth<sup>2,3</sup> measured the elastic differential scattering cross section for  $\text{He}^+$  on He, Ne, and Ar from 20 to 600 eV. In their very careful investigation a great deal of structure was discovered in the cross section curves which provided many new insights into the various mechanisms controlling the scattering. With the appearance of these results, reexamination of earlier work (i.e., that of Fedorenko and of Everhart) showed that similar structure in the cross section curves could have been completely missed, due to the limited angular resolution that was possible at the time of these early measurements. In fact, V. V. Afrosimov has detected structure in a careful reexamination of the total differential scattering in heavy noble ion-noble gas collisions at 25 and 50 keV.<sup>4,12,59</sup> One purpose in undertaking the present measurements was to see if similar structure could be found in the cross section curves at high keV energies for  $\text{He}^+$  projectiles.

Several technological advances now make it possible to measure the differential scattering cross sections with much higher resolution than was possible in 1955. It is the purpose of this chapter to present a résumé of the experimental conditions and limitations in the differential scattering cross sections which have been measured to date. This résumé will provide a background against which to compare the experimental con-

ditions of the present measurements, as well as a framework of the data that have been accumulated to the present time.

As shown in Chapter II, the experimental differential scattering cross section is given by

$$\frac{d\sigma^n}{d\omega}(\theta) = \frac{N^n(\theta)}{N_0} \frac{1}{N_t} \frac{1}{G(\theta)} \quad (15)$$

where  $\frac{N^n(\theta)}{N_0}$  is the ratio of scattered beam of charge state  $n$  to the incident beam in the collision region,  $N_t$  is the target density, and  $G(\theta)$  is the geometrical factor. These three factors plus the scattering angle,  $\theta$ , must be measured to determine the differential scattering cross section. The charge state of the scattered particles must also be measured to determine the scattering cross sections for electron capture or electron stripping. The methods employed in the measurement of these quantities will play the dominant role in the following discussion of the measurements of Fedorenko, Everhart, Pivovar, and Afrosimov.

#### Previous Experiments

N. V. Fedorenko<sup>52,62,63</sup>

The work of this group is covered in three papers which are summarized in Table 1. This work concentrates on the scattering of noble gas ions and alkali ions by noble gas atoms from five to 150 keV. The measurements provide an overall view of a large amount of information; i.e., they present a broad outline of data on scattering.

Following are specific points about this group of measurements.

1. The scattered particles were measured as a current into a

Table 1. Experimental Work of N. V. Fedorenko's Group (Differential Scattering Cross Sections Were Measured)

Title, Reference, Date	Cases Examined	Energy Range (keV)	Angular Range (°)	Angular Resolution (°)	Comments
"Single Scattering of Positive Ions in a Gas" [52] (1954)	<p>Many cases investigated but only a few reported.</p> <p>Examples:</p> <p>(1) Scatter without change of charge</p> $\left. \begin{matrix} \text{He}^+ \\ \text{Kr}^+ \\ \text{Na}^+ \\ \text{I}^+ \end{matrix} \right\} + \left\{ \begin{matrix} \text{Ne} \\ \text{Kr} \end{matrix} \right\}$ <p>(2) Stripping</p> $\text{Ar}^+ + ( ) \rightarrow \text{Ar}^{2+}$ <p>(3) Dissociation</p> $\text{H}_2^+ + ( ) \rightarrow \text{H}^+$	5-30; most work at 10	$2\frac{1}{2}$ -15	$\approx 2.2$	<p>Deflected ions were magnetically analyzed.</p> <p>Measured currents with Faraday cup.</p> <p>Pressure measured with radiometric manometer</p> <p><math>\frac{d\sigma}{d\omega}</math> may be in error by a factor of 2; but random error 10-15%.</p>
"Single Scattering of Stripped Argon Ions" [62] (1955)	$\text{Ar}^+ + \text{Ar} \rightarrow \text{Ar}^{0-5+}$ $\text{Ar}^+ + \left\{ \begin{matrix} \text{He} \\ \text{Ne} \\ \text{Kr} \end{matrix} \right\} \rightarrow \text{Ar}^{4+}$	40-150; most work at 75 with Ar target	0-15	$\approx 0.5$	<p>Working pressure <math>\approx 2 \times 10^{-4}</math> Torr.</p> <p>Data had <math>\sim \pm 10\%</math> reproducibility. Systematic error in <math>\theta \pm 1^\circ</math>.</p> <p>Calculated integral cross section from measurements.</p>

Table 1. Experimental Work of N. V. Fedorenko's Group (Differential Scattering Cross Sections Were Measured)(Concluded)

Title, Reference, Date	Cases Examined	Energy Range (keV)	Angular Range (°)	Angular Resolution (°)	Comments
"Scattering of Multiply Charged Ions and Electron Capture" [63] (1960)	$Kr^{+,2+,3+} + \{Ne\} \rightarrow Kr^{0,+}$ $Ne^{2+} + \{Kr\} \rightarrow Ne^{0,+}$	33	0-2.5	$\approx 0.5$	Error of $\approx \pm 20-25\%$ . This represents reproducibility of results.  The angular range was $0.5^\circ \leq \theta \leq 2.5^\circ$ without charge exchange, $0 \leq \theta \leq 2^\circ$ with charge exchange.

Faraday cup with an electrometer. This technique limits the minimum measurable scattered current to values greater than  $(10)^{-14}$  amperes, which in turn limited the accessible angular range. (The cross sections in general decrease rapidly with increasing angle.)

2. The limitations of the current measuring techniques also required the slit dimension be relatively large, which, in turn, decreased the angular resolution.

3. The scattered beam was magnetically analyzed. This introduction of a magnetic field near the scattering chamber could have led to a distortion of the angular distribution, particularly at low energies. Everhart<sup>64</sup> notices general agreement in magnitude of his results for the differential cross sections (as a function of angle) with those of Fedorenko, but a disagreement on the slope of the curves.

4. The incident beam current could not be measured simultaneously with the scattered current when  $\theta < 10^\circ$ . Therefore, these currents had to be measured sequentially most of the time. Since it is the ratio of these currents that is needed, the experimenter is forced to assume constancy of the beam current while measuring scattered current if only sequential measurements are made. As is well known, this can be a very dangerous assumption. (This comment about sequential rather than simultaneous current measurements is common to the work of all four groups.)

5. The random error in the measurements was 10 to 15 percent, but the absolute differential scattering cross sections could have been in error by a factor of two.

E. Everhart<sup>8,53,64</sup>

The work of this group represents the most systematic body of data

considered. After the original measurement of total differential scattering cross sections, the apparatus was continually modified and improved as different phenomena were investigated. The measurements all seem to originate from the same basic stem -- large angle scattering of single collisions. These papers form a very comprehensive set; it is almost like reading the log of one long continuous experiment rather than many separate works. Table 2 lists the pertinent facts concerning the experiments that measured differential scattering cross sections.

Many further experiments followed those listed in Table 2. While much of this work (reporting charge state fractions in the scattered beam) is relevant to the present investigation, it does not involve substantial changes in those aspects of the experimental techniques discussed here.

General comments about this work follow.

1. A Faraday cup was initially used to detect the scattered current; this was supplemented later by a secondary electron detector which was used for single particle detection. First, a thermal detector, then later the secondary electron detector, was used to detect the neutral beam.
2. The angular definition was continually improved, being approximately  $2.3^\circ$  initially but improving to  $\pm 0.5^\circ$  in the last paper in Table 2.
3. The scattered currents were electrostatically analyzed.
4. The beam current was measured sequentially with scattered current.
5. A McLeod gauge was used to measure the pressure.
6. The absolute accuracy was stated to be 30 to 50 percent; vary-

Table 2. Experimental Work of E. Everhart's Group (Measurements Include Both the Differential Scattering Cross Sections and  $P_n$ )

Title, Reference, Date	Cases Examined	Energy Range (keV)	Angular Range (°)	Angular Resolution (°)	Comments
"Differential Cross- Section Measurements for Large-Angle Col- lisions of Helium, Neon, and Argon Atoms at Energies to 100 keV" [53] (1955)	$\left. \begin{matrix} \text{He}^+ \\ \text{Ne}^+ \\ \text{Ar}^+ \end{matrix} \right\} + \text{Ar}$	25, 50, 100	$4\frac{1}{2}$ -38	$\approx 2.3$	<p>Scattered current measured with Faraday cup--no charge analy- sis.</p> <p>Pressure measured with McLeod gauge.</p> <p>Accuracy of measure- ment <math>\pm 30\%</math>.</p> <p>Compared data to Rutherford cross section.</p>
"Charge Analysis and Differential Cross Section Measurements for Large-Angle Argon Ion-Argon Atom Colli- sions with Energies between 25 and 138 keV" [64] (1956)	$\text{Ar}^+ + \text{Ar}$ $\text{He}^+ + \text{Ar}$	Several energies between 25 and 138	4-20	$\pm 0.5$	<p>Scattered beam elec- trostatically ana- lyzed.</p> <p>Used (i) Faraday cup, (ii) secondary elec- tron multiplier, and (iii) thermal detec- tor to measure scat- tered current.</p> <p>Relative value on <math>\frac{d\sigma}{d\omega}</math> <math>\pm 20\%</math>.</p> <p>Absolute error on <math>\frac{d\sigma}{d\omega}</math> <math>\pm 50\%</math>.</p>

Table 2. Experimental Work of E. Everhart's Group (Measurements Include Both the Differential Scattering Cross Sections and  $P_n$ ) (Concluded)

Title, Reference, Date	Cases Examined	Energy Range (keV)	Angular Range (°)	Angular Resolution (°)	Comments
					Error in $P_n$ data ± 10%.
					Compare $Ar^+$ scatter- ing with screened Coulomb potential; $He^+$ scattering with Coulomb potential.
"Measurements of Large- Angle Single Collisions between Helium, Neon, and Argon Atoms at Energies to 100 keV" [8] (1957)	$He^+ + \begin{Bmatrix} He \\ Ne \\ Ar \end{Bmatrix}$ $Ne^+ + \begin{Bmatrix} Ne \\ Ar \end{Bmatrix}$ $Ar^+ + Ar$	25, 50, 100	4-40	± 0.5	Improved accuracy of $\frac{d\sigma}{dw}$ by: (i) measuring beam current in col- lision chamber with a Faraday cup, (ii) improving scattering geometry.  Compare $He^+$ data with Rutherford scatter- ing.  Compares data with Fedorenko <sup>16</sup> --agree- ment as to magnitude, but some difference on slope.



ing with the particular reported work; the relative accuracy was much better than this. The error in  $P_n$  was  $\pm 10$  percent.

7. The scattering cross sections all compared well with theoretical predictions which used a screened Coulomb type potential (a Bohr potential). The scattering of  $\text{He}^+$  ions was compared with calculations based on a simple Coulomb potential.

L. I. Pivovar<sup>37,56-58</sup>

This series of papers, Table 3, concentrated on the scattering of heavy ions ( $\text{Ar}^+$  and  $\text{Kr}^+$ ) by noble gases heavier than He. The total differential scattering cross sections were reported. These measurements were differential in energy at a fixed scattering angle; they were not measured as a function of scattering angle.

As the energy dependence of these cross sections was given at only three different angles, it is possible to compare these measurements with other reported work at only three points. This fact was unfortunate; it would have been very interesting to see if structure exists in the differential scattering cross sections at the high energies of this set of experiments, since structure has been reported at 50 keV in the differential scattering cross section curves as a function of angle for some of the same projectile-target combinations.<sup>21</sup>

In this work Pivovar also measured the fraction of the scattered projectiles in each particular charge state. These data compare very well with the statistical theory of Russek.<sup>18</sup> The data do not show the definite plateaus and "breaks" as exhibited by the data of Afrosimov which are discussed below. (Pivovar and Afrosimov do not measure exactly the same thing; Pivovar plots  $P_n$  as a function of energy--250 to 1400 keV--

Table 3. Experimental Work of L. I. Pivovar's Group (Measurements Include Both Differential Scattering Cross Sections and  $P_n$ )

Title, Reference, Date	Cases Examined	Energy Range (keV)	Angular Range (°)	Angular Resolution (°)	Comments
"Differential Scattering Cross Section and Charge State Distribution of an Argon-Ion Beam in Single Collisions with Gas Atoms at 250-1400 keV" [37] (1963)	$\text{Ar}^+ + \text{Ar}$ $+ \text{Kr}$	250-1400	1,2,3 Does not measure as function of angle	Divergence of scattered beam 0.5	Electrostatic separation of charge state.  Measured scattered currents with Faraday cups.  Pressure measured with ionization gauge calibrated against McLeod gauge.  $P_0$ negligible even at $1^\circ$ .
"Differential and Integral Cross Sections for the Loss and Capture of Electrons by Singly Charged Ions at 250-1400 keV Energies" [56] (1964)	$\text{Ar}^+ + \text{Ar}$ $+ \text{Kr}$	250-1400	0-3	Divergence of scattered beam 0.5	Measures differential scattering cross section at $1^\circ, 2^\circ, 3^\circ$ as in [37]; opened slits to count all ions $0-1^\circ$ .
"Deep 'Stripping' and Scattering of $\text{Kr}^+$ Ions in Single Collisions with Ne, Ar, Kr, and Xe Atoms" [57] (1966)	$\text{Kr}^+ + \begin{Bmatrix} \text{Ne} \\ \text{Ar} \\ \text{Kr} \\ \text{Xe} \end{Bmatrix}$	250-850	0-3	Divergence of scattered beam 0.5	Measured charge state $n = 12+$ .  Random error in differential scat-

Table 3. Experimental Work of L. I. Pivovar's Group (Measurements Include Both Differential Scattering Cross Sections and  $P_n$ )(Concluded)

Title, Reference, Date	Cases Examined	Energy Range (keV)	Angular Range (°)	Angular Resolution (°)	Comments
					tering cross section $\approx 25\%$ .  Differential scattering cross section agrees well with screened Coulomb potential.
"Differential and Integral Cross Sections for the Loss and Capture of Electrons by Fast $N^+$ , $Ne^+$ , and $Ar^+$ Ions" [58] (1966)	$\left. \begin{matrix} N^+ \\ Ne^+ \\ Ar^+ \end{matrix} \right\} + \left\{ \begin{matrix} Ne \\ Ar \\ Kr \\ Xe \end{matrix} \right\}$	250-1400; some data to 1800	0-3	Divergence of scattered beam 0.5	

at three fixed angles, whereas Afrosimov shows  $P_n$  as a function of angle--five to 40 degrees--at a fixed energy, 25 keV.)

Specific comments on the experimental apparatus of Pivovar follow.

1. Scattered currents were measured with a Faraday cup. Previous comments about this technique are equally applicable here.

2. The scattered particle current was electrostatically analyzed.

3. The scattered particle current and beam current were measured sequentially.

4. Pressure was measured with an ionization gauge which was in turn calibrated against a McLeod gauge.

5. Pivovar estimates that his random error in differential cross section measurement was approximately 25 percent. His data agree with theoretical curves based on a screened Coulomb potential. No estimate is given of his absolute error.

V. V. Afrosimov<sup>4,21,59</sup>

Afrosimov measured the differential scattering cross section for several noble ion-atom combinations. This work is summarized in Table 4. A number of deviations from smooth curves were found (when the differential cross sections were plotted as a function of angle) which appear in the form of bumps superimposed on the smooth curve. The existence of this structure was used to support the concept of collective oscillations in the electron shells which had been advanced to explain coincidence data.<sup>21,65</sup>

These data are presented to supplement other work, and they suffer badly in this role because the experimental conditions were not specified and must be inferred. Specific comments follow.

1. The particle detection system is unknown; however, it is

Table 4. Experimental Work of V. V. Afrosimov's Group (Differential Scattering Cross Sections Were Measured)

Title, Reference, Date	Cases Examined	Energy Range (keV)	Angular Range (°)	Angular Resolution (°)	Comments
"Ionization and Scat- tering with Character- istic Energy Losses in Atomic Collisions" [4, 21] (1965)	Ar <sup>+</sup> + Ne	25, 50	4-25	1	Gives NO direct information on experimental apparatus. Implied that angular resolu- tion ≈ 1°. Daly type count- ing system used for particle detection.  Shows graph, dσ/dω for Kr <sup>+</sup> + Kr at 50 keV; deviates from screened Coulomb curve in form of bumps superimposed on smooth curve; deviations ≈ 10-30%.  Concludes from curve: "Form of dσ/dω curves give grounds for assuming that the real interaction potential is not a continuous function of the shortest distance (of ap- proach), and apparently chan- ges abruptly on going from the excitation of one char- acteristic line to the exci- tation of another."
	Ar <sup>+</sup> + Ar				
	Kr <sup>+</sup> + Kr				
"Peculiarities of Scat- tering in Violent Colli- sions of Atomic Par- ticles [59] (1967)	ions + atoms of noble gases. Specific cases: Kr <sup>+</sup> + Xe Kr <sup>+</sup> + Kr	25, 50	5-40	≈ 1/6	Kr <sup>+</sup> + Kr most pronounced ir- regularity.

believed that it was probably a Daly-type device such as was used in the coincidence work.<sup>55</sup> A Daly-type detector is suitable for single-particle counting.

2. The angular resolution in the initial measurements was improved to 10 minutes in subsequent work.

3. The separate charge states were not analyzed in the measurement of the differential scattering cross section curves. However, the fraction of charge states was analyzed as a function of angle in at least one case. The charge states were magnetically analyzed.

4. The method of measurement of the incident beam was not specified.

5. The method of measuring the target gas pressure was also not mentioned.

6. The error in these measurements was not stated.

In this work, projectile-target combinations were examined that had been measured earlier by both Fedorenko and Everhart. It is not surprising that the structure found had not been seen previously. Improved angular resolution and detector efficiency made possible the observation of the features reported by Afrosimov. It is regrettable that these data have not been reported in a more thorough manner.

#### Present Experiment

Prior to the present measurements, total differential scattering cross sections as a function of scattering angle have been measured at fixed energies up to 100 keV for  $\text{He}^+$  projectiles. The angular resolution in these measurements was approximately one degree. Total differential scattering cross sections have been measured as a function of energy to

1400 keV at fixed scattering angles. Also, total differential scattering cross sections have been measured as a function of scattering angle at fixed energies to 50 keV with fine angular resolution; however, these extensions have been made only in heavy noble gas ions-atom collisions.

The present work measures the total differential scattering cross section (also the differential scattering cross section for electron capture, electron stripping, and scattering without change of charge) as a function of scattering angle at several specific energies between 150 and 830 keV with an angular resolution of approximately 10 minutes. Additionally, the probability of electron capture and electron stripping at fixed angles for  $\text{He}^+$  ions was measured from approximately 150 to 830 keV. (These probabilities had been previously reported from 10 to 200 keV.) Thus, the present measurements fill a gap in the overall data picture by extending to higher energy measurements of the scattering of  $\text{He}^+$  ions, and it complements the extensive low energy measurements<sup>2,3</sup> for these same collision partners.

The experimental techniques and apparatus are considerably different in the present measurements from those used by other workers. These differences will not be specified here; they are discussed in detail in Chapter IV.

## CHAPTER IV

### APPARATUS AND TECHNIQUES OF MEASUREMENT

The present apparatus was originally designed to perform a coincidence experiment.<sup>66</sup> To accomplish this task and also to have a most versatile piece of equipment, the design provided the capability of measuring the cross section differential in either the scattering angle of the projectile or the recoil angle of the target. Thus, there exist two detection systems which rotate about a common axis and which view a common volume of the incident beam in the collision chamber. The present experiment utilizes only one of these detection systems, the analysis system for the fast scattered particle.

In discussing the apparatus, we shall consider the source of projectiles, the hardware of the scattering experiment, i.e., the mechanical construction, the vacuum system and the electronics, the tests used to evaluate the experimental equipment, and the techniques which were employed in making the actual measurements. Also, the source of possible errors in the measurements will be discussed.

#### Source of Projectiles

A one MV Van de Graaff positive ion accelerator was the source of projectiles in this experiment. This accelerator has been previously described in detail.<sup>66,67</sup> During the present measurements, the energy calibration was verified empirically by measuring with a nuclear magnetic resonance gaussmeter the field of the beam analyzing magnet that corres-



ponds to the 1.019 MeV threshold energy<sup>68</sup> of the  $\text{H}^3(\text{p},\text{n})\text{He}^3$  nuclear reaction.

$\text{He}^+$  ions were the projectiles used during this investigation. In order that the states of the collision partners be precisely defined, it was very important that these projectiles be in their ground state when entering the collision chamber. The following discussion will present the reasons for believing the projectiles were in the ground state upon entering the collision chamber.

Certainly, when the ions were first formed in the ion source bottle in the Van de Graaff, they populated all excited states of the ion. Between the source bottle and the collision chamber the projectiles traveled a path of approximately 10 meters with a velocity of  $10^8$  cm/sec, thus, the flight time from source to collision chamber was of the order 10  $\mu\text{sec}$ . Along this path the projectile (1) traveled through the accelerator tube where the field strength was of the order of  $8 \times 10^3$  volts/cm, (2) traveled through a set of deflection plates in which the field strength was approximately 500 volts/cm, (3) were deflected by the analyzing magnet which sorts the proper charge state with an "equivalent" electric field ( $E = v \times B$ ) of approximately  $10^4$  volts/cm, and (4) passed through a final set of deflection plates where the field was of the order 200 volts/cm, before entering the collision chamber.

The lifetime of an excited state of a hydrogen-like atom of nuclear charge  $Z$  is of order  $Z^{-4}(10)^{-9}$  sec.<sup>69</sup> Hence, the lifetimes of the excited states of the hydrogen atom, which are tabulated,<sup>70</sup> are certainly an upper limit on the lifetimes of the allowed states of a  $\text{He}^+$  ion. For the following estimates these tabulated lifetimes have been used.

Excited states with  $n \leq 6$  have very short lifetimes and will decay before reaching the collision chamber. The 2s state is an exception and will receive special attention below. Excited states (ns) where  $6 \leq n \leq 18$  have lifetimes too long to decay in the flight time of the projectile; however, Stark mixing of the substates of each n state in the electric field of the accelerator tube will cause these states to decay before reaching the collision chamber. The mixed states have a transition probability approximately equal to the transition probability of the (n,p) level. The lifetime,  $\tau$ , of these states is given by

$$\tau(n,p) \approx 0.054 n^3 \times 10^{-8} \text{ sec}$$

for all states  $n \leq 25$ .<sup>71</sup> Excited states for  $n \geq 18$  will be stripped of their electron due to Lorentz ionization<sup>72</sup> in the electric field of the accelerator tube and will be eliminated when the beam is charge selected by the deflecting magnet. Hence, all allowed excited states of the projectile will have undergone radiative decay or will have been Lorentz ionized before reaching the collision chamber.

Particular attention must be given to the metastable 2s state. Harrison, et al.<sup>73</sup> report that the lifetime of this state as a function of the quenching field,  $\xi$ , (volts/cm) is

$$\tau = \frac{1.4(10)^{-2}}{\xi^2} \text{ sec} .$$

The electric fields in both the accelerator tube and the analyzing magnet are sufficient to quench this metastable state; thus, it should be ef-

fectively removed from the beam before the projectiles reach the collision chamber.

One other problem that must be considered is the repopulation of excited states through collisions with residual gas. The background pressure in the connecting tubing between the deflecting magnet and the collision chamber is better than  $10^{-5}$  Torr. Assuming a cross section of excitation into excited states of  $10^{-19}$  cm<sup>2</sup>, less than 0.01 percent of the incident beam will be excited between the analyzing magnet and the collision chamber. Therefore, it is concluded that the projectiles entering the collision chamber are He<sup>+</sup> ions in their ground state.

### Description of Scattering Apparatus

#### Mechanical Construction

The apparatus utilized in this experiment is composed of four principal parts: the support and rotation assembly, the collision chamber, the projectile collimation, and the analysis system. These subsystems which will be described can be seen in Figure 4.

Support and Rotation Assembly. A stainless steel shaft, Figure 5, is the kingpin of the entire apparatus. It is mounted vertically, and this shaft supports and aligns the entire experiment. Its center line is the axis of rotation for both detection systems. The bottom of the shaft has a close-tolerance fit through a massive piece of thick-walled steel tubing. A lip on the shaft rests on the top of this tubing (these are both finished surfaces) and these support not only the shaft but the entire apparatus. A lock nut holds the shaft rigidly to the tubing. The tubing itself is welded both to the top and bottom flanges of three I-beams which are in turn welded together along both flanges. A steel plate

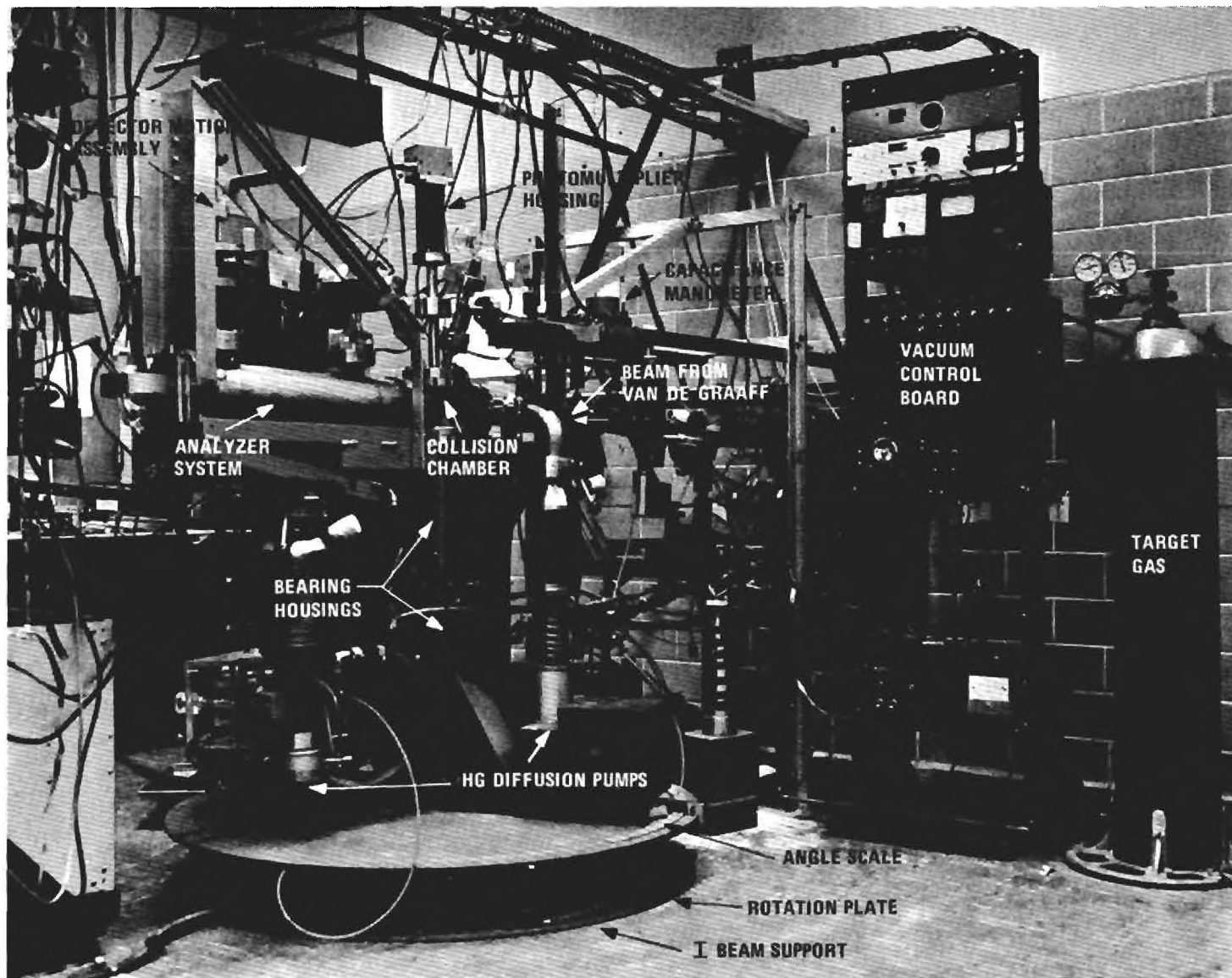


Figure 4. Apparatus.

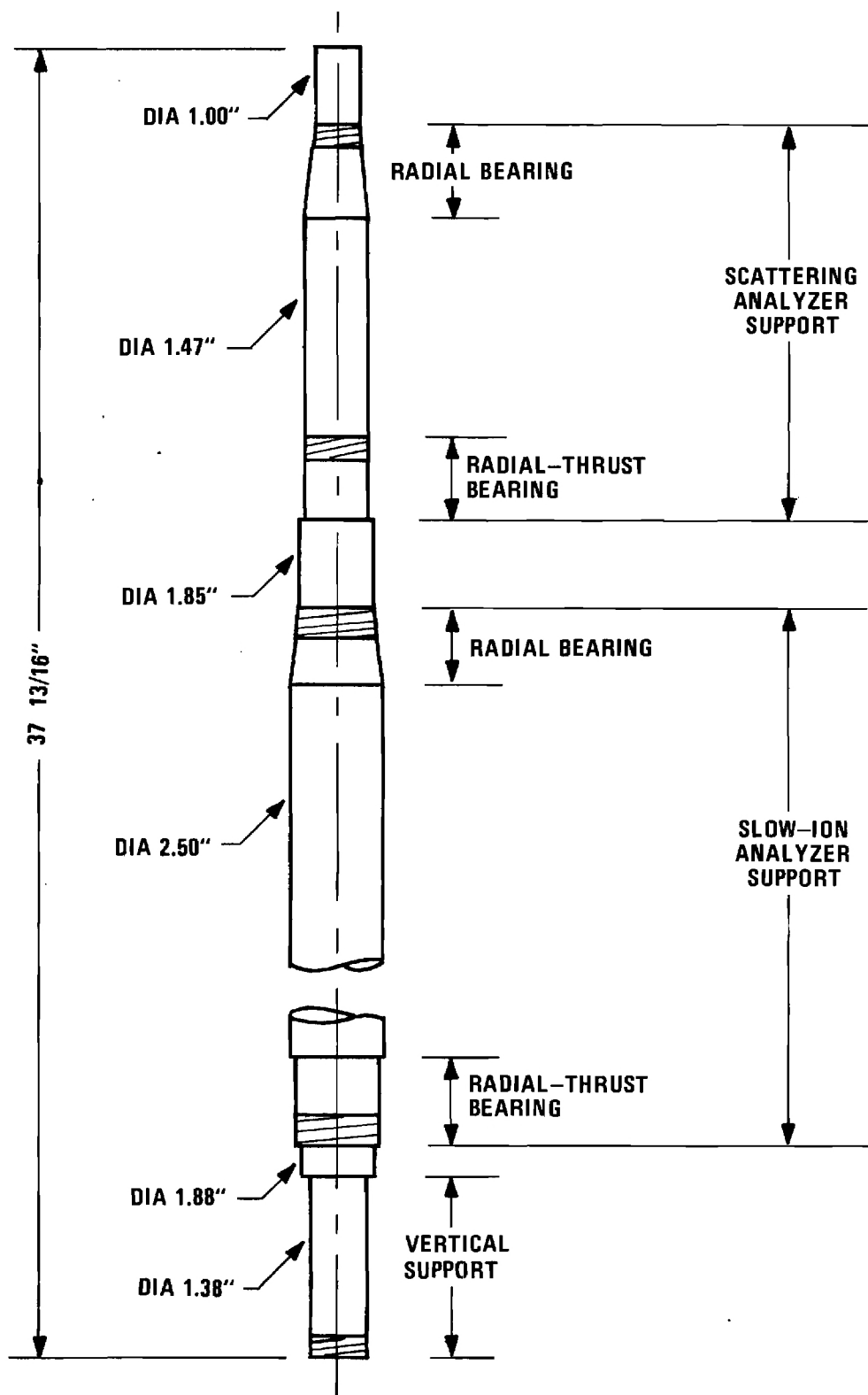


Figure 5. Main Support Shaft.

of diameter 48.6 inches is screwed to the top of the I-beams, and it has the angle scale mounted on it. (The thick-walled tubing and joints of the I-beams are hidden beneath this steel plate and cannot be seen in the photograph, Figure 4.)

A five-eighths inch bolt located at the end of each I-beam provides the apparatus with a vertical degree of movement and tilt for alignment with the ion beam from the Van de Graaff. The five-eighths inch bolts rest on a plate which can be rotated relative to the base plate providing a horizontal degree of freedom in aligning the apparatus. These features are visible in the photograph, Figure 4. These two degrees of movement are for gross alignment of the entire apparatus with the projectile beam from the accelerator. The internal alignment procedures and provisions for steering the projectile beam will be discussed below.

Two identical rotation systems are attached to the shaft, one mounted vertically above the other. The lower rotation system supports the slow-ion recoil assembly (which was not utilized in the present experiment); the upper rotation system supports the fast beam analyzer (referred to henceforth as the analyzer system). The mounting positions of these analyzers are shown in Figure 5.

Each rotating detection system is suspended by two high-precision bearings. The bottom bearing is of a two-way radial thrust type. It is slipped on the shaft to a machined shoulder which supports it. This bearing is actually a pair of back-to-back radial-thrust ball bearings which were prestressed to remove all clearance and preload the bearing. The top bearing is a double row radial roller bearing in which zero clearance is attained in a different manner. The inside of the inner race has a

slight taper, matched by a taper on the shaft at that location. A nut on the shaft above this bearing is tightened, driving the bearing down the taper to stretch the inner race and stress the rollers. The high precision performance of this bearing is dependent on proper tightening of this nut.

Rigidly attached to a massive steel housing that is closely fitted to the outer race of these bearings is a massive arm supporting the analyzer system and, exactly opposite it, an angle indicator and counterweight arm. The counterweight is adjusted to eliminate, as far as possible, any net torques from acting on the shaft. These features are visible in Figure 4.

Collision Chamber. The collision chamber rests atop the main axle shaft. Three bellows connect the collision chamber to the rest of the apparatus. These bellows are welded to the chamber and flanged to the bases of three brass cones. The tips of these cones protrude into the collision chamber proper to within approximately an inch of the rotation axis. These cones hold the collimating apertures for the projectile beam, for the recoiling slow ions, and for the scattered fast particles. Figure 6 is a photograph of the interior of the collision region where the tips of the three cones are visible.

In the present experiment it was necessary to provide a means of measuring the projectile current in the collision region and, further, to be able to monitor this current continuously. Mounted to the top of the collision chamber is a retractable Faraday cup, for absolute measurement of the beam current, and a photomultiplier and lens assembly, for continuous monitoring of the product of the beam current and target gas

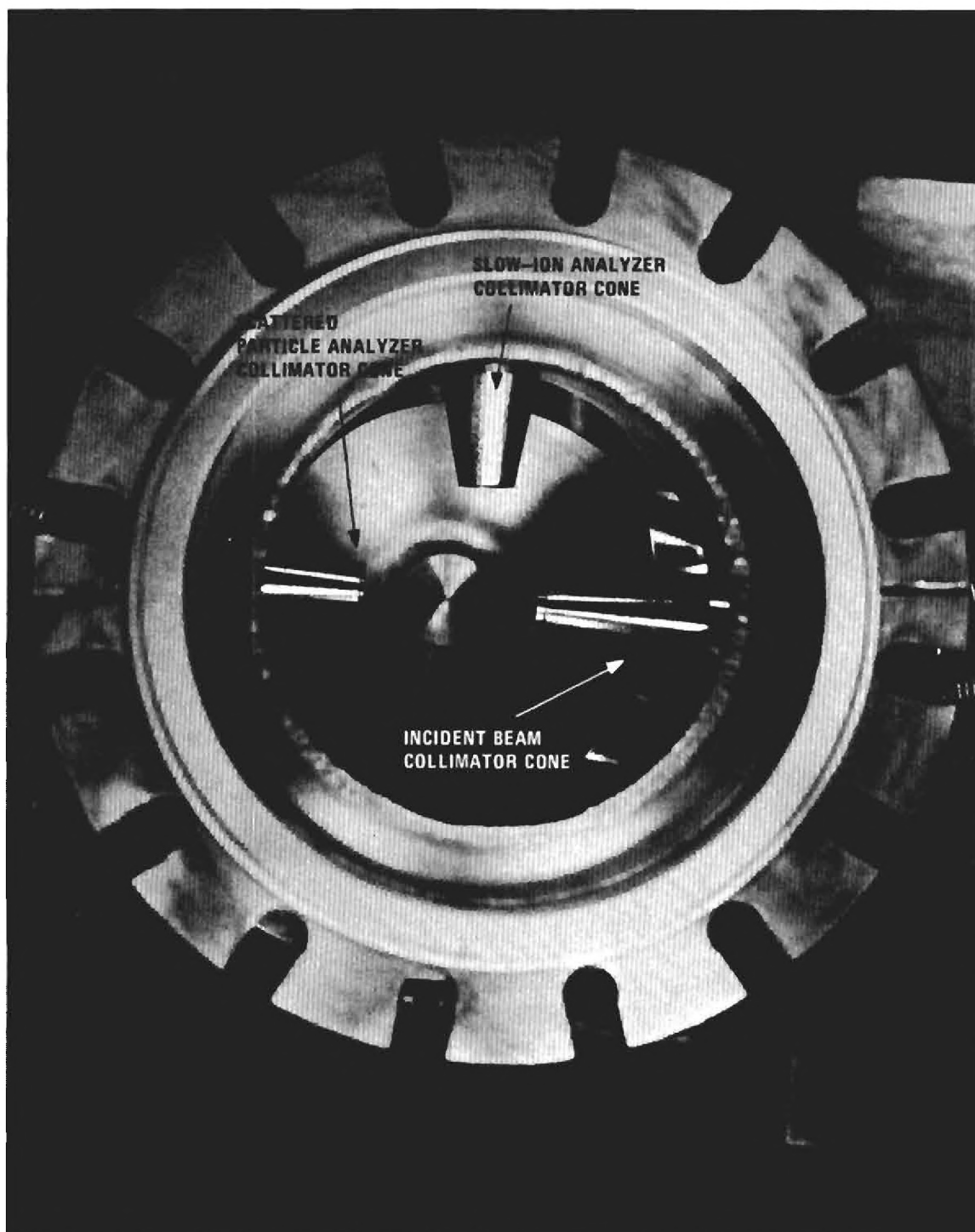


Figure 6. Interior of Collision Chamber.



pressure. This monitoring system will be discussed in a later section of this chapter. The top of the collision chamber can be seen in the photograph, Figure 7.

The Faraday cup has a slanted back surface so that secondary electrons emitted when the projectile beam impinges on the back of the cup are directed preferentially to the walls of the Faraday cup. Additionally, there is a secondary electron suppressor plate in front of the cup and insulated from it. The projectile beam entered the Faraday cup through a circular hole, three-sixteenths inch in diameter, located in the center of the suppressor plate. The beam diameter at this point was less than 0.042 inch. (The beam diameter is discussed below.) This shield was negatively biased (typically -20 to -60 volts) to return any secondary electrons near the mouth back into the cup. Current to this shield could be monitored. When the cup was in fully extended (down) position, it was observed that no current was collected on this shield (whether it was negatively biased or not).

The photomultiplier was an E. M. I. #6256S tube. It measured the collisionally induced photon emission from the target gas. The properties of this photomultiplier tube and associated optical components will be discussed in a later section of this chapter.

These mounting arrangements of the Faraday cup and the photomultiplier require that the top of the chamber remain stationary with respect to the projectile path through the collision chamber. This chamber was mounted so that it was free to rotate about the vertical axis as the angular positions of the two analyzers were varied. However, the slight rotations accompanying movement of only the fast beam analyzer over the angular

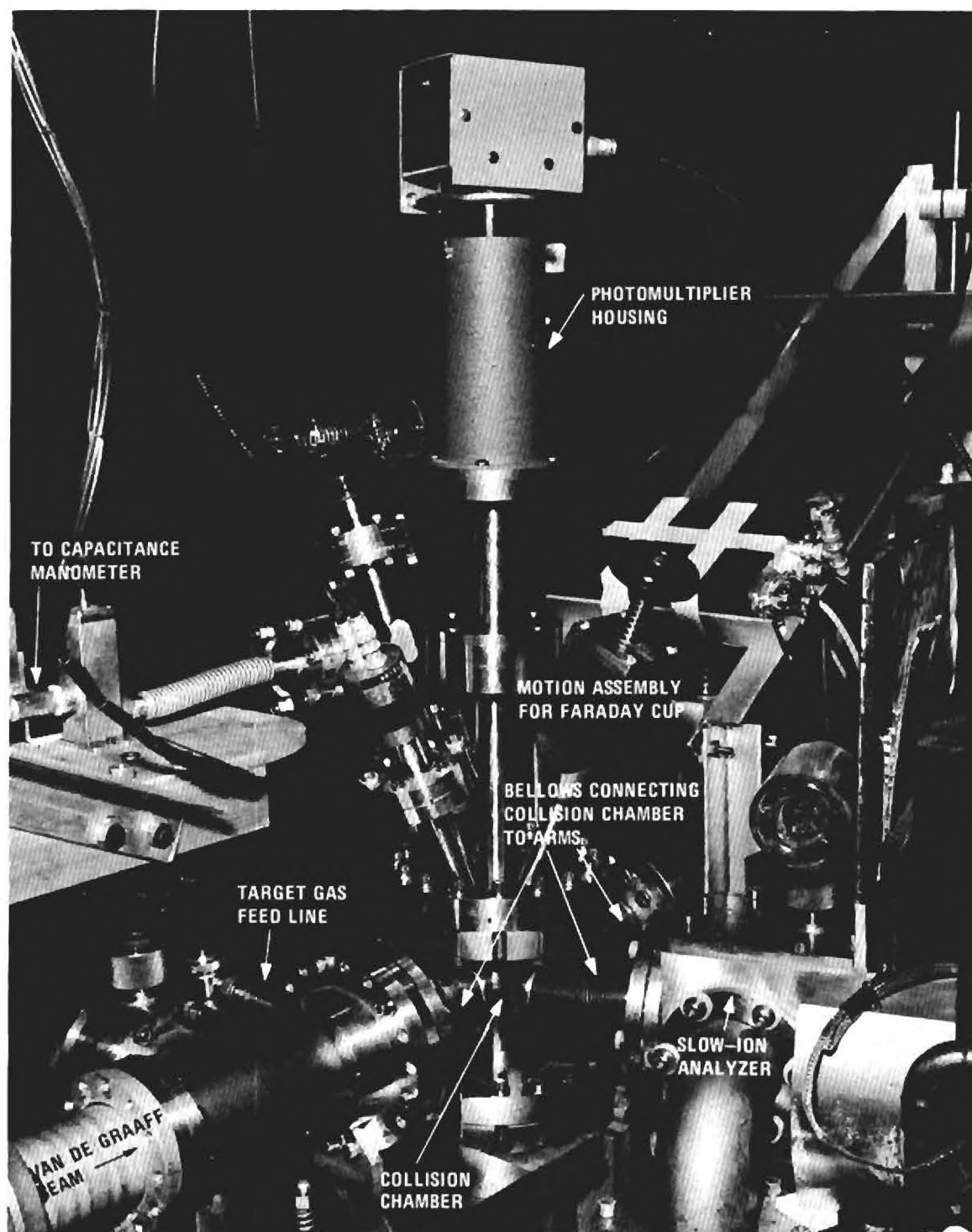


Figure 7. Top of Collision Chamber.

range involved in the present measurements were observed not to affect the photon counting rate or the projectile current measured with the Faraday cup. Also mounted to the collision chamber is an ionization gauge and a flexible connection to a capacitance manometer.

To better illustrate exactly how the Faraday cup and photomultiplier are mounted, a cross sectional view of the top of the collision chamber is shown in Figure 8. A bellows assembly from a two inch Veeco gate valve provides motion for the retractable Faraday cup. In its "down" position the collimated beam from the Van de Graaff is intercepted by this cup; while in its "up" position the cup does not obscure the view of the beam region of the photomultiplier. The Faraday cup collected the beam at the same location as that viewed by the photomultiplier; therefore, these measurements could not be made simultaneously.

A two-lens system focuses the photons on the photocathode. The first lens is mounted on the top of the collision chamber approximately two and one-half inches from the beam path. A fine Ni mesh of 97 percent transparency is mounted in front of this lens to prevent any charge buildup on this dielectric surface from producing fields in the beam region. The second lens (see Figure 8) then focuses the photons onto the photocathode. This lens also provides the vacuum seal. These features, as well as the Faraday cup in its retracted position, can be seen in Figure 8. The optics of this lens system are further described later in this chapter.

Projectile Collimation. The projectile beam was collimated by two apertures located in a non-rotating arm attached to the main support shaft. These apertures were 0.025 inch in diameter and were separated by five inches. The projectiles pass through a third aperture of larger diameter

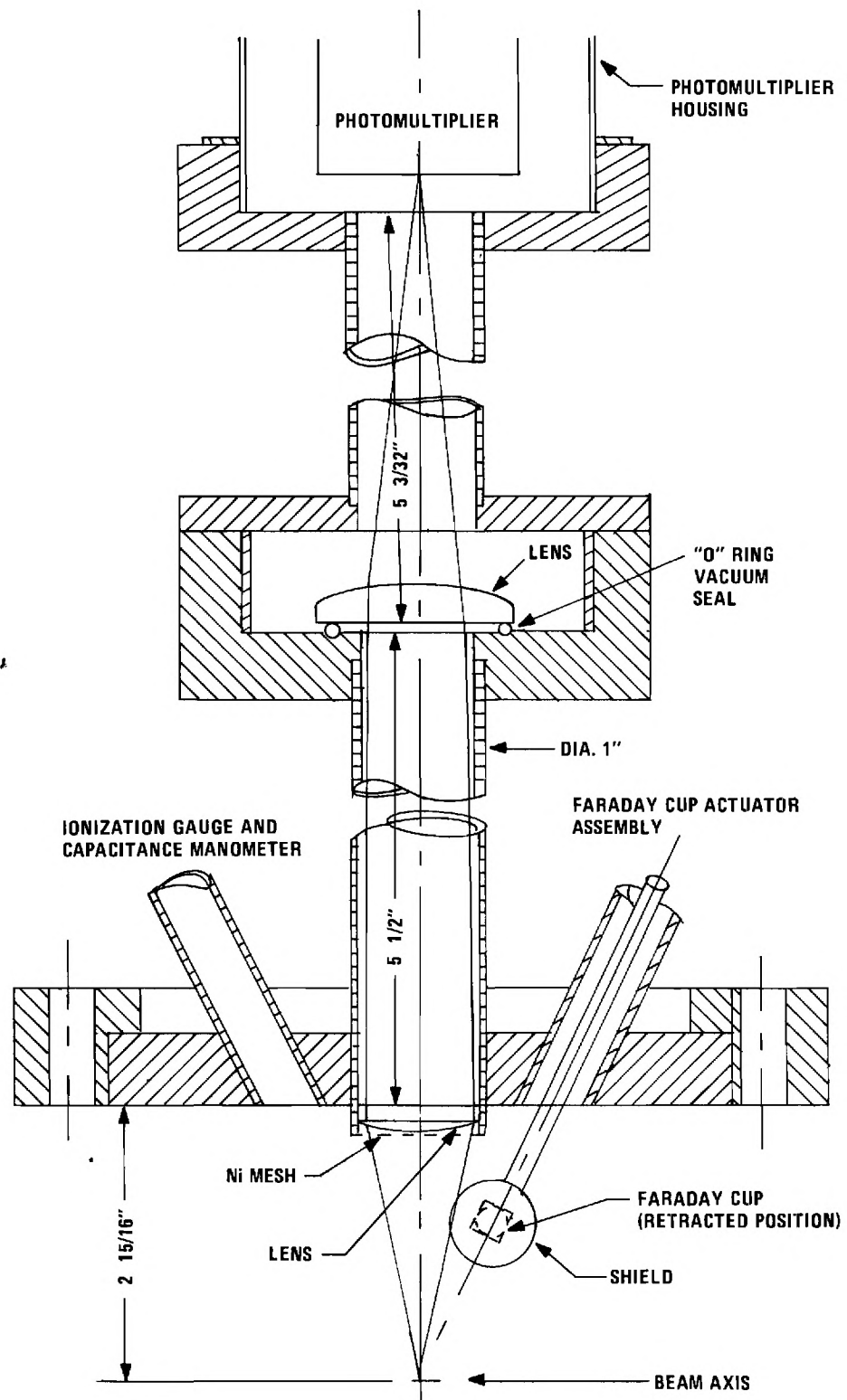
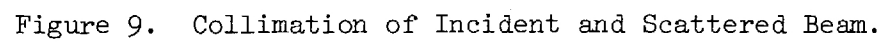


Figure 8. Cross Sectional View of Top of Collision Chamber.

to enter the collision region itself. This aperture is 0.048 inch in diameter and is located 1.48 inches from the axis of rotation. Its purpose is to confine the target gas to the collision region. The beam should not strike the edge of this aperture; however, some ion burn has been detected around the edge of this aperture. A diagram of the projectile beam collimation as well as the collimation of the scattered beam is given in Figure 9.

The maximum angular divergence of two rays defined by the 0.025 inch apertures is 34 minutes of arc. The third aperture (diameter 0.048 inch) limits this maximum divergence to 26 minutes of arc, which would produce a beam diameter of 0.059 inch over the rotation axis. However, the actual projectile beam is, in principle, nearly paraxial when it enters the two collimating apertures, because it comes from a small focus 10 feet away. Scattering from residual gas degrades this paraxial quality of the beam. Measurement of the smallest scattering angle indicates a maximum divergence of the projectile beam to be between 12 and 18 minutes of arc, but most of the intensity is much more paraxial than these maximum limits, as indicated by measuring the intensity profile. This leads to the conclusion that the diameter of the projectile beam was between 0.028 inch (only 0.003 inch greater than the geometrical optimum beam diameter) and 0.042 inch (considerably smaller than the worst possible case).

Analyzer System. Particles scattered through an angle  $\theta$  were collimated and passed into the analyzer system by a two-slit geometry. This beam of scattered particles passed through a parallel plate electrostatic deflector for separating the charge states and was then counted individually with a surface barrier detector. At the energies of the present experiment



this detector was 100 percent efficient. A schematic drawing of the entire apparatus, showing the relation of the analyzer to the projectile beam and the collision chamber, is presented in Figure 10.

The size and location of the slits forming the collimation geometry are shown in Figure 9. The calculated "maximum angular spread" of this geometry is 18 minutes; however, measurements of the width of the scattered beam at the detector, to be described later in this chapter, indicate an angular spread of approximately 10 minutes. The minimum angle possible before an edge of the first aperture (0.0156 inch x 0.040 inch) entered the unscattered beam in the collision region was approximately one degree. As soon as an edge of this aperture entered the main projectile beam, many particles of degraded pulse height (apparently scattered from the slit edge) were counted by the detector, and it became impossible to make measurements below this limit. (The method of detecting these slit-edge scattered particles will be described in the "Techniques" section of this chapter.)

The scattered beam was collimated by two rectangular slits, thus, at the detector, the scattered projectiles formed a rectangularly shaped beam. Measurements (to be described below) indicated the size of this beam to be approximately 0.070 inch x 0.090 inch (width by height), and these dimensions are in good agreement with calculated estimates based on the geometry of the two-slits. The calculated maximum divergence of a beam that could pass through these two-slits would give an image 0.120 inch x 0.150 inch at the detector.

The scattered particle analyzer section of the apparatus is contained in a long stainless steel tube whose supporting frame is rigidly

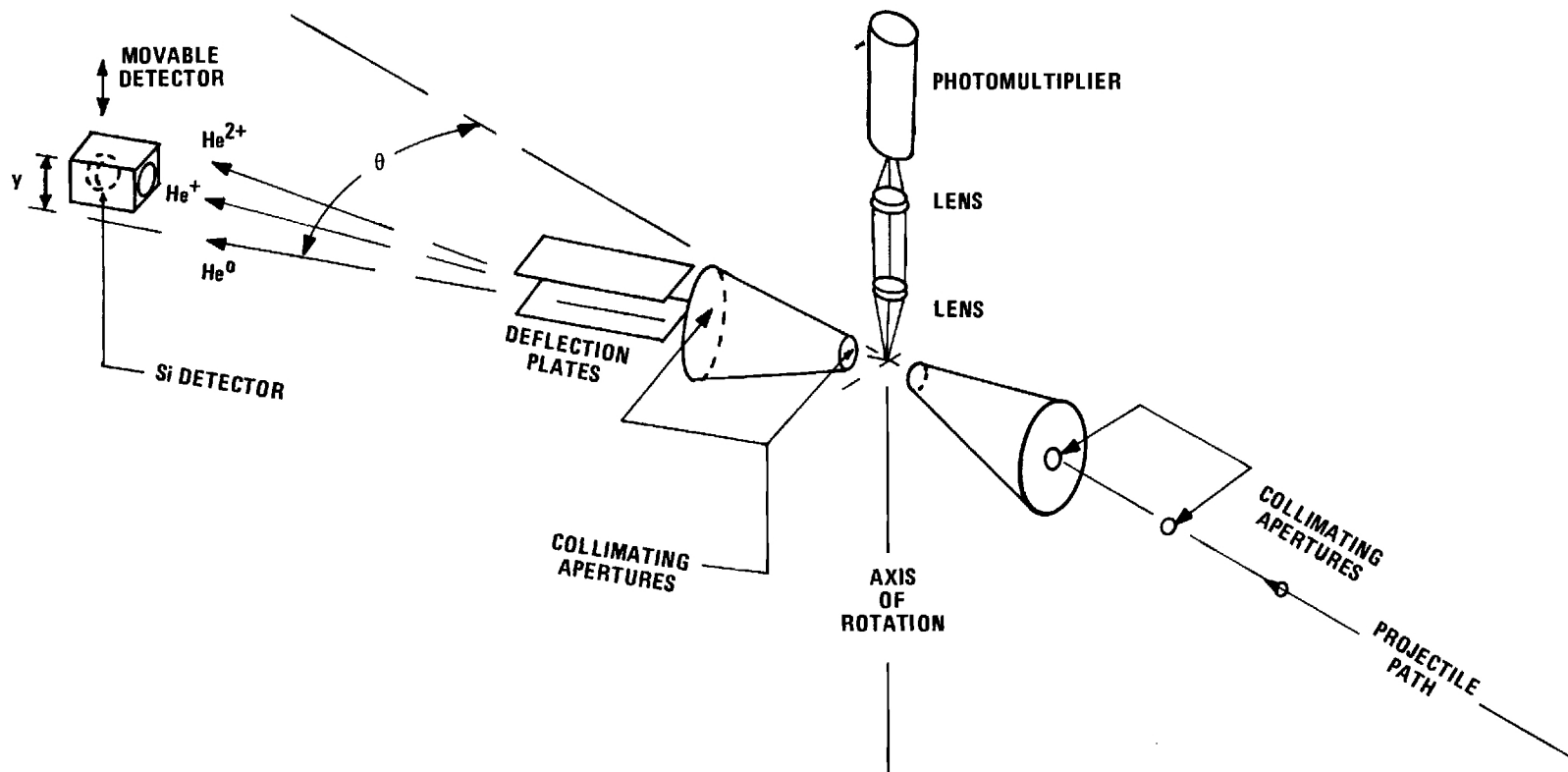


Figure 10. Schematic of Scattering Apparatus.



secured to the bearing housing (see Figure 4). As previously described, this bearing housing, and thus the entire analyzer, rotates about the main support shaft. The base of one of the three cones previously mentioned was attached to the front of the analyzer. This cone protruded through the bellows connection with the collision region to a point approximately one inch from the rotation axis. The small apertures which define the collection geometry are located in the front and rear of the cone.

Immediately following the second aperture, at the base of the cone, are a pair of parallel plates. The surface of these plates lies in the horizontal plane so that deflections produced by them are in the vertical plane. This is shown schematically in Figure 10. The bottom plate is grounded, while an electric potential can be applied to the upper plate to deflect the beam of charged particles.

Eighteen inches past the center of the deflection plates is the vertical plane containing the silicon surface-barrier detector. At the rear of the chamber is a Faraday cup which can be used to measure the beam current in the analyzer section when  $\theta \approx 0$  degrees. It is useful for studying the beam profile and to locate the true  $\theta = 0$  position. The design of this cup is very similar to the design of the Faraday cup in the collision chamber, i.e., this cup has a slanted back surface and also an electron suppressor plate, insulated from the Faraday cup, the particles entering the cup through a circular hole in the center of the suppressor plate. This Faraday cup collects scattered beam measured as a current only for scattering angles less than 20 minutes. This limitation is imposed by the current measuring capability of an electrometer,

which was used to measure this current. (The current sensitivity of the electrometer was mentioned in the preceding chapter.) The projectile current in the collision chamber cannot be measured with this Faraday cup in the analyzer section even with  $\theta = 0$ , because the defining apertures into this analyzer are smaller than the cross sectional area of the beam in the collision chamber. Measurement of the total incident current was provided by the retractable Faraday cup directly in the collision chamber, which has already been discussed.

A silicon surface-barrier detector was used to count all particles scattered through angle  $\theta$  and entering the two-slit collimation assembly of the analyzer system. This detector counts the scattered projectiles with 100 percent efficiency. (The properties of this detector will be described later in this chapter.) This detector is shielded from the environment of the analyzer system by a small box which is completely enclosed except for a hole allowing the particles passing through the two collimators to strike the front of the detector. The detector, with a portion of the box removed, is shown in the photograph, Figure 11.

The shielding box containing the detector was mounted to a drive mechanism, through a bellows, which allows it to be moved, both horizontally and vertically, in the plane perpendicular to the analyzer axis. Figure 12 shows a photograph of this drive mechanism with the detector connected to it. This movement capability was provided so that the silicon detector could be aligned on the axis of the analyzer section, as defined by the undeflected beam of scattered particles, and also moved vertically to receive particles deflected a particular distance. It was necessary that the vertical motion be very uniform and reproducible because

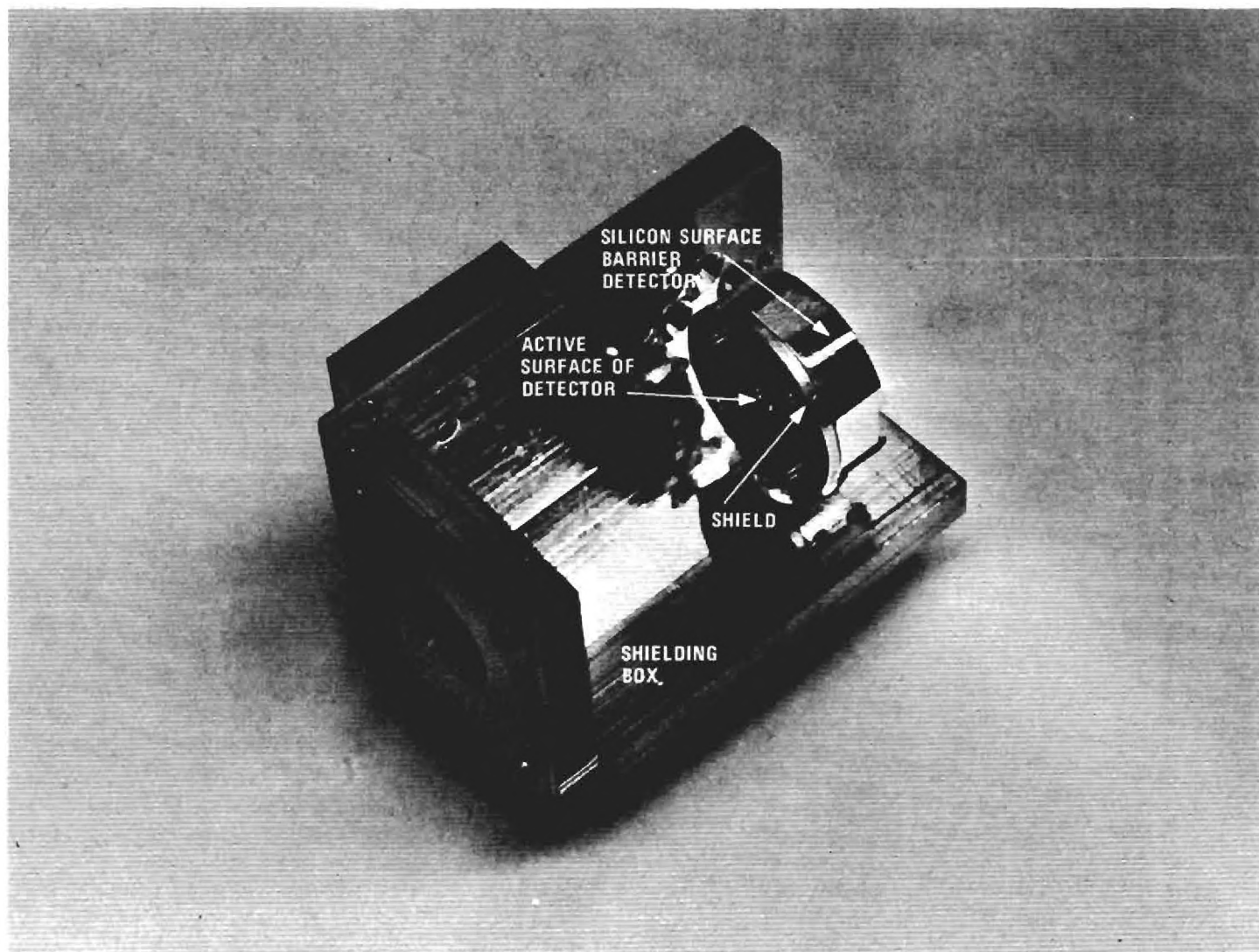


Figure 11. Silicon Surface Barrier Detector.

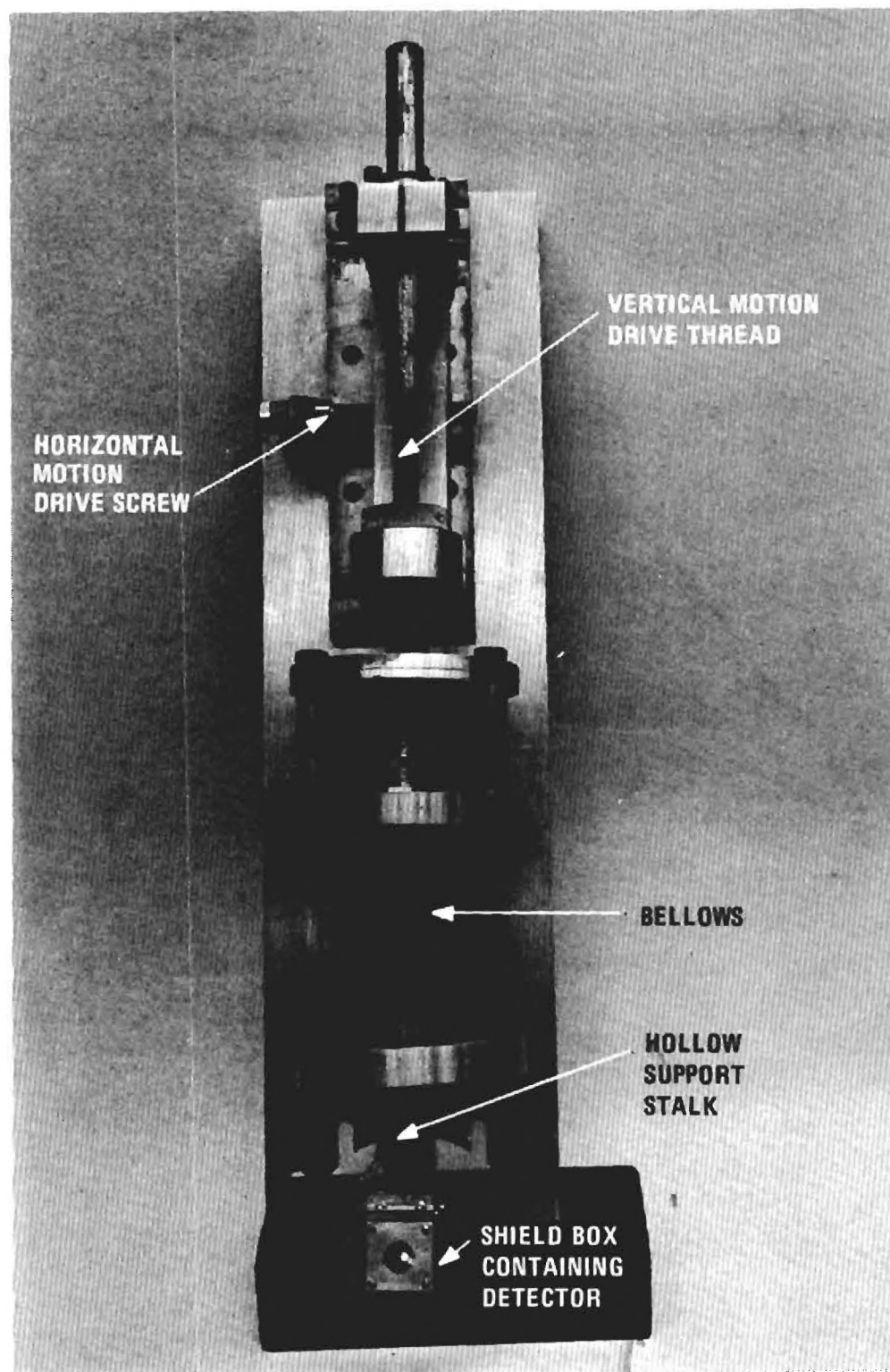


Figure 12. Two-Dimensional Motion Assembly for Silicon Detector.

the detector had to be moved vertically to a precisely defined position each time the number of particles of a particular charge state was to be counted. (The charge states of the scattered beam were separated by the deflection plates, see Figure 10.)

A case-hardened steel rod moving in a precision roller bearing provided the vertical motion for the detector. The bottom portion of the rod was threaded, and a drive nut served to move the rod a known distance to determine the position of the detector. This motion was used frequently throughout the measurements; it appeared to be uniform and reproducible to within 0.015 inch.

The horizontal motion was required only to optimize the centering of the detector in the deflected-particle plane. The movement was accomplished by a screw which drives the entire "vertical motion drive" in a horizontal track. This motion proved to have quite a bit of backlash; however, as it was only very infrequently used (only when the silicon detector was replaced), it presented no particular difficulties and was adequate.

The stalk which supports the detector shielding box in the collision chamber is actually a hollow tube, open to the atmosphere at the top but vacuum sealed at the bottom, which can be filled with a refrigerant ( $\text{CO}_2$  or  $\text{LN}_2$ ) to cool the detector and thus reduce thermal noise. However, this measure was found not to be necessary. The features of the mounting and motion assembly of the silicon detector can be seen in the photograph, Figure 12.

Initial tests indicated some spurious effects which were attributed to particles striking the glue around the edge of the detector face, which

holds it in a ceramic ring. A brass shield placed immediately in front of the detector and having a knife-edged hole opening only onto the active area of the detector eliminated this problem.

#### Alignment Procedures

Two stages were involved in the alignment of the apparatus; first, the apertures for collimating both the incident beam and the scattered particles were aligned (the internal alignment), and second the entire assembly was adjusted (using vertical and rotation adjustments described earlier) to receive the projectile beam from the Van de Graaff. As the external alignment simply rotates, elevates, and tilts the entire assembly, only the internal alignment procedures will be described.

A He-Ne laser was mounted so that its beam traveled along approximately the same path as the ion beam. It was possible to remove the bottom plate of the collision chamber and place a small pointer in the axis of rotation so that it extended into the laser beam path. With this point as a guide, the laser was moved to aim its beam directly at the rotation axis. Once this was accomplished, the laser was not moved. The apertures collimating the projectile beam and the two apertures collimating the scattered beam were individually aligned on the laser beam. The procedure itself was actually a series of successive approximations, because the construction and mounting of the incident beam collimator was such that one aperture could not be moved without affecting the position of the others. This feature was also true of the apertures collimating the scattered beam.

This alignment set the  $\theta = 0$  position of the scattering analyzer. It was estimated, by observing the shifts in the diffraction pattern of

the laser beam, that the zero degree position was determined to less than five minutes of arc. Later scattering measurements with the ion beam determined that the zero angle determined with the laser beam was two and one-half minutes. (Following a later partial realignment, zero degrees was found to be at five minutes.)

A further set of variables which was used on a day-to-day basis after these initial mechanical alignments was provided by two sets of electrostatic deflection plates for steering the incident beam into the apparatus. One of these sets of plates was located before the beam analyzing magnet, the other set was located after this magnet. The voltages on these plates were empirically adjusted to maximize the projectile current in the collision chamber.

With the apertures thus aligned, the projectiles were collimated to a narrow beam of particles whose diameter was greater than 0.025 inch but less than 0.042 inch, and this beam passed through the axis of rotation. The two collimators leading to the analyzer section were aligned on the projectile beam, and the zero position of the angular scale was known within five minutes of the true path of the projectile beam. This fact was verified by subsequent measurements with the projectile beam from the accelerator.

#### Vacuum System

The vacuum in the experimental apparatus was obtained by three two-inch Edwards mercury diffusion pumps. The three pumps were mounted beyond the bases of the three cones protruding into the collision chamber, i.e., one pump was mounted in the beam input region between the two 0.025 inch apertures collimating the projectile beam, one was located in the



fast beam analyzer, while the third diffusion pump was in the recoil ion analyzer. Each of these pumps was mounted beneath a liquid nitrogen trap. The base pressure in the regions directly above each of these pumps was typically 7 to  $8 \times 10^{-7}$  Torr.

The collision chamber was semi-isolated from the highly evacuated incident-beam and analyzer region by the small apertures which collimated the incident and scattered beams. This semi-isolation was necessary because the latter regions were held at high vacuum while there was a finite pressure of target gas in the collision chamber. Sufficient pumping speed for preliminary evacuation of the collision chamber was provided by a three-eighths inch hole in the side of the incident-beam cone. Additionally, since the slow ion analyzer was not being used, the small aperture which would normally be installed in the tip of its cone was omitted, leaving a three-eighths inch hole into the collision region. A base pressure in the collision region of  $7 \times 10^{-7}$  Torr has been obtained; however, a base pressure of  $1 \times 10^{-6}$  Torr was more typical.

While taking data, the target gas pressure in the collision chamber ranged from  $5 \times 10^{-4}$  Torr to approximately  $2 \times 10^{-3}$  Torr. A large portion of the measurements was made with a target gas pressure of approximately one micron ( $1 \times 10^{-3}$  Torr). Under operating conditions, when the pressure was one micron in the collision chamber, the pressure in the analyzer system remained approximately  $1 \times 10^{-6}$  Torr; in the beam collimation region, between the first two apertures, the pressure would be 1 to  $2 \times 10^{-4}$  Torr, because of the extra pumping hole in the side of the cone separating this region from the collision chamber. This was a cause of concern; however, careful investigation indicated that the collision chamber pressure had



to be four microns or greater before the measurements began to be noticeably perturbed by multiple collisions. Figure 13 shows this fact graphically. The ratio of the number of scattered particles to the number of incident beam particles is plotted against the target gas pressure. This graph should be a straight line of the form  $y = sx$  where the slope,  $s$ , is proportional to the product of the differential scattering cross section and the geometrical factor. Deviations from the straight line indicate the onset of multiple scattering. (The effect of the increased gas pressure in the input region would cause a scattering of the incident beam, thus a larger incident beam in the collision region. Also, charge changing collisions could occur, which would destroy precise knowledge of the state of the incident beam.) Since the data were taken at pressures well below four microns, it was concluded that multiple collisions did not affect the measurements.

Pressure in the tubulation connecting the apparatus to the accelerator was approximately  $5 \times 10^{-6}$  Torr during operation. This was maintained by two two-inch Edwards oil diffusion pumps.

The target gas is fed into the system through an Edwards needle valve. The feed line was originally maintained at approximately atmospheric pressure; however, this procedure was changed and throughout a large part of this work the line was maintained at five to 10 psig. This gas line passed through a trap immersed in dry ice and acetone to remove condensible vapors. The major features of this gas feed system can be seen in Figure 4.

During the early part of this work the pressure in the collision chamber was measured using only an ionization gauge. This method was not

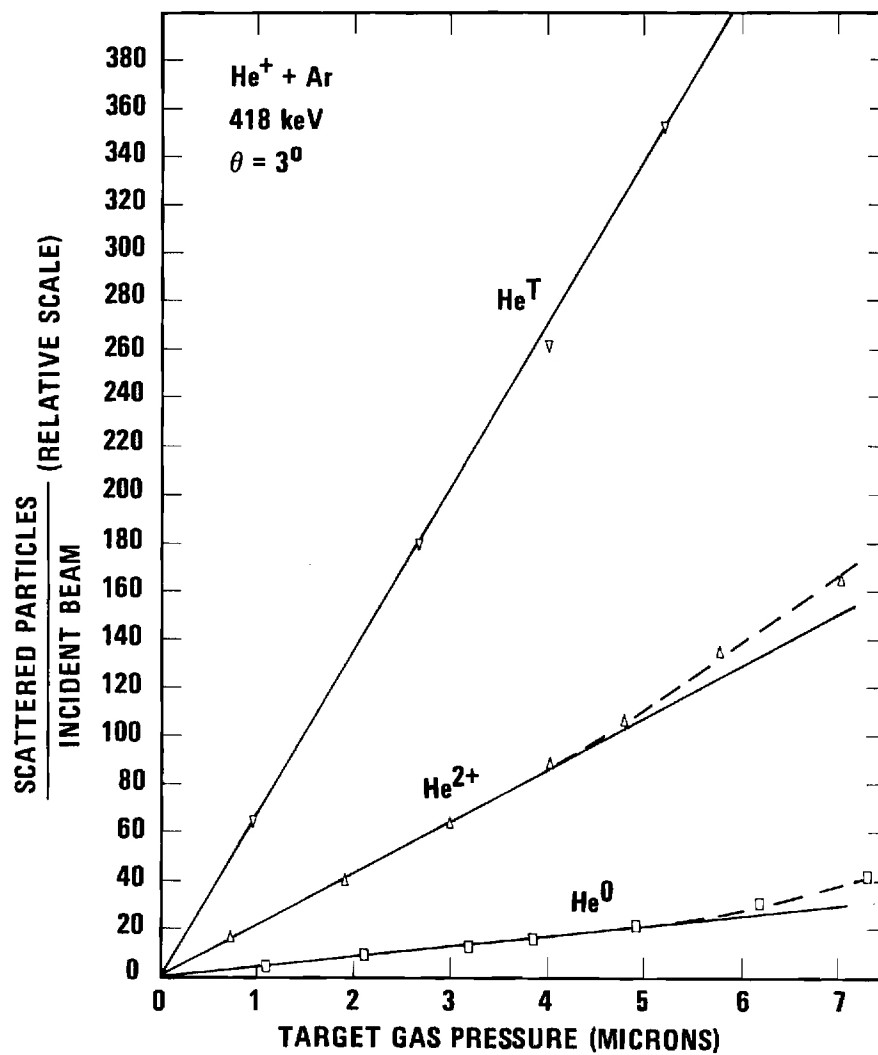


Figure 13. Scattered Projectiles Versus Pressure.

reliable enough for absolute determination of differential scattering cross sections; therefore, a capacitance manometer was added to the apparatus. This device has many advantages over the much older accepted standard, the McLeod gauge. The most notable of these advantages is that a capacitance manometer measures pressure in the sense of the definition<sup>74</sup> (i.e., as a force/unit area) and does not depend on the properties of a particular gas. The capacitance manometer was calibrated at the factory before shipment, but this calibration was at a much higher pressure than those used in this experiment. Therefore, it was felt necessary to calibrate the capacitance manometer against a standard in the pressure range that would actually be used. This calibration is described in Appendix B.

The reference side of the capacitance manometer was evacuated by a one inch Edwards oil diffusion pump with a liquid nitrogen trap. It maintained a reference pressure of less than  $5 \times 10^{-6}$  Torr.

### Electronics

In this section we shall discuss the signal handling from its origin, the detector, to its conclusion where the information was presented in a useable form by displaying it on a scaler, by printing out the results on a teletype, and/or by punching a paper tape. The information handled consisted of sets of numbers representing (1) scattered particles, (2) photons, (3) target gas pressure, and (4) beam current. The procedures used are shown schematically in Figure 14. All identifying numbers referred to in this block diagram are Ortec equipment model numbers.<sup>75</sup> Other data used in this work were recorded by direct observation of meters or scales.

A silicon surface-barrier detector, which was used to count the

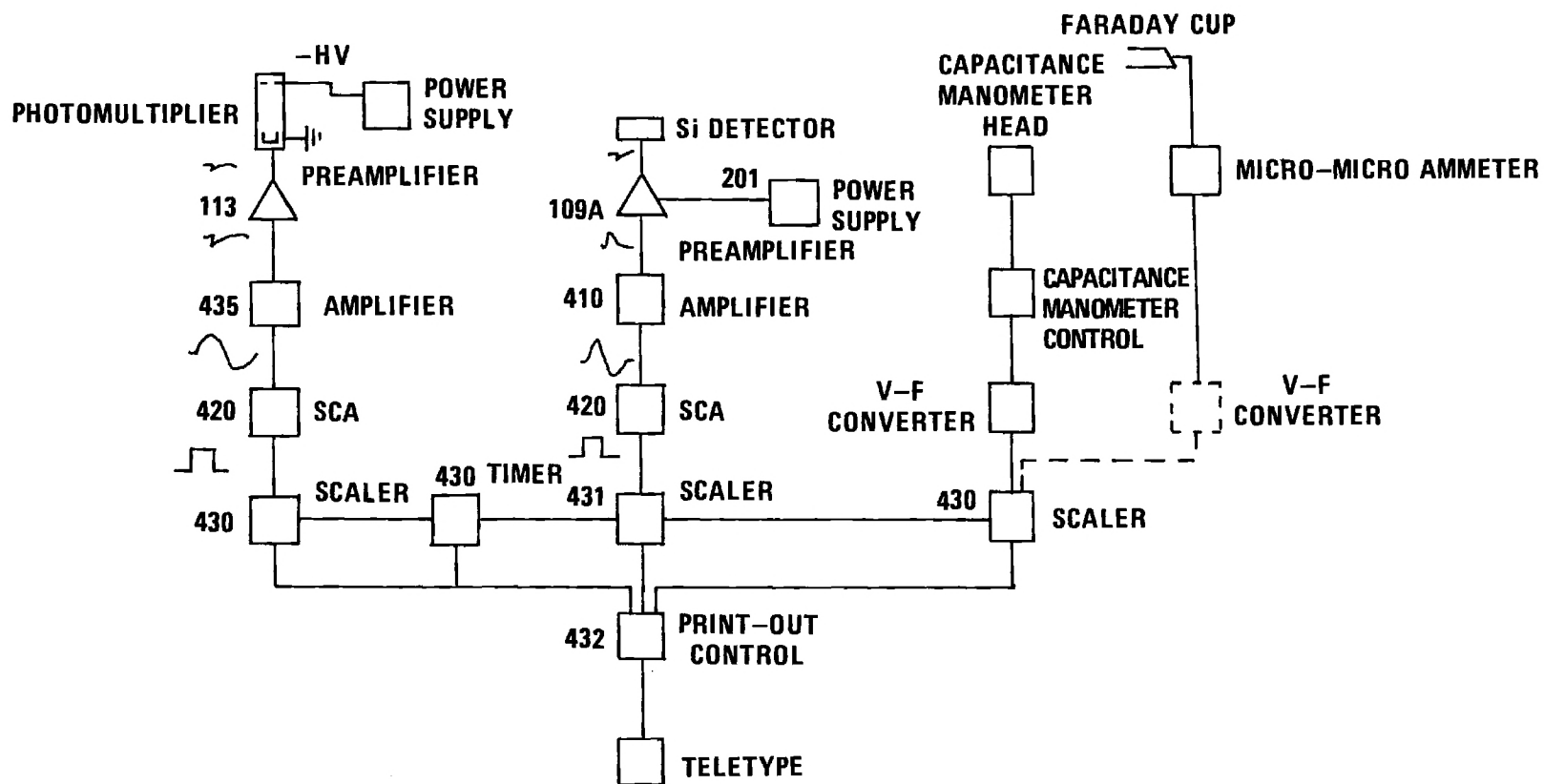


Figure 14. Wiring Schematic.

scattered particles, is a large area diode functioning as a solid state ionization chamber. A pulse of charge collects on the plate of this detector for each particle penetrating the thin gold window on the front of this device. The window has a thickness of approximately  $40 \mu\text{g}/\text{cm}^2$ . The size of the pulse is dependent only on the energy of the incoming particle, not upon its charge state. (The charge of the counted particle is determined geometrically by the position of the detector and by the voltage applied to the deflection plates.) A single lead connects the detector, which is inside the vacuum chamber, with the preamplifier which is just outside the vacuum. This lead serves both to supply the operating voltage to the detector and to conduct the signals from the detector to the preamplifier.

The preamplifier, Ortec #109A, is a charge sensitive device having a field effect transistor (FET) input. In the preamp the pulse is amplified, inverted, and shaped to a rise time of approximately 40 nsec and a fall time of 50  $\mu\text{sec}$ . This pulse travels to a linear amplifier, Ortec #410, which provides great flexibility in pulse shaping. This pulse shaping capability was found to be useful for optimization of the signal to noise ratio. During this work, a doubly differentiated RC shaping was used with time constants from 0.1 to 10  $\mu\text{sec}$ . It was possible to separately adjust the two differentiation times and the integration time, but these were kept equal in the present measurements. Time constants of two  $\mu\text{sec}$  and 10  $\mu\text{sec}$  were most commonly used; but, when working with high counting rates, it was necessary to use very small time constants to prevent dead time losses. The 10  $\mu\text{sec}$  setting was particularly useful, for it discriminated rather strongly against picked-up noise. Some pulse

shapes and the useable count rates obtained with different time constants, are shown in Figure 15.

The shaped pulses were next fed into an Ortec #420 timing single-channel analyzer (SCA). This instrument was used primarily to provide a discrimination level, i.e., to reject pulses whose amplitudes were less than a preset value. The "window" of the single channel analyzer was employed to verify that a narrow pulse height spectrum was being produced and also to see that the center of the pulse height spectrum, which was set by the gain of the amplifier, was large enough to easily discriminate against random noise. (The distribution of the pulse height spectrum was also continuously monitored by observing the amplifier output on an oscilloscope. This monitoring paid large dividends in time saved by making it immediately evident when the scaler was recording counts from noise, slit-edge scatter, or other extraneous sources.)

When a linear pulse at the input of the #420 SCA exceeded the discriminator threshold, the unit developed an output logic pulse, five volts in magnitude and 500 nsec in width. The logic pulses were counted with a scaler, Ortec #430 or #431. The accumulated count could be automatically printed by a teletype machine or punched on a paper tape. These last two features in the data handling were accomplished by an Ortec #432 print-out control system.

An E.M.I. #6256S photomultiplier tube was used to detect collisionally induced photons in the collision region. (The photons were counted to provide a monitor of the beam current.) This photomultiplier tube is a 13 stage venetian blind type having a fused silica window. The photocathode was held at high voltage (typically -1100 volts) with the

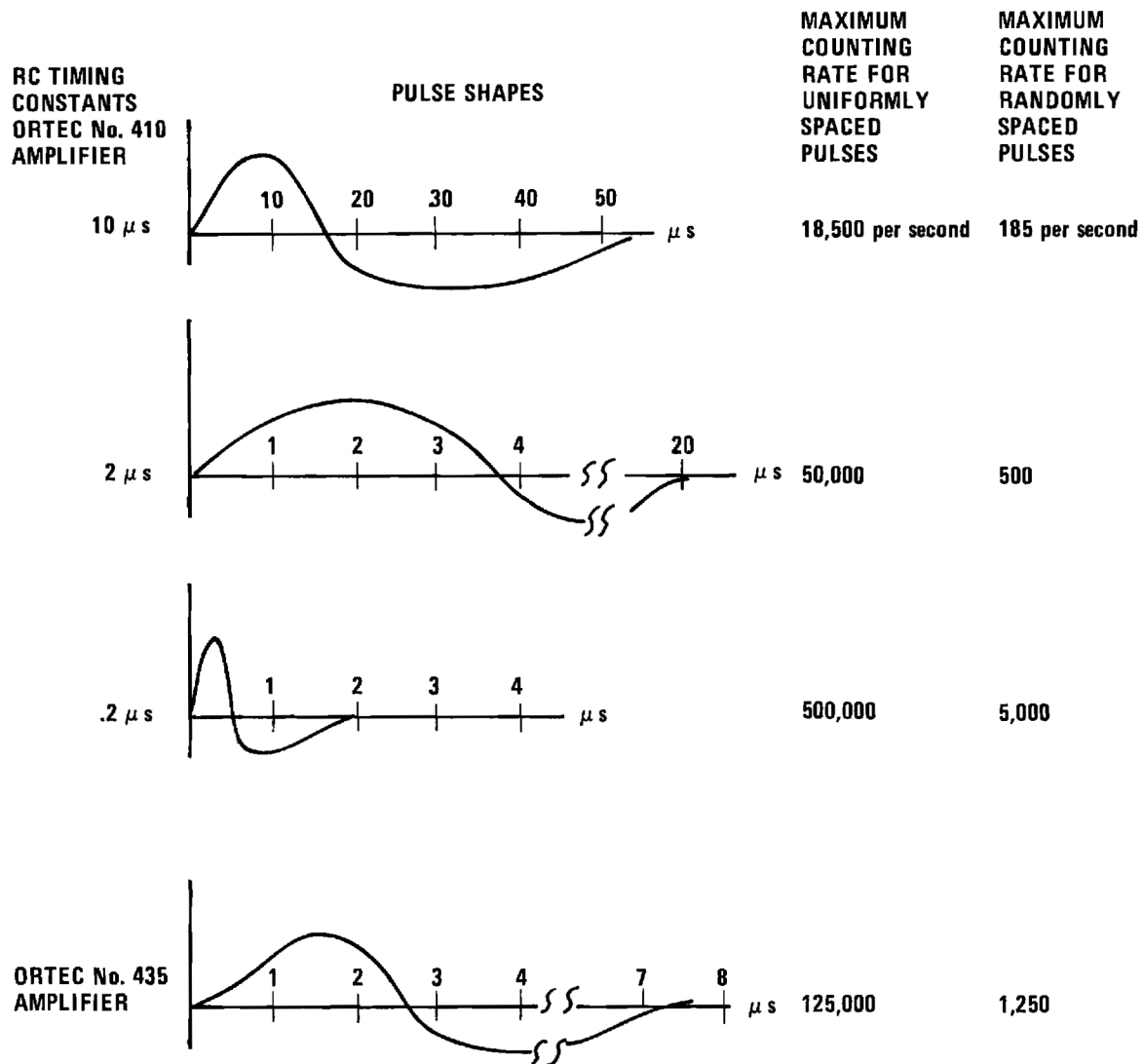


Figure 15. Pulse Shapes and Maximum Counting Rates.

anode end at ground. The wiring of the tube is shown in Figure 16. The high voltage was furnished by a Hamner model N-413 supply.

The signal collected at the anode was fed to a voltage sensitive preamplifier, Ortec #113. This is a non-inverting device with unit gain having low output impedance to drive the cable to the amplifier. It shapes the pulse to a rise time of less than 60 nsec and a fall time of 50  $\mu$ sec.

The pulse from this preamp was fed into an Ortec #435 amplifier which gave a Gaussian shaped bipolar output. From here the signal was handled identically to the scattered particle signal, i.e., passing first to an Ortec #420, SCA used as a discriminator and then to a scaler, Ortec #430.

The pressure was measured during the latter half of the work with a capacitance manometer. The instrument provided, in addition to a meter readout, a dc voltage output which gave a 100 millivolt output for a full scale meter deflection. This dc level was fed into a voltage-to-frequency (V-F) converter (Hewlett-Packard model DY 2210). A V-F converter produces output pulses at a frequency that is proportional to an input dc voltage. The output pulses were counted on a scaler (Ortec #430) over the same time interval as the incident and scattered beam count. This arrangement digitizes the pressure reading and simultaneously integrates over the time of the measurement.

A very convenient feature of the Ortec #430 and #431 scalers is that one scaler can start and stop the counting of any number of other scalers simultaneously. This feature is provided by interconnections between these units. When a preselected "master" scaler reaches a preset



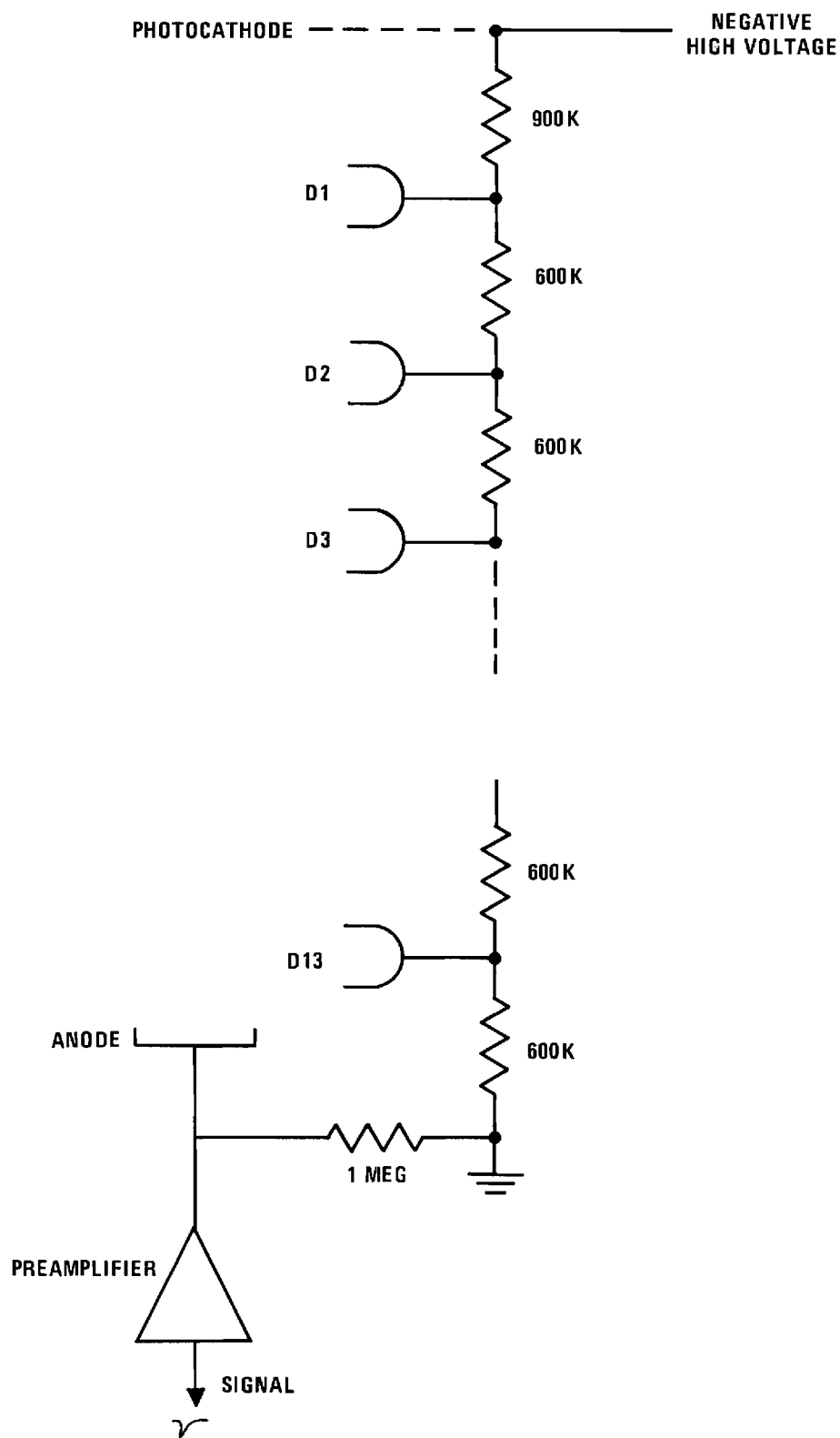


Figure 16. Wiring of E.M.I. #6256S Photomultiplier.

count, all scalers stop counting. During the present measurements, the scaler counting the number of photons was used as the master and all counting stopped when a preselected number of photon counts was reached. Thus, all counts were automatically normalized to constant incident beam for any given gas pressure. Four of these scalers were used: the three already described plus one used as a timer. (Any #430 can be switched to count the line frequency and thus display the elapsed time.) Therefore, the number of photons, the time to record this preset number of photons, the number of scattered particles, and the target gas pressure were simultaneously recorded for each data point.

During the calibration of the photon count rate versus beam current, it was necessary to read and record the current collected in the collision chamber with the Faraday cup which has been described in a previous section. This current was measured by a Keithley #415 micro-microammeter. When making this measurement, the dc output from the Keithley was fed to the V-F converter so that a number proportional to the integrated beam current was counted with a scaler.

An extremely wide range of counting rates was encountered during the measurements (from less than one per second to greater than 5,000 per sec). A counting system, when fed pulses randomly spaced in time, will lose some counts due to dead time in the electronics at count rates much less than the maximum for regularly spaced pulses. From Poisson statistics it can be shown that small time intervals have a greater probability of occurrence than larger time intervals when considering randomly spaced events<sup>76</sup>; i.e., the pulses tend to arrive in clusters thus straining the electronics for brief increments of time. When the dead

time losses are small, the fraction of counts lost will be  $\lambda\tau$ , where  $\lambda$  is the observed average random pulse counting rate and  $\tau$  is the resolving time of the system. In the present experiment, the count rate was kept at least two orders of magnitude below the maximum counting rate for uniformly spaced pulses; therefore, dead time losses were considered negligible in the present experiment.

### Evaluation of Detection Systems

#### Scattered Particle Analyzer

The scattered particle analyzer was designed to detect particles scattered into its acceptance aperture with 100 percent efficiency and to determine their charge state. A silicon surface-barrier detector and an electrostatic deflection field were used to accomplish these tasks. Figure 10 gives an isometric view of the principal features of the analyzer section while Figure 17 gives a side view showing the important dimensions.

Scattered particles must pass through two collimating apertures to enter the analyzer. The geometrical considerations of such a two-slit arrangement are considered in Appendix A. Just inside the second aperture the particles are subjected to an electrostatic field, produced by a parallel-plate arrangement. Such a field functions as an energy analyzer, the deflections being independent of mass for given energy (actually, for given  $E/q$ , where  $q$  is the charge of the particle). In the present situation where a monoenergetic beam enters the analyzer, the deflection serves to separate the various charge components of the beam.

The voltage necessary to produce a given deflection is given by

$$y = \frac{V_q x d}{2Eb} \quad (40)$$

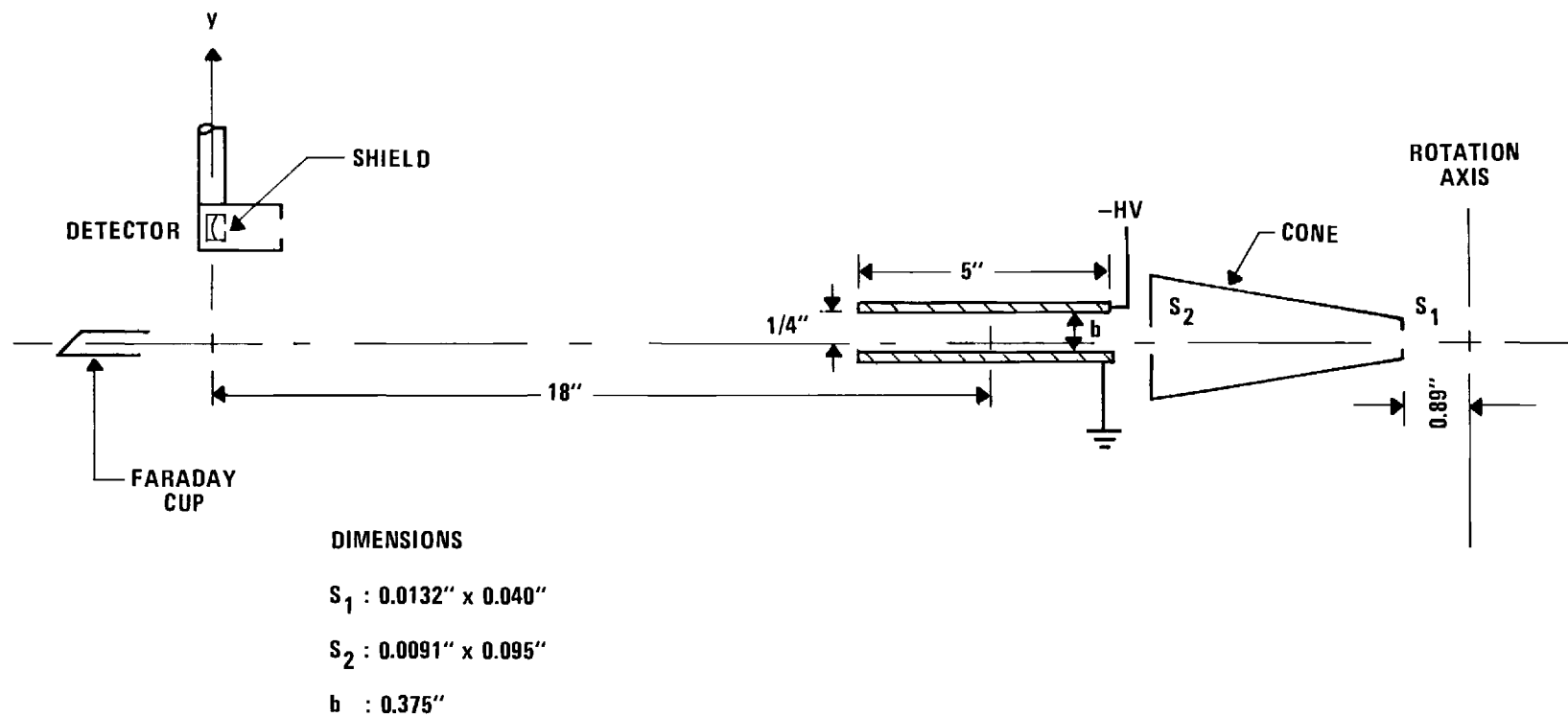


Figure 17. Side View of Scattered Particle Analyzer.

where  $y$  is the vertical displacement of the ions at the detector plane,  $q$  is the charge,  $V$  is the voltage applied across the plates,  $x$  is the horizontal distance from the center of the plates to the plane of the detector,  $d$  is the length of the deflection plates,  $E$  is the energy of the ion, and  $b$  is the separation of the plates. In this calculation fringe fields were ignored. When the actual dimensions of the present apparatus are substituted into the equation it becomes

$$yE = 120 qV \quad (41)$$

where  $y$  is in inches,  $E$  is in electron volts,  $q$  is in units of  $e$ , and  $V$  is in volts.

Thus, it can be seen that for a given energy  $E$ , there are two different methods by which this system may be used to detect scattered particles. One is to hold  $y$  fixed, thus making the left side of equation (41) a constant, since  $E$  is constant. Then, to satisfy the equation,  $qV$  must equal a constant.  $q$  has fixed values ( $q = 1$  and  $q = 2$ ); thus, as the voltage  $V$  is continuously varied, there will be two values of  $V$  for which equation (41) will be satisfied, these values corresponding to the physical situation when the different charge states are swept across the face of the detector. Notice that the highest charge state corresponds to the smallest voltage. For example, at 400 keV with  $y = 0.40$  inch,  $\text{He}^{2+}$  ions are swept onto the detector when  $V = 660$  volts, and  $\text{He}^{+}$  ions strike the detector when  $V = 1330$  volts. Figure 18 illustrates this use of the detection system.

An alternate manner of detecting separately the various charge

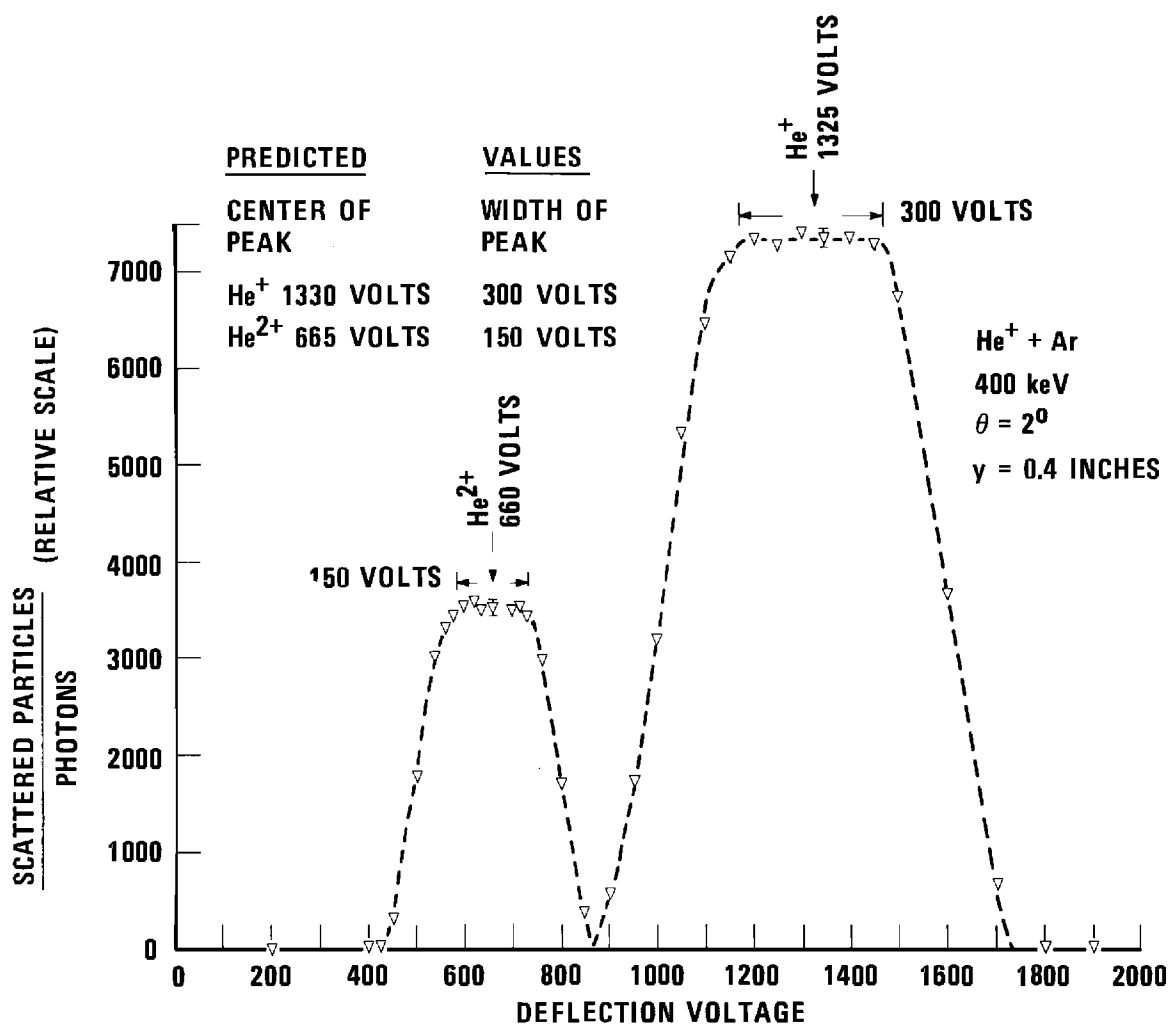


Figure 18. Scattered Particles Versus Deflection Voltage.

states consists of holding the voltage  $V$  constant and moving the detector along its vertical path. The results of this procedure are illustrated in Figure 19. In practice it has been found most convenient to utilize a combination of these two methods, particularly since it is impossible to detect neutral particles by the means first described.

By its very nature this deflection system is also an energy analyzer; however, this aspect is only of marginal value in the present experiment.

For the Si detector to produce an output pulse for an incoming particle, the projectile must pass through an Au window on the front of the detector. This window was a source of some concern, initially, for there was insufficient information at hand to predict whether or not the lowest energy particles could be detected with high efficiency.

To determine the response of the detector to the lowest energy projectiles in this experiment, 158 keV Ne ions were fired into the detector. Ne particles, being heavier than He, travel at slower velocities for a given energy; thus, straggling will be more pronounced for Ne as it passes through the Au window to the silicon wafer. Ne projectiles were used to test the detector under "worst case" conditions. Pulse height spectra showed the detector clearly separated Ne particles from the background noise. The pulse height spectra for 158 and 217 keV Ne particles are shown in Figure 20; spectra are presented for 217 keV particles at two different scattering angles. Figure 21 shows a pulse height spectrum for He projectiles. It is impossible to compare the relative positions of the peaks on these two figures, since different pulse height analyzers were used in taking the data, and it was not possible to normalize them.

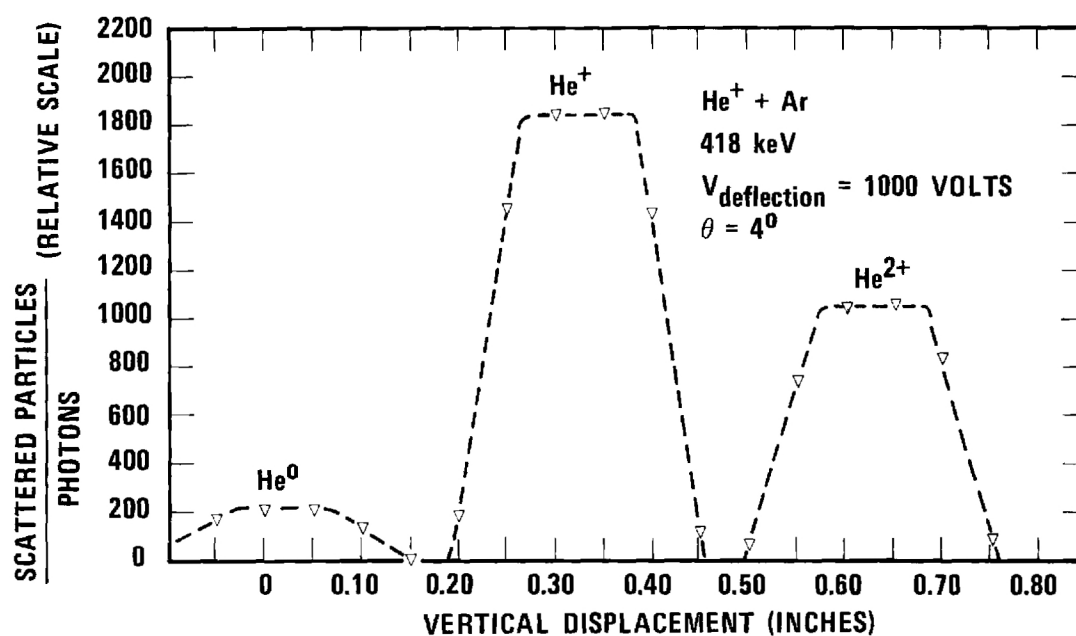


Figure 19. Scattered Particles Versus Vertical Position of Detector.



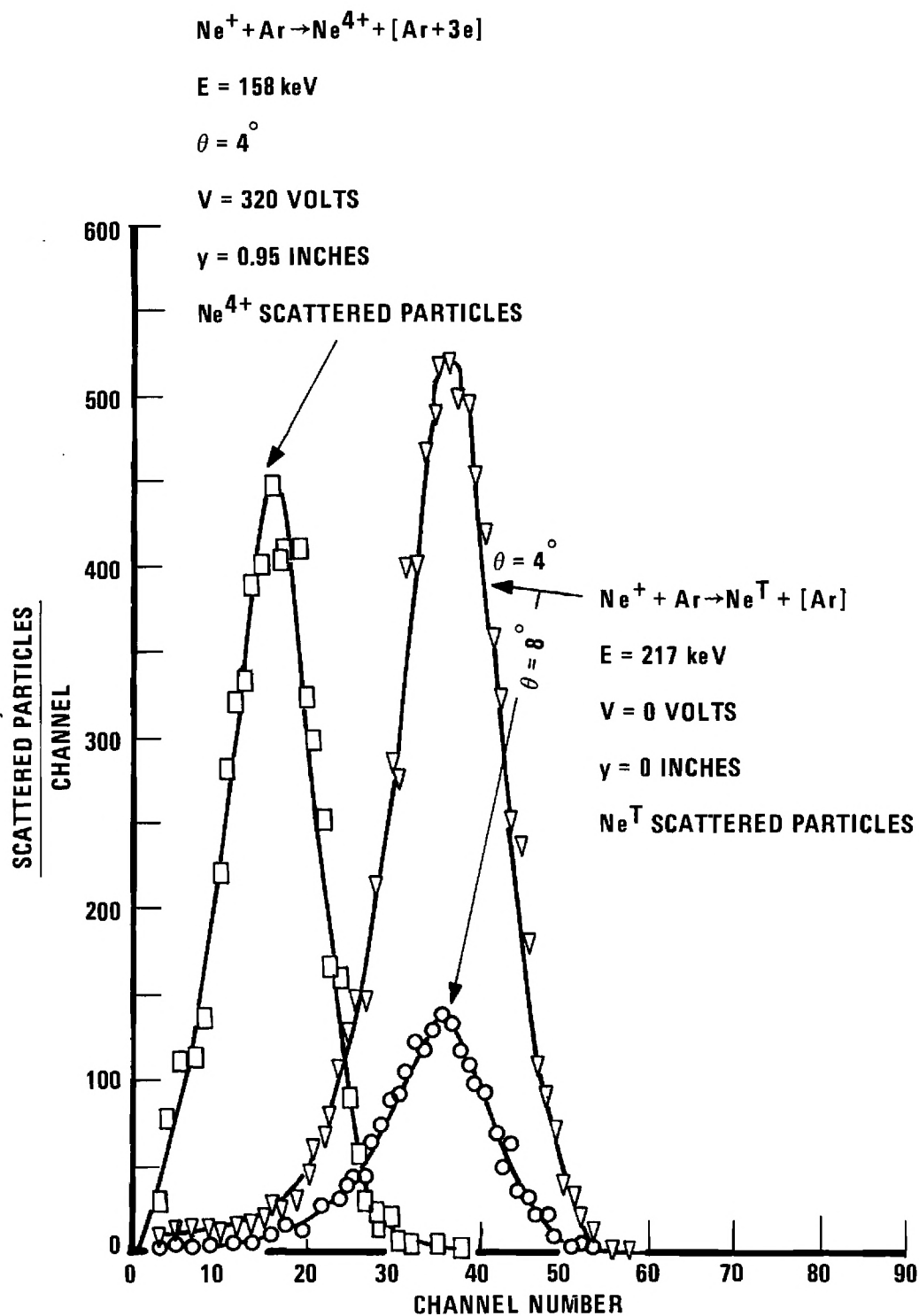


Figure 20. Pulse Height Spectra for Scattered Ne Particles.

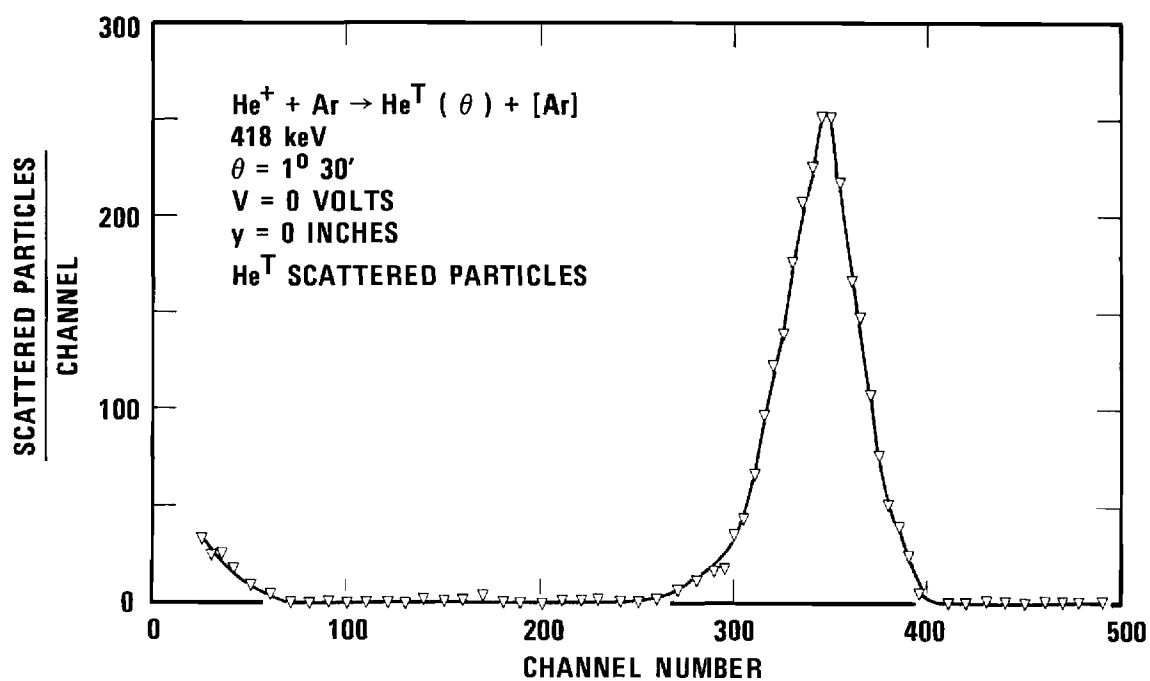


Figure 21. Pulse Height Spectrum for Scattered He Particles.

The narrow distribution of the pulse height spectrum for Ne projectiles at 158 keV, the separation of this distribution from background noise, and the increase in pulse height with increased particle energy lead to the conclusion that the detection efficiency of these detectors for a Ne beam whose energy is at least 158 keV is 100 percent. Straggling will be far less of a problem for He than for Ne particles in passing the Au window. Therefore, it was concluded that the detector used in the present measurement was 100 percent efficient for He projectiles.

Before making measurements it was necessary to insure that all particles of a given charge scattered into the solid angle  $d\omega$  defined by the entrance collimator at scattering angle  $\theta$  struck the detector. This was accomplished by sweeping the detector through the beam first in the vertical direction and then in the horizontal direction.

Figure 22 illustrates the beam profile measured in the horizontal plane. The width of this pattern and its shape are consistent with geometrical calculations estimating the spread of the beam in the detector plane. The measured beam profile is approximately 0.130 inch wide; however, most of the intensity originates in a narrow band, the "umbra", which is defined in Appendix A, having an approximate width of 0.070 inch on the detector surface.\*

Once the horizontal position had been optimized, it was not again disturbed unless the detector itself had to be removed from the analyzer.

---

\* During the course of the measurements, four different detectors were used. The first two had an active area of 25 sq mm. The shield used with these detectors had a knife-edged hole of diameter 0.188 inch. To verify that no particles were striking the horizontal edge of this shield, the last two detectors had an active area 50 sq mm and employed a rectangular shield of dimensions 0.250 inch x 0.188 inch. Results with these two detector and shield combinations were identical.

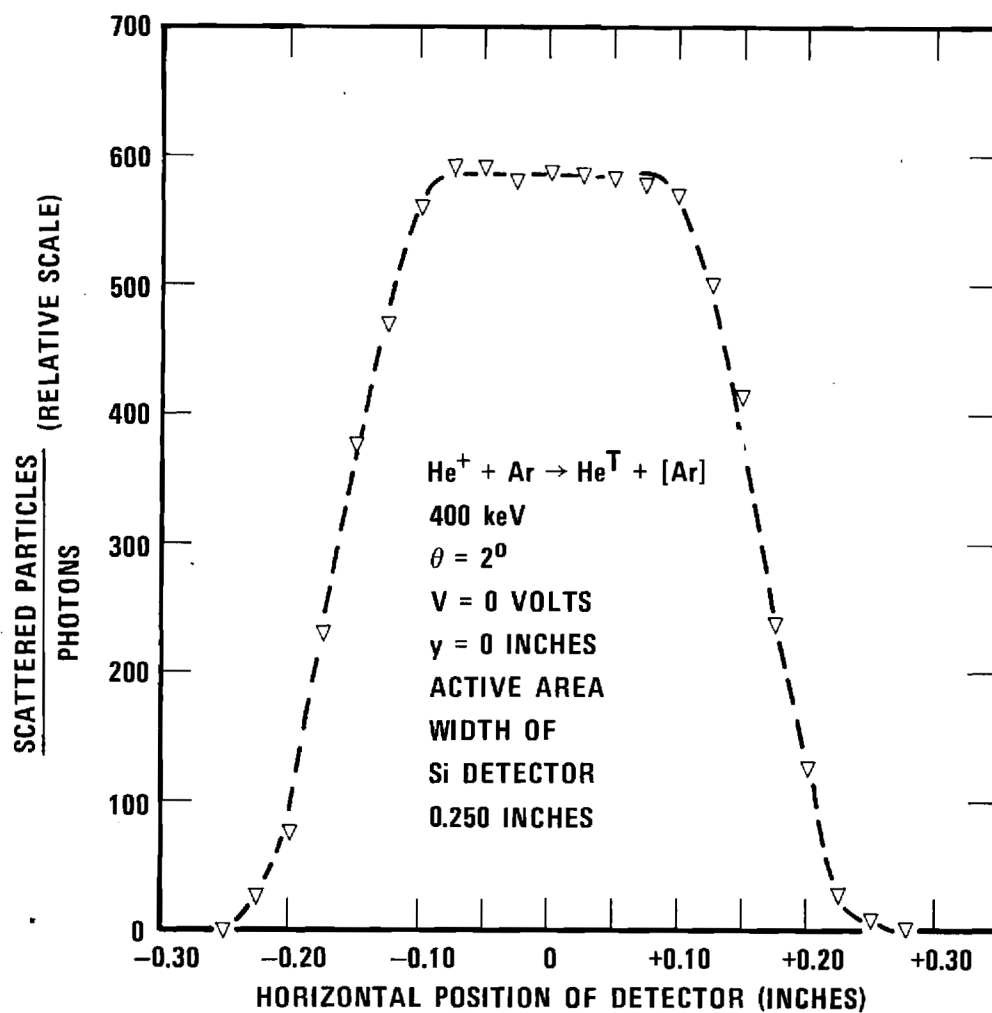


Figure 22. Horizontal Profile of Scattered Beam in Detector Plane.

The vertical positioning, however, was used extensively throughout the measurements (its motion was quite reproducible and dependable with no apparent backlash). Figure 23 shows the vertical profile of the beam measured with no deflection voltage. Shown on this diagram are measurements made at two different energies and two different scattering angles. The vertical spread of the beam was measured to be 0.090 inch for each of these different cases; a value in good agreement with geometrical estimates based on aperture sizes.

When a constant deflection field was applied, the  $\text{He}^0$ ,  $\text{He}^+$ , and  $\text{He}^{2+}$  peaks not only appeared in the exact predicted location, but they also had the expected profiles. This agreement is shown both in Figures 18 and 19. Knowing the height of the beam at the detector, it is possible to predict (using equation (41)) for a given vertical position, the voltage necessary to bring each charge state onto the center of the detector, the width of the flat-topped peak for each charge state, and the voltage at which each of these charge states should begin to rise toward its peak as well as the voltage at which counts should cease. To verify these predictions, the detector was placed 0.40 inch above the neutral beam position and the deflection voltage varied to sweep various He peaks across its face. Figure 18 shows the excellent agreement between the predictions and the experiment.

A great deal of information is presented in Figure 18. On each peak is an arrow identifying the center of the peak and a set of limits showing the width of the plateau. Also included on this figure is a table showing the predicted center and width of the peak. Excellent agreement exists between the measured and the predicted values. These patterns

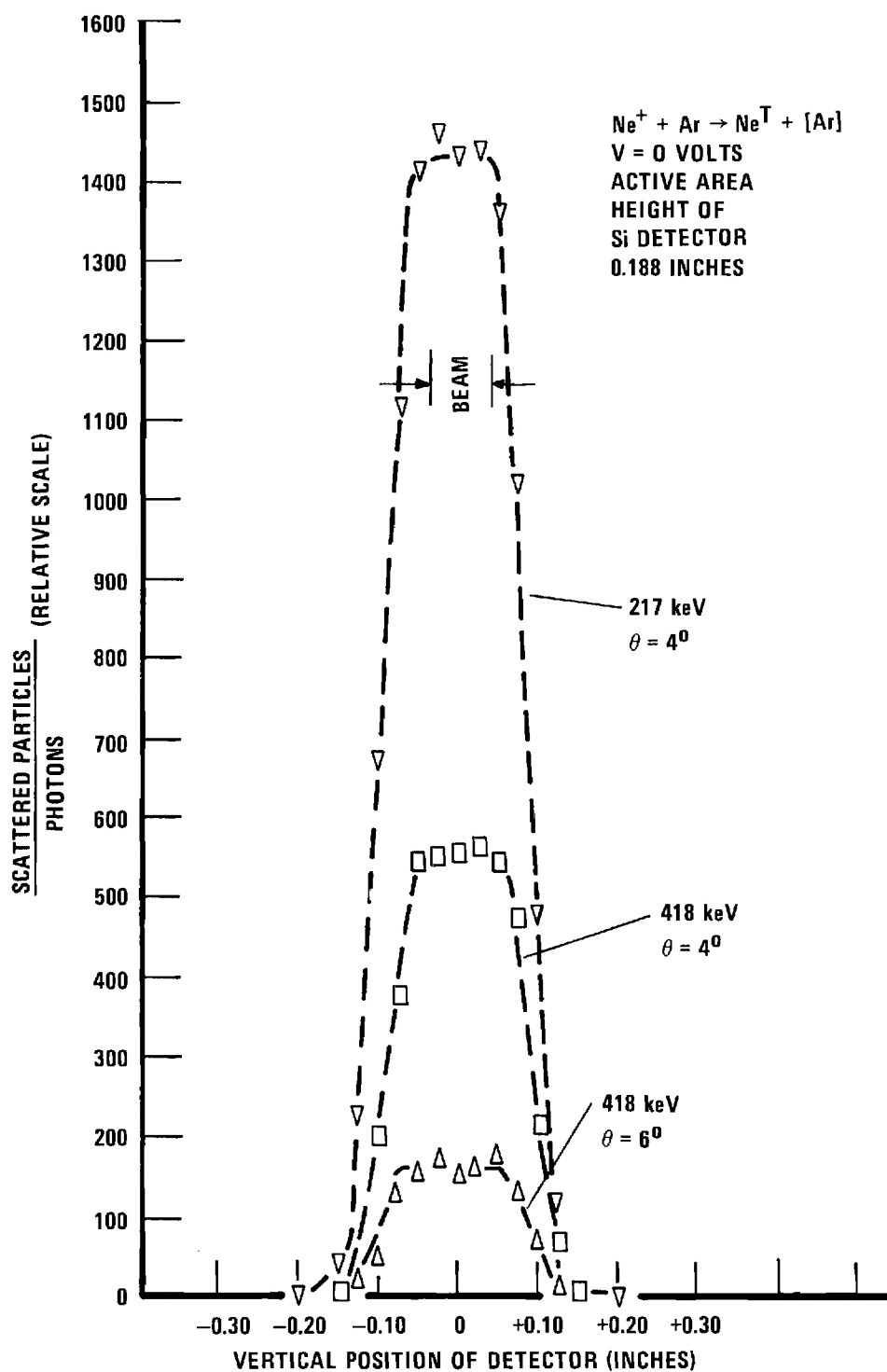


Figure 23. Vertical Profile of Scattered Beam in Detector Plane.

arise because the vertical extent of the beam is much less than the height of the shield aperture in front of the detector. Hence, the distribution changes from zero as the charge state component first strikes the detector, rising to the plateau when the entire beam is striking the detector. The plateau value is maintained as the beam is swept across the face of the detector. The observed count rate falls from the plateau value as the leading edge of the beam is intercepted by the shield, reaching zero when the trailing edge of the beam is intercepted by the shield.

Therefore, it is concluded from (1) the shape of the pulse height spectrum, (2) the agreement between the measured and predicted horizontal distribution, (3) the agreement between the measured and predicted height of the beam of scattered particles, and (4) the excellent agreement between the prediction and the observed vertical position and shape of the scattered beam when deflected that this analyzer system (1) detects all atoms or ions, and (2) determines the charge, for all particles scattered through angle  $\theta$  into the solid angle  $d\omega$  with 100 percent efficiency. The pulse-height spectrum is clear indication that there are no large energy losses. The sensitivity to energy loss of the apparatus is such that it is only possible to assert an upper limit to the energy loss of less than 15 percent.

#### Measurement and Monitoring of Projectile Beam

The beam current was measured with a Faraday cup which could either be placed in the beam path or removed from the beam, by means of a bellows-sealed actuator which has been previously described in the discussion of the collision chamber. Continuous monitoring of the beam was accomplished by counting photons emitted from collisionally excited target atoms. Two

quartz lenses focused these photons on the photocathode of an E.M.I. #6256S tube. An all-quartz system was employed to extend the range of wavelengths which could reach the multiplier since argon, as well as the other target gases used, has emissions in the ultraviolet as well as the visible range.<sup>77,78</sup>

During the first part of the measurements, only a single glass lens had been employed at the position closest to the multiplier tube. By adding the second lens, to increase the solid angle focused on the tube, and by using an all-quartz system, to extend into the ultraviolet range, the photon counting rate for given beam intensity and gas pressure was increased almost an order of magnitude.

Pumping ports were provided so that the region above the first lens was at the same vacuum as the collision chamber. The vacuum seal was formed by the second lens. A cross section view, Figure 8, shows the position of both lenses. Both lenses were plano-convex lenses; the lens in the collision chamber had a focal length of 64.7 mm while the top lens had a focal length of 124.8 mm. The beam in the collision region is at the focal point of the first lens; light emitted into the solid angle subtended by this lens is thus collimated into a parallel beam of light. This light is in turn focused onto the photocathode of the photomultiplier which is located at the focal point of the second lens.

#### Techniques of Measurement

As shown in Chapter II, the differential scattering cross section is given by the relation



$$\frac{d\sigma^n(\theta)}{d\omega} = \frac{N^n(\theta)}{N_o} \frac{1}{N_t} \frac{1}{G(\theta)} . \quad (15)$$

To measure this cross section it is necessary to measure only three items:

(1) the ratio of the number of particles of charge  $n$  scattered into  $d\omega$  at angle  $\theta$  to the number of incident projectiles, i.e.,  $\frac{N^n(\theta)}{N_o}$ ; (2) the target density,  $N_t$ , which is experimentally determined by measuring the target pressure and the temperature; and (3) the geometrical factor  $G(\theta)$ .

We have described in this chapter the various detectors which were used during these investigations; now, it is necessary to consider how they were actually employed in conjunction with one another to experimentally determine the differential scattering cross section.

There were two distinct phases of the measurements and they shall be considered in their chronological order, the difference in these phases being due to the change from an ionization gauge to a capacitance manometer for measuring the target pressure.

The analyzer determined  $N^n(\theta)$ . Actually, as described in the "analyzer system" section of this chapter, the detector determined the count rate of scattered particles; the position of the detector in conjunction with the voltage applied to the deflection plates determined the electrical charge of the particles being counted. Thus,  $N^o$ ,  $N^+$ ,  $N^{2+}$ , and  $N^T$  ( $N^T$  is the total number of scattered particles of all charge states) were counted, and it was verified that  $N^S = N^T$  (within counting statistics) where

$$N^S = N^o + N^+ + N^{2+} .$$

The measurement of scattering angle was dependent on the mechanical

construction. The scale was such that it could be read to an accuracy better than two and one-half minutes.

The ratio of the count rates  $N^n(\theta)/N_0$  could not be measured directly since  $N^n(\theta)$  and the incident beam intensity  $I_0 = eN_0$  could not be measured simultaneously, as explained previously. Here,  $e$  is the charge of the incident ions (the electron charge for  $\text{He}^+$ ). For this reason, the intermediate step was introduced of observing the collisionally induced excitation of the target gas. The excitation photon count rate  $N_p$  could be counted simultaneously with the counting of  $N^n(\theta)$ , and it served as a continuous monitor and integrator of the incident beam; i.e., it provided an indirect measurement of  $N_0$ .

Calibration of the relation between  $N_0$  and the photon count rate will be discussed presently. Associated with the photomultiplier was a constant background count rate,  $n_{\text{TN}}$ , due to thermal noise. Thus the "true" photon count was  $(N_p - n_{\text{TN}})$ . (A fraction of the true count rate was in principle contributed by excitation of the residual background gas in the collision chamber, but this fraction was always less than one percent and was neglected.)

Thus the quantities directly measured for each data point provided the ratio  $N^n(\theta)/(N_p - n_{\text{TN}})$ . Calibration of the ratio  $(N_p - n_{\text{TN}})/N_0$  was performed in two somewhat different fashions during the two phases of the measurements mentioned above, for reasons contained in the discussion to follow.

During the first phase (the November 1968 data), an ionization gauge provided the only measurement of the target gas pressure. The absolute accuracy of the cross section measurement was therefore no better

than the nominal calibration of the gauge, and even the relative measurements tended to suffer from some of the well known vagaries of ionization gauges. An additional difficulty arose from the fact that the gauge could not be operated simultaneously with the photon counting, because light from the gauge was reflected inside the collision chamber into the photomultiplier. The procedures followed in these measurements were designed to reduce the relative uncertainties as much as possible, with the intention of normalizing the data according to a later absolute calibration of the ionization gauge.

Great care was taken always to read the gauge under exactly reproducible conditions. In addition, the calibration of the ratio  $(N_p - n_{TN})/N_0$  was carried out over as wide a range of target gas pressure as feasible. At each pressure, the photon count rate  $N_p$  was counted, and the projectile current  $I_0$  was measured with an electrometer, by collecting the beam into the Faraday cup in the collision chamber. (As previously described, these measurements could not be performed simultaneously. They were always performed alternately several times, until a reliable average value of their ratio was obtained.) In this manner, an average value of the ratio  $(N_p - n_{TN})/I_0$  was computed for the given pressure. The values of this ratio for different pressures were then plotted against the pressure, in Torr, as measured by the ionization gauge, and a straight line through the origin was fitted to the points by the method of least squares. Figure 24 is such a calibration graph. The slope,  $\gamma$ , of this line then represented the quantity

$$\gamma = \frac{(N_p - n_{TN})}{I_0} \frac{1}{P}$$

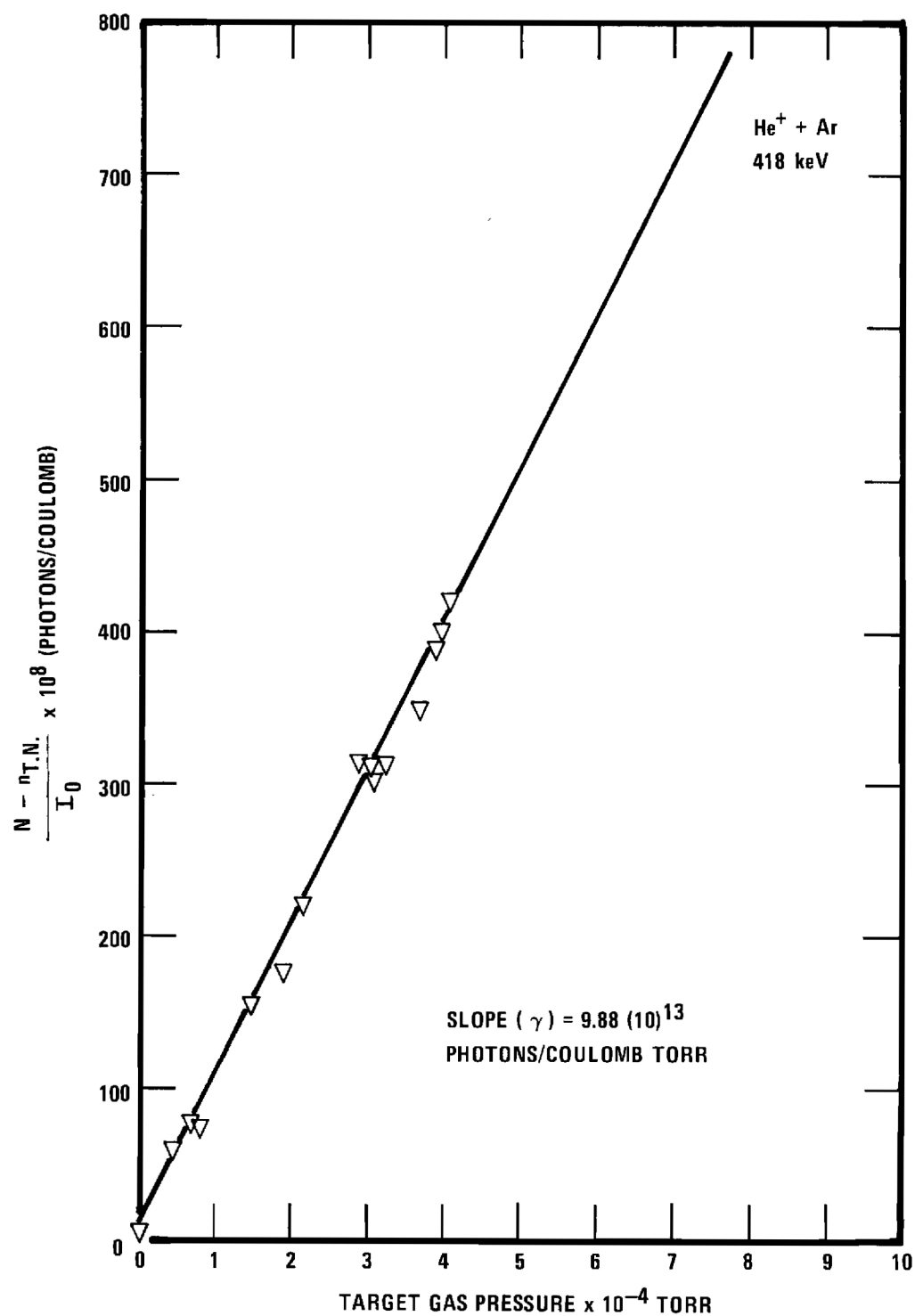


Figure 24. Calibration of Photon Count Rate Against Projectile Beam Using Ionization Gauge.

Such graphs were obtained repeatedly over the course of several days, and the average value of  $\gamma$  obtained for a particular beam energy was subsequently used for all data at that energy.

In terms of the measured quantities in the first phase of the measurements (the November 1968 data), the cross section (15) was, therefore,

$$\frac{d\sigma^n(\theta)}{d\omega} = \frac{N^n(\theta)}{(N_p - n_{TN})} e\gamma \frac{1}{L'} \frac{T}{T_0} \frac{1}{G(\theta)} \quad (42a)$$

where  $L'$  is the number density of a gas at standard temperature  $T_0$  and a pressure of one Torr, and  $T$  is the temperature of the target gas.

During the later phase of the measurements (1969 data), a capacitance manometer was used for measurement of the target gas pressure. In addition to having a much more reliable absolute calibration than the ionization gauge (the calibration is discussed in Appendix B), this instrument provided a much more stable pressure reading, and it could also be read simultaneously with the photon count. (As previously explained, its output was digitized through the use of a V-F converter whose output was counted by a scaler, which effects an integration of the pressure reading over the same time interval as the photon count.) These factors permitted some simplification in the calibration of the ratio  $(N_p - n_{TN})/N_0$ . As before, the photon count and the measurement of the incident beam intensity had to be performed alternately several times, at a constant gas pressure, to obtain an average value of the ratio

$$\gamma' = \frac{N_p - n_{TN}}{I_0} .$$

However, the former step of obtaining this ratio at a number of pressures and plotting against the pressure to obtain an average slope was no longer found to be necessary. Single measurements of  $\gamma'$  now proved to be quite reliable, due partly to the better performance of the capacitance manometer and partly to the fact that a coincidental improvement in the optics of the photon counter had increased the photon count rates by an order of magnitude.  $\gamma'$  was measured at least once every day and was remeasured whenever the pressure was changed or was found to have drifted.

Thus, in terms of the quantities measured in the latter phase of the measurements (the 1969 data), the cross section (15) was given by

$$\frac{d\sigma^n}{d\omega}(\theta) = \frac{N^n(\theta)}{N_p - n_{TN}} e\gamma' \frac{1}{N_t} \frac{1}{G(\theta)} \quad (42b)$$

The measured cross sections obtained when using the capacitance manometer were some 20 percent higher than those previously obtained when only the ionization gauge was available. This much difference could easily be attributed to the absolute uncertainties in the ionization gauge, particularly since the gauge was used on its highest range where it was observed to have two distinctly different modes of operation differing in scale reading by about a factor of two. To conclusively lay this difference to the ionization gauge, it would have been desirable to calibrate the gauge directly against the capacitance manometer. Unfortunately, the ionization gauge which had been used in the work was accidentally broken before more than a very preliminary comparison had been completed. Thus, the direct evidence is inconclusive; but, the calibration of the capacitance manometer, plus its inherently more stable operation and its con-

tinuous operation (opposed to the infrequent "look" with the ionization gauge) led us to place full confidence in the cross section measured using the capacitance manometer. For this reason, the data taken early in the program were normalized to the latter data. Relative measurements with the ionization gauge are much better than the absolute measurements, so that the data taken when employing the ionization gauge were useable with a single normalization. Only Ar data were taken in this fashion and normalized to later data also using an Ar target.

The geometrical factor,  $G(\theta)$ , was evaluated using equation (57). As shown in Appendix A, an excellent approximation to it is given by

$$G(\theta) \approx \frac{a b h}{d(d + \ell)} \frac{1}{\sin \theta} \quad (59)$$

Exact knowledge of the aperture sizes was crucial to assigning absolute magnitudes to the measured cross sections. This is readily seen in the fact that  $b$  and  $h$  were nominally machined to be 0.010 inch; however, the actual sizes, while within less than one thousandth of an inch of the specified sizes, introduced a 14 percent error into the calculations until the correct sizes were substituted for design sizes. The actual sizes were determined to within plus or minus two percent by a two-dimensional traveling microscope and also by measuring the diffraction patterns produced when a laser beam is passed through the apertures. These two very different methods agreed within the assigned errors. The best values obtained for the sizes of the apertures were as follows:

$a = 0.0132$  inch (used in November 1968 data)

$a = 0.0156$  inch (used in 1969 data)

$b = 0.0091$  inch

$h = 0.0095$  inch

### Errors in Measurement

The experimental differential scattering cross section is evaluated by

$$\frac{d\sigma^n}{d\omega}(\theta) = \frac{N^n(\theta)}{N_0} \frac{1}{N_t} \frac{1}{G(\theta)} . \quad (15)$$

As shown in the previous section, the cross section was actually computed from

$$\frac{d\sigma^n}{d\omega}(\theta) = \frac{N^n(\theta)}{N_p - n_{TN}} e\gamma' \frac{1}{N_t} \frac{1}{G(\theta)} . \quad (42b)$$

It is necessary to consider the errors associated with the measurement of each of the quantities in this equation.

Counting statistics determines the error introduced in measuring the number of scattered particles,  $N^n$ . Let the possible error associated with a counted number of particles be represented by one standard deviation which is approximately equal to the square root of the number counted.<sup>79</sup> Thus, if a scaler records only 100 scattered particles, the probable error associated with this count would be  $\pm 10$  counts and would contribute a probable error of  $\pm 10$  percent to the cross section calculated by equation (42b). Table 5 shows some typical errors introduced from this source for argon and helium targets at the various energies investigated. As can be seen in Table 5, this error is small at small angles, but it becomes appreciable at larger angles. The smallest cross section in each case (i.e., the cross section for either the charge transfer or electron stripping) suffers most from counting statistics.

The statistical error introduced by counting the photons was ap-



Table 5. Typical Values for Statistical Errors

$\theta$	$d\sigma^+/d\omega$	$d\sigma^{2+}/d\omega$	$d\sigma^0/d\omega$	$d\sigma^T/d\omega$
<u>He<sup>+</sup> + Ar</u>				
<u>E = 208 keV</u>				
50'	0.4	0.9	0.5	0.3
2°	1.5	3.6	2.1	1.2
4°	5.4	12.4	7.7	4.1
7° 30'	5.8	11.2	7.6	4.1
<u>E = 418 keV</u>				
1°	0.5	0.6	1.3	0.4
4°	2.7	3.5	7.6	2.0
6°	3.5	4.8	9.5	2.7
8°	7.3	9.3	21.1	5.5
<u>E = 627 keV</u>				
35'	0.2	0.2	1.2	0.2
2° 30'	1.7	1.5	12.6	1.1
4°	5.4	4.9	19.0	3.5
6°	6.2	5.0	28.8	3.9
<u>He<sup>+</sup> + He</u>				
<u>E = 400 keV</u>				
1° 35'	1.4	3.2	2.1	1.1
3°	5.2	8.2	7.3	
5°	9.1	21.5	12.8	7.1
<u>E = 600 keV</u>				
1° 35'	1.8	3.0	3.9	1.4
3° 35'	6.2	11.3	14.4	5.0

proximately plus or minus two percent in the worst situation. The counting time varied over wide limits, from a few seconds to several minutes which in turn caused a spread in the error assigned to  $N_p - n_{TN}$ . The error in measuring this quantity,  $N_p - n_{TN}$ , is estimated to be plus or minus three percent. This is from worst case consideration.

$\gamma'$  is the ratio of the photon count rate to the beam current. The maximum possible random error associated with this ratio is estimated to be plus or minus two percent at 400 keV incident energy and plus or minus three percent at 600 keV incident energy. These errors were assigned from the spread of the observed ratios about the mean value. They were the same for all target gases. This ratio could also introduce a possible systematic error of plus or minus three percent from use of the Keithley micro-microammeter.

The target density was determined by measuring the target gas pressure and the room temperature. The random error in reading the capacitance manometer was estimated to be plus or minus two percent. A possible systematic error of plus or minus five percent could have been introduced through the calibration of the capacitance manometer (see Appendix B). The error arising from the room temperature measurement was negligible.

The geometrical factor was the source of the largest of the systematic errors in the cross sections. As shown in Appendix A

$$G(\theta) \simeq \frac{a b h}{d(d + \ell)} \frac{1}{\sin \theta} . \quad (59)$$

Aperture dimensions  $a$ ,  $b$ , and  $h$  were measured to within  $\pm 2$  percent; the denominator,  $d(d + \ell)$ , was also known to within  $\pm 2$  percent. Hence, the

possible systematic error in  $G(\theta)$  from these measurements was  $\pm 8$  percent.

A random error in  $G(\theta)$  comes from the measurement of the scattering angle,  $\theta$ . It was possible to determine the angle to within two and one-half minutes. At a scattering angle of one degree, the possible error in  $\sin \theta$  is four percent; however, this error decreases rapidly with increasing  $\theta$ .

Considering the random errors involved in the measurement of each of these quantities, the differential scattering cross sections have a random error of  $\pm 8$  percent plus the statistical error from Table 5. The possible systematic error associated with these data is approximately  $\pm 13$  percent.

$\text{He}^+ + \text{Ar}$  with an incident energy of 418 keV was the pilot case in these measurements; the data accumulated for this case were far more extensive than for the other cases measured. Most data points shown in Figure 26 represent the average of many separate measurements, a few points being the average of 20 or more values. The individual points had a distribution of less than  $\pm 10$  percent about the mean value in almost all cases. When the mean values for the total differential scattering cross sections were plotted as a function of angle (Figure 26), the spread about a smooth curve was approximately  $\pm 10$  percent. The spread about a smooth curve for the charge transfer differential scattering cross section was 12 to 15 percent. Thus, the best estimate of the relative error for the total differential scattering cross section is  $\pm 10$  percent which is consistent with the previous estimate of the random error from consideration of the individual measurements which were performed.

The absolute error assigned to the total differential scattering

cross sections is  $\pm 23$  percent. In all cases measured the experimental and theoretical values differed by less than 23 percent.

If the ratio  $N^n/N^T$  could be counted simultaneously, the random error in  $P_n$  would arise solely from counting statistics. However, since the counting must be sequentially performed, the random error in  $P_n$  should be the sum of the random errors in measuring  $d\sigma^n/d\omega$  and  $d\sigma^T/d\omega$ . For the  $P_n$  versus  $\theta$  curves (Figures 33 through 37), the scatter about the mean is always less than the predicted random error, and, as expected, the fractional error increases for smaller values of  $P_n$ . The random error associated with the  $P_n$  versus energy curves (Figures 38 through 40) depends on the energy and the particular charge state fraction being considered. The spread of the data about a smooth curve is the best estimate of the error, being generally less than  $\pm 10$  percent.

## CHAPTER V

## EXPERIMENTAL RESULTS

The measured differential scattering cross sections as a function of angle at fixed energy are displayed graphically. The total differential scattering cross section agrees, within experimental error, with a classical theoretical calculation, assuming a Bohr potential.  $P_n$ , the fraction of scattered projectiles in charge state  $n$ , is shown as a function of both angle and energy. These data are compared with other measurements and with available theories.

During the course of the measurements, it proved necessary to completely realign the scattering geometry. The measurements before and after this realignment were in complete agreement, which provided a good consistency check on the data.

Differential Scattering Cross Sections

Figures 25 through 30 show the experimentally determined differential scattering cross sections plotted as a function of scattering angle for several fixed energies for the target gases Ar, He, and Ne. Each figure contains the total differential scattering cross section which is the sum of the differential scattering cross section for charge transfer, for electron stripping, and for scattering without change of charge. These three individual differential scattering cross sections are also displayed on each graph. In each case the total differential scattering cross section was directly measured (by counting all particles scattered

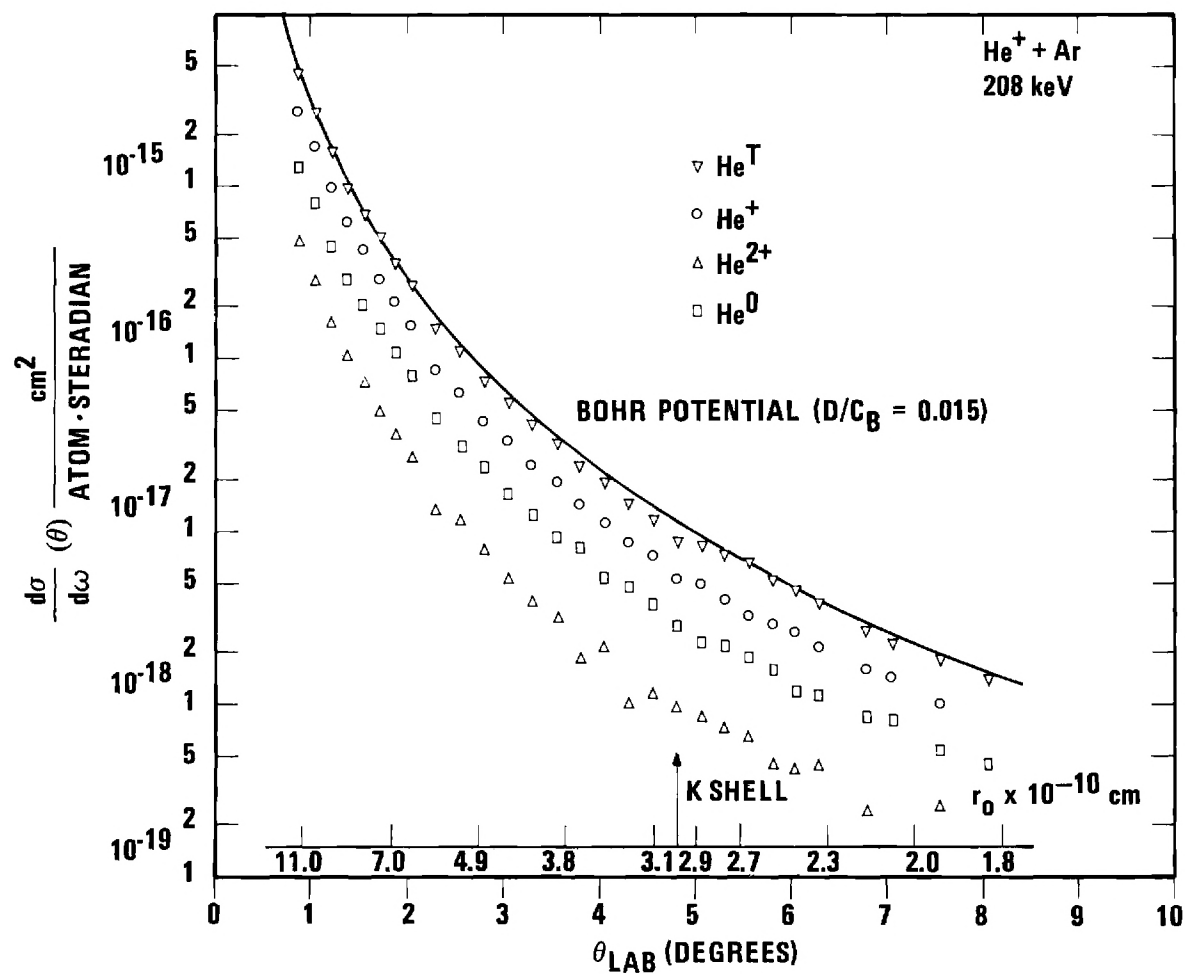


Figure 25. Differential Scattering Cross Sections Versus Angle for  $\text{He}^+ + \text{Ar}$  with Incident Energy of 208 keV.

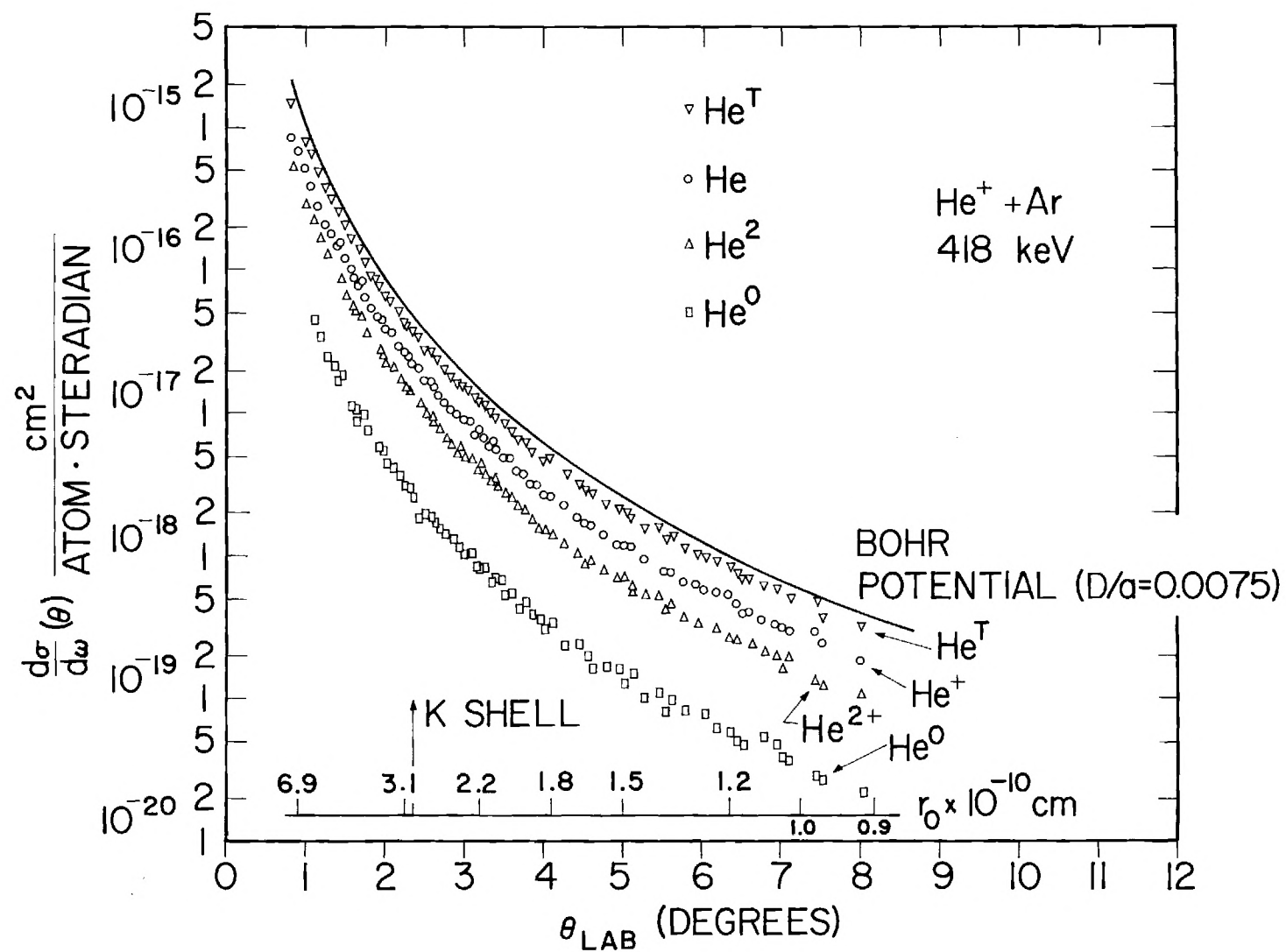


Figure 26. Differential Scattering Cross Sections Versus Angle for  $\text{He}^+ + \text{Ar}$  with Incident Energy of 418 keV.

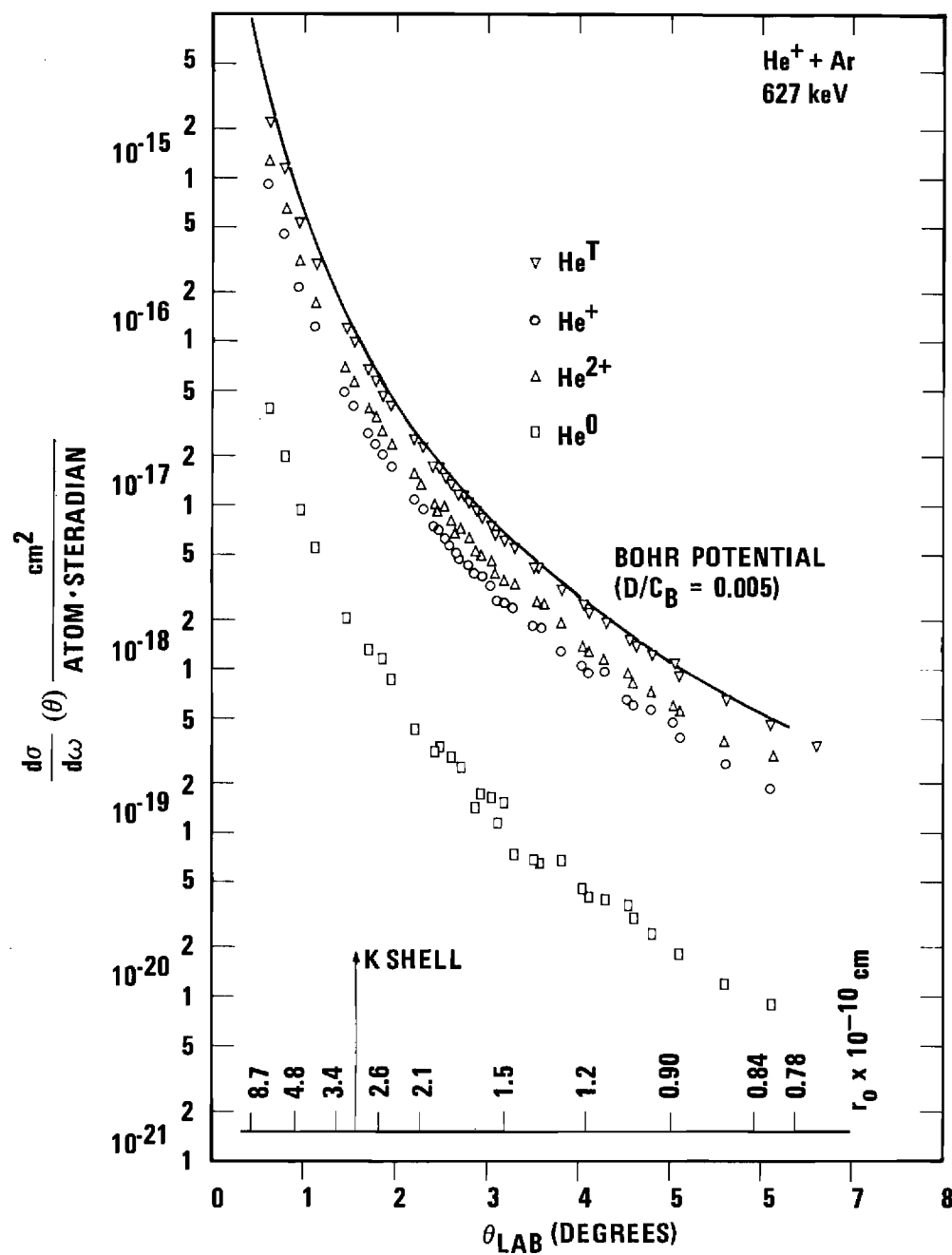


Figure 27. Differential Scattering Cross Sections Versus Angle for  $\text{He}^+ + \text{Ar}$  with Incident Energy of 627 keV.



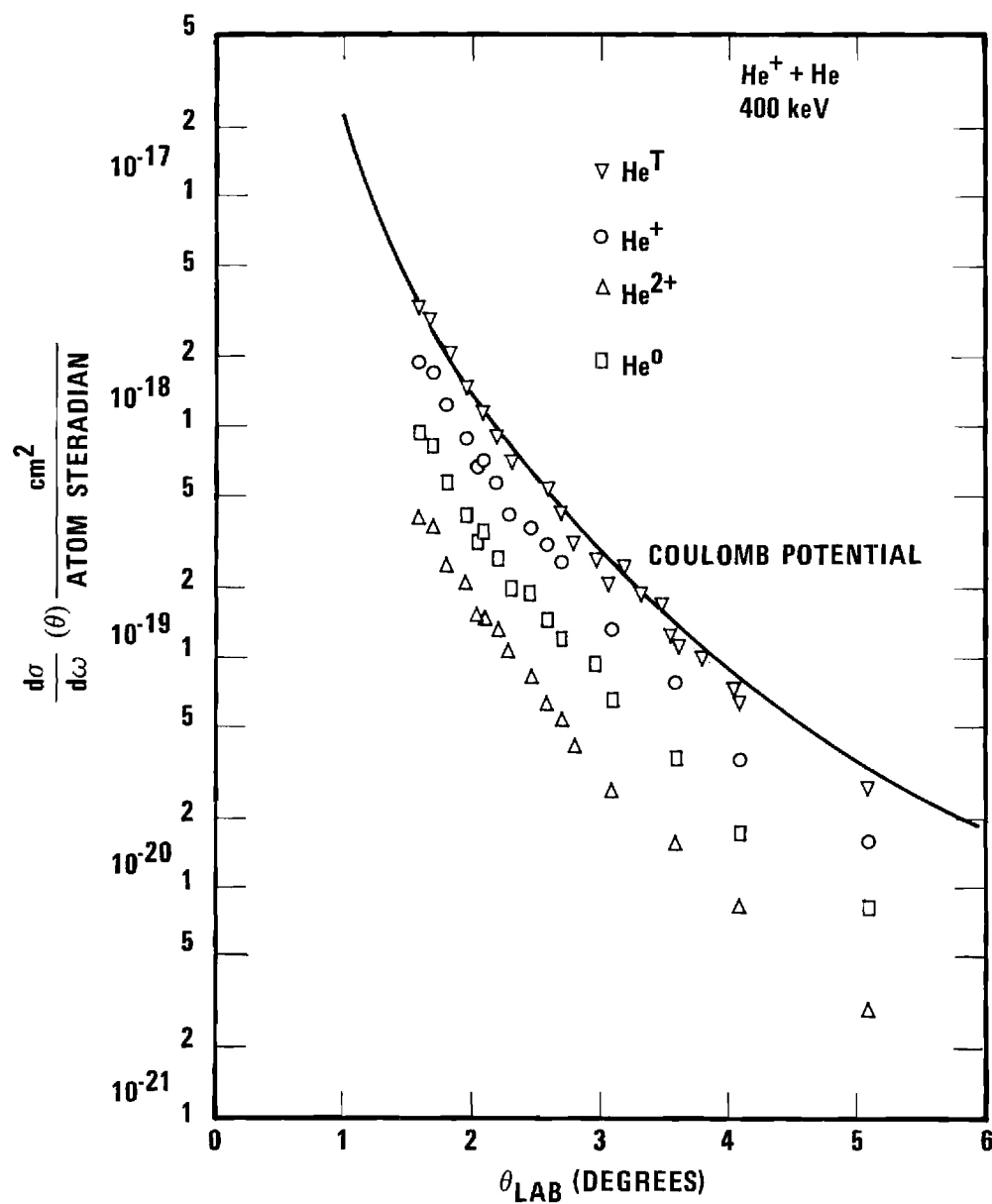


Figure 28. Differential Scattering Cross Sections Versus Angle for  $\text{He}^+ + \text{He}$  with Incident Energy of 400 keV.

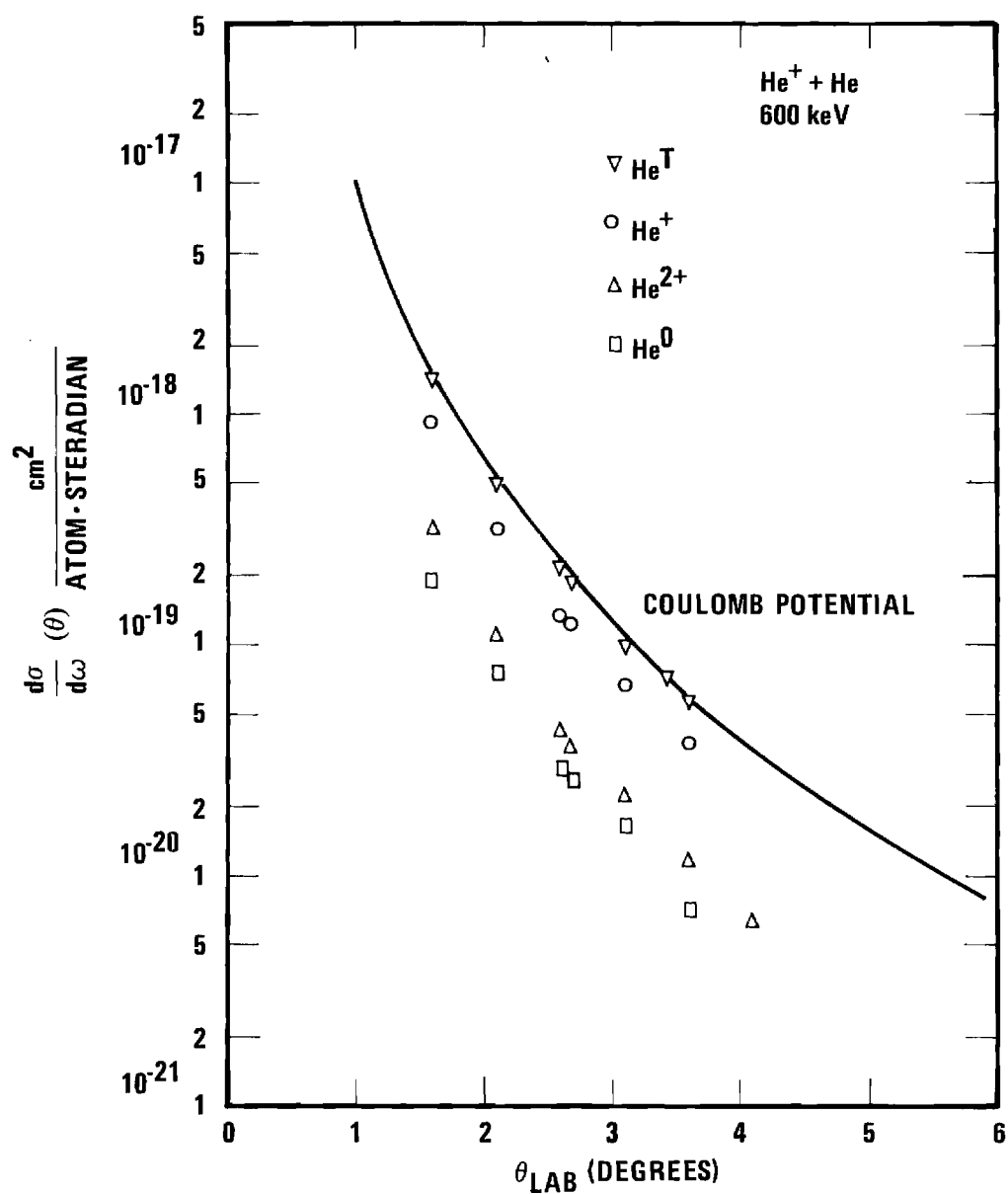


Figure 29. Differential Scattering Cross Sections Versus Angle for  $\text{He}^+ + \text{He}$  with Incident Energy of 600 keV.

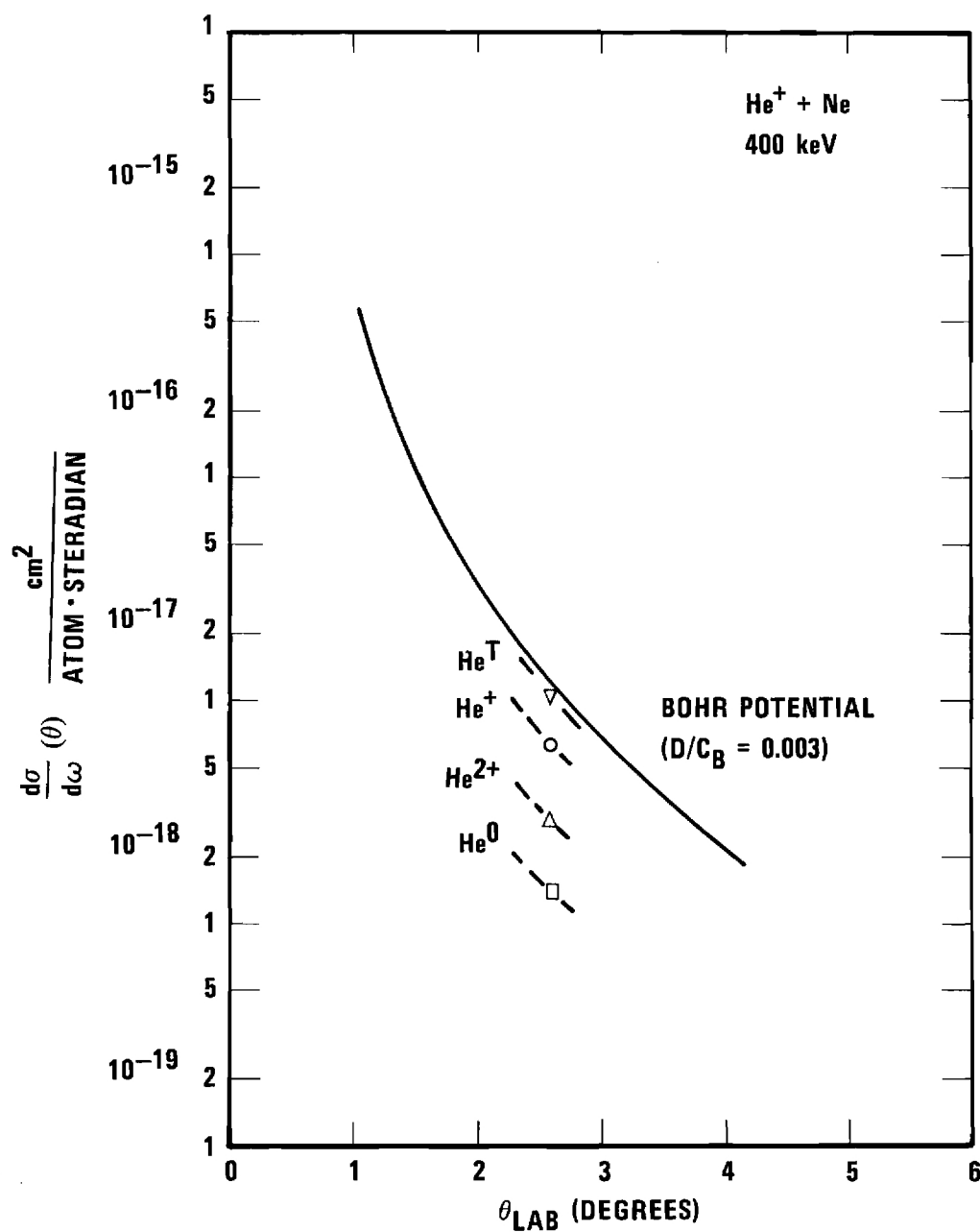


Figure 30. Differential Scattering Cross Sections Versus Angle for He<sup>+</sup> + Ne with Incident Energy of 400 keV.

into solid angle  $d\omega$  at angle  $\theta$  irrespective of their charge state) and compared with the sum; the measured total agreed with the sum of the individual cross sections within counting statistics in every case.

The data were accumulated over a period of seven months. During this time, several important additions were made to the apparatus, the most important being the capacitance manometer. With the capacitance manometer an accurate absolute measurement of the target gas pressure was made. Cross sections measured prior to the time of using this instrument (i.e., data taken in November and December, 1968) were normalized to later measurements. This normalization shifted all of the data taken in November and December of 1968 by a uniform 20 percent. Only Ar data were accumulated during this time period.

Figures 25, 26, and 27 show the cross sections as a function of scattering angle  $\theta$  for  $\text{He}^+$  ions incident on argon atoms at 208, 418, and 627 keV, respectively. There is excellent agreement between the shapes of the measured curves and the theoretical curve based on a classical calculation using a Bohr potential, equation (23). The shielding factor,  $D/c_B$ , is shown on each individual graph. The values of the theoretical cross sections were taken from the tabulation of Bingham.<sup>36</sup> It is equally interesting that the sum of the three cross sections,

$$\frac{d\sigma^T}{d\omega} = \frac{d\sigma^+}{d\omega} + \frac{d\sigma^{2+}}{d\omega} + \frac{d\sigma^0}{d\omega}$$

agrees absolutely (within experimental error) with the theoretical curve.

The theoretical differential scattering cross section based on a classical calculation using a Bohr potential is valid for elastic colli-

sions. The present measurements could not distinguish elastic from inelastic collisions. Although  $\frac{d\sigma^+}{d\omega}$  did contain all the elastic scattering events, it also contained all inelastic events in which the projectile did not change its electrical charge.  $\frac{d\sigma^T}{d\omega}$  contained all elastic plus all the inelastic events. But, reported measurements<sup>11,12</sup> indicate that the inelastic energy loss in high energy heavy body collisions is small when the fast particle undergoes appreciable scatter so that  $\frac{d\sigma^T}{d\omega}$  can be considered as "almost" or "quasi-" elastic. From these considerations it was not obvious a priori whether the theoretical curve should compare with  $\frac{d\sigma^+}{d\omega}$ , with  $\frac{d\sigma^T}{d\omega}$ , or possibly with neither.

As the data, Figures 25 through 30, clearly demonstrate,  $\frac{d\sigma^T}{d\omega}$  agrees with the theoretical curve within the experimental errors. The good agreement between these curves indicates that the scattering is governed by the nuclear-nuclear force and is independent of the final arrangement of the electrons after the collision. Also, the agreement confirms Smith's<sup>35</sup> contention that such high energy collisions can be considered as "quasi-elastic." Additionally, it suggests that the inelastic energy loss under these conditions must be very small, which confirms measurements from other laboratories.

The area under the total differential scattering curves is proportional to the "total cross sections" for the particular process, i.e.,

$$\sigma^{\text{stripping}}(E) = 2\pi \int_0^\pi \frac{d\sigma^{2+}}{d\omega}(\theta, E) \sin \theta \, d\theta$$

and

$$\sigma^{\text{transfer}}(E) = 2\pi \int_0^\pi \frac{d\sigma^0}{d\omega}(\theta, E) \sin \theta \, d\theta .$$

These total cross sections have been measured experimentally<sup>80, 81, 82, 83</sup> and theoretical<sup>84, 85</sup> calculations on some collision combinations have been made. It would be very interesting to compare the present measurements with these other works. However, Jones, et al.<sup>83</sup> have shown that greater than 99 percent of these total cross sections comes from collisions where the scattering was less than one degree. Thus, the area under the experimental differential scattering curves amounts to roughly only one percent of the total cross section for the given process. This was confirmed in a single case by comparing the area under the charge changing cross section with the experimental value<sup>83</sup> of  $\sigma^{\text{transfer}}$ . Hence, this comparison was not pursued.

The scattering force can be represented by the interaction potential

$$U(r) = \frac{Z_1 Z_2 e^2}{r} e^{-r/c_B} \quad (23)$$

The effect of the screening factor (the exponential factor) becomes negligibly small when the scattering angle is greater than a few degrees. In Figure 31 is plotted, as was suggested by Smith,<sup>35</sup> a "reduced cross section"  $\rho = \Theta \sin \Theta \frac{d\sigma}{d\Omega}(\Theta)$  as a function of the product  $\tau = \Theta E_{\text{cm}}$ . The advantage of this presentation of the data is that it combines the differential cross section for all angles and energies into a single graph; i.e., it shows the total differential scattering cross sections contained in Figures 25, 26, and 27. Also, the theoretical cross sections based on both the Coulomb and the Bohr potentials are shown. Notice that the two theoretical curves separate only below  $8 \times 10^5$  eV degrees. This is equivalent to a scattering angle in the laboratory of approximately three



degrees 45 minutes when  $E = 208$  keV, two degrees 15 minutes when  $E = 418$  keV, and one degree zero minutes when  $E = 627$  keV. Outside these angular limits, the "pure" Coulomb force between the two nuclei essentially governs the scattering.

The experimental data for  $\text{He}^+ + \text{He}$  are compared with the differential cross section curve for the pure Coulomb potential (Figures 28 and 29). The screening constant,  $D/c_B$ , is extremely small, indicating that the electron shielding is negligible for this case. The agreement between experiment and theory is very good. Only one point was measured for  $\text{He}^+ + \text{Ne}$  (Figure 30). As in the other cases, the total differential scattering cross section agrees with the calculated value.

Fuls, et al.<sup>8</sup> measured the total differential scattering cross section for  $\text{He}^+$  incident on the same target gases as were investigated in the present measurement for incident energies between 25 and 100 keV. His results also agreed with the cross sections computed using the screened Coulomb potential.

Figure 32 shows the differential scattering cross sections at fixed angle for all charge changing processes measured as a function of energy. Also shown are the results of Fuls, et al.<sup>8</sup> for energies down to 25 keV, and the theoretical curves predicted classically from both the screened (Born) and the "pure" Coulomb potentials. Figure 32 shows that the differential scattering cross section for charge transfer falls off very rapidly, approximately as  $v^{-5}$ . The Born approximation for the "total" charge transfer cross section (i.e.,  $\sigma(E)$ ) predicts a  $v^{-12}$  dependence on impact velocity; however, various experimental measurements<sup>86</sup> have shown an extremely wide range in this velocity dependence, from  $v^{-3.7}$  to  $v^{-10}$ .



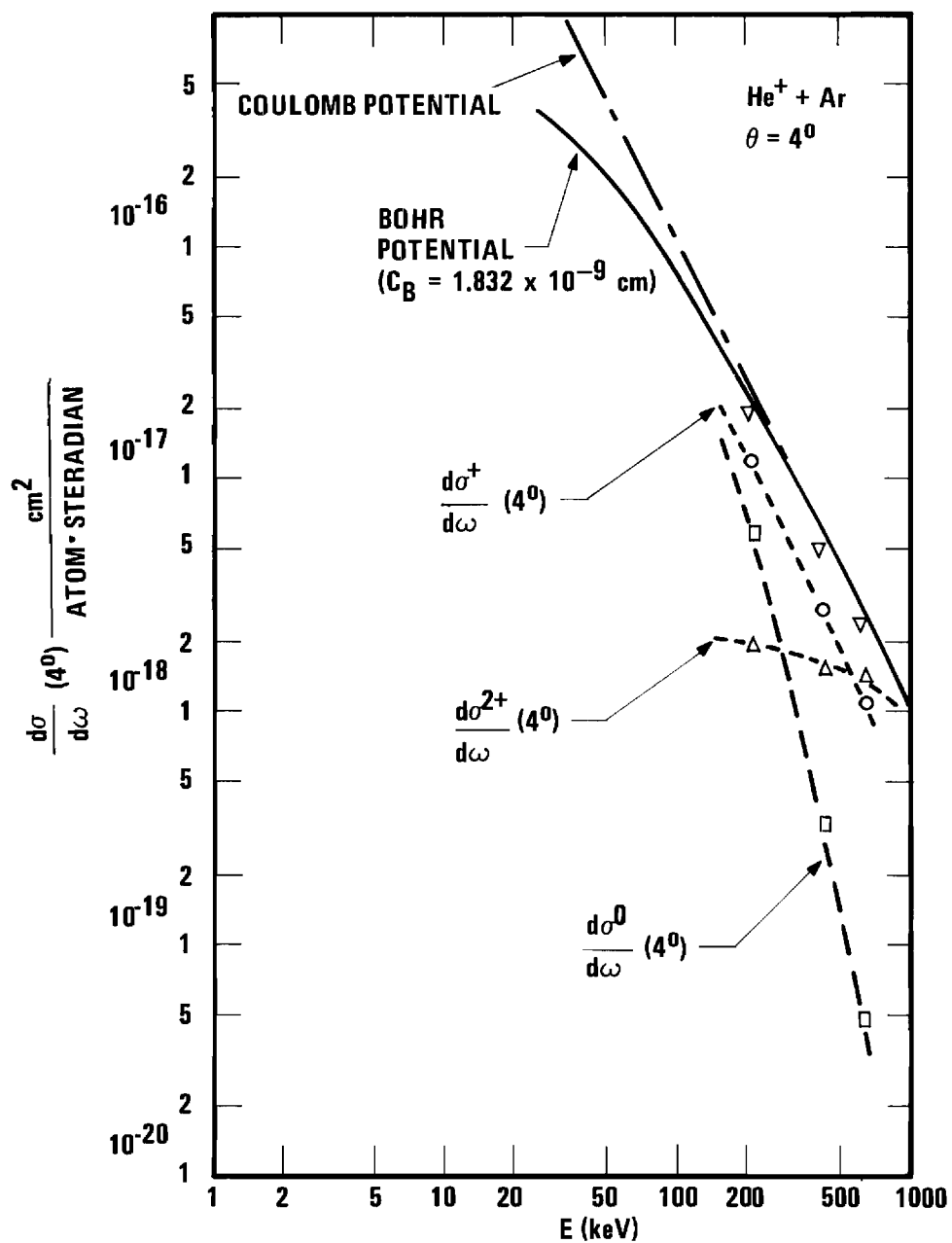


Figure 32: Differential Scattering Cross Sections Versus Energy for  $\text{He}^+ + \text{Ar}$  at a Scattering Angle of  $4^\circ$ .

From 200 to 600 keV the differential scattering cross section for electron stripping shows a velocity dependence approximately equal to  $v^{-0.5}$ ; however, from 600 to 800 keV the velocity dependence of this cross section changes rapidly apparently approaching a  $v^{-2}$  dependence. This velocity dependence is similar to reported total loss cross sections.<sup>86</sup>

It is very interesting that these differential cross sections show an energy dependence similar to the total cross sections for charge transfer and stripping. Remembering that the total cross section is the integral of the differential scattering cross section, i.e.,

$$\sigma(E) = 2\pi \int_0^\pi \frac{d\sigma}{d\omega}(\theta, E) \sin \theta \, d\theta ,$$

one would not expect a priori that  $\frac{d\sigma}{d\omega}$  and  $\sigma$  would necessarily show the same energy dependence.

Results using the Born approximation have not been published for differential scattering cross sections. As the higher energies in the present experiment are in the region where the Born approximations should be applicable, such a comparison would be very interesting.

A "distance of closest approach" scale has also been included in Figures 25, 26, and 27. These distances were taken from tabulated values<sup>36</sup> computed classically for the Born potential. Also on this scale is found the radius of the K shell of argon. (This K shell radius is based on the ionization potential.<sup>20</sup>) The data in these figures were closely examined for any evidence of structure in the curves, especially near the K shell radius. Figure 25 shows suspicious behavior when  $r_0 \approx 2.9 \times 10^{-10}$  cm, a separation distance of approximately the K shell radius. However, this

feature is not seen at higher projectile energies, even though the data span the  $r = 2.9 \times 10^{-10}$  cm region. Hence, it must be concluded that slight fluctuations in Figure 25 are probably not significant. Based on the accuracy of these measurements, if any anomalies giving rise to structure in the differential scattering curves exist within the investigated energy and angular ranges, they deviate from a smooth curve by less than 12 percent.

### Charge State Fractions

#### Angular Dependence

Figures 33 through 37 show the fraction,  $P_n$ , of charge states,  $n$ , as a function of scattering angle,  $\theta$ .

$$P_n(\theta) = \frac{N^n(\theta)}{N^I(\theta)} \quad (17)$$

These figures show that  $P_n$  has no dependence on the scattering angle within the range of conditions investigated. This fact is consistent with Russek's prediction for the high energy behavior of  $P_0$ . Angular independence of  $P_n$  has been reported at 100 keV, also at 50 keV when  $\theta \geq 4$  degrees.<sup>8,87</sup>

#### Energy Dependence

Figures 38, 39, and 40 display the energy dependence of  $P_n$ . The data in these graphs are presented in tabular form in Tables 6, 7, and 8. As  $P_n$  has no angular dependence under the conditions investigated, these curves were measured at several angles. The particular angles were chosen to minimize errors due to counting statistics, while at the same time

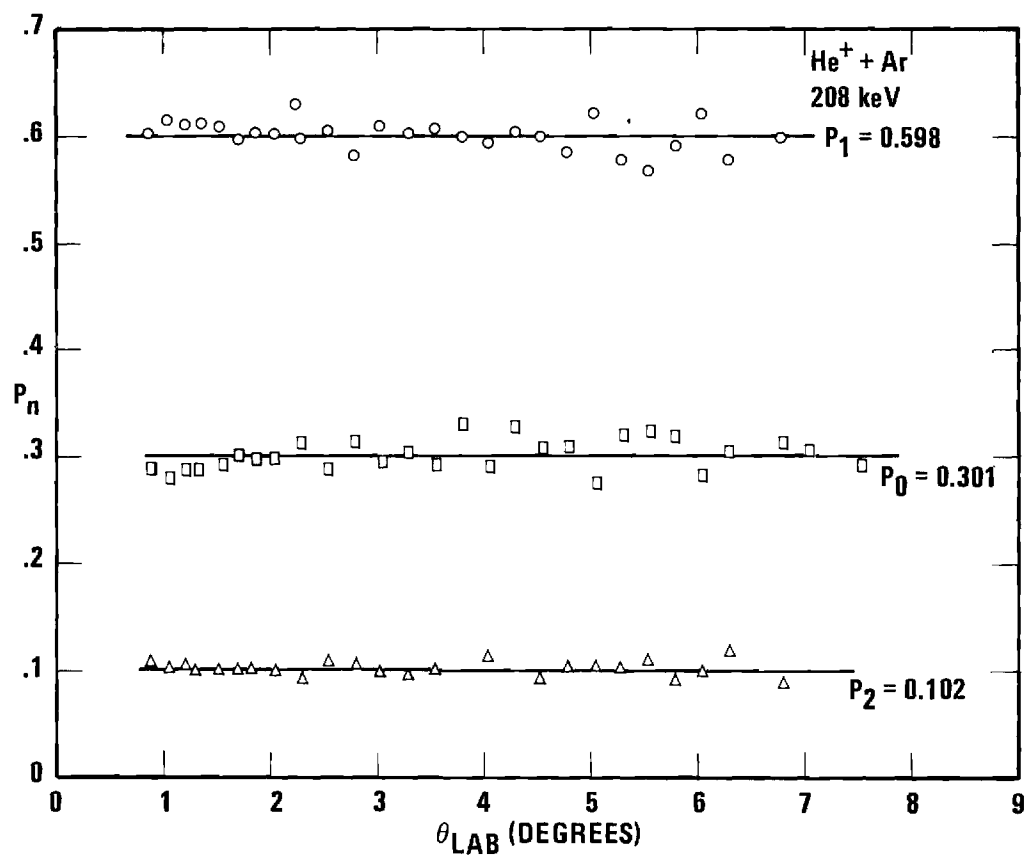


Figure 33. Fraction of Scattered Beam in Charge State  $n$  Versus Scattering Angle for He<sup>+</sup> + Ar with Incident Energy of 208 keV.

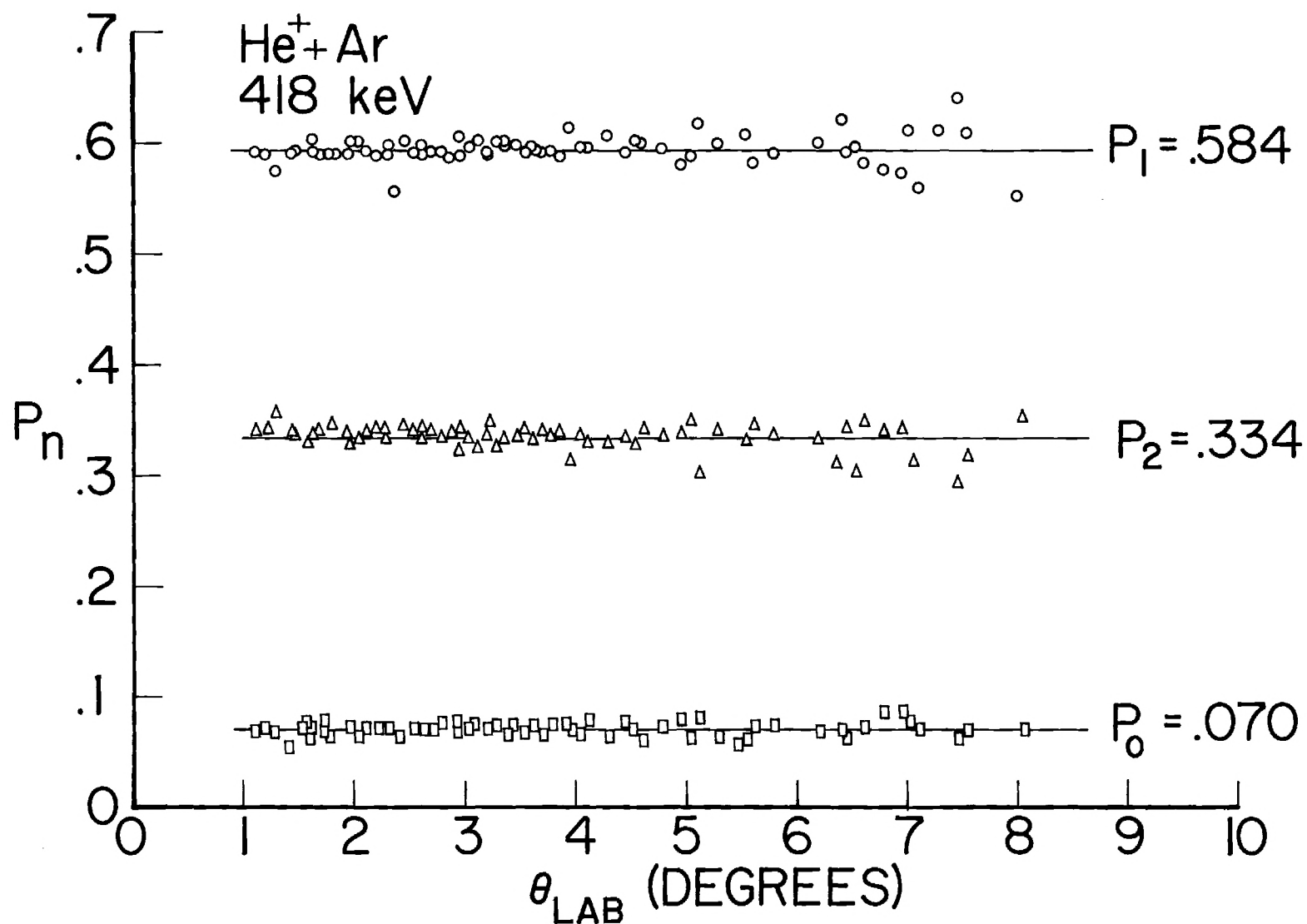


Figure 34. Fraction of Scattered Beam in Charge State  $n$  Versus Scattering Angle for He<sup>+</sup> + Ar with Incident Energy of 418 keV.

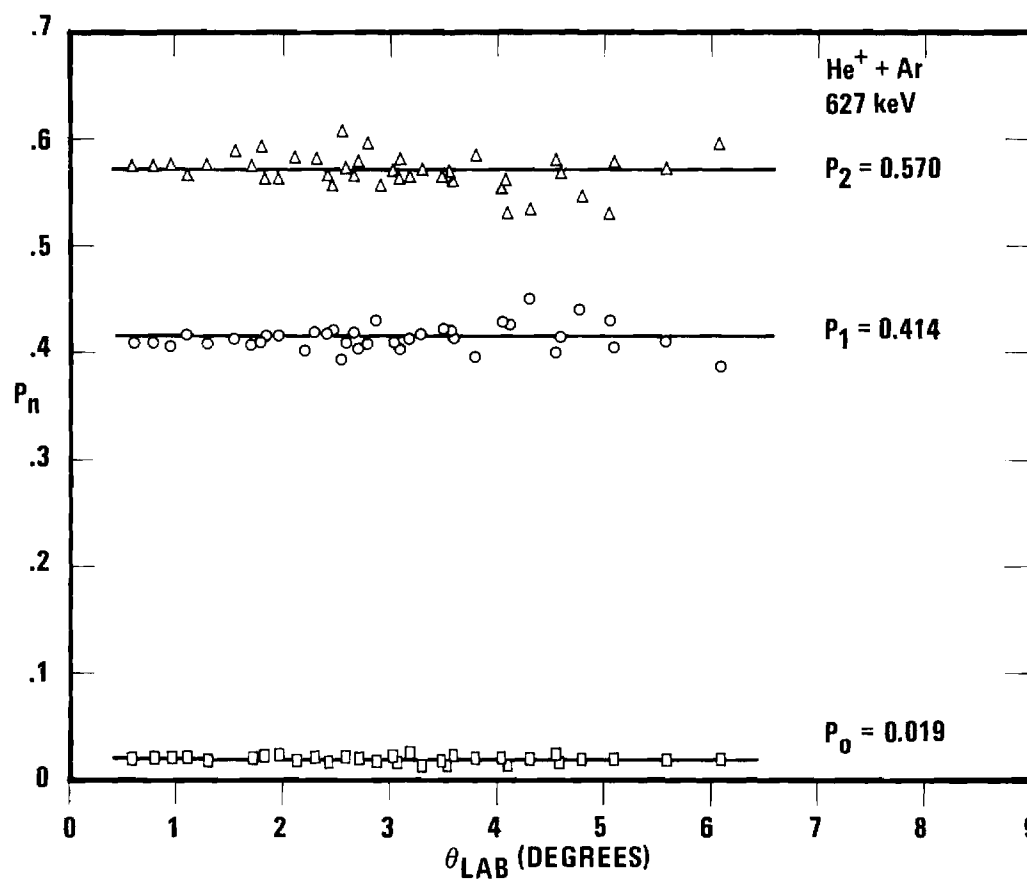


Figure 35. Fraction of Scattered Beam in Charge State  $n$  Versus Scattering Angle for He<sup>+</sup> + Ar with Incident Energy of 627 keV.

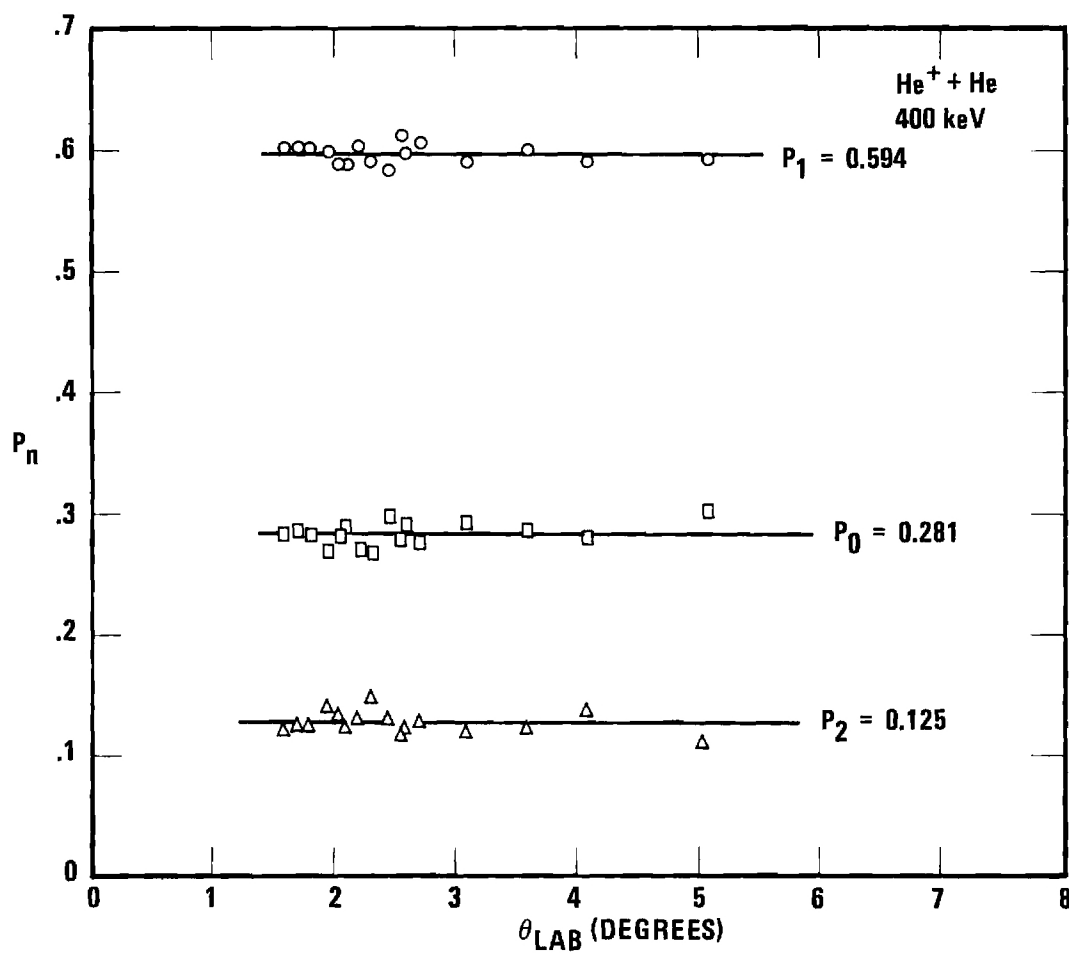


Figure 36. Fraction of Scattered Beam in Charge State  $n$  Versus Scattering Angle for  $\text{He}^+ + \text{He}$  with Incident Energy of 400 keV.

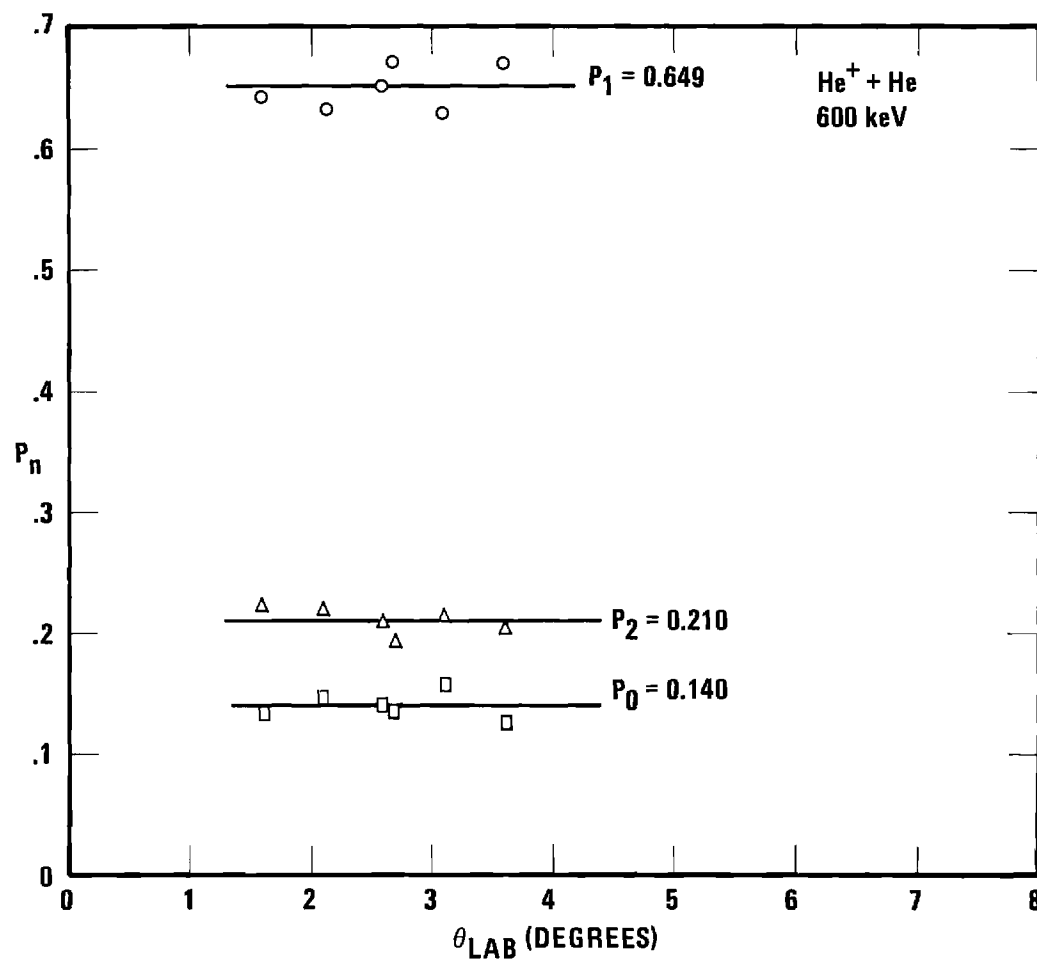


Figure 37. Fraction of Scattered Beam in Charge State  $n$  Versus Scattering Angle for  $\text{He}^+ + \text{He}$  with Incident Energy of 600 keV.



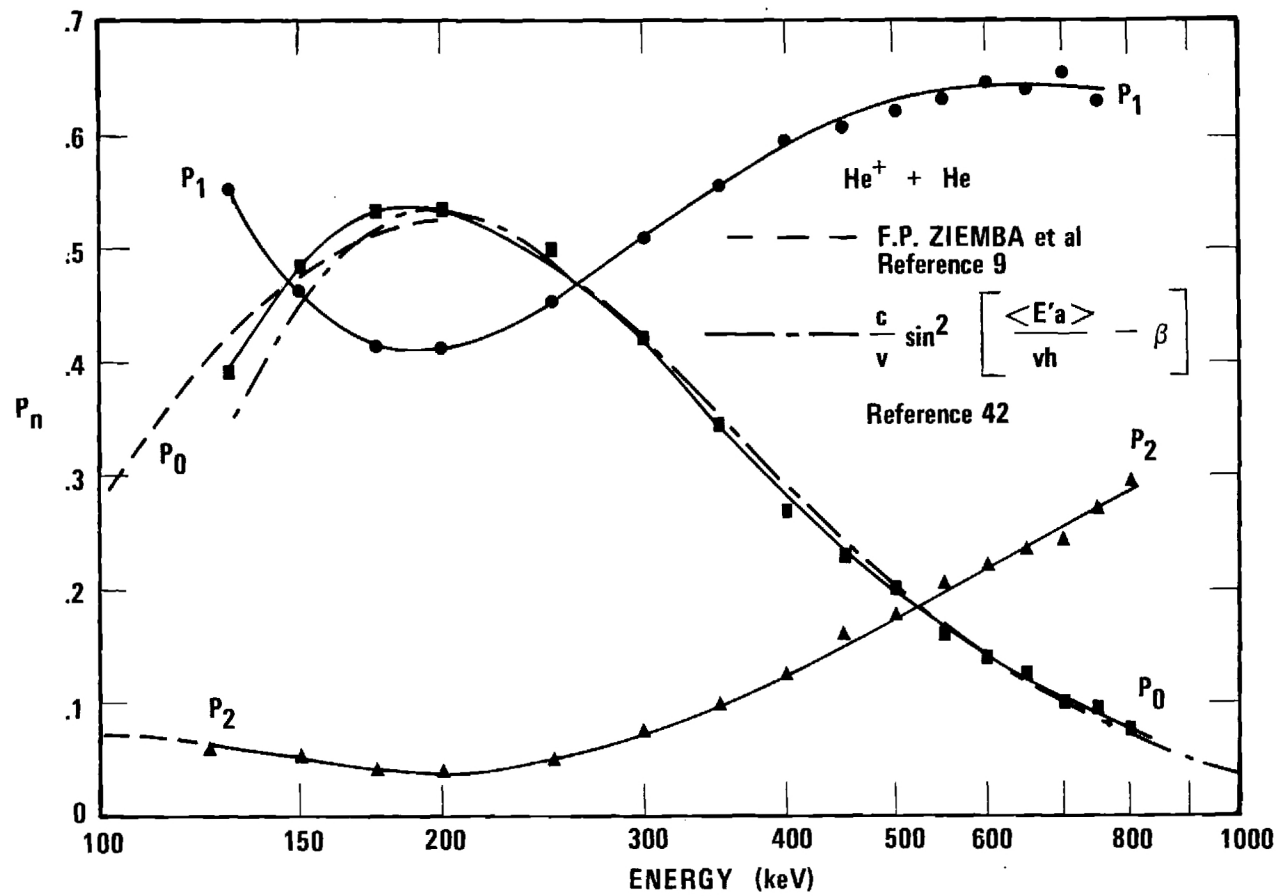


Figure 38. Fraction of Scattered Beam in Charge State  $n$  Versus Energy for  $\text{He}^+ + \text{He}$ .

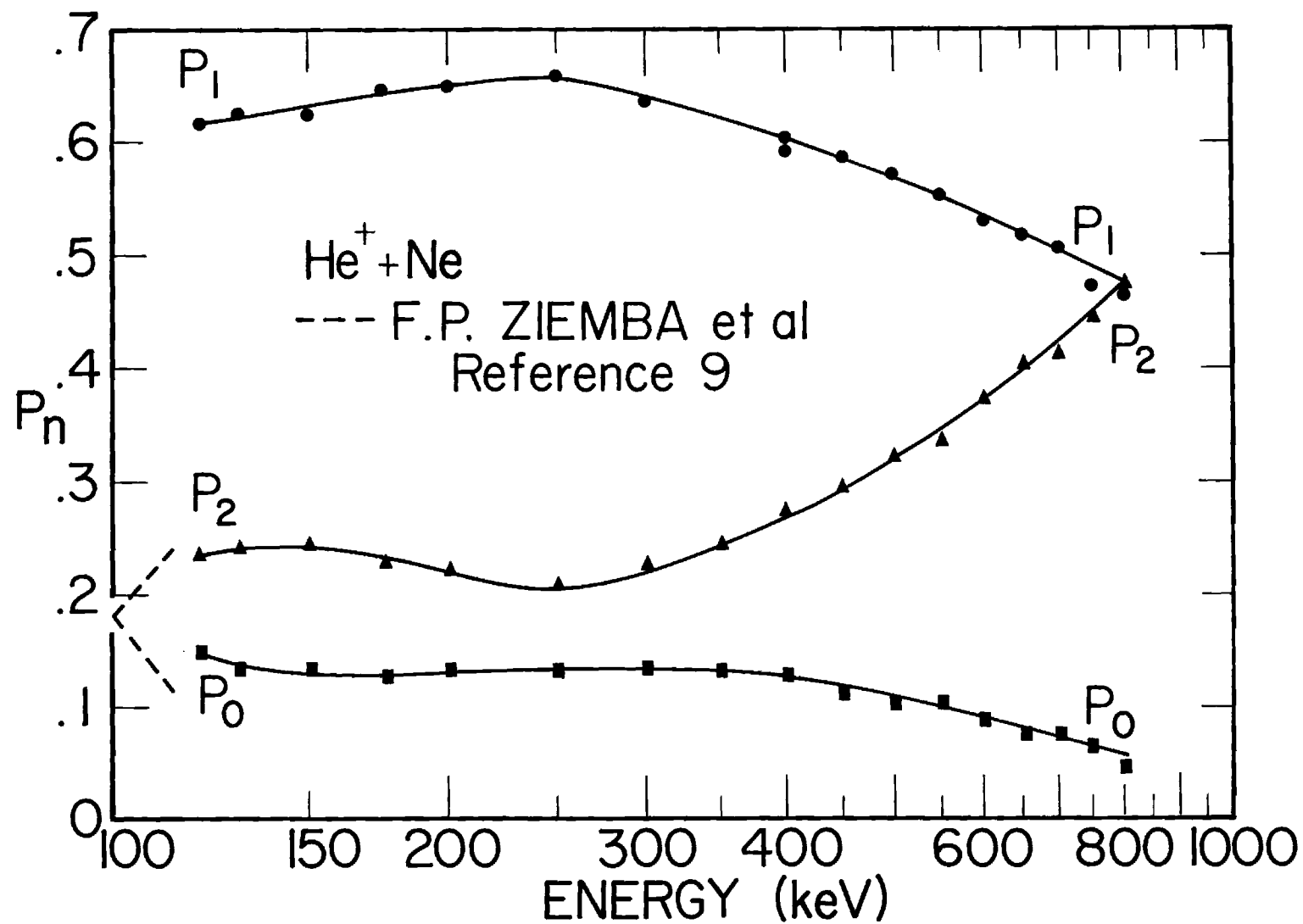


Figure 39. Fraction of Scattered Beam in Charge State  $n$  Versus Energy for  $\text{He}^+ + \text{Ne}$ .

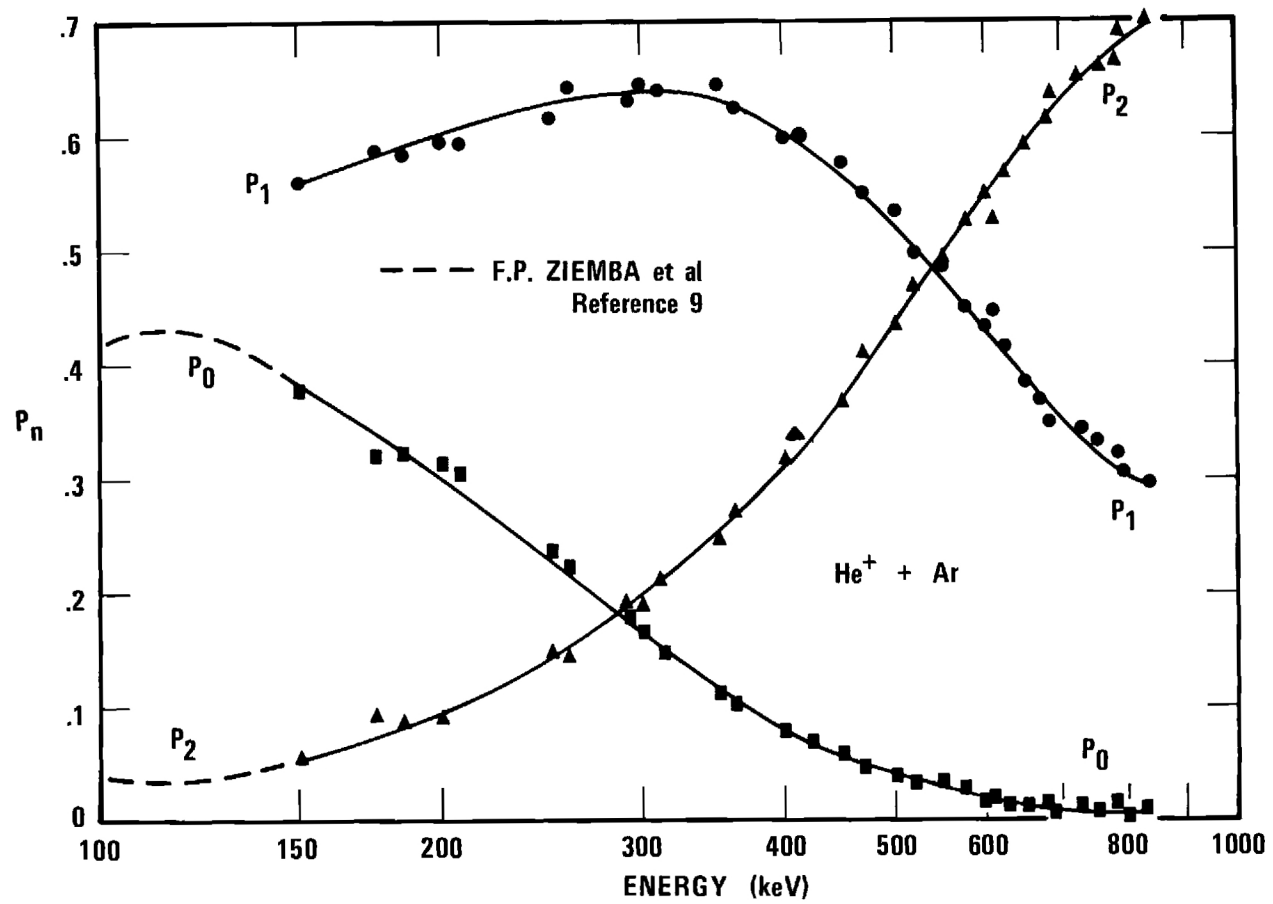


Figure 40. Fraction of Scattered Beam in Charge State  $n$  Versus Energy for  $\text{He}^+ + \text{Ar}$ .

Table 6. Energy Dependence of  $P_n$  for  $\text{He}^+ + \text{He}$ 

E	$P_0$	$P_1$	$P_2$
130	0.391	0.551	0.059
150	0.488	0.464	0.049
175	0.537	0.421	0.042
200	0.538	0.420	0.041
250	0.502	0.455	0.053
300	0.412	0.515	0.073
350	0.345	0.559	0.095
400	0.281	0.594	0.125
450	0.232	0.607	0.162
500	0.202	0.621	0.181
550	0.164	0.631	0.204
600	0.140	0.649	0.212
650	0.128	0.637	0.235
700	0.101	0.654	0.245
750	0.098	0.633	0.270
800	0.076	0.633	0.293

Table 7. Energy Dependence of  $P_n$  for  $\text{He}^+ + \text{Ne}$ 

E	$P_0$	$P_1$	$P_2$
120	0.148	0.600	0.250
130	0.134	0.627	0.240
150	0.131	0.624	0.244
175	0.127	0.647	0.226
200	0.133	0.650	0.217
250	0.132	0.659	0.208
300	0.134	0.639	0.228
350	0.131	0.620	0.248
400	0.126	0.601	0.275
450	0.110	0.589	0.297
500	0.101	0.575	0.322
550	0.105	0.557	0.338
600	0.088	0.536	0.374
650	0.078	0.519	0.404
700	0.075	0.508	0.416
750	0.066	0.478	0.449
800	0.043	0.464	0.474

Table 8. Energy Dependence of  $P_n$  for  $\text{He}^+ + \text{Ar}$ 

E	$P_0$	$P_1$	$P_2$
158	0.375	0.560	0.055
187	0.332	0.584	0.085
208	0.306	0.594	0.100
261	0.218	0.640	0.142
292	0.180	0.630	0.190
313	0.149	0.639	0.216
351	0.112	0.639	0.346
365	0.102	0.626	0.272
400	0.082	0.600	0.317
418	0.069	0.605	0.326
450	0.060	0.575	0.365
470	0.045	0.549	0.407
501	0.040	0.530	0.432
522	0.034	0.498	0.468
551	0.030	0.483	0.487
603	0.023	0.448	0.527
653	0.016	0.383	0.593
685	0.015	0.360	0.625
734	0.010	0.342	0.648
759	0.009	0.331	0.658
781	0.013	0.321	0.665
793	0.007	0.304	0.689
830	0.008	0.295	0.697

keeping the counting rate within the limitations of the electronics. The scattering angles were varied from one and one-half degrees to three degrees while taking these data; the smaller angles were used primarily when He was the target. Some individual runs were made over the entire energy span at a single fixed angle, but these runs were weighted equally with data at other angles.

Measurements<sup>9,41</sup> have been reported of the energy dependence of  $P_n$  for  $\text{He}^+$  ions incident on He from one to 200 keV,  $\text{He}^+$  ions incident on Ne and Ar from 10 to 200 keV.<sup>9</sup> These data are shown by dashed lines on Figures 38, 39, and 40. There is excellent agreement between the two sets of data in all cases. Taken together, these two sets of data furnish the energy dependence of  $P_n$  over an extremely wide energy range.

For the resonant case,  $\text{He}^+ + \text{He}$ , Everhart predicted<sup>87</sup> that the last peak in the oscillation of  $P_0$  would occur at 250 keV. His data, which stop at 200 keV, seem to support the supposition; however, the present data indicate the peak in  $P_0$  to occur at approximately 190 keV. The present data and Everhart's data do not disagree outside their stated errors, although he shows a slightly different curve of best fit through his data.

The dashed line in Figure 38 shows the semi-empirical equation

$$P_0 = K_0\left(\frac{1}{v}\right) + K_2\left(\frac{1}{v}\right) \sin^2 \left[ \frac{\pi \langle E'a \rangle}{vh} - \beta \right]. \quad (39)$$

$K_1$  and  $K_2$  are slowly varying functions of reciprocal velocity. This equation correctly reproduces the data of Everhart.<sup>42</sup> For  $\text{He}^+ + \text{He}$ , Everhart<sup>42</sup> lists  $\langle E'a \rangle = 102 \pm 3 \text{ eV-Å}$ ,  $\beta = (0.23 \pm 0.08)\pi$ ,  $K_0 = 0$  and  $K_2 = 1$ .

It has been found that this equation agrees extremely well with the present experimental data from 150 keV to 1000 keV if the same values of  $\langle E'a \rangle$  and  $\beta$  are used, but with  $K_1 = 0$  and  $K_2 = 1.729 \times 10^8/v$ ,  $v$  being the projectile velocity in cm/sec. The curve of this equation is shown on Figure 38.

One last comparison to be made with the present data is with Russek's statistical theory.<sup>18,19</sup> As discussed in Chapter II, this theory was initially designed to describe heavy particle interaction and was then extended to consider interactions involving helium projectiles. This theory predicts the ordinates for the peak of each  $P_n$  curve (except  $P_0$ ), and the ordinate for each  $P_n \times P_m$  crossing. These predictions are presented in the form of a graph, the abscissa of the graph being a function that is indirectly relatable to the impact energy. The comparison between theory and experiment is shown in Table 9. As can be seen from examining this table, the  $P_0 \times P_1$  and  $P_1 \times P_2$  crossings are predicted remarkably closely; however, the prediction for the  $P_0 \times P_2$  crossing and the  $P_1$  peak are not as close.

Two values listed in the table ( $P_0$  in Ar and  $P_0 \times P_2$  in Ne) were not measured in the present experiment, but these values have been experimentally determined elsewhere<sup>9</sup> and are listed for comparative purposes.



Table 9. Heights of Intersections and Peaks of  $P_n$  Compared with Statistical Theory

	Target Gas			Theory <sup>19</sup>
	He	Ne	Ar	
$P_0$	0.54	-----	0.43 <sup>*</sup>	----
$P_0 \times P_1$	0.46-0.47	-----	-----	0.48
$P_0 \times P_2$	0.18	0.18 <sup>*</sup>	0.18	0.00
$P_1$	0.64	0.66	0.64	1.00
$P_1 \times P_2$	----	0.47	0.48	0.52
$P_2$	----	-----	-----	----

<sup>\*</sup> These values taken from other experimental work.<sup>9</sup>

## CHAPTER VI

## CONCLUSIONS

The total differential scattering cross section, the differential scattering cross sections for electron capture, for electron stripping, and for scattering without change of charge have been measured for fast  $\text{He}^+$  ions incident on the noble gases helium, neon, and argon. These cross sections were measured at several specific energies in the angular range from approximately one to eight degrees.

At each specific energy, the total differential scattering cross section (which was equal to the sum of the differential scattering cross sections for electron capture, for electron stripping, and for scattering without change of charge) agreed, within experimental errors, with the theoretically predicted cross section. The scattering is correctly predicted by classical theory where the interaction potential between the nuclei is a screened Coulomb function. The electronic screening is introduced to the Coulomb potential by an exponential factor ( $e^{-r/c_B}$ ) where  $c_B$  is the screening length originally suggested by Bohr.<sup>13</sup> This agreement strongly supports the approximation of separating the nuclear motion from the final electronic configuration. Also, this agreement between the data and the classical scattering theory confirms Smith's suggestion of considering such high energy collisions as "quasielastic." It was not possible to distinguish elastic from inelastic collisions in this work; however, it was possible to estimate an upper limit on the

inelastic energy loss to be less than 15 percent of the incident energy. Measurements in other laboratories<sup>11,12</sup> indicate that actually the inelastic energy loss is less than 0.01.

The estimated error in the total differential scattering cross section is  $\pm 23$  percent. Of this total possible error,  $\pm 13$  percent is considered systematic. The differential scattering cross sections for electron capture and for electron stripping have a possible random error of approximately  $\pm 15$  percent. The random error is dependent on the energy, scattering angle, and target gas.

It is estimated that any structure in the total differential scattering cross section which might exist within the investigated energy and angular region deviates less than 12 percent from the smoothly varying cross section curve. Such structure has been reported for the same projectile-target combinations in elastic collisions at low energies<sup>2,3</sup>; also, it has been reported for noble gas ion-atom collisions<sup>21</sup> at 25 and 50 keV.

The present investigation also measured the fraction of the charge states of the projectile as a function of both angle and energy. It was found that these fractions were independent of angle within the investigated region, a conclusion which is supported both by other experiments<sup>8</sup> and by theory.<sup>43</sup>

The energy dependence of these fractions was measured at fixed angle from approximately 150 to 830 keV. In the target gases Ne and Ar,  $\text{He}^{2+}$  became the dominant charge state at the higher energies. For the He target,  $\text{He}^{2+}$  was increasing at the highest energy of the present measurement, but  $\text{He}^+$  was still the largest charge state component of the

scattered beam. In the range 150 to 200 keV, the present measurements agree with the work of Ziemba, et al.<sup>9</sup> which covers the energy region from approximately 200 keV down to 10 keV.

For the case of  $\text{He}^+ + \text{He}$ , the probability of electron transfer has previously been represented at energies below 200 keV by the semi-empirical equation<sup>42</sup>

$$P_0 = K_0 \left( \frac{1}{v} \right) + K_2 \left( \frac{1}{v} \right) \sin^2 \left[ \frac{\pi \langle E' a \rangle}{v h} - \beta \right] \quad (39)$$

where  $K_0 = 0$  and  $K_2 = 1$ .  $\langle E' a \rangle$  and  $\beta$  were determined from experimental data.<sup>42</sup> It was found that this expression could also describe  $P_0$  in the energy region 150 to 1000 keV if  $K_2$  was set equal to  $1.729 \times 10^8/v$  where  $v$  is the projectile velocity in cm per second.

As the projectile energy approaches one MeV, the cross sections for charge changing should be adequately described by the Born approximation. However, differential scattering cross sections for charge changing collisions have not been published for the high energy case; therefore, it is not possible at present to make these comparisons.

## APPENDIX A

## GEOMETRICAL FACTOR IN SCATTERING EXPERIMENT

The differential scattering cross section is given by equation (15). Before evaluating this equation, it is first necessary to calculate the geometrical factor,  $G(\theta)$ . As shown in Chapter II,  $G(\theta)$  is the integral  $\int_L \omega dx$ . This integral represents the product of the average solid angle defined by the detection system and the length of beam path viewed by this solid angle. In evaluating this integral the treatment of Skalskaya<sup>88</sup> will be followed.

Consider a narrow parallel beam of projectiles passing through the target gas. The beam will define the x coordinate axis. Two rectangular apertures whose line of centers make an angle  $\theta$  with the beam axis define the scattered projectiles which will reach the detector (see Figure 41). The origin of x is taken at the point on the beam line where it is intersected by the line of centers of the scattered-particle apertures. Second order effects, such as the finite dimensions of the beam, are ignored for the present; however, later a generalization to finite beam dimensions is made in this appendix.

The first aperture ( $S_1$ ) had a width (a) and is a distance ( $l$ ) from the origin. The second aperture ( $S_2$ ) has a width (b), a height (h), and is a distance (d) behind the first aperture. The height of this first aperture is greater than the beam diameter; only the height of the second aperture limits particles from reaching the detector.  $\omega$  is the

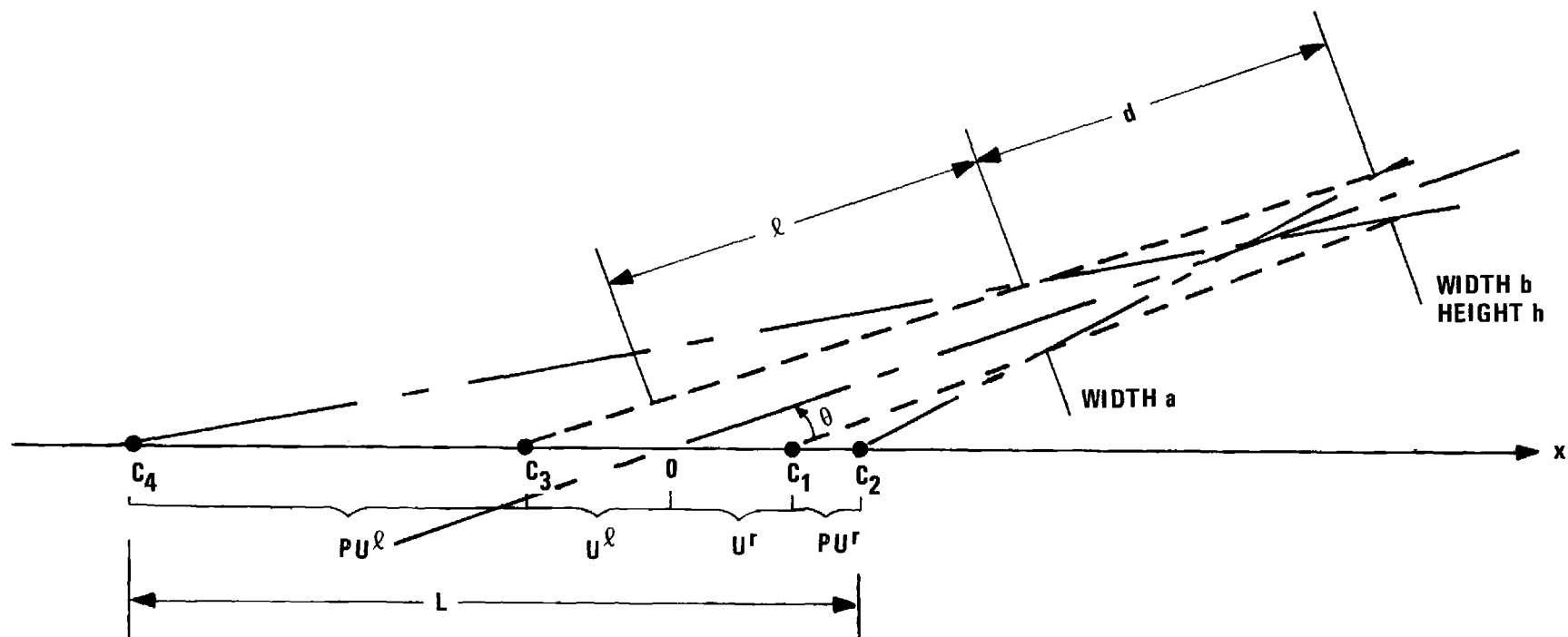


Figure 41. Umbra and Penumbra Regions in Scattering.

solid angle subtended by the bundle of all rays, from a given point  $(x)$  on the beam path, which pass through both apertures. The total length of beam path that may contribute to the scattered signal is  $(L)$ , the distance from point  $c_4$  to point  $c_2$ , in Figure 41. The points  $c_1$  and  $c_3$  divide the "umbra" region, in which all points of the beam can "see" the full width of aperture  $S_2$ , from the "penumbra" region in which part of the width of aperture  $S_2$  is occluded by the edge of aperture  $S_1$ .

To simplify the calculation, divide  $L$  into four regions; the umbra and penumbra to the right of the origin, the umbra and penumbra to the left of the origin. Considering first the umbra region to the right of the origin (region  $U^r$ ),

$$\omega_1(x) = \frac{b h}{(d + \ell - x \cos \theta)^2} \quad (43)$$

where

$$(0 \leq x \leq c_1) .$$

Using only the point-slope formula from analytical geometry, it can be shown that

$$c_1 = \frac{ad + \ell(a-b)}{2d \sin \theta + (a-b) \cos \theta} . \quad (44)$$

The solid angle for the penumbra regions is more difficult to compute since the aperture  $S_1$  partially occludes aperture  $S_2$ . In the penumbra to the right of the origin (region  $PU^r$ )

$$\omega_2(x) = \left\{ \frac{(a+b) l + ad - [(a+b) \cos \theta + 2d \sin \theta] x}{[d+l - x \cos \theta]^2 (\ell - x \cos \theta)} \right\} \frac{h}{2} \quad (45)$$

where

$$(c_1 \leq x \leq c_2)$$

and

$$c_2 = \frac{ad + \ell(a+b)}{2d \sin \theta + (a+b) \cos \theta} . \quad (46)$$

$c_2$  represents the limiting point to the right of the origin from which a particle may pass through both collimators.

For the region  $U^\ell$  (umbra left of origin)

$$\omega_3(x) = \frac{b h}{(d+l - x \cos \theta)^2} \quad (47)$$

where

$$(c_3 \leq x \leq 0) .$$

Carefully observe that  $x$  is negative in this region, and

$$c_3 = - \frac{ad + \ell(a-b)}{2d \sin \theta - (a-b) \cos \theta} . \quad (48)$$

In the region  $PU^\ell$  (penumbra left);

$$\omega_4(x) = \left\{ \frac{ad + (a+b) \ell + \{2d \sin \theta - (a+b) \cos \theta\} x}{[d+l - x \cos \theta]^2 (\ell - x \cos \theta)} \right\} \frac{h}{2} \quad (49)$$

where

$$(c_4 \leq x \leq c_3) .$$



$$c_4 = - \frac{ad + (a+b) \ell}{2d \sin \theta - (a+b) \cos \theta} . \quad (50)$$

$c_4$  is the limiting point to the left of the origin from which a particle may pass through both collimators.

The total path length which will contribute to the integral will be  $c_2 - c_4$  or

$$L = \frac{4d \sin \theta [ad + \ell(a+b)]}{(2d \sin \theta)^2 - (a+b)^2 \cos^2 \theta} . \quad (51)$$

The integration to be performed resolves itself into four integrals.

$$\int_L \omega(x) dx = \int_0^{c_1} \omega_1(x) dx + \int_{c_3}^0 \omega_3(x) dx + \int_{c_1}^{c_2} \omega_2(x) dx + \int_{c_4}^{c_3} \omega_4(x) dx \quad (52)$$

The first two integrals represent the umbra region, the last two the penumbra. These integrations are straightforward, though lengthy.

The integral for the umbra region gives

$$\int_0^{c_1} \omega_1(x) dx + \int_{c_3}^0 \omega_3(x) dx = \frac{bh}{d + \ell} \left\{ \frac{c_1}{d + \ell - c_1 \cos \theta} - \frac{c_3}{d + \ell - c_3 \cos \theta} \right\}. \quad (53)$$

For penumbra right,

$$\begin{aligned} \int_{c_1}^{c_2} \omega_2(x) dx &= \frac{h}{2} [2(d + \ell) \tan \theta + b] \left\{ \frac{c_2 - c_1}{(d + \ell - c_2 \cos \theta)(d + \ell - c_1 \cos \theta)} \right\} \\ &+ \frac{h[2\ell \tan \theta - a]}{2d \cos \theta} \ln \frac{\ell - c_2 \cos \theta}{\ell - c_1 \cos \theta} \cdot \frac{d + \ell - c_1 \cos \theta}{d + \ell - c_2 \cos \theta} . \end{aligned} \quad (54)$$

And for penumbra left

$$\int_{c_4}^{c_3} \omega_4(x) dx = + \frac{h}{2} [2(d+l) \tan \theta + b] \left\{ \frac{c_4 - c_3}{(d+l - c_3 \cos \theta)(d+l - c_4 \cos \theta)} \right\} \\ + \frac{h[2l \tan \theta - a]}{2d \cos \theta} \ln \frac{l - c_4 \cos \theta}{l - c_3 \cos \theta} \cdot \frac{d+l - c_3 \cos \theta}{d+l - c_4 \cos \theta} . \quad (55)$$

Thus, the complete analytical expression for the geometrical factor is:

$$\int_L \omega(x) dx = \frac{bh}{d+l} \left\{ \frac{c_1}{d+l - c_1 \cos \theta} - \frac{c_3}{d+l - c_3 \cos \theta} \right\} \\ + \frac{h[2(d+l) \tan \theta + b]}{2[d+l - c_2 \cos \theta]} \frac{[c_2 - c_1]}{[d+l - c_1 \cos \theta]} \\ + \frac{h[2(d+l) \tan \theta + b]}{2[d+l - c_3 \cos \theta]} \frac{[c_4 - c_3]}{[d+l - c_4 \cos \theta]} \\ + \frac{h[2l \tan \theta - a]}{2d \cos \theta} \ln \frac{l - c_2 \cos \theta}{l - c_1 \cos \theta} \cdot \frac{d+l - c_1 \cos \theta}{d+l - c_2 \cos \theta} \\ + \frac{h[2l \tan \theta + a]}{2d \cos \theta} \ln \frac{l - c_4 \cos \theta}{l - c_3 \cos \theta} \cdot \frac{d+l - c_3 \cos \theta}{d+l - c_4 \cos \theta} . \quad (56)$$

This relation is very similar to the expression derived by Fillippenko,<sup>23</sup> which seems to contain certain errors.

This equation can be greatly simplified by substituting the expressions for the four c's; i.e., equations (44), (46), (48), and (50) into equation (56). When this is done, the first three terms exactly cancel. Also, the two ln terms may be combined giving,

$$\int_L \omega(x) dx = \frac{ah}{d \cos \theta} \ln \frac{2(d+l) \sin \theta + b \cos \theta}{2(d+l) \sin \theta - b \cos \theta} . \quad (57)$$

This equation is identical to the expression derived by Skalskaya.<sup>88</sup>

Upon expanding the  $\ln$  term, one obtains

$$\int_L \omega(x) dx = \frac{ah}{d \cos \theta} \left\{ 2\zeta + \frac{2}{3} \zeta^3 + \dots \right\} \quad (58)$$

where

$$\zeta = \frac{b \cos \theta}{2(d+l) \sin \theta} .$$

Keeping only the first term,

$$\int_L \omega dx \approx \frac{abh}{d(d+l)} \frac{1}{\sin \theta} . \quad (59)$$

This is the Jordan-Brode equation.<sup>89</sup> It has been employed by all investigators measuring absolute differential scattering cross sections.<sup>37,52,53</sup>

Ignoring the higher order terms requires that

$$b^3 \cos^3 \theta \ll 12 (d+l)^3 \sin^3 \theta .$$

In this experiment this condition would be well satisfied down to angles less than 30 minutes. For example, with  $\theta = 30$  minutes,  $b = 0.0091$  inch, and  $d = 5.65$  inches; the inequality requires that  $7.5 \times 10^{-4} \ll 1.4$ .

#### Beam Thickness

In Chapter II it is shown that, in evaluating the differential scattering cross section  $\frac{d\sigma}{d\omega}$ , one actually needs to evaluate the integral  $\int \omega dA dx$ , where  $dA$  is a differential cross sectional area of the beam. The integral  $\int \omega dx$  has been evaluated. Now we shall show that  $A \int \omega dx$  is a very

good approximation for  $\int \omega dA dx$ , for the geometry of the present experiment.

We shall assume that the cross sectional area of the beam is square. This is a "worst case" approximation; the beam is actually circular in cross section in the present experiment. Let the scattering plane be the  $x - z$  plane. For a given  $x$ , the distance to the first aperture  $S_1$  from points in the beam volume is much more dependent on the width  $z$  of the beam in the scattering plane than on its height  $y$  perpendicular to that plane. Hence, we need to consider only the two-dimensional "volume" of the beam, or its area in the scattering plane.

Let the origin be at the center with the beam extending to  $\pm \eta/2$  along both the  $y$  and  $z$  axes, Figure 42.

$$\int \omega dA dx = \int_{-\eta/2}^{\eta/2} dy \int_{-\eta/2}^{\eta/2} dz \int_L \omega dx$$

The  $x$  integration proceeds exactly as in the development leading to equation (59) except that everywhere we must replace  $l$  by  $l - z/\sin \theta$ . The result is

$$\int \omega dx \simeq \frac{abh}{d \left( d+l - \frac{z}{\sin \theta} \right)} \frac{1}{\sin \theta} \quad (60)$$

The  $y$  integration gives the factor  $\eta$ ; performing the  $z$  integration, we get

$$\begin{aligned} \int \omega dA dx &\simeq \frac{\eta abh}{d} \ln \frac{d+l + \frac{\eta}{2 \sin \theta}}{d+l - \frac{\eta}{2 \sin \theta}} \\ &\simeq \frac{\eta abh}{d} \left( 2\zeta + \frac{2}{3} \zeta^3 + \dots \right) \end{aligned} \quad (61)$$

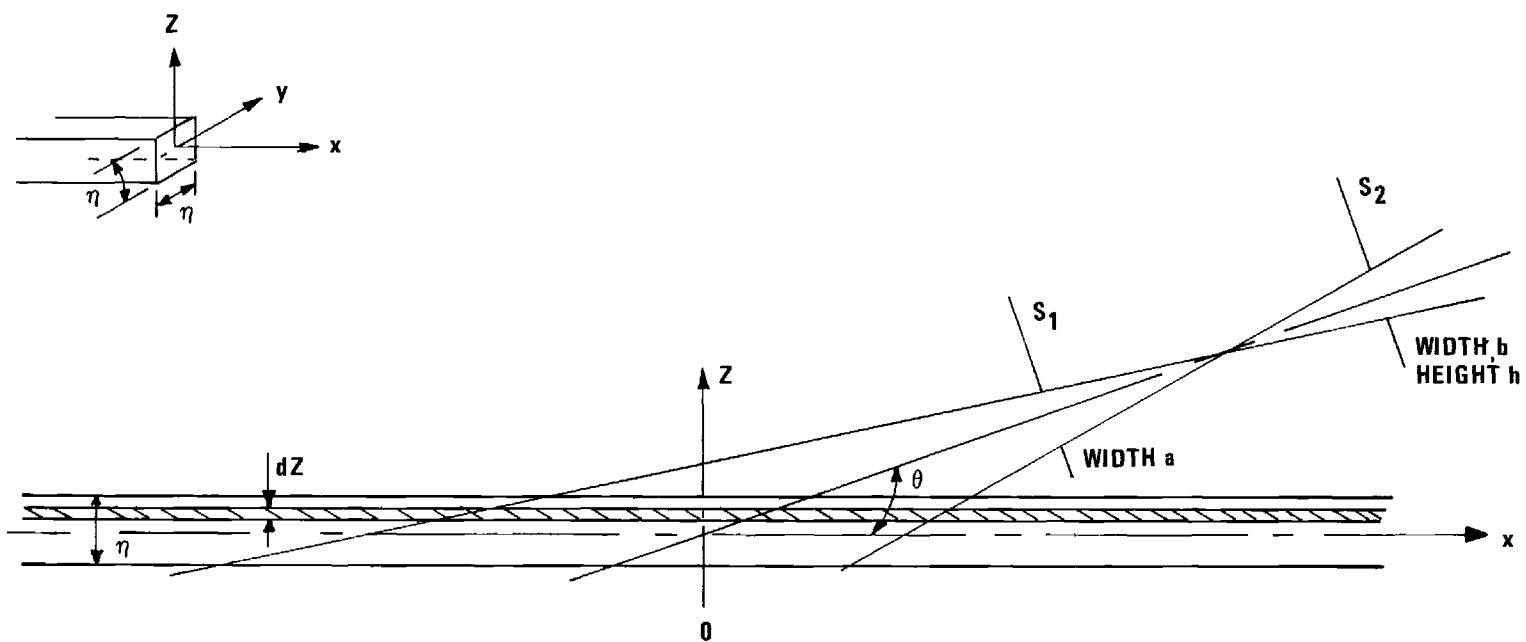


Figure 42. Finite Dimensions of Incident Beam.

where

$$\zeta = \frac{\eta}{2(d+l) \sin \theta} .$$

Keeping only the first term in the expansion

$$\int \omega dA dx \simeq \left( \frac{abh}{d(d+l)} \frac{1}{\sin \theta} \right) A \quad (62)$$

where

$$A = \eta^2 .$$

In dropping the higher order terms, one requires that

$$\eta^3 \ll 12(d+l)^3 \sin^3 \theta . \quad (63)$$

This approximation is certainly satisfied in the present experiment down to angles less than 30 minutes. The error introduced by ignoring the height of the beam is even less than this. Therefore, the finite size of the beam will not affect the present measurements.

## APPENDIX B

## CALIBRATION OF THE CAPACITANCE MANOMETER

The capacitance manometer was calibrated at the factory before shipment, but that calibration was at much higher gas pressures than those used in the present experiment. Since the measurement of the target gas pressure is the primary measure of the target density and the cross sections which were measured were inversely proportional to the target density, it was necessary to calibrate the capacitance manometer against a reference standard in the gas pressure range in which the present measurements were made, before the accuracy of the experimentally determined absolute differential scattering cross sections could be known.

The capacitance manometer was calibrated at Oak Ridge National Laboratory against two McLeod gauges. The gauge constants were

$$c_1 = 1.022 \times 10^{-7} \text{ Torr/mm}^2$$

$$c_2 = 2.473 \times 10^{-8} \text{ Torr/mm}^2$$

(Actually, a third gauge was also used, but its readings were consistently above the other two McLeod gauges by 13 percent; therefore, it was not used for the calibration.)

One of the McLeod gauges was refrigerated (gauge 1). This was done to reduce the streaming of mercury vapor from the McLeod gauge reservoir through connecting tubulation to cold traps in the system.<sup>66</sup> (This effect produces a pressure difference between the gauge and the rest of

the system, which is known as the Gaede effect.) The gas used during the calibration was hydrogen, this choice also being made to reduce the Gaede effect.

During the calibration, the refrigerated McLeod gauge was at the temperature  $T = 266^\circ\text{K}$ , the second McLeod gauge was at room temperature, the same as the sample gas ( $T = 302^\circ\text{K}$ ), while the capacitance manometer operated at an elevated temperature ( $T = 324^\circ\text{K}$ ). (The capacitance manometer normally operates at this elevated temperature. The operating temperature of this device affects its calibration, and an elevated temperature can quite readily be stabilized by means of electrical heaters and a thermostat.) These different temperatures in various parts of the system cause different pressures to exist within the system. A correction for this effect (thermal transpiration effect) is given by<sup>90</sup>

$$\frac{P_1}{P_2} = \sqrt{\frac{T_1}{T_2}} . \quad (64)$$

This correction increases the pressures measured by the refrigerated McLeod gauge by six percent, while the correction decreases the pressure measured with the capacitance manometer by two and one-half percent. With this correction for thermal transpiration applied to both the refrigerated McLeod gauge and the capacitance manometer, the calibration is shown in Figure 43.

This calibration covered the range from  $7.5 \times 10^{-5}$  Torr to  $9.2 \times 10^{-3}$  Torr, thus including approximately an order of magnitude on either side of the pressure range used in the cross section measurements. Below approximately one micron ( $10^{-3}$  Torr), the capacitance manometer



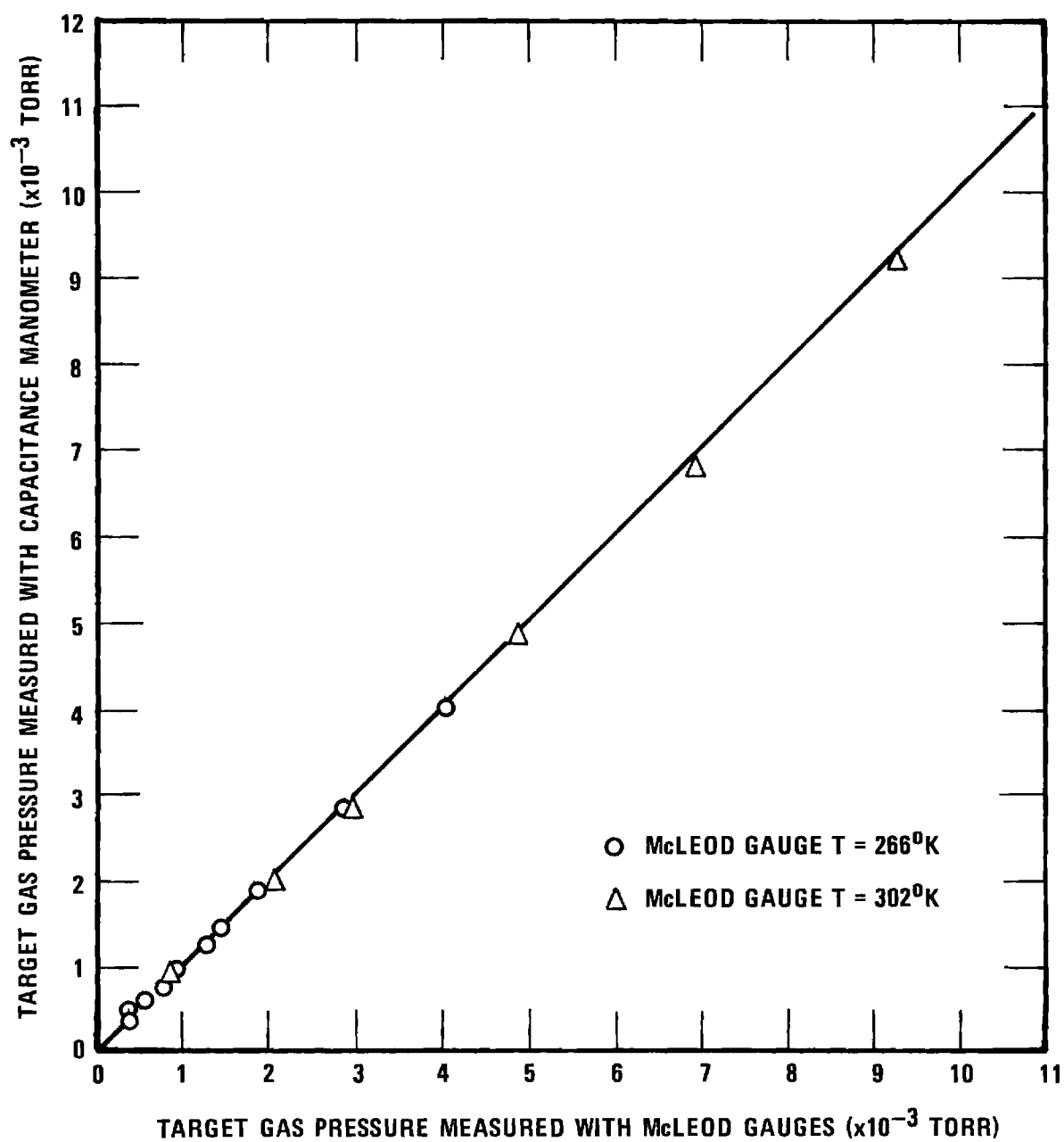


Figure 43. Calibration of Capacitance Manometer.

reading was higher than the McLeod gauge reading by approximately six percent; above one micron the two agreed to within one percent (see Figure 43).

The random error in reading the McLeod gauges was estimated to be plus or minus four percent. Many sources exist for possible systematic errors when using a McLeod gauge. The use of a refrigerated gauge and the choice of the sample gas were attempts to minimize systematic errors. The uncertainty in the gauge constants could introduce a systematic error. The accuracy of these constants was unknown; however, from the stated number of significant figures, it was estimated that the systematic error from this source would be less than one percent. It is therefore estimated that the possible systematic error in using these McLeod gauges was less than plus or minus one percent.

The possible random error in reading the capacitance manometer was estimated to be plus or minus two percent; possible systematic errors are estimated to be very small, less than 0.5 percent.

Therefore, the results from this calibration were that the capacitance manometer measures the absolute gas pressure through the pressure region used in the present experiment within plus or minus four percent. Scale reading errors are estimated to be plus or minus two percent, systematic errors are estimated to be plus or minus one percent.

## BIBLIOGRAPHY\*

1. F. T. Smith, Atomic Physics Proceedings of the First International Conference on Atomic Physics, June 3-7, 1968 (Plenum Press, New York, 1969), p. 353.
2. D. C. Lorents and W. Aberth, Phys. Rev. 139, A1017 (1965).
3. W. Aberth and D. C. Lorents, Phys. Rev. 144, 109 (1966).
4. V. V. Afrosimov, Yu. S. Gordeev, M. N. Panov, and N. V. Fedorenko, Zh. Eksperim. i Teor. Fiz. Pis'ma u Redaktsiyu 2, 291 (1965) [English Transl.: Soviet Phys.--JETP Letters 2, 185 (1965)].
5. P. R. Jones, T. L. Batra, and H. A. Rauga, Phys. Rev. Letters 17, 281 (1966).
6. H. H. Fleischmann and R. A. Young, Phys. Rev. Letters 19, 941 (1967).
7. P. Hoftager and G. Claussen, Sixth International Conference of the Physics of Electronic and Atomic Collisions (M.I.T. Press, Cambridge, 1969), p. 518.
8. E. N. Fuls, P. R. Jones, F. P. Ziemba, and E. Everhart, Phys. Rev. 107, 704 (1957).
9. F. P. Ziemba, G. J. Lockwood, G. H. Morgan, and E. Everhart, Phys. Rev. 118, 1552 (1960).
10. O. B. Firsov, Zh. Eksperim. i Teor. Fiz. 34, 447 (1958) [English Transl.: Soviet Phys.--JETP 34, 308 (1958)].
11. Q. C. Kessel and E. Everhart, Phys. Rev. 146, 16 (1966).
12. Q. C. Kessel, P. H. Rose, and L. Grodzins, Phys. Rev. Letters 22, 1031 (1969).
13. N. Bohr, Kgl. Danske Videnskab. Selskab, Mat.-fys. Medd. 18, No. 8 (1948).
14. D. R. Bates and R. McCarroll, Proc. Roy. Soc. (London) A245, 175 (1958).

---

\* Abbreviations used herein conform to those found in the American Institute of Physics Style Manual, 1965.

## BIBLIOGRAPHY (Continued)

15. E. Everhart, Phys. Rev. 132, 2083 (1963).
16. W. Lichten, Phys. Rev. 131, 229 (1963).
17. R. P. Marchi and F. T. Smith, Phys. Rev. 139, A1025 (1965).
18. A. Russek and M. T. Thomas, Phys. Rev. 109, 2015 (1958).
19. J. B. Bulman and A. Russek, Phys. Rev. 122, 506 (1961).
20. F. T. Smith, R. P. Marchi, W. Aberth, D. C. Lorents, and O. Heinz, Phys. Rev. 161, 31 (1967).
21. V. V. Afrosimov, Yu. S. Gordeev, M. N. Panov, and N. V. Fedorenko, Zh. Techn. Fiz. 36, 123 (1966)[English Transl.: Soviet Phys.--Tech. Phys. 11, 89 (1966)].
22. E. W. Thomas, Private Communications.
23. L. G. Filippenko, Zh. Techn. Fiz. 30, 57 (1960).
24. W. B. Maier, II, LASL-3972 (1968).
25. N. F. Mott and H. S. W. Massey, The Theory of Atomic Collisions (Oxford University Press, London, 1965), third edition, Chapt. V, Sec. 5.
26. E. Everhart, G. Stone, and R. J. Carbone, Phys. Rev. 99, 1287 (1955).
27. Earl W. McDaniel, Collision Phenomena in Ionized Gases (John Wiley & Sons, Inc., New York, 1964), Sections 3-10 and 4-10.
28. L. H. Thomas, Proc. Camb. Phil. Soc. 23, 542 (1927).
29. E. Fermi, Zeits. F. Physik 48, 73 (1928).
30. L. I. Schiff, Quantum Mechanics (McGraw-Hill Book Company, Inc., New York, 1955), second edition, p. 170.
31. H. Goldstein, Classical Mechanics (Addison-Wesley, Reading, Mass., 1950), Chapt. 3.
32. E. H. S. Burhop, Quantum Theory I. Elements, edited by D. R. Bates (Academic Press, Inc., New York, 1961), Chapt. 9.
33. O. B. Firsov, Zh. Eksperim. i Teor. Fiz. 24, 279 (1953).

## BIBLIOGRAPHY (Continued)

34. G. H. Lane and E. Everhart, Phys. Rev. 120, 2064 (1960).
35. F. T. Smith, R. P. Marchi, and K. G. Dedrick, Phys. Rev. 150, 79 (1966).
36. Felton W. Bingham, J. Chem. Phys. 46, 2003 (1967).
37. L. I. Pivovarov, M. T. Nivikov, and V. M. Tubaev, Proceedings of the Third International Conference on the Physics of Electronic and Atomic Collisions, London 1963 (North Holland Publishing Co., Amsterdam, 1964), p. 883.
38. O. B. Firsov, Zh. Eksperim. i Teor. Fiz. 33, 696 (1957)[English Transl.: Soviet Phys.--JETP 6, 534 (1958)].
39. Albert Messiah, Quantum Mechanics (John Wiley & Sons, Inc., New York, 1962), p. 618.
40. J. Lindhard, V. Nielsen, and M. Scharff, Kgl. Danske Videnskab. Selskab, Mat.-fys. Medd. 36, No. 10 (1968).
41. G. J. Lockwood, H. F. Helbig, E. Everhart, Phys. Rev. 132, 2078 (1963).
42. G. J. Lockwood and E. Everhart, Phys. Rev. 125, 567 (1962).
43. F. P. Ziemba and A. Russek, Phys. Rev. 115, 922 (1959).
44. D. R. Bates, H. S. W. Massey, and A. L. Stewart, Proc. Roy. Soc. (London) A216, 437 (1958).
45. P. E. Phillipson, Phys. Rev. 125, 1981 (1962).
46. William Lichten, Phys. Rev. 164, 131 (1967).
47. F. T. Smith, Phys. Rev. 179, 111 (1969).
48. N. F. Mott and H. S. W. Massey, Op. cit., Chapt. XIX, Sec. 7.
49. A. Russek, Phys. Rev. 132, 246 (1963).
50. Q. C. Kessel, M. P. McCaughey, and E. Everhart, Phys. Rev. Letters 16, 1189 (1966).
51. M. E. Rudd, T. Jorgensen, Jr., and D. L. Volk, Phys. Rev. 151, 28 (1966).
52. N. V. Fedorenko, Zh. Techn. Fiz. 24, 784 (1954).

## BIBLIOGRAPHY (Continued)

53. E. Everhart, R. J. Carbone, and S. Stone, Phys. Rev. 98, 1945 (1955).
54. N. V. Fedorenko, V. V. Afrosimov, and D. M. Kaminker, Zh. Techn. Fiz. 26, 1929 (1956)[English Transl.: Soviet Phys.--Tech. Phys. 1, 1861 (1957)].
55. V. V. Afrosimov, Yu. S. Gordeev, M. N. Panov, and N. V. Fedorenko, Zh. Techn. Fiz. 34, 1613 (1964)[English Transl.: Soviet Phys.--Tech. Phys. 9, 1248 (1965)].
56. L. I. Pivovar, M. T. Novikov, and V. M. Tubaev, Zh. Eksperim. i Teor. Fiz. 46, 471 (1964)[English Transl.: Soviet Phys.--JETP 19, 318 (1964)].
57. L. I. Pivovar, M. T. Novikov, and A. S. Dolgov, Zh. Eksperim. i Teor. Fiz. 49, 734 (1965)[English Transl.: Soviet Phys.--JETP 22, 508 (1966)].
58. L. I. Pivovar, M. T. Novikov, and A. S. Dolgov, Zh. Eksperim. i Teor. Fiz. 50, 537 (1966)[English Transl.: Soviet Phys.--JETP 23, 357 (1966)].
59. V. V. Afrosimov, Yu. S. Gordeev, Am. M. Polyansky, and A. P. Shergin, V International Conference on the Physics of Electronic and Atomic Collisions, Leningrad, U.S.S.R., July 17-23, 1967 (Publishing House, Nauka, 1967), p. 475.
60. A. B. Whittkower and H. B. Gilbody, Proc. Phys. Soc. (London) 90, 343 (1967).
61. H. B. Gilbody, R. Browning, and G. Levy, J. Phys. B (Proc. Phys. Soc.) 2, 230 (1968).
62. D. M. Kaminker and N. V. Fedorenko, Zh. Techn. Fiz. 25, 2239 (1955).
63. N. V. Fedorenko, L. G. Filippenko, and I. P. Flaks, Zh. Techn. Fiz. 30, 49 (1960)[English Transl.: Soviet Phys.--Tech. Phys. 30, 45 (1960)].
64. R. J. Carbone, E. N. Fuls, and E. Everhart, Phys. Rev. 102, 1524 (1956).
65. M. Ya. Amus'ya, Zh. Techn. Fiz. 36, 1409 (1966)[English Transl.: Soviet Phys.--Tech. Phys. 11, 1053 (1967)].

## BIBLIOGRAPHY (Continued)

66. L. J. Puckett, Absolute Total Apparent Ionization, Electron Stripping, Electron Capture, and Partial Ionization Cross Section in the Energy Range 0.15 - 1.00 MeV, Unpublished Ph.D. Thesis, Atlanta: Georgia Institute of Technology (1966).
67. J. W. Hooper, Ionization Cross Sections for Protons Incident on Helium, Neon, Argon, Hydrogen, Nitrogen, Oxygen, and Carbon Monoxide in the Energy Range 0.15 - 1.10 MeV, Unpublished Ph.D. Thesis, Atlanta: Georgia Institute of Technology (1961).
68. R. F. Taschek, H. V. Argo, A. Hemmendinger, and G. A. Jarvis, *Phys. Rev.* 76, 325 (1949).
69. H. A. Bethe and E. Salpeter, Quantum Mechanics of One and Two-Electron Atoms (Academic Press, Inc., New York, 1957), p. 251.
70. W. L. Wiese, M. W. Smith, and B. W. Glennon, Atomic Transition Probabilities, Vol. I Hydrogen Through Neon, National Bureau of Standards, U. S. Department of Commerce, Distributed by: Superintendent of Documents, U. S. Government Printing Office, Wash., D.C.
71. S. T. Butler and R. M. May, *Phys. Rev.* 137, A10 (1968).
72. N. V. Fedorenko, V. A. Ankudinov, and R. N. Il'in, *Zh. Techn. Fiz.* 35, 585 (1965)[English Transl.: *Soviet Phys.--Tech Phys.* 10, 461 (1965)].
73. M. F. A. Harrison, D. F. Dance, K. T. Dolder, and A. C. H. Smith, *Rev. Sci. Instr.* 36, 1443 (1965).
74. N. G. Utterback and T. Griffith, Jr., *Rev. Sci. Instr.* 37, 866 (1966).
75. ORTEC Catalogue 1001, Ortec, Oak Ridge, Tennessee.
76. R. D. Evans, The Atomic Nucleus (McGraw-Hill Book Company, Inc., New York, 1955), Chapt. 26.
77. Charlotte E. Moore, A Multiplet Table of Astrophysical Interest, PB151 395, Distributed by: Clearinghouse for Federal Scientific and Technical Information, National Bureau of Standards, U. S. Department of Commerce, Springfield, Va.
78. Charlotte E. Moore, An Ultraviolet Multiplet Table, National Bureau of Standards, U. S. Department of Commerce, Distributed by: Superintendent of Documents, U. S. Government Printing Office, Washington, D. C.

## BIBLIOGRAPHY (Concluded)

79. Evans, op. cit., p. 750.
80. D. W. Martin, R. A. Langley, D. S. Harmer, J. W. Hooper, and E. W. McDaniel, Phys. Rev. 136A, 185 (1964).
81. F. J. DeHeer, J. Schutten, and H. Moustafa, Physica 32, 1793 (1966).
82. S. K. Allison, Rev. Mod. Phys. 30, 1137 (1958).
83. P. R. Jones, F. P. Ziemba, H. A. Moses, E. Everhart, Phys. Rev. 113, 182 (1959).
84. B. L. Moiseiwitsch, Proc. Phys. Soc. A59, 653 (1956).
85. H. Schiff, Canad. J. Phys. 32, 393 (1954).
86. J. B. Hasted, Physics of Atomic Collisions (Butterworths, London, 1964), p. 437.
87. F. P. Ziemba and E. Everhart, Phys. Rev. Letters 2, 299 (1959).
88. I. P. Skalskaya, Zh. Techn. Fiz. 24, 1912 (1954).
89. E. B. Jordan and R. B. Brode, Phys. Rev. 43, 112 (1933).
90. Saul Dushman, Scientific Foundations of Vacuum Technique (John Wiley & Sons, Inc., New York, 1962) second edition, p. 58.